MODELING AND CONTROL OF A HELICOPTER SLUNG LOAD SYSTEM

A THESIS SUBMITTED TO
THE GRADUATE SCHOOL OF NATURAL AND APPLIED SCIENCES
OF
MIDDLE EAST TECHNICAL UNIVERSITY

BY

ÖMER OĞUZHAN GÜNGÖREN

IN PARTIAL FULFILLMENT OF THE REQUIREMENTS
FOR
THE DEGREE OF MASTER OF SCIENCE
IN
MECHANICAL ENGINEERING

SEPTEMBER 2024

Approval of the thesis:

MODELING AND CONTROL OF A HELICOPTER SLUNG LOAD SYSTEM

submitted by **ÖMER OĞUZHAN GÜNGÖREN** in partial fulfillment of the requirements for the degree of **Master of Science** i**n Mechanical Engineering, Middle East Technical University** by,

Prof. Dr. Naci Emre Altun
Dean, **Graduate School of Natural and Applied Sciences** _____

Prof. Dr. Serkan Dağ
Head of the Department, **Mechanical Engineering** _____

Assist. Prof. Dr. Hakan Çalışkan
Supervisor, **Mechanical Engineering, METU** _____

Examining Committee Members:

Prof. Dr. Yiğit Yazıcıoğlu
Mechanical Engineering, METU _____

Assist. Prof. Dr. Hakan Çalışkan
Mechanical Engineering, METU _____

Prof. Dr. Ender Ciğeroğlu
Mechanical Engineering, METU _____

Assoc. Prof. Dr. Ulaş Yaman
Mechanical Engineering, METU _____

Assist. Prof. Dr. Yakup Özkazanç
Electrical and Electronics Engineering, Hacettepe University _____

Date: 03.09.2024

I hereby declare that all information in this document has been obtained and presented in accordance with academic rules and ethical conduct. I also declare that, as required by these rules and conduct, I have fully cited and referenced all material and results that are not original to this work.

Name, Last name : Ömer Oğuzhan Güngören

Signature :

ABSTRACT

MODELING AND CONTROL OF A HELICOPTER SLUNG LOAD SYSTEM

Güngören, Ömer Oğuzhan
Master of Science, Mechanical Engineering
Supervisor : Assist. Prof. Dr. Hakan Çalışkan

September 2024, 179 pages

Carrying slung loads has always been an important mission for both civil and military helicopters. Considering that with a proper implementation of a slung load system, cargo and ammunition delivery, search and rescue operations and even fire intervention can be performed very effectively, this is not surprising. However, beside these benefits, slung load systems bring about problems related to the stability and handling quality of the helicopter, which can also affect control of the helicopter adversely and increase the pilot workload.

This study aims to provide a proper slung load modeling approach and a control strategy with the capability of yielding efficient slung load damping. Development of the mathematical model is based on generic Newton-Euler equations. Regarding the slung load control, several schemes are considered, including input shaping, delayed feedback control, angular rate feedback control and model predictive control. Based on the simulation results, proposed control algorithm with optimal characteristics is selected as the combination of input shaping and model predictive control. Moreover, a Kalman Filter algorithm is generated such that slung load states can be efficiently estimated with measured helicopter states.

Given that there is a strong coupling between the helicopter and the slung load, the study considers the development of a full nonlinear helicopter model and implementation of a flight control system as well. The flight control system of the helicopter involves inner loop-outer loop control architecture. The proposed flight control system is evaluated by considering the maximum overshoot and settling time characteristics as well as the robustness.

Keywords: Helicopter, Slung Load, Input Shaping, Delayed Feedback Control, Angular Rate Feedback, Model Predictive Control

ÖZ

HELİKOPER ASILI YÜK SİSTEMİNİN MODELLENMESİ VE KONTROLÜ

Güngören, Ömer Oğuzhan
Yüksek Lisans, Makina Mühendisliği
Tez Yöneticisi: Dr. Öğr. Üyesi Hakan Çalışkan

Eylül 2024, 179 sayfa

Asılı yüklerin taşınması hem sivil hem de askeri helikopterler için her zaman önemli bir görev olmuştur. Asılı yük sisteminin doğru bir şekilde entegre edilmesiyle kargo ve mühimmat sevkiyatının, arama kurtarma operasyonlarının ve hatta yangına müdahalenin çok etkili bir şekilde yapılabileceği düşünüldüğünde bu durumun pek de şaşırtıcı olmadığı söylenebilir. Ancak, asılı yük sistemi bu faydalarının yanı sıra helikopterin stabilitesi ve kullanım kalitesi ile ilgili sorunları da beraberinde getirmekte, bu da helikopterin kontrolünü olumsuz yönde etkileyebilmekte ve pilotun iş yükünü artırabilmektedir.

Bu çalışma, uygun bir asılı yük modelleme yaklaşımı ve etkili asılı yük sönümlemesi sağlama kapasitesine sahip bir kontrol stratejisi geliştirmeyi amaçlamaktadır. Matematiksel modelin geliştirilmesi genel Newton-Euler denklemlerine dayanmaktadır. Asılı yük kontrolü ile ilgili olarak, giriş şekillendirme, gecikmeli geri beslemeli kontrol, açısal hız geri beslemeli kontrol ve model öngörülü kontrol dahil olmak üzere çeşitli yöntemler incelenmiştir. Simülasyon sonuçlarına dayanarak, optimal özelliklere sahip önerilen kontrol algoritması, girdi şekillendirme ve model öngörülü kontrolün birleşimi olarak seçilmiştir. Bununla birlikte, asılı yük

durumlarının, ölçülen helikopter durumlarıyla verimli bir şekilde tahmin edilebilmesini sağlayacak bir Kalman Filtre algoritması oluşturulmuştur.

Helikopter ile asılı yük arasında güçlü bir bağlantı olduğu göz önüne alındığında, çalışmada doğrusal olmayan bir helikopter modelinin geliştirilmesi ve bir uçuş kontrol sisteminin uygulanması da ele alınmaktadır. Helikopterin uçuş kontrol sistemi iç döngü-dış döngü kontrol mimarisini içerir. Önerilen uçuş kontrol sistemi gürbüzlüğün yanı sıra maksimum aşma ve yerleşme zamanı özellikleri de dikkate alınarak değerlendirilmiştir.

Anahtar Kelimeler: Helikopter, Asılı Yük, Girdi Şekillendirme, Gecikmeli Geri Beslemeli Kontrol, Açısal Hız Geri Besleme, Model Öngörülü Kontrol

To my family

ACKNOWLEDGMENTS

I would like to sincerely thank my supervisor Assist. Prof. Dr. Hakan Çalışkan for his guidance, advice, support and encouragement throughout this research.

I would like to thank Ilgaz Doğa Okcu and Cenk Çetin from Turkish Aerospace for their support and for everything I have learned from them as an engineer, starting from my undergraduate internship years.

I would like to thank Muhammed Enes İsanç, Melih Kaan Kayapınar, Emre Batuhan Baloğlu and Burak Kerem Demirdağ for their support and years of valuable friendship.

Finally, I would like to express my deepest gratitude to my dear family for their invaluable support and love.

TABLE OF CONTENTS

ABSTRACT v

ÖZ vii

ACKNOWLEDGMENTS x

TABLE OF CONTENTS xi

LIST OF TABLES xv

LIST OF FIGURES xvi

LIST OF ABBREVIATIONS xxi

LIST OF SYMBOLS xxii

CHAPTERS

1 INTRODUCTION 1

1.1 Motivation 1

1.2 Contribution 1

1.3 Thesis Outline 2

2 LITERATURE REVIEW 5

2.1 Mathematical Modeling of the Helicopter Slung Load System 5

2.2 Control of the Helicopter Slung Load System 7

3 DEVELOPMENT OF A HELICOPTER MATHEMATICAL MODEL 9

3.1.1 Coordinate Systems Utilized in the Mathematical Model 10

3.1.2 Main Rotor and Tail Rotor Modules 12

3.1.3 Control System Module 18

3.1.4 Fuselage Aerodynamics Module 18

3.1.5 Equations of Motion Module 22

3.2 Trim Algorithm for the Nonlinear Helicopter Model 25

3.3 Linearization of the Helicopter Model 28
4 STABILITY AUGMENTATION SYSTEM (SAS) AND AUTOPLIT DESIGN FOR THE HELICOPTER 35
4.1 Stability Augmentation System (SAS) Design 35
4.1.1 Design of Pitch Axis Stability Augmentation System 36
4.1.2 Design of Lateral-Directional Stability Augmentation System 38
4.2 Autopilot Design 42
4.2.1 Pitch Attitude Hold Autopilot 42
4.2.2 Roll Attitude Hold Autopilot 44
4.2.3 Heading Hold Autopilot 46
4.2.4 Altitude Hold Autopilot 48
5 MATHEMATICAL MODELING OF THE HELICOPTER SLUNG LOAD SYSTEM 57
5.1 Mathematical Modeling of the Slung Load System 57
5.1.1 Derivation of the Governing Equations of Motion 60
5.1.2 Slung Load Aerodynamics 66
5.2 Trim Algorithm for the Compound Helicopter and Slung Load System 68
5.3 Linearization of the Compound Helicopter and Slung Load System 68
5.4 Validation of the Mathematical Model 69
6 CONTROL OF THE HELICOPTER SLUNG LOAD SYSTEM 75
6.1 Helicopter-Slung Load Dynamics Inspection with the Existing Helicopter Controllers 75
6.2 Slung Load Control with Input Shaping 79
6.2.1 Theoretical Background for Input Shaping 79
6.2.2 Application of Input Shaping to Slung Load Control 85

6.3 Slung Load Control with Delayed Cable Angle Feedback 95
6.3.1 Particle Swarm Optimization Algorithm 97
6.3.2 Application of Particle Swarm Optimization on Slung Load Control 98
6.4 Slung Load Control with Cable Angle Rate Feedback 100
6.5 Kalman Filter Design for Slung Load System State Estimation 110
6.5.1 Simulation Results with Kalman Filter and Delayed Feedback Control 115
6.5.2 Simulation Results with Kalman Filter and Cable Angle Rate Feedback controllers 116
6.5.3 Kalman Filter Performance Evaluation..... 117
6.6 Slung Load Control Strategy Comparison 121
6.7 Model Predictive Control of Slung Load System 122
6.7.1 Theoretical Background for Model Predictive Control 122
6.7.2 Application of Model Predictive Control on Slung Load System .. 129
6.7.3 Application of Model Predictive Control to Full-Nonlinear Model 140
6.7.4 Application of Input Shaping and Model Predictive Control for Forward Flight 142
7 CONCLUSION.....163
7.1 Conclusion..... 163
7.2 Future Work 165
REFERENCES 167
APPENDICES 171
A. Helicopter Mathematical Model Parameters..... 171
B. Aerodynamic Coefficient Tables for Fuselage..... 173

C. Slung Load Mass and Inertia Values 179

LIST OF TABLES

TABLES

Table 3.1. Longitudinal Dynamic Modes 31
Table 3.2. Lateral Dynamic Modes..... 32
Table 4.1. List of Autopilots for Hovering Flight Condition..... 51
Table 6.1. Oscillatory Slung Load Poles..... 87
Table 6.2. Natural Frequency and Damping Ratio of the Slung Load Pendulum Modes..... 87
Table 6.3. Natural Frequency and Damping Ratio Parameters Calculated by Logarithmic Decrement Method..... 89
Table 6.4. Impulse Amplitudes and Instances for ZVD Input Shapers 90
Table 6.5. Impulse Amplitudes and Instances for ZV Input Shapers 93
Table 6.6 Oscillatory Slung Load Poles..... 101
Table 6.7. Proposed Autopilots for 60 Knots Forward Flight 143
Table 6.8. Oscillatory Slung Load Poles at 60 Knots Forward Flight..... 149
Table 6.9. Natural Frequency and Damping Ratio of the Slung Load Pendulum Modes at 60 Knots Forward Flight 149
Table 6.10. Impulse Amplitudes and Instances for ZVD Input Shapers at 60 Knots 150
Table A.1. Values of Parameters for CH-53 Helicopter..... 171
Table A.2. Values of Parameters for CH-53 Helicopter (Continued)..... 172

LIST OF FIGURES

FIGURES

Figure 3.1. Block Diagram of the Overall System 10
Figure 3.2. Frames of Reference and Rotor Flapping Angle Definitions [1] 11
Figure 3.3. Trim Results Comparison with GENHEL Model 26
Figure 3.4. Time History Comparison with Flight Test Data 28
Figure 3.5. Dynamic Modes of the Linear System 30
Figure 3.6. Dynamic Modes of the Linear System (Comparison with Literature) 33
Figure 3.7. Nonlinear and Linear Model Time History Comparison 34
Figure 4.1. Block Diagram for Pitch Axis SAS 36
Figure 4.2. Root Locus Diagram for $q/\delta lon$ 37
Figure 4.3. Root Locus Diagram for $q/\delta lon$ with Compensator 38
Figure 4.4. Block Diagram for the Lateral SAS 39
Figure 4.5. Root Locus Diagram for $p/\delta lat$ 39
Figure 4.6. Block Diagram for the Directional SAS 40
Figure 4.7. Root Locus Diagram for $r/\delta pedal$ 41
Figure 4.8. Pitch Attitude Hold Autopilot 42
Figure 4.9. Unit Step Response for Pitch Attitude Hold Autopilot 43
Figure 4.10. Bode Diagram for Pitch Attitude Hold Autopilot 44
Figure 4.11. Roll Attitude Hold Autopilot 44
Figure 4.12. Unit Step Response for Roll Attitude Hold Autopilot 45
Figure 4.13. Bode Diagram for Roll Attitude Hold Autopilot 46
Figure 4.14. Heading Hold Autopilot 46
Figure 4.15. Unit Step Response for Heading Hold Autopilot 47
Figure 4.16. Bode Diagram for Heading Hold Autopilot 48
Figure 4.17. Altitude Hold Autopilot 49
Figure 4.18. Step Response for Altitude Hold Autopilot 49
Figure 4.19. Bode Diagram for Altitude Hold Autopilot 50
Figure 4.20. Block Diagram of the Closed Loop System 52

Figure 4.21. Input Profiles for Simulation 53
Figure 4.22. Nonlinear and Linear Model Comparison with Engaged Flight Control System 53
Figure 4.23. Control Effort Comparison for Nonlinear and Linear Models 54
Figure 5.1. Overall Block Diagram for Compound Helicopter-Slung Load System 58
Figure 5.2. Left View of Slung Load System 59
Figure 5.3. Rear View of Slung Load System 59
Figure 5.4. Top View of Slung Load System 60
Figure 5.5. Frames of Reference and Kinematic Relations for the Compound Model 61
Figure 5.6. Pole Locations for the Compound Helicopter-Slung Load Model in Hovering Flight 70
Figure 5.7. Pole Locations for the Compound Helicopter-Slung Load Model in Hovering Flight (Comparison with Literature) 71
Figure 5.8. Variation of System Poles with Increasing Cable Length 73
Figure 6.1. Block Diagram for the Closed Loop System with Helicopter and Slung Load 76
Figure 6.2. Input Profiles for Simulation 77
Figure 6.3. Slung Load Cable Angles 77
Figure 6.4. Helicopter States 78
Figure 6.5. Concept of Input Shaping [28] 79
Figure 6.6. Process of Input Shaping [28] 82
Figure 6.7. Sensitivity Curves for Input Shaping Process [28] 83
Figure 6.8. Response Characteristics Comparison for Different Input Shapers [28] 84
Figure 6.9. Closed Loop Poles of the Compound System without Slung Load Controller (Close View) 86
Figure 6.10. Time History of Longitudinal and Lateral Slung Load Cable Angles 88
Figure 6.11. ZVD Input Shaping Filter [30] 90

Figure 6.12. Block Diagram for the Closed Loop System with Input Shaping Filters 90
Figure 6.13. Input Shaped Reference Commands 91
Figure 6.14. Slung Load Cable Angles with ZVD Input Shaped Reference Commands 91
Figure 6.15. Helicopter States with ZVD Input Shaped Reference Commands 92
Figure 6.16. ZV Input Shaped Reference Commands 93
Figure 6.17. Slung Load Cable Angles with ZV Input Shaped Reference Commands 94
Figure 6.18. ZV vs ZVD Input Shaper Response Comparison 95
Figure 6.19. Block Diagram of the Closed Loop System with Delayed Feedback Controllers 96
Figure 6.20. Slung Load Cable Angles with Delayed Cable Angle Feedback 99
Figure 6.21. Helicopter States with Delayed Cable Angle Feedback 100
Figure 6.22. Closed Loop Compound System with Cable Angle Rate Feedback 102
Figure 6.23. Root Locus Diagram for Longitudinal Cable Angle 104
Figure 6.24. Root Locus Diagram for Longitudinal Cable Angle (Closed-Up View) 104
Figure 6.25. Closed Loop System Poles with Cable Angle Rate Feedback Controller 106
Figure 6.26. Slung Load Cable Angles with Cable Angle Rate Feedback Controllers 108
Figure 6.27. Helicopter States with Cable Angle Rate Feedback Controllers 109
Figure 6.28. Kalman Filter for Estimation of Slung Load States 113
Figure 6.29. Simulation Results with Delayed Feedback Controllers and Kalman Filter 115
Figure 6.30. Simulation Results with Cable Angle Rate Feedback Controllers and Kalman Filter 116
Figure 6.31. Measurement Noise Injected to Linear Velocity States 118
Figure 6.32. Pole Locations of the Linearized Models 119

Figure 6.33. Kalman Filter Performance in the Presence of Noise and Disturbance 120
Figure 6.34 Comparison of Slung Load Control Strategies 121
Figure 6.35. MPC Strategy [37] 123
Figure 6.36. Block Diagram for MPC Algorithm [38] 124
Figure 6.37. Block Diagram of the Closed Loop System with MPC 130
Figure 6.38. Reference Slung Load Trajectories 132
Figure 6.39. Slung Load Cable Angles with MPC and Full-State Output 134
Figure 6.40. Helicopter Reference Roll and Pitch Attitudes with MPC 135
Figure 6.41. Slung Load Cable Angles with MPC and Kalman Filter 136
Figure 6.42. Effect of Disturbance on Controller Performance 137
Figure 6.43. Effect of Measurement Noise and Plant Model Discrepancy on Model Predictive Controller Performance 139
Figure 6.44. Linear-Nonlinear Model MPC Comparison 141
Figure 6.45. Pole Locations of the Linearized Model at 60 Knots Forward Flight 144
Figure 6.46. Comparison of the Pole Locations of the Compound Helicopter-Slung Load Model with the Reference in [4] 145
Figure 6.47. Slung Load Cable Angles at 60 Knots Forward Flight 147
Figure 6.48. Pole Locations of the Closed Loop Compound System at 60 Knots 148
Figure 6.49. Input Shaped Reference Commands 150
Figure 6.50. Slung Load Cable Angles with ZVD Input Shaped Reference Commands 151
Figure 6.51. Model Predictive Controller Structure for 60 Knots Forward Flight 153
Figure 6.52. Reference Trajectories for Lateral Channel 154
Figure 6.53. Reference Trajectories for Longitudinal Channel 154
Figure 6.54. Slung Load Cable Angles with MPC and Full-State Output 155
Figure 6.55. Helicopter Pitch and Roll Attitudes with MPC and Full-State Output 156
Figure 6.56. Slung Load Cable Angles with MPC and Kalman Filter 157

Figure 6.57. Helicopter Pitch and Roll Attitudes with MPC and Kalman Filter...157
Figure 6.58. Linear-Nonlinear Model MPC Comparison of Slung Load Cable Angles.....159
Figure 6.59. Linear-Nonlinear Model MPC Comparison of Helicopter Pitch and Roll Attitudes.....161
Figure B.1. Fuselage Incremental Drag as a Function of Angle of Attack [1].....173
Figure B.2. Fuselage Incremental Lift as a Function of Angle of Attack [1].....174
Figure B.3. Fuselage Incremental Lift as a Function of Sideslip [1] 174
Figure B.4. Fuselage Side Force as a Function of Sideslip [1] 175
Figure B.5. Fuselage Incremental Rolling Moment as a Function of Angle of Attack [1].....175
Figure B.6. Fuselage Incremental Rolling Moment as a Function of Sideslip [1] 176
Figure B.7. Fuselage Incremental Pitching Moment as a Function of Angle of Attack and Incidence at the Tail [1] 177
Figure B.8. Fuselage Incremental Pitching Moment as a Function of Sideslip [1] 177
Figure B.9. Fuselage Yawing Moment as a Function of Sideslip and Angle of Attack [1].....178

LIST OF ABBREVIATIONS

ABBREVIATIONS

PID	Proportional-Integral-Derivative Controller
ZV	Zero Vibration Input Shaper
ZVD	Zero Vibration and Derivative Input Shaper
SAS	Stability Augmentation System
AFCS	Automatic Flight Control System
MPC	Model Predictive Control
MR	Main Rotor
TR	Tail Rotor
c.g.	Center of Gravity

LIST OF SYMBOLS

SYMBOLS

A_1, B_1	Lateral and longitudinal swashplate angle commands, [rad]
a	Rotor blade lift-curve slope, [1/rad]
a'	Small angle used to define rotor drag force, [rad]
a_0	Coning angle, [rad]
a_1, b_1	Longitudinal and lateral flapping angles in control axes, [rad]
a_{1s}, b_{1s}	Longitudinal and lateral flapping angles in shaft axes, [rad]
B	Rotor blade tip-loss constant, [n.d.]
b	Number of blades per rotor, [n.d.]
$C_{c/s}$	Transformation matrix from shaft to control axes, [n.d.]
$C_{h/e}$	Transformation matrix from earth to body axes, [n.d.]
$C_{h/wt}$	Transformation matrix from wind tunnel to body axes, [n.d.]
C_Q	Nondimensional torque coefficient, [n.d.]
C_T	Nondimensional thrust coefficient, [n.d.]
C_Y	Rotor side force coefficient, [n.d.]
c	Blade chord, [m]
D_{wt}	Fuselage drag in wind tunnel axes, [N]
e	Flapping hinge offset, [m]
e_{kf}, e_{kt}	Fuselage and tail angle of attack corrections due to downwash, [n.d.]
e_{mr}	Main rotor downwash factor, [n.d.]
g	Gravitational acceleration, [m/s^2]
H	Rotor drag force, [N]
h	Altitude, [m]
I_b	Blade moment of inertia about flapping axis, [kg×m^2]
I_h	Inertia matrix of helicopter in body axes, [kg×m^2]
I_{mr}	Polar moment of inertia of main rotor, [kg×m^2]

i_t	Horizontal tail incidence angle, [deg]
i_{t0}	Horizontal tail default set angle, [deg]
J	Rotor side force, [N]
K_f	Fuselage pitching moment coefficient due to MR Thrust, [m]
$K_i, i = 1 \ldots$	Constant gains in control system module
$[L, M, N]_{d,h}$	Body axes moments due to angular velocity, [Nm]
$[L, M, N]_{f,h}$	Body axes moments due fuselage aerodynamics, [Nm]
$[L, M, N]_{hub,h}$	Body axes moments due to rotor moments, [Nm]
$[L, M, N]_{hub,s}$	Shaft axes moments due to rotor moments, [Nm]
$[L, M, N]_{r,h}$	Total body axes moments due to rotors, [Nm]
$[L, M, N]_{wt}$	Body axes aerodynamic moments acting on the fuselage, [Nm]
$\tilde{L}_{wt}$	Fuselage lift in wind tunnel axes, [N]
M_w	Mass moment of rotor blade, [kg×m]
m	Helicopter mass, [kg]
$[p, q, r]_c$	Angular velocities in control axes, [rad/sec]
$[p, q, r]_h$	Angular velocities in body axes, [rad/sec]
$[p, q, r]_s$	Angular velocities in shaft axes, [rad/sec]
Q_{am}	Aerodynamic torque acting on main rotor, [Nm]
Q_{at}	Aerodynamic torque acting on tail rotor, [Nm]
$\bar{q}$	Dynamic pressure, [N/m^2]
R	Rotor radius, [m]
T	Rotor thrust, [N]
$[u, v, w]_{as,h}$	True airspeed of the helicopter c.g. in body axes [m/s]
$[u, v, w]_c$	True airspeed of rotor hub in control axes [m/s]
$[u, v, w]_{cg,e}$	Inertial velocity of helicopter c.g. in earth axes, [m/s]
$[u, v, w]_{gust,h}$	Gust velocity in body axes, [m/s]
$[u, v, w]_s$	True airspeed of the rotor hub in shaft axes
$[u, v, w]_{wind,h}$	Wind velocity in body axes, [m/s]
$V_{as,h}$	Total true airspeed, [m/s]

X_{col}	Pilot control displacement of the collective stick, [cm]
X_{lon}	Pilot control displacement of the longitudinal cyclic stick, [cm]
X_{lat}	Pilot control displacement of the lateral cyclic stick, [cm]
X_{ped}	Pilot control displacement of the pedal, [cm]
$[X, Y, Z]_{f,h}$	Body axes forces due to fuselage aerodynamics, [N]
$[X, Y, Z]_{r,h}$	Body axes forces due to rotors, [N]
$[x, y, z]_{cg,e}$	Inertial position in earth axes, [m]
$[x, y, z]_{r,h}$	Rotor hub location in body axes, [m]
$[x, y, z]_{wt,h}$	Wind tunnel mounting point in body axes, [m]
Y_{wt}	Fuselage side force in wind tunnel axes, [N]
α_f	Fuselage angle of attack, [deg]
β_f	Fuselage angle of sideslip, [deg]
α_{fl}	Fuselage local angle of attack, [deg]
β	Rotor orientation angle, [deg]
γ	Rotor lock number, [n.d.]
θ_{ct}	Tail rotor collective pitch command, [rad]
θ_{0m}	Main rotor collective pitch command, [rad]
θ_{0t}	Effective value of tail rotor collective pitch, [rad]
θ_s	Longitudinal shaft tilt angle, [deg]
θ_1	Blade twist angle, [deg]
$\theta_{0.75}$	Blade pitch at 3/4 radius, [deg]
λ	Inflow ratio, [n.d.]
μ	Tip speed ratio, [n.d.]
ν	Induced inflow ratio, [n.d.]
ρ	Atmospheric density, [kg/m^3.]
σ	Rotor solidity, [n.d.]
τ_v	Inflow time constant, [n.d.]
ϕ_s	Lateral shaft tilt angle, [deg]
$[\phi, \theta, \psi]$	Euler angles of the helicopter, [rad]

ψ_{wt}	Wind tunnel yaw angle, [deg]
Ω	Rotor angular velocity, [rad/s]

CHAPTER 1

INTRODUCTION

1.1 Motivation

Motivation of this thesis study is to propose a realistic mathematical modeling approach for a generic helicopter slung load system and put forward effective control strategies that are capable of enhancing its stability characteristics and eliminating undesirable oscillatory behavior.

It is known that strong coupling exist between the helicopter and slung load systems. Hence, development of a nonlinear helicopter model and design of a helicopter flight control system are also considered so that the characteristics of the overall compound system can be inspected in detail.

1.2 Contribution

This thesis study provides an easy to implement slung load modeling approach that is verified with existing studies in the literature. In addition, various strategies that can be found in the literature regarding the slung load control, including the input shaping, delayed cable angle feedback control and cable angle rate feedback control, are examined and compared to find the most effective approach in terms of stability characteristics and oscillatory behavior suppression. Moreover, for slung load cable angle and angular rate feedback applications, a Kalman Filter algorithm is designed in order to perform an estimation based on the measured helicopter states.

Finally, for further enhancement of the slung load dynamic characteristics, a new control methodology that involves the combination of input shaping and model predictive control is put forward.

1.3 Thesis Outline

This thesis study consists of seven chapters.

In the first chapter, motivation of the study and its contributions to the literature are discussed.

The second chapter is the literature review and it is dedicated to elaboration on the existing mathematical modeling and control approaches regarding the helicopter slung load systems.

In the third chapter, a complete nonlinear helicopter mathematical model is designed based on a document published by NASA [1]. Moreover, a trim algorithm for the generated mathematical model is proposed and a linearization method is put forward in order to obtain the linearized models to be used in control law development. Finally, the helicopter mathematical model is verified by comparing the trimmed flight results with Sikorsky's well known validated GenHel Model as well as making a time history comparison with real-life flight test data.

In the fourth chapter, development of an automatic flight control system for the helicopter based on the linearized models obtained in the third chapter is discussed. Generic inner loop-outer loop control structure is implemented. The proposed control system is evaluated by taking the time response characteristics (maximum overshoot and settling time) as well the robustness criteria (minimum gain and phase margins) into account.

In the fifth chapter, mathematical modeling approach for the slung load system is presented. The governing equations of motion are derived based on generic Newton-Euler equations. The helicopter model designed in the second chapter is also

included in the derivation to account for the coupling between the helicopter and the slung load. The generated nonlinear mathematical model is trimmed and linearized in a similar manner to the helicopter by itself for the control law development. Mathematical model validation of the compound helicopter-slung load system is performed based on a comparison with a study in the literature that uses a similar configuration, by inspecting the pole locations of the linearized model in the complex plane.

In the sixth chapter, control of the slung load system is discussed by proposing several different methodologies including input shaping, delayed cable angle feedback control and cable angle rate feedback control. Regarding the feedback control applications, a Kalman Filter algorithm is implemented in order to estimate the slung load states based on the measured helicopter states. Also, performance of the designed Kalman Filter is tested in the presence of measurement noise and plant model discrepancy to verify its robustness. Finally, a new control methodology that involves combination of input shaping and model predictive control is put forward in order to obtain the optimal approach in terms of closed loop slung load dynamic characteristics. In the proposed controller, robustness verification is accounted for by inclusion of the measurement noise and plant model discrepancy as in the case of Kalman Filter.

The seventh and final chapter involves the conclusions that are drawn from this study as well as future research work that can be performed for further improvement.

CHAPTER 2

LITERATURE REVIEW

Mathematical modeling and control of the slung load systems have been important fields of study in the aviation industry for many years and there are numerous viable research work that can be found in the literature.

The discussion is provided under two subsections that account for the mathematical modeling and control of the slung load separately.

2.1 Mathematical Modeling of the Helicopter Slung Load System

In a relatively early study conducted in 1975, Cliff and Bailey [2], developed a simplified mathematical model that involves connection of two particles with an inextensible link to represent the helicopter-slung load configuration by neglecting all the aerodynamic affects other than load drag. They performed linearization about steady flight condition and showed that the perturbation equations are separated into longitudinal and lateral/directional sets. The modes of the linearized model are examined in terms of variation with respect to helicopter mass and link length and conclusions regarding the effect on stability are drawn. It is also suggested that a more complicated helicopter-slung load model is needed for proper identification.

In the study carried out by Prabhakar [3], aerodynamic properties of a two-point longitudinal slung load configuration are determined experimentally and the stability characteristics of the compound full scale helicopter-slung load configuration are examined.

In a later study conducted by Ronen [4], a dynamic model for the compound helicopter-slung load system is developed based on Newton-Euler equations. As an additional improvement over the previous studies, this particular one involved the main rotor downwash effect on the slung load in hovering and low-speed flight regime. In addition, unsteady aerodynamic characteristics of the slung load are also taken into account.

In the study that can be found in [5], a mathematical model for the CH-54 helicopter with a single attachment point slung load configuration is developed. The slung load aerodynamics are included in the derivation of the model by using wind tunnel aerodynamic data obtained from [6]. The helicopter portion of the proposed model is validated through time history comparison with real-life flight data. The slung load portion on the other hand, is verified by comparing the measured frequencies of the different modes with theoretical values as well as pilot evaluation.

In the study carried out by Cicolani and Kanning [7] a generalized slung load modeling approach is implemented based on Newton-Euler formulation for a variety of configurations including the ones with several attachment points and multi-lift systems. Later in another study conducted by Stuckey [8], a similar approach is followed and a generalized mathematical modeling approach for the systems consisting of a single helicopter and various slung load configurations is proposed. Also, in [7] and [8], both the rigid and elastic attachment cable approaches are included in the generalized formulation through constraints in the governing equations.

In more recent years, different modeling approaches are also presented regarding the slung load modeling. One such study is carried out by Bisgaard [9] and it includes the derivation of equations of motion for the compound helicopter-slung load system through the Udwadia-Kalaba formulation.

A more recent study carried out by Cao et al. [10], involves a slung load modeling approach that utilizes Kane's method with a spring-mass-damper model that represents flexible cables with weight. The base helicopter mathematical model is

taken as that of Sikorsky's UH-60 helicopter. In this particular study, the simulation results with rigid cable assumption are also taken into account and a comparison provided among two approaches in terms of consistency between flight test data. The comparison is performed upon varying collective and longitudinal cyclic position with respect to increasing airspeed. It is concluded that flexible cable approach yields closer results to the flight test data with the chosen slung load configuration.

2.2 Control of the Helicopter Slung Load System

In the literature, there are several methodologies regarding the slung load control. In a relatively early study, Gupta and Bryson [11] proposed an automatic flight control system for precision hover task of a single rotor helicopter with a slung load. The measurement of the helicopter and slung load states necessary for the developed control law is accomplished by a light weight cable attached from the helicopter to the ground.

With the advancements in the data acquisition systems, more advanced control systems that utilizes slung load states in feedback control are proposed throughout the years. One such study conducted by Ivler [12], contains the additional feedback controllers that can function in conjunction with helicopter flight control system by processing slung load cable angle and angular rates. It is stated that reason of including both the cable angle and angular rate is to obtain the optimal solution by taking slung load oscillation damping as well as the helicopter trajectory tracking into account.

Another study that utilizes cable angular rate feedback controllers on top of the existing helicopter flight control system is carried out by Brenner [13]. In the study, the necessary dynamic compensators for the cable angle rates are determined based on an optimization algorithm that takes robustness into account through resultant minimum gain and phase margins.

There are other studies that utilizes optimization algorithm to determine the necessary feedback controllers. One such study is carried out by Bisgaard [14]. In this study a delayed feedback controller is utilized in conjunction with the input shaping. The delayed feedback controller is included for providing additional load oscillation suppression and the necessary controller gain and time delay are determined based on an optimization algorithm, in which the damping ratio of the load oscillation is maximized.

Another study that involves feedback controller design with optimization is conducted by Omar [15]. This particular study utilizes delayed feedback control for the load swing suppression as well. For the optimization algorithm, Particle Swarm Optimization is utilized and the cost function to be minimized is determined as the integral of the square sum of the longitudinal and lateral cable angles and angular rates.

In the study carried out by Adams [16], the slung load control is accomplished by implementing input shaping over the already existing model following controller of the helicopter and cable angle or angular rate feedback is not utilized. It is stated that even though this approach is easy to integrate to a real-life helicopter system due to lack of data acquisition system such as sensors or estimators, the load swing suppression ability is susceptible to outside disturbances.

As it is stated above, the study carried out by Bisgaard [14] also involves input shaping for swing damping. However, the proposed input shaper is augmented with delayed cable angle feedback control for further enhancement in the controller performance.

A more recent study conducted by Ren et al [17], involves a slung load control approach that is based on desired trajectory tracking in the presence of input constraints and external disturbances. The control algorithm tries to minimize the deviation from desired trajectory for the longitudinal helicopter position in inertial reference frame as well as the slung load swing angle and helicopter pitch attitude.

CHAPTER 3

DEVELOPMENT OF A HELICOPTER MATHEMATICAL MODEL

In this study, a mathematical model for the CH-53 helicopter is utilized. The model is developed by NASA and explained in detail in [1]. The model consists of the following submodules:

- Main Rotor Module
- Tail Rotor Module
- Control System Module
- Fuselage Aerodynamics Module
- Engine and Governor Module
- Equations of Motion Module

It should be pointed out that Engine and Governor Module is left out of the overall model and engine was treated as it was operating at steady state. The reason is that this particular module has an important role at the initial phase of engine start and in the presence of engine failure in terms of adjusting the main rotor speed. However, as far as the hovering and forward flight are concerned, the main rotor generally operates at its nominal speed and it is not necessary to examine the change in this particular value unless it is particularly desired. Also, the original control system module contains controllers that are capable of performing various tasks. However, the control system submodule used in this study consists of only the conversion formulation between the pilot stick inputs and main/tail rotor control angles. Instead of the default controllers, the current study involves development of its own controllers to have more freedom over the autopilot and stability augmentation system capabilities. The model is generated in MATLAB/Simulink environment and the block diagram of the overall system is provided below:

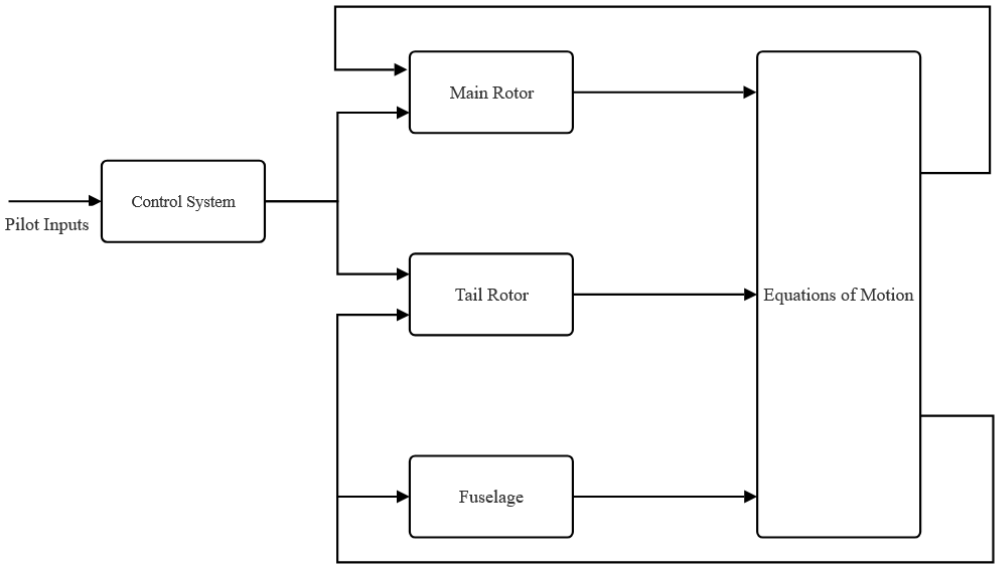


Figure 3.1. Block Diagram of the Overall System

In the following subsections of this chapter, each module of the helicopter model and their respective governing equations will be discussed.

3.1.1 Coordinate Systems Utilized in the Mathematical Model

Before representing the modules that constitute the mathematical model in detail, it is beneficial to elaborate on the utilized coordinate systems (frames of reference). These coordinate systems can be listed as follows:

a) **Earth Axes (denoted by subscript e):** In this reference frame the origin is fixed on Earth's surface, x_e axis is point north and y_e axis is pointing east. z_e axis follows the right-hand rule.
b) **Helicopter Body Axes (denoted by subscript h):** In this reference frame origin is at the center of gravity (c.g.), x_h axis is pointing forward in the plane of symmetry and z_h axis is pointing down in the plane of symmetry. y_h axis follows the right-hand rule.
c) **Shaft Axes (denoted by subscript s):** In this reference frame the origin is placed at the rotor hub, x_s axis is rotated through the longitudinal shaft tilt

angle θ_s about y_h axis and y_s axis is rotated through the lateral shaft tilt angle ϕ_s about the x_s axis. Finally, z_s axis is coincident with the rotor shaft. This notation applies to both the main and tail rotors.

d) Control Axes (denoted by subscript c): In this reference frame the origin is at the rotor hub, z_c axis is directed towards the fuselage along the axis of no-feathering (an axis perpendicular to the swashplate) and x_c axis points into the relative wind so that the y_c component of the relative wind is zero. This notation is valid for both the main and tail rotors.

e) Wind Tunnel Axes (denoted by subscript wt): In this reference frame, the origin is at the wind tunnel mounting point, x_{wt} axis points into the relative wind and z_{wt} pointing downwards and it is perpendicular to the relative wind.

Schematics for these reference frames (except for the wind tunnel axes) along with the rotor flapping angle definitions can be accessed from the figure below:

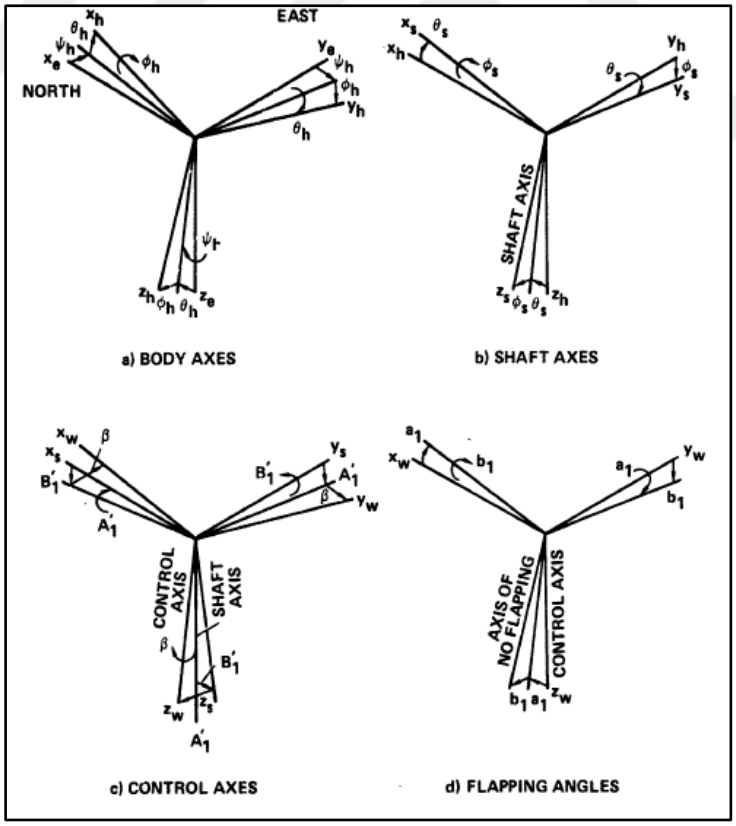


Figure 3.2. Frames of Reference and Rotor Flapping Angle Definitions [1]

3.1.2 Main Rotor and Tail Rotor Modules

The forces and moments generated by the rotors are calculated using nonlinear classical rotor theory, specifically a modified Bailey representation discussed in detail in references [18], [19] and [20]. Important aspects regarding the modeling approach are listed below:

- Inflow over the rotor disk is assumed to be uniform.
- Compressibility and stall effects are neglected
- Lagging motion of the rotor blades is neglected.
- Only the first harmonic motion of the rotor blades is considered.
- The blade coning and flapping angles are assumed to be quasi-static.

Aforementioned discussion applies to both the main and tail rotors, except where it is explicitly mentioned. In the case of a specific application, the subscript m stands for the main rotor whereas the subscript t designates the tail rotor.

3.1.2.1 Rotor Hub Airspeed Calculation in Control Axes

In order to obtain the forces and moments generated by the rotors, total airspeed of the rotor hub should be calculated. This airspeed is initially determined in the shaft axes using the airspeed and angular velocity of the helicopter and then it is transformed to the control axes as it can be seen from the following set of equations:

$$\begin{bmatrix} u \\ v \\ w \end{bmatrix}_s = C_{s/h} \left[\begin{bmatrix} u \\ v \\ w \end{bmatrix}_{as,h} + \begin{bmatrix} 0 & z & -y \\ -z & 0 & x \\ y & -x & 0 \end{bmatrix}_{r,h} \begin{bmatrix} p \\ q \\ r \end{bmatrix}_h \right] \tag{3.1}$$

In equation (3.1), $C_{s/h}$ can be written in the following expanded form

$$C_{s/h} = \begin{bmatrix} \cos(\theta_s) & 0 & -\sin(\theta_s) \\ \sin(\theta_s)\sin(\phi_s) & \cos(\phi_s) & \cos(\theta_s)\sin(\phi_s) \\ \sin(\theta_s)\cos(\phi_s) & -\sin(\phi_s) & \cos(\theta_s)\cos(\phi_s) \end{bmatrix} \tag{3.2}$$

The airspeed at the hub is transferred into the control axes using the rotor orientation angle given by the following equation:

$$\beta = \tan^{-1}\left(\frac{v_s + A_1 w_s}{u_s + B_1 w_s}\right) \tag{3.3}$$

Using the small angle assumption for the main rotor cyclic control inputs given by A_1 and B_1, following identity can be written:

$$\begin{bmatrix} u \\ v \\ w \end{bmatrix}_c = C_{c/s} \begin{bmatrix} u \\ v \\ w \end{bmatrix}_s \tag{3.4}$$

In Equation (3.4), $C_{c/s}$ denotes the following transformation matrix:

$$C_{c/s} = \begin{bmatrix} \cos(\beta) & \sin(\beta) & B_1\cos(\beta) + A_1\sin(\beta) \\ -\sin(\beta) & \cos(\beta) & A_1\cos(\beta) - B_1\sin(\beta) \\ -B_1 & -A_1 & 1 \end{bmatrix} \tag{3.5}$$

It should be pointed out that the tail rotor does not have cyclic controls and therefore corresponding A_1 and B_1 are equal to zero.

3.1.2.2 Rotor Tip Speed Ratio (μ) and Inflow Ratio (λ) Calculation

Forces and moments generated by rotors are functions of the rotor tip speed and inflow ratios. These quantities are obtained in terms of the hub airspeed in control axes as it can be seen from the following set of equations:

$$\mu = \frac{u_c}{\Omega R} \tag{3.6}$$

$$\lambda = \frac{w_c}{\Omega R} - \nu \tag{3.7}$$

The induced inflow ratio ν, is obtained by filtering the steady state value of ν. The governing differential equation is provided below:

$$\dot{\nu} = \frac{1}{\tau_\nu}\left(\frac{C_T}{2\sqrt{\mu^2 + \lambda^2}} - \nu\right) \tag{3.8}$$

3.1.2.3 Rotor Thrust and Coning Angle Calculation

The rotor thrust in control axes and the coning angle a_0 are calculated to the third power of the tip speed ratio. The governing equations are provided below [1]:

$$T = bcR\rho(R\Omega)^2\left(\frac{C_T}{\sigma}\right) \tag{3.9}$$

$$a_0 = \gamma\left[\left(\frac{1}{6}B^3 + 0.04\mu^3\right)\lambda + \left(\frac{1}{8}B^4 + \frac{1}{8}B^2\mu^2\right)\theta_0 + \left(\frac{1}{10}B^5 + \frac{1}{12}B^3\mu^2\right)\theta_1\right] \tag{3.10}$$

Where,

$$\frac{C_T}{\sigma} = \frac{a}{2}\left[\left(\frac{1}{2}B^2 + \frac{1}{4}\mu^2\right)\lambda + \left(\frac{1}{3}B^3 + \frac{1}{2}B\mu^2 - \frac{4}{9\pi}\mu^3\right)\theta_0 + \left(\frac{1}{4}B^4 + \frac{1}{4}B^2\mu^2\right)\theta_1\right] \tag{3.11}$$

In Equation (3.11), θ_0 denotes the effective blade pitch angle at the root and θ_1 stands for the blade twist.

3.1.2.4 Calculation of Rotor Flapping Angles in Control Axes

To calculate the rotor flapping angles, the helicopter angular velocity should be expressed control axes:

$$\begin{bmatrix} p \\ q \\ r \end{bmatrix}_c = C_{c/s}C_{s/h}\begin{bmatrix} p \\ q \\ r \end{bmatrix}_h \tag{3.12}$$

The lateral and longitudinal flap angles are denoted by a_1 and b_1 respectively and they are expressed in the following set of equations:

$$a_1 = \frac{1}{[1 - (\mu^2/2B^2)]}\left[\left(2\lambda + \frac{8}{3}\theta_{0.75}\right)\mu + \frac{p_c}{\Omega} - \frac{16q_c}{B^4\gamma\Omega}\right] \tag{3.13}$$

$$b_1 = \frac{1}{[1 + (\mu^2/2B^2)]}\left[\frac{4}{3}\mu a_0 - \frac{q_c}{\Omega} - \frac{16p_c}{B^4\gamma\Omega}\right] \tag{3.14}$$

In Equation (3.13), $\theta_{0.75}$ denotes the blade pitch angle at a distance of 3/4 radius from the feathering hinge and for a linearly twisted blade it can be expressed as follows:

$$\theta_{0.75} = \theta_0 + 0.75\theta_1 \tag{3.15}$$

3.1.2.5 Calculation of Rotor Drag Force and Side Force in Control Axes

The downwind component of the rotor force, in other words the rotor drag force, can be expressed in control axes as follows:

$$H = Ta' \tag{3.16}$$

The formula for the angle a' is obtained from the reference [18] and it can be written in the following expanded form:

$$a' = \frac{1}{[1-(\mu^2/2B^2)]}\left[\left(2\lambda + \frac{8}{3}\theta_{0.75}\right)\mu - \frac{24q_c}{B^4\gamma\Omega}\left(1 - \frac{0.29\theta_{0.75}}{C_T/\sigma}\right)\right] \tag{3.17}$$

The rotor side force, on the other hand can be expressed in control axes as shown below:

$$J = bcR\rho(R\Omega)^2\frac{C_y}{\sigma} \tag{3.18}$$

The nondimensional coefficient C_y in Equation (3.18), can be expanded in the following form:

$$\frac{C_y}{\sigma} = \frac{a}{2}\left[\frac{3}{4}b_1\lambda - \frac{3}{2}a_0\mu\lambda + \frac{1}{4}a_1b_1\mu - a_0a_1\mu^2 + \frac{1}{6}a_0a_1 - \left(\frac{3}{4}\mu a_0 - \frac{1}{3}b_1 - \frac{1}{2}\mu^2 b_1\right)\theta_{0.75}\right] \tag{3.19}$$

Calculated rotor forces can be expressed in the helicopter body frame by using the related transformation matrices as shown below:

$$\begin{bmatrix} X \\ Y \\ Z \end{bmatrix}_{r,h} = C_{s/h}^T C_{c/s}^T \begin{bmatrix} -H \\ J \\ -T \end{bmatrix}_c \tag{3.20}$$

3.1.2.6 Calculation of Rotor Torque in Shaft Axes

The rotor aerodynamic torque is defined by the following equation:

$$Q_a = bcR^2\rho(R\Omega)^2\left(\frac{C_Q}{\sigma}\right) \tag{3.21}$$

The nondimensional torque coefficient C_Q can be expressed as shown below:

$$\begin{aligned}\frac{C_Q}{\sigma} = {} & 0.00109 - 0.0036\lambda - 0.0027\theta_{0.75} - 1.10\lambda^2 - 0.545\lambda\theta_{0.75} \\ & + 0.122\theta_{0.75}^2 \\ & + \left(0.00109 - 0.0027\theta_{0.75} - 3.13\lambda^2 - 6.35\lambda\theta_{0.75}\right. \\ & \left. - 1.93\theta_{0.75}^2\right)\mu^2 - 0.133\lambda\theta_{0.75}\mu^3 \\ & + \left(-0.976\lambda^2 - 6.38\lambda\theta_{0.75} - 5.26\theta_{0.75}^2\right)\mu^4\end{aligned} \tag{3.22}$$

It should be noted that due to the fact that the engine dynamics is not included in the model and the engine is treated to be operating at steady state, following relation can be written for the torque applied to the fuselage by the main rotor, i.e., $N_{hub,s}$:

$$N_{hub,s} = Q_a \tag{3.23}$$

Equation (3.23) can be interpreted such that the aerodynamic torque generated by the main rotor is acting directly on the fuselage for steady state engine dynamics. As a further remark, the same discussion is valid for the tail rotor as well regardless of the inclusion of the engine dynamics.

3.1.2.7 Calculation of Rotor Hub Moments in Shaft Axes:

The hub moments resulting from the flap hinge offset are calculated by the following formula:

$$\begin{bmatrix} L \\ M \end{bmatrix}_{hub,s} = \frac{1}{2} eb\Omega^2 M_w \begin{bmatrix} b_1 \\ a_1 \end{bmatrix}_s \tag{3.24}$$

It should be noted that $b_{1,s}$ and $a_{1,s}$ denote the rotor flapping angles in shaft axes and they can be expressed by the following formula:

$$\begin{bmatrix} b_1 \\ a_1 \\ - \end{bmatrix}_s = \begin{bmatrix} A_1 \\ -B_1 \\ 0 \end{bmatrix} + C_{c/s}^T \begin{bmatrix} b_1 \\ a_1 \\ 0 \end{bmatrix} \tag{3.25}$$

The calculated rotor hub moments $L_{hub,s}$, $M_{hub,s}$ and $N_{hub,s}$ are expressed in the helicopter body frame by using the related transformation matrix as shown below:

$$\begin{bmatrix} L \\ M \\ N \end{bmatrix}_{hub,h} = C_{s/h}^T \begin{bmatrix} L \\ M \\ N \end{bmatrix}_{hub,s} \tag{3.26}$$

Total moment acting on the fuselage by the rotor consists of the hub moments given in Equation (3.26) and the moments created by the rotor hub forces given in Equation (3.20) as a result of the offset between the rotor hub and helicopter center of gravity. The governing equation for the total rotor moment is given below:

$$\begin{bmatrix} L \\ M \\ N \end{bmatrix}_{r,h} = \begin{bmatrix} L \\ M \\ N \end{bmatrix}_{hub,h} + \begin{bmatrix} 0 & -z & y \\ z & 0 & -x \\ -y & x & 0 \end{bmatrix}_{r,h} \begin{bmatrix} X \\ Y \\ Z \end{bmatrix}_{r,h} \tag{3.27}$$

3.1.2.8 Tail Rotor Pitch-Flap Coupling (δ_3 Angle) Effect

The rotor model that has been represented so far does not take the blade pitch and flap angle coupling into account. Even though this approach is valid for the main rotor, the hinges of the tail rotor of CH-53 helicopter is designed such that there is a certain amount of coupling between these two individual blade motion. In other words, the amount of pitch the tail rotor blades is subjected to is affected by the blade coning. Hence, following equation that describes this particular effect is also included in the mathematical model:

$$\theta_{0t} = \theta_{ct} - a_{0t} \tan(\delta_{3t}) \tag{3.28}$$

In Equation (3.28), θ_{ct} denotes the collective tail rotor pitch angle commanded by the control system.

3.1.3 Control System Module

The control system module proposed by reference [1] includes the conversion between the pilot stick inputs and rotor pitch angles, cross couplings between input channels, an automatic flight control system and servo actuators for the main rotor inputs. However, as it was stated previously, only the pilot stick conversions and input channel cross coupling are included in this study and an original fight control system is developed from scratch, which is discussed in detail in Chapter 4.

The conversion formulation between the pilot inputs and the respective rotor pitch angles are provided in the following set of equations. It should be noted that the pilot inputs are expressed in centimeters.

$$\theta_{0m} = K_1 + K_2 X'_{col} \tag{3.29}$$

$$B_1 = K_3 + K_4 X_{lon} \tag{3.30}$$

$$A_1 = K_5 + K_6 X_{lat} + K_7 X'_{col} \tag{3.31}$$

$$\theta_{ct} = K_8 + K_9 X_{ped} + K_{10} X'_{col} \tag{3.32}$$

$$X'_{col} = X_{col} - 2.54 \tag{3.33}$$

In Equations (3.29)-(3.32), K_n values represent certain constants and they can be accessed from the Appendix A. In Equation (3.33), when the collective stick displacement drops below 2.54 centimeters, X'_{col} value is taken as zero.

3.1.4 Fuselage Aerodynamics Module

Fuselage aerodynamics module involves certain governing equations as well as force and moment acquisition from tabular data based on the angle of attack and angle of sideslip the fuselage is subjected to. It should be noted that there are not separate aerodynamic databases for horizontal tail and vertical tail. Instead, effect of these aerodynamic surfaces are integrated to the fuselage module.

The aerodynamic tables utilized for obtaining the required aerodynamic forces and moments are provided in Appendix B and the governing equations are explained hereafter.

In order to calculate the dynamic pressure, angle of attack and angle of sideslip; the total airspeed of the helicopter should be calculated as an initial step. Calculation of the total airspeed in helicopter body frame involves inertial helicopter velocity as well as the additional wind and gust speeds as can be seen from the equation given below:

$$\begin{bmatrix} u \\ v \\ w \end{bmatrix}_{as,h} = \begin{bmatrix} u \\ v \\ w \end{bmatrix}_{cg,h} - \begin{bmatrix} u \\ v \\ w \end{bmatrix}_{gust,h} - \begin{bmatrix} u \\ v \\ w \end{bmatrix}_{wind,h} \tag{3.34}$$

It should be noted that, in this study, the presence of wind and gust is not considered. Hence, the total airspeed of the helicopter can be taken as its inertial velocity:

$$\begin{bmatrix} u \\ v \\ w \end{bmatrix}_{as,h} = \begin{bmatrix} u \\ v \\ w \end{bmatrix}_{cg,h} \tag{3.35}$$

Once the airspeed is obtained, free stream angle of attack and angle of sideslip can be calculated by the following:

$$\alpha_f = \tan^{-1}\left(\frac{w}{u}\right), \quad -\pi \leq \alpha_f \leq \pi \tag{3.36}$$

$$\beta_f = \sin^{-1}\left(\frac{v}{V_{as,h}}\right), \quad -\frac{\pi}{2} \leq \beta_f \leq \frac{\pi}{2} \tag{3.37}$$

In equation (3.37), $V_{as,h}$ represents the total airspeed in scalar form and it can be expressed as follows:

$$V_{as,h} = \sqrt{u_{as,h}^2 + v_{as,h}^2 + w_{as,h}^2} \tag{3.38}$$

Also, the free stream dynamic pressure can be obtained from the following identity:

$$\bar{q} = \frac{1}{2}\rho V_{as,h}^2 \tag{3.39}$$

In this module, effect of main rotor downwash on the fuselage is included by modifying local angle of attack with certain correction parameters as it can be seen from the following equation:

$$\alpha_{fl} = \alpha_f - e_{mr} e_{kf} \tag{3.40}$$

In Equation (3.40), e_{mr} is the rotor downwash factor whereas e_{kf} is an empirical constant. These quantities can be expressed by the following equations:

$$e_{mr} = \frac{C_{Tm}}{2(\lambda_m^2 + \mu_m^2)} \tag{3.41}$$

$$e_{kf} = 0.5 \tag{3.42}$$

In order to utilize certain aerodynamic tables provided in Appendix B, local incidence angle at the tail plane needs to be calculated according to the following equation:

$$i_t = i_{t0} - (e_{kt} - e_{kf}) e_{mr} \tag{3.43}$$

In Equation (3.43), i_{t0} is the default set angle of the horizontal tail and e_{kt} is an empirical constant correction factor to account for the main rotor downwash effect on the tail. These parameters are provided below:

$$i_{t0} = 3° \tag{3.44}$$

$$e_{kt} = 1.8 \tag{3.45}$$

As a final remark regarding the fuselage aerodynamics module is that an additional quantity called the wind tunnel yaw angle shall be defined in order to be used in certain aerodynamic tables given in Appendix B. This angle is simply defined as follows:

$$\psi_{wt} = -\beta_f \tag{3.46}$$

Upon the calculation of the aforementioned quantities, fuselage forces and moments in wind tunnel reference frame can be calculated by using the aerodynamic tables given in Appendix B.

The curves are entered with the fuselage local angle of attack, local incidence at the tail, wind tunnel yaw angle and the dynamic pressure. It should also be noted that the wind tunnel data do not cover the full range of angle of attack and sideslip that the helicopter can be subjected to depending on the flight regime. Hence, it is assumed that the force and moment coefficients remain constant beyond the given angle limits in the respective tables. According to reference [1], this approach does not yield a significant degradation in model performance due to the fact that large angles of attack and sideslip can occur at low airspeed flight regime and corresponding forces and moments generated by fuselage are relatively small.

The governing equations of the fuselage module are provided in the following set of equations for each force and moment term:

$$D_{wt} = \left(\frac{\Delta D_{1,wt}}{\bar{q}} + \frac{\Delta D_{2,wt}}{\bar{q}}\right)\bar{q} \tag{3.47}$$

$$\tilde{L}_{wt} = \left(\frac{\Delta \tilde{L}_{1,wt}}{\bar{q}} + \frac{\Delta \tilde{L}_{2,wt}}{\bar{q}}\right)\bar{q} \tag{3.48}$$

$$Y_{wt} = \left(\frac{Y_{wt}}{\bar{q}}\right)\bar{q} \tag{3.49}$$

$$L_{wt} = \left(\frac{\Delta L_{1,wt}}{\bar{q}} + \frac{\Delta L_{2,wt}}{\bar{q}}\right)\bar{q} \tag{3.50}$$

$$M_{wt} = \left(\frac{\Delta M_{1,wt}}{\bar{q}} + \frac{\Delta M_{2,wt}}{\bar{q}}\right)\bar{q} \tag{3.51}$$

$$N_{wt} = \left(\frac{N_{wt}}{\bar{q}}\right)\bar{q} \tag{3.52}$$

In Equations (3.47)-(3.52), D_{wt}, $\tilde{L}_{wt}$, Y_{wt}, L_{wt}, M_{wt} and N_{wt} represent the drag force, lift force, side force, rolling moment, pitching moment and yawing moment respectively.

Once the fuselage aerodynamic forces are obtained, they are expressed in the helicopter body frame to be used in the equations of motion module:

$$\begin{bmatrix} X \\ Y \\ Z \end{bmatrix}_{f,h} = C_{h/wt} \begin{bmatrix} -D \\ Y \\ -\tilde{L} \end{bmatrix}_{wt} \tag{3.53}$$

In Equation (3.53), $C_{h/wt}$ denotes the transformation matrix from the wind tunnel axes system to the helicopter body frame and it is given in the following equation:

$$C_{h/wt} = \begin{bmatrix} \cos(\alpha_f)\cos(\beta_f) & -\cos(\alpha_f)\sin(\beta_f) & -\sin(\alpha_f) \\ \sin(\beta_f) & \cos(\beta_f) & 0 \\ \sin(\alpha_f)\cos(\beta_f) & -\sin(\alpha_f)\sin(\beta_f) & \cos(\alpha_f) \end{bmatrix} \tag{3.54}$$

The aerodynamic moments generated by the fuselage are also transformed to the helicopter body frame by using the following equation:

$$\begin{bmatrix} L \\ M \\ N \end{bmatrix}_{f,h} = \begin{bmatrix} L \\ M \\ N \end{bmatrix}_{wt} + \begin{bmatrix} 0 & -z & y \\ z & 0 & -x \\ -y & x & 0 \end{bmatrix}_{wt,h} \begin{bmatrix} X \\ Y \\ Z \end{bmatrix}_{f,h} + \begin{bmatrix} L \\ M \\ N \end{bmatrix}_{d,h} + \begin{bmatrix} 0 \\ k_f \\ 0 \end{bmatrix} T_m \tag{3.55}$$

In Equation (3.55), the third term on the right hand-side denotes the aerodynamic moments resulting from the angular velocity of the helicopter and it can be expressed by the following identity:

$$\begin{bmatrix} L \\ M \\ N \end{bmatrix}_{d,h} = \begin{bmatrix} 0 \\ -899q_h \\ -520r_h \end{bmatrix} V_{as,h} \tag{3.56}$$

In addition, k_f in Equation (3.55), is the pitching moment coefficient due to main rotor thrust and it is an empirical constant whose value is given below:

$$k_f = 0.099 \tag{3.57}$$

3.1.5 Equations of Motion Module

This module is used for calculation of the helicopter linear and angular acceleration by accounting for the forces and moments generated by the rotors and fuselage. The governing equations expressed in the helicopter body frame and the solution procedure is based on generic Newton-Euler equations.

Following set of equations illustrate the calculation of the translational and angular accelerations respectively.

3.1.5.1 Translational Acceleration Calculation

Governing equation for the translational motion of the helicopter is provided below:

$$m\left[\begin{bmatrix}\dot{u}\\ \dot{v}\\ \dot{w}\end{bmatrix}_{cg,h}+\begin{bmatrix}0 & -r & q\\ r & 0 & -p\\ -q & p & 0\end{bmatrix}_{h}\begin{bmatrix}u\\ v\\ w\end{bmatrix}_{cg,h}\right]=C_{h/e}\begin{bmatrix}0\\ 0\\ mg\end{bmatrix}+\begin{bmatrix}X\\ Y\\ Z\end{bmatrix}_{f,h}+\begin{bmatrix}X\\ Y\\ Z\end{bmatrix}_{rh} \quad (3.58)$$

In Equation (3.58), $C_{h/e}$ denotes the transformation matrix from the earth axes to the helicopter body axes and it can be written in the expanded form as follows:

$$C_{h/e}=\begin{bmatrix}1 & 0 & 0\\ 0 & \cos(\phi) & \sin(\phi)\\ 0 & -\sin(\phi) & \cos(\phi)\end{bmatrix}\begin{bmatrix}\cos(\theta) & 0 & -\sin(\theta)\\ 0 & 1 & 0\\ \sin(\theta) & 0 & \cos(\theta)\end{bmatrix}\begin{bmatrix}\cos(\psi) & \sin(\psi) & 0\\ -\sin(\psi) & \cos(\psi) & 0\\ 0 & 0 & 1\end{bmatrix} \quad (3.59)$$

As it is evident from the notation, ϕ, θ and ψ are the Euler angles of the helicopter that designate the roll, pitch and yaw motions respectively.

Upon performing a slight modification for convenience, Equation (3.58) can be rewritten in the following form:

$$\begin{bmatrix}\dot{u}\\ \dot{v}\\ \dot{w}\end{bmatrix}_{cg,h}=\frac{1}{m}\left[\begin{bmatrix}X\\ Y\\ Z\end{bmatrix}_{f,h}+\begin{bmatrix}X\\ Y\\ Z\end{bmatrix}_{rh}\right]-\begin{bmatrix}0 & -r & q\\ r & 0 & -p\\ -q & p & 0\end{bmatrix}_{h}\begin{bmatrix}u\\ v\\ w\end{bmatrix}_{cg,h}+C_{h/e}\begin{bmatrix}0\\ 0\\ g\end{bmatrix} \quad (3.60)$$

If it is preferred, the inertial velocity and position can also be derived based on Equation (3.60). This is done by transforming the velocity to inertial frame and taking the integral of the obtained expression with respect to time. The procedure is provided in the following set of equations:

$$\begin{bmatrix}u\\ v\\ w\end{bmatrix}_{cg,e}=C_{h/e}^{T}\begin{bmatrix}u\\ v\\ w\end{bmatrix}_{cg,h} \quad (3.61)$$

$$\begin{bmatrix} x \\ y \\ z \end{bmatrix}_{cg,e} = \int \begin{bmatrix} u \\ v \\ w \end{bmatrix}_{cg,e} dt \tag{3.62}$$

3.1.5.2 Angular Acceleration Calculation

Governing equation for the rotational motion of the helicopter is provided below:

$$\begin{bmatrix} L \\ M \\ N \end{bmatrix}_{f,h} + \begin{bmatrix} L \\ M \\ N \end{bmatrix}_{r,h} = I_h \begin{bmatrix} \dot{p} \\ \dot{q} \\ \dot{r} \end{bmatrix}_h + \begin{bmatrix} 0 & -r & q \\ r & 0 & -p \\ -q & p & 0 \end{bmatrix}_h I_h \begin{bmatrix} p \\ q \\ r \end{bmatrix}_h \tag{3.63}$$

In Equation (3.63), I_h represents the inertia matrix of the helicopter an it is given in the expanded form in the following equation:

$$I_h = \begin{bmatrix} I_{xx} & 0 & I_{xz} \\ 0 & I_{yy} & 0 \\ I_{xz} & 0 & I_{zz} \end{bmatrix} \tag{3.64}$$

Equation (3.63) is rearranged for convenience in the following form:

$$\begin{bmatrix} \dot{p} \\ \dot{q} \\ \dot{r} \end{bmatrix} = I_h^{-1} \left[\left[\begin{bmatrix} L \\ M \\ N \end{bmatrix}_{f,h} + \begin{bmatrix} L \\ M \\ N \end{bmatrix}_{r,h} - \begin{bmatrix} 0 & -r & q \\ r & 0 & -p \\ -q & p & 0 \end{bmatrix}_h I_h \begin{bmatrix} p \\ q \\ r \end{bmatrix}_h \right] \right] \tag{3.65}$$

The Euler angle rates can be obtained from the helicopter angular acceleration by using the following identity:

$$\begin{bmatrix} \dot{\phi} \\ \dot{\theta} \\ \dot{\psi} \end{bmatrix} = \begin{bmatrix} 1 & 0 & -\sin(\theta) \\ 0 & \cos(\phi) & \sin(\phi)\cos(\theta) \\ 0 & -\sin(\phi) & \cos(\phi)\cos(\theta) \end{bmatrix}^{-1} \begin{bmatrix} \dot{p} \\ \dot{q} \\ \dot{r} \end{bmatrix} \tag{3.66}$$

It should be pointed out that in Equation (3.66), the transformation matrix can become singular when the pitch attitude obtains a value of ±90° and its inverse cannot be obtained in this situation. This particular instance corresponds to the full pitch up or pitch down positioning of the helicopter and it is unlikely to occur in an operational flight envelope. Considering that this study involves investigation of

hovering flight and generic forward flight conditions, the singularity issue does not constitute a problem.

3.2 Trim Algorithm for the Nonlinear Helicopter Model

The aforementioned helicopter model is highly nonlinear and for the implementation of control laws, it needs to be properly linearized. As a general rule, the linearization is performed around trim (equilibrium) points. These equilibrium points can be chosen at a variety of airspeed values according to the flight condition of interest, including level flight, coordinated turn, climb and descent maneuvers. In this study, the control law development is considered for steady level flight and in the trim algorithm to be proposed, the sideslip angle is forced to be zero, which yields that the helicopter does not attain velocity in the y-axis of its respective body frame. Application of this particular constraint stems from the intention of being consistent with the validated reference model that will be mentioned later on. However, it should also be noted that trimmed flight condition for the remaining flight regimes mentioned above can be also easily obtained by imposing appropriate constraints.

In order to develop the aforementioned trim algorithm, MATLAB's "fmincon" function is utilized based on the principles of simulation-based optimization. This function is used for finding the minimum of a constrained nonlinear multi-variable function. In this particular trim algorithm, the cost function, minimum of which is to be found is determined as follows by taking the linear and angular accelerations of the helicopter into account:

$$J = \dot{u}^2 + \dot{v}^2 + \dot{w}^2 + \dot{p}^2 + \dot{q}^2 + \dot{r}^2 \tag{3.67}$$

This particular cost function is selected because of the fact that when it reduced down to zero, overall forces and moments acting on the helicopter are balanced out and steady flight condition at equilibrium is obtained. Calculation of the cost function is performed by killing off every single integral dynamics in the overall model and taking the linear and angular accelerations as outputs of the simulation. At the end,

the helicopter states and control inputs that result in the cost function in the vicinity of zero are obtained according to tolerances defined in “fmincon”. Hence, the terminating tolerance between successive iterations is kept at a quite low value. The constraints in the trim algorithm necessary for using “fmincon” are determined as the upper and lower limits of the control inputs and certain limits on the Euler angles of the helicopter according to the flight regime of interest. However, several simulation results have shown that the resultant Euler angles at trimmed flight are certainly not excessive and control inputs are the constraints with major importance.

To verify the validity of the helicopter model and trim algorithm, the trimmed helicopter inputs and states are compared to the results of the well-known verified GENHEL model of CH-53 provided in [21] for various forward flight speeds ranging from 0 to 150 knots. Results are provided in the following superimposed figure:

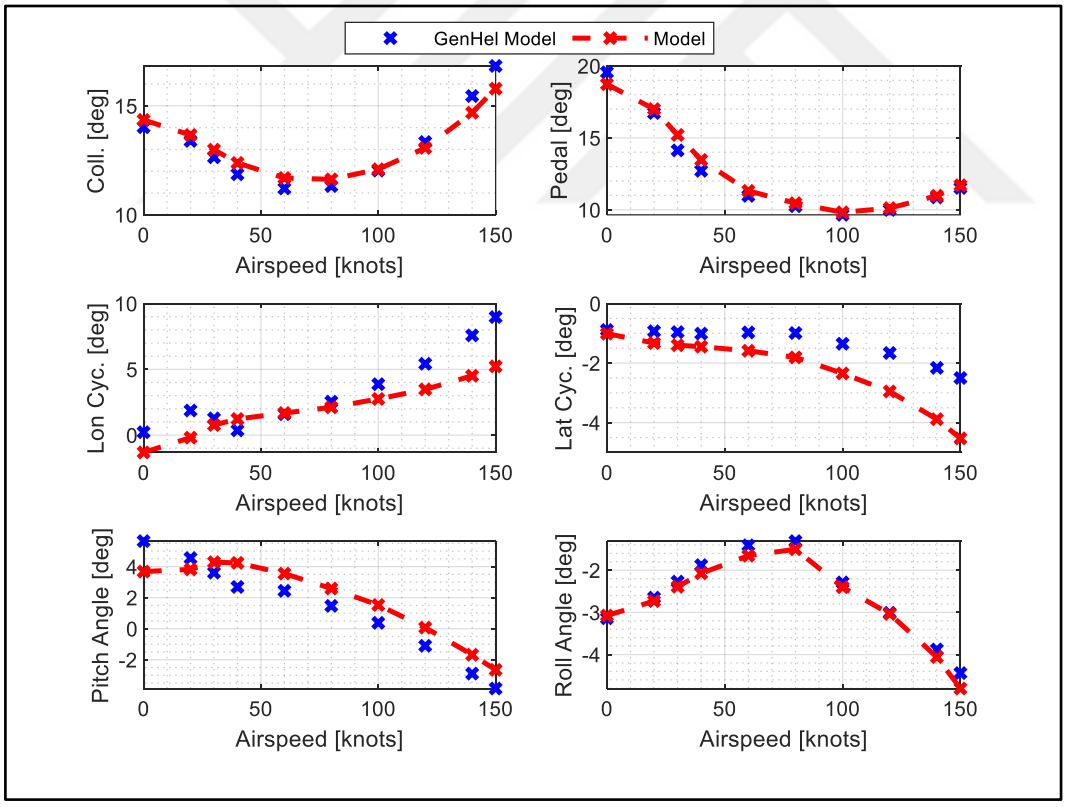


Figure 3.3. Trim Results Comparison with GENHEL Model

From Figure 3.3, it can be seen that the overall agreement of the generated mathematical model agrees quite well with the GENHEL model. That is, the overall trend of all the parameters of concern are consistent with the reference model. Also, maximum deviation observed in the collective input, pedal input, pitch angle and roll angle are in the vicinity of 1 degree, which can be evaluated as reasonable. On the other hand, the same figure also shows that, there are some visible discrepancy in the longitudinal and lateral cyclic inputs with increasing airspeeds, which stems from the fact that the fuselage aerodynamic data in the model used in this study is relatively coarse and there are no separate detailed database available for the horizontal/vertical tail components. Given that major focus of this study is the slung load itself, and it will be examined for hovering flight and forward flight with 60 knots of airspeed, the accuracy of the developed model can be evaluated as satisfactory.

As a further verification, the time history comparison with available flight test data is also performed. The flight test results are provided in [22], for a variety of airspeeds with both AFCS on and off conditions. The figure below shows the comparison results for 113 knots (58 m/s) forward flight case with AFCS off condition with 1 cm longitudinal cyclic pulse input. Due to lack of autopilot engagement, the helicopter deviates from the trim condition relatively fast, so 2 seconds of consistency can be regarded as sufficient.

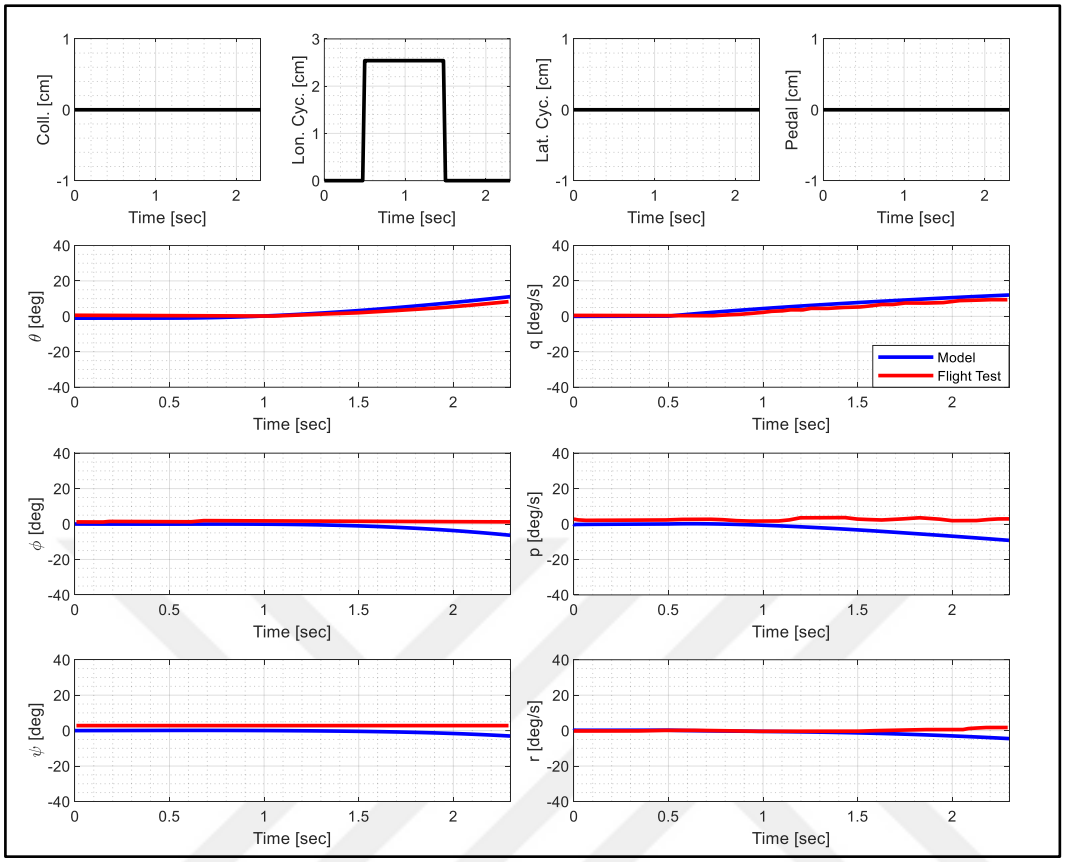


Figure 3.4. Time History Comparison with Flight Test Data

From Figure 3.4, it can be seen that even though there are certain amount of discrepancy in the off-axis response, the on-axis response agrees quite well with the flight test data, which also indicates the sufficiency of the developed mathematical model.

3.3 Linearization of the Helicopter Model

As it was mentioned previously, the development of control laws for the helicopter requires linearized model. Regarding this, small perturbation theory is utilized. The dynamics of the nonlinear model can be expressed by the following formula [23]:

$$\dot{\underline{x}} = F(\underline{x}, \underline{u}, t) \tag{3.68}$$

In Equation (3.68), $\underline{x}$ denotes the helicopter state vector whereas the control input vector is designated by $\underline{u}$. Due to complexity of the nonlinear model, the function F that describes the dynamics cannot be obtained explicitly, and the linearization is performed by simulation with perturbed states and central differencing scheme. This approach needs further elaboration. The intention behind this linearization procedure is to write the overall system dynamics in the following state space format:

$$\dot{x} = Ax + Bu \tag{3.69}$$

$$y = Cx + Du \tag{3.70}$$

Using Equation (3.68) the matrices A and B can be expressed as the partial derivatives of F [23]:

$$A = \left(\frac{\partial F}{\partial x}\right)_{x=x_e} \tag{3.71}$$

$$B = \left(\frac{\partial F}{\partial u}\right)_{u=u_e} \tag{3.72}$$

Where, x_e and u_e denote the helicopter states and control inputs at trim. According to small perturbation theorem, perturbed states and control inputs can be written as follows [24]:

$$x = x_e \pm \delta x \tag{3.73}$$

$$u = u_e \pm \delta u \tag{3.74}$$

For enhanced accuracy, the states and control inputs are perturbed in both positive and negative directions and central differencing scheme is applied for the derivative calculation [25]. The perturbation of each state leads to the following perturbed state matrix:

$$\vec{x}_{j\pm} = \begin{Bmatrix} x_{e_{j-2}} \\ x_{e_{j-1}} \\ x_{e_j} \pm \delta x_j \\ x_{e_{j+1}} \\ x_{e_{j+2}} \end{Bmatrix} \tag{3.75}$$

Then, the j^{th} column of the state matrix A can be calculated as follows:

$$A_j = \frac{\dot{x}_{j+} - \dot{x}_{j-}}{2\delta x_j} \tag{3.76}$$

The same procedure can be carried out by perturbing control inputs at trim to determine the control matrix B. Finally, the output matrix C and the feedthrough matrix D in the Equation (3.70), are determined as identity matrix of size [8×8] and zero matrix of size [8×4] respectively.

To verify the validity of the linearized model, the eigenvalues of the A matrix are examined to investigate the dynamic modes of the helicopter and the results are compared to a study with verified mathematical model given in [8]. The study upon which the comparison is made includes the CH-53 helicopter as well and the model parameters are close to those used in this study. The following figure illustrates pole locations in forward flight regime without sideslip, in which the airspeed is ranging from 0 to 100 knots. The related dynamic modes, which were determined based on the eigenvectors of the A matrix, are also included in the same figure.

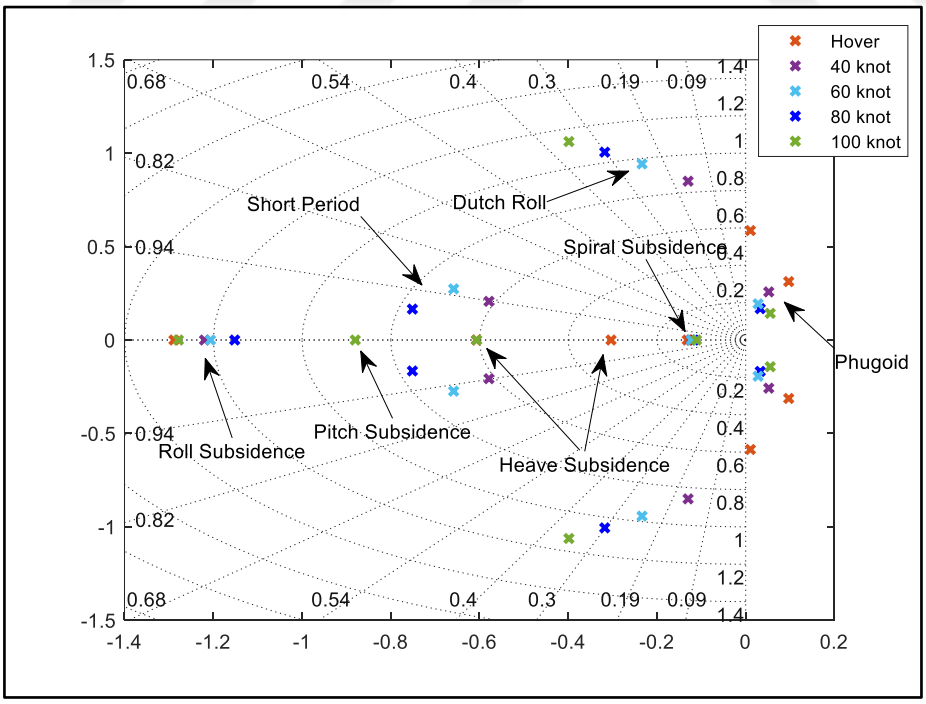


Figure 3.5. Dynamic Modes of the Linear System

Figure 3.5 shows that the linearized model captures the expected dynamic modes of the helicopter. As it was mentioned above, identification of the dynamic modes is performed based on the eigenvectors of the state matrix. That is, the states that contribute the most to the eigenvector of the corresponding dynamic mode determines its characteristics. To illustrate the procedure, eigenvalues and eigenvectors of the state matrix of the linearized model in hovering flight condition are provided in the following set of tables. For a clear demonstration, the longitudinal and lateral modes are provided separately.

Table 3.1. Longitudinal Dynamic Modes

		Eigenvalues & Dynamic Modes			
		$0.097 + 0.313i$	$0.097 - 0.313i$	$-0.303 + 0i$	$-0.607 + 0i$
		Phugoid	Phugoid	Heave Subs.	Pitch Subs.
Eigenvectors	u	$-0.9622 + 0.0000i$	$-0.9622 - 0.0000i$	-0.5850	0.8597
	w	$-0.0452 - 0.0091i$	$-0.0452 + 0.0091i$	-0.7978	0.0945
	q	$-0.0082 + 0.0064i$	$-0.0082 - 0.0064i$	0.0035	-0.0285
	θ	$0.0107 + 0.0310i$	$0.0107 - 0.0310i$	-0.0184	0.0492
	v	$-0.1846 - 0.1912i$	$-0.1846 + 0.1912i$	0.1388	0.4965
	p	$0.0033 + 0.0005i$	$0.0033 - 0.0005i$	-0.0006	0.0200
	ϕ	$0.0040 - 0.0080i$	$0.0040 + 0.0080i$	-0.0045	-0.0308
	r	$-0.0098 - 0.0009i$	$-0.0098 + 0.0009i$	0.0410	-0.0282

The eigenvalues and eigenvectors corresponding to the longitudinal dynamic modes can be seen from Table 3.1. The dominant states in each mode are highlighted to distinguish them easily. Regarding the table, it should be pointed out that units of the angular states are radians and radians per second and corresponding values of these particular states appear lower than those of the linear velocity states. Hence, while making a comparison among states to determine their dominance, this should be taken into account.

From this point on, each respective mode will be examined one by one. As far as the phugoid mode is concerned, the velocity in the body x-axis, u is the dominant state and effect of the remaining states is relatively small. In heave subsidence mode, the vertical velocity in the body z-axis, w is the most prominent state and body x-velocity u also has noticeable contribution, which meets the expectation. In pitch subsidence mode, the contribution of the state u is the most dominant and different from the previous longitudinal modes, the velocity in the body y-axis also has noticeable

impact. As for the rest of the states, the pitch angle, θ also has certain amount of contribution, which is consistent with the characteristics of this particular mode.

As it was mentioned above, the lateral dynamic modes are examined in a separate table provided below:

Table 3.2. Lateral Dynamic Modes

		Eigenvalues & Dynamic Modes			
		$0.0106 + 0.5859i$	$0.0106 - 0.5859i$	$-0.1318 + 0i$	$-1.2885 + 0i$
		Dutch Roll	Dutch Roll	Spiral Subs.	Roll Subs.
Eigenvectors	u	$-0.0418 + 0.2205i$	$-0.0418 - 0.2205i$	-0.6163	-0.3529
	w	$0.0336 + 0.0356i$	$0.0336 - 0.0356i$	-0.0818	-0.0783
	q	$-0.0017 + 0.0102i$	$-0.0017 - 0.0102i$	-0.0053	0.0391
	θ	$0.0155 + 0.0021i$	$0.0155 - 0.0021i$	-0.0081	-0.0318
	v	$0.9703 + 0.0000i$	$0.9703 - 0.0000i$	0.7731	-0.9111
	p	$-0.0355 + 0.0032i$	$-0.0355 - 0.0032i$	-0.0046	-0.1490
	ϕ	$0.0027 + 0.0595i$	$0.0027 - 0.0595i$	-0.0109	0.1143
	r	$0.0127 - 0.0211i$	$0.0127 + 0.0211i$	0.1247	0.0378

The method of inspection of the lateral dynamic modes is similar to that of the longitudinal modes. Regarding the Dutch roll mode, it can be seen that the major contributor is the velocity in body y-axis, v. Also, effect of the roll rate, p is noticeable, which is consistent with the characteristics of this mode. Regarding the spiral subsidence, velocity v and the yaw rate r contribute the most, which meets with the expectations. Finally, in the roll subsidence mode, the major contributors are v, p and the roll angle ϕ, which agrees with the roll subsidence mode characteristics.

The dynamic modes are also provided in the following figure in a superimposed manner with the aforementioned study [8], for a further verification:

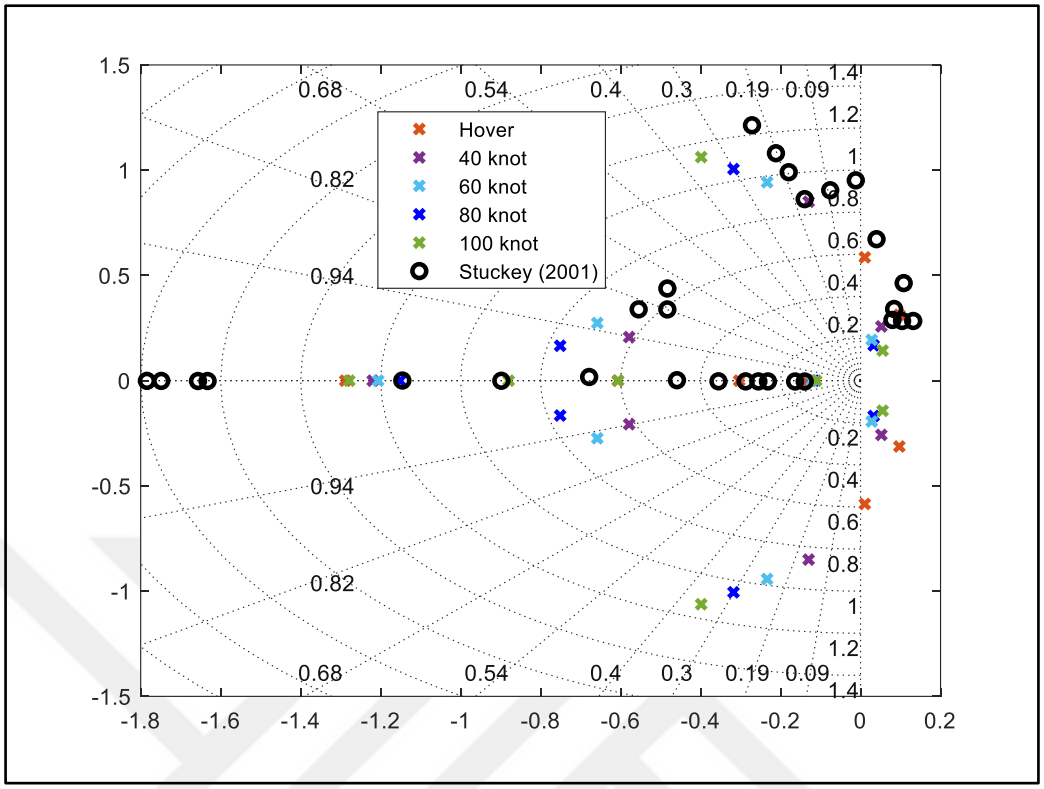


Figure 3.6. Dynamic Modes of the Linear System (Comparison with Literature)

From Figure 3.6, one can observe that apart from the roll subsidence mode in left most side of the real axis, the overall consistency can be evaluated as satisfactory in terms of pole locations. That is, the same dynamic modes exist in both studies and the trend observed in all pole locations with increasing airspeed agrees with the reference study. Considering that the roll subsidence mode is placed on the far-left plane and it dies out in a quite fast manner, the discrepancy in this particular mode does not have a significant effect on the overall system dynamics.

The linearization procedure can also be verified by performing the same simulation with both linear and nonlinear models. Given that there is no controller implemented to the system at this stage and the system is unstable due to phugoid poles, doublet input with a magnitude of 1 cm is given in all channels to prevent excessive divergence. Following figure illustrates the comparative results of the nonlinear and linear models in hovering flight condition:

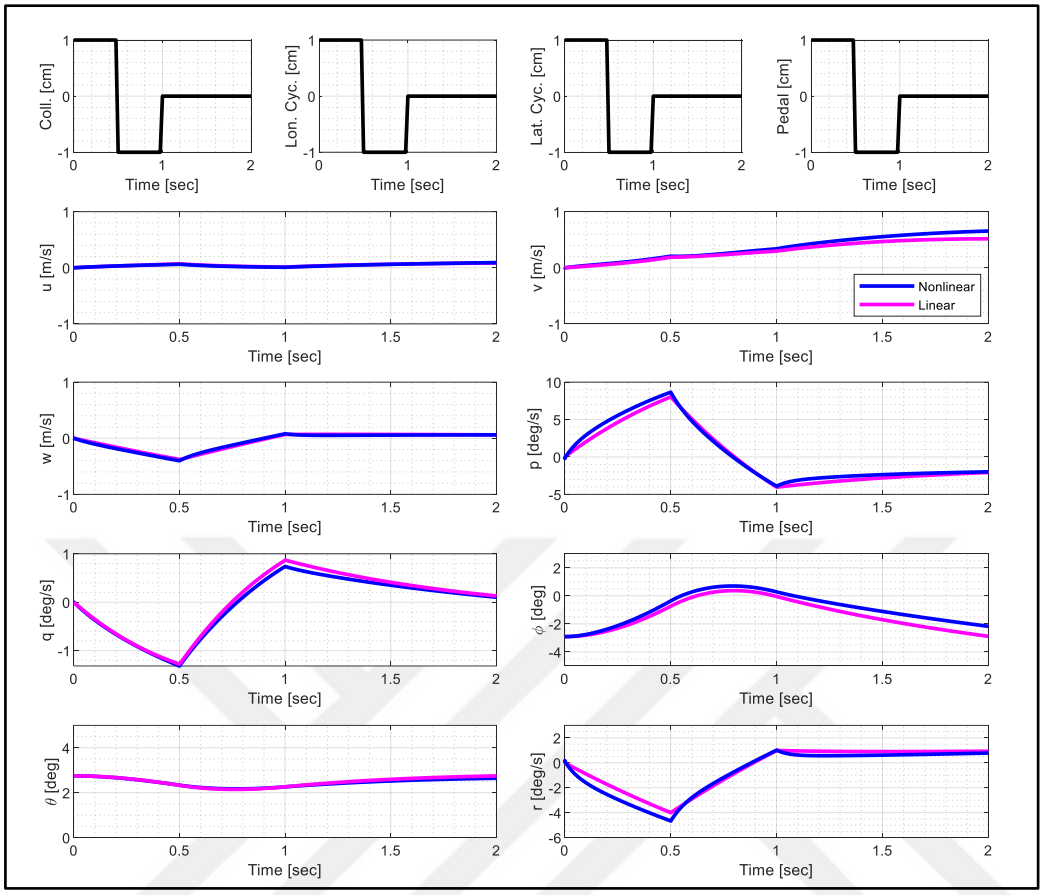


Figure 3.7. Nonlinear and Linear Model Time History Comparison

From Figure 3.7, it can be seen the overall agreement of the nonlinear and linear models is quite well in all axes for a simulation duration of 2 seconds. Hence, it can be asserted that the linearized model is capable of capturing the dynamics of the nonlinear model accurately.

The discussion so far regarding the mathematical model validation indicates that the generated linear models can indeed be used for the control law development, which is discussed in the next chapter.

CHAPTER 4

STABILITY AUGMENTATION SYSTEM (SAS) AND AUTOPLIT DESIGN FOR THE HELICOPTER

4.1 Stability Augmentation System (SAS) Design

The controller structure for the helicopter involves sequential loop closing scheme. That is, firstly the inner loop stability augmentation systems are implemented based on the root locus plots of the SISO transfer functions from the longitudinal cyclic, lateral cyclic and pedal inputs to the respective angular rates in each axis. Then, outer loop PID controllers that perform attitude and altitude hold autopilot functions are designed. In this section, development of the respective controllers in hovering flight is shown. However, the similar approach can be followed for any airspeed of interest.

It should be noted that as a practical approach, the SAS design is performed for the uncoupled longitudinal and lateral linear systems. That is, the original linear system mentioned above consists of a total of 8 longitudinal and lateral states and to develop SAS, these are separated. There are two available options regarding the decoupling process namely the model truncation and Matched DC gain method. The examination of each method has shown that, the truncation of the cross-coupling terms provides longitudinal and lateral dynamics with the related mode locations closer to the full [8×8] system. Hence, this particular method is used in the controller development.

The truncation procedure is summarized below:

$$\dot{x} = \begin{bmatrix} A_{11} & A_{12} \\ A_{21} & A_{22} \end{bmatrix} x + \begin{bmatrix} B_{11} & B_{12} \\ B_{21} & B_{22} \end{bmatrix} \begin{bmatrix} \delta_{coll} \\ \delta_{lon} \\ \delta_{lat} \\ \delta_{pedal} \end{bmatrix} \tag{4.1}$$

Here each of A_{11}, A_{12}, A_{21}, A_{22} is of dimension of [4×4] and each of B_{11}, B_{12}, B_{21}, B_{22} is of dimension of [4×2]. The longitudinal and lateral states are defined as follows:

$$x = \begin{bmatrix} u \\ w \\ q \\ \theta \\ v \\ p \\ \phi \\ r \end{bmatrix} \rightarrow [x_{lon}] = \begin{bmatrix} u \\ w \\ q \\ \theta \end{bmatrix} \quad [x_{lat}] = \begin{bmatrix} v \\ p \\ \phi \\ r \end{bmatrix} \tag{4.2}$$

This leads to the following state space representations of the longitudinal and lateral dynamics:

$$\dot{x}_{lon} = A_{11}x_{lon} + B_{11}\begin{bmatrix} \delta_{coll} \\ \delta_{lon} \end{bmatrix} \quad \dot{x}_{lat} = A_{22}x_{lat} + B_{22}\begin{bmatrix} \delta_{lat} \\ \delta_{pedal} \end{bmatrix} \tag{4.3}$$

Next, design of pitch axis and lateral-directional stability augmentation systems will be discussed.

4.1.1 Design of Pitch Axis Stability Augmentation System

Block diagram of the pitch axis SAS is provided below:

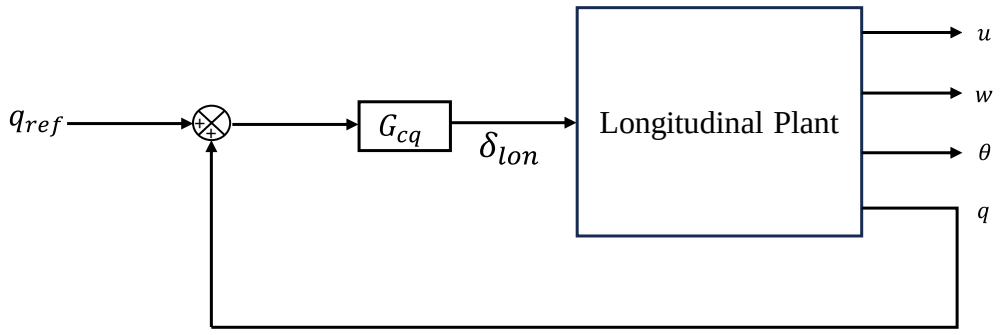


Figure 4.1. Block Diagram for Pitch Axis SAS

Pitch axis SAS is designed based on root locus diagram of the SISO transfer function from the longitudinal cyclic to the pitch rate:

$$\frac{q}{\delta_{lon}} = \frac{-0.05627s^3 - 0.01749s^2 - 4.693 \times 10^{-5}s}{s^4 + 0.5961s^3 + 0.0825s^2 + 0.0517s + 0.01569} \tag{4.4}$$

It should be noted that due to the negative sign in the numerator coefficients, the feedback loop is integrated with positive sign. The root locus diagram for this transfer function is provided below:

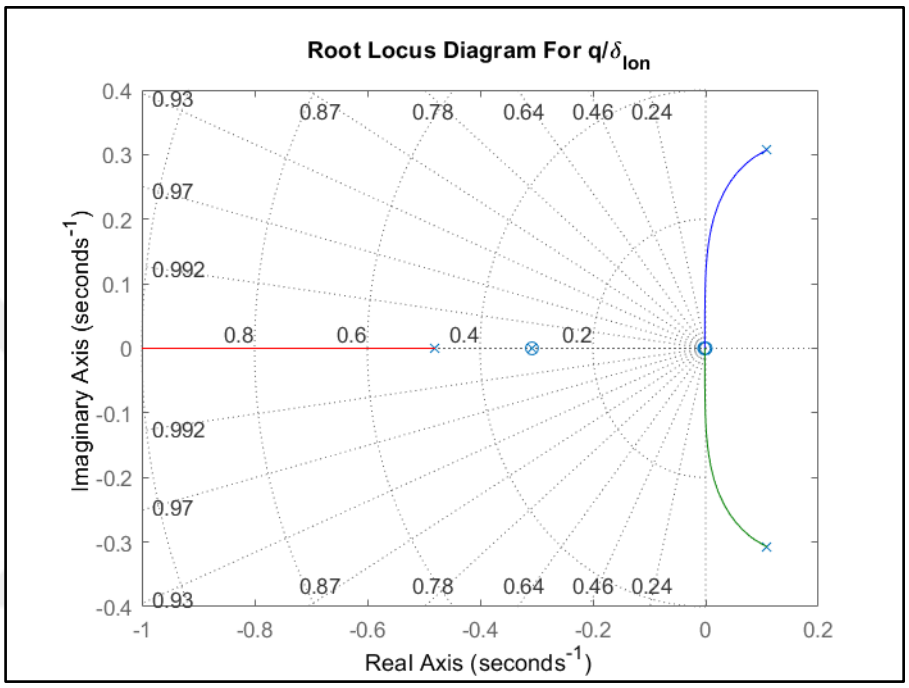


Figure 4.2. Root Locus Diagram for q/δ_{lon}

Figure 4.2 shows that it is not possible to obtain a stable system with only proportional gain due to the fact that the right-hand side phugoid poles cannot be moved to left half plane no matter how large the gain is. Hence, candidate lead-lag compensators were investigated and it turned out that implementation of a suitable lag compensator indeed moves the unstable poles to left half plane with sufficient damping. The proposed controller and resultant Root-Locus diagram are provided below:

$$G_{cq} = 9.95\frac{s + 0.5}{s + 0.05} \tag{4.5}$$

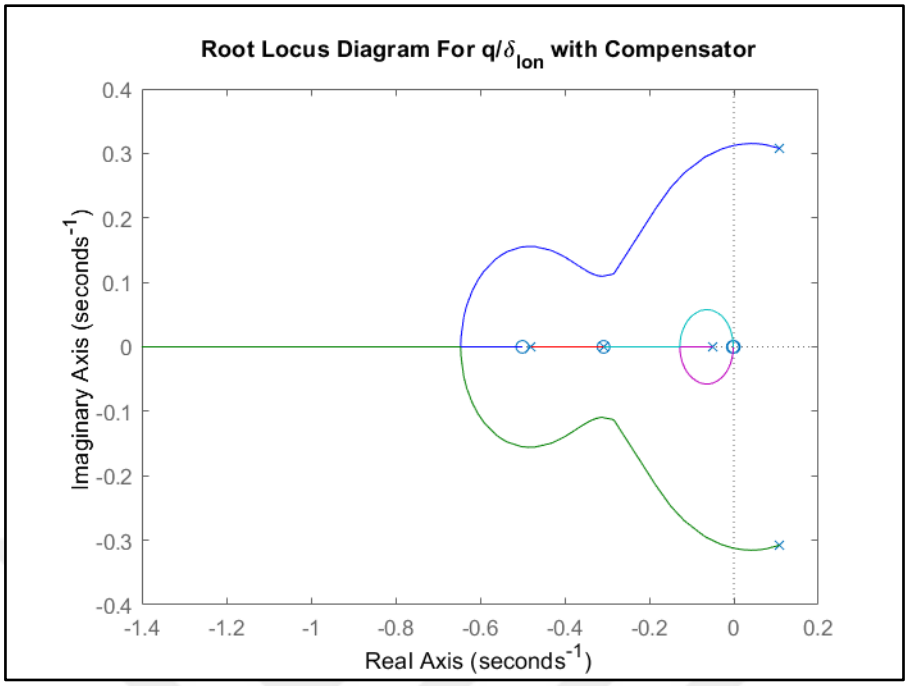


Figure 4.3. Root Locus Diagram for q/δ_{lon} with Compensator

Figure 4.3 shows that the unstable poles indeed become stable with the proposed controller. Next section investigates the design of lateral-directional stability augmentation system.

4.1.2 Design of Lateral-Directional Stability Augmentation System

For these particular SAS, a similar approach to the pitch axis SAS is implemented. Due to the coupling between the lateral and directional motion, the proposed stability augmentation systems in both axes are examined simultaneously. Firstly, the loop from the roll rate (p) to the lateral cyclic input (δ_{lat}) is closed. Then, the loop is closed from the yaw rate (r) to the pedal input (δ_{pedal}). The required controllers are determined based on the respective root locus plots.

The SISO transfer function from the lateral cyclic to the roll rate is given below:

$$\frac{p}{\delta_{lat}} = \frac{0.1836s^3 + 0.04404s^2 + 3.291 \times 10^{-5}s - 0.001465}{s^4 + 1.547s^3 + 0.3055s^2 + 0.513s + 0.06259} \qquad (4.6)$$

The proposed controller structure is provided in the following block diagram:

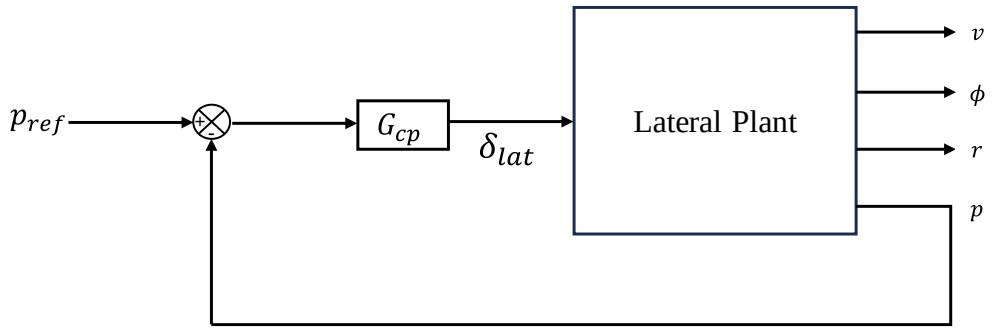


Figure 4.4. Block Diagram for the Lateral SAS

The root locus diagram for the transfer function given in Equation (4.6) is provided below:

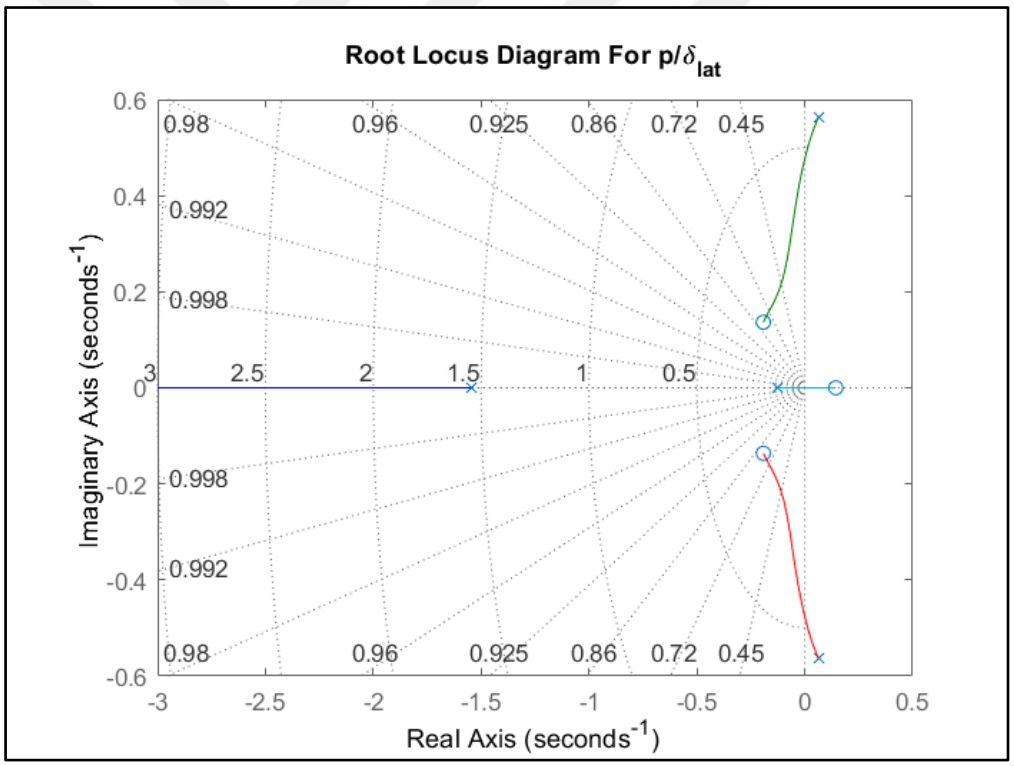


Figure 4.5. Root Locus Diagram for p/δ_{lat}

Figure 4.5 shows that the unstable Dutch-Roll poles can be moved to the left half plane with only proportional controller. By giving certain amount of damping to the unstable poles as well, the controller G_{cp} is determined as follows:

$$G_{cp} = 26.5 \tag{4.7}$$

Now that the lateral SAS is obtained, the loop from the roll rate to the lateral cyclic input is closed and the transfer function from the pedal input to the yaw rate is determined as follows:

$$\frac{r}{\delta_{pedal}} = \frac{-1732s^3 - 0.9261s^2 - 002472s - 0.04258}{s^4 + 6.413s^3 + 1.473s^2 + 0.5139s + 0.02375} \tag{4.8}$$

The proposed controller structure for the lateral-directional SAS is provided below:

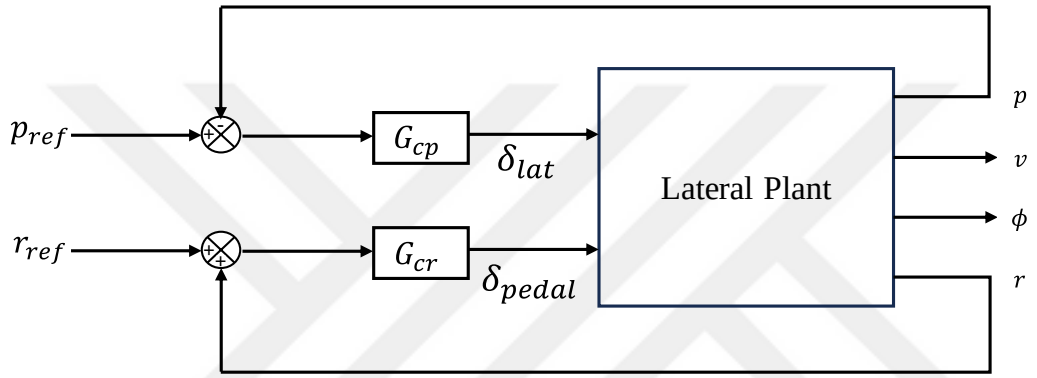


Figure 4.6. Block Diagram for the Directional SAS

It should be noted that due to the negative sign in the numerator coefficients, the feedback loop is integrated with positive sign. The root locus diagram for the transfer function is provided below:

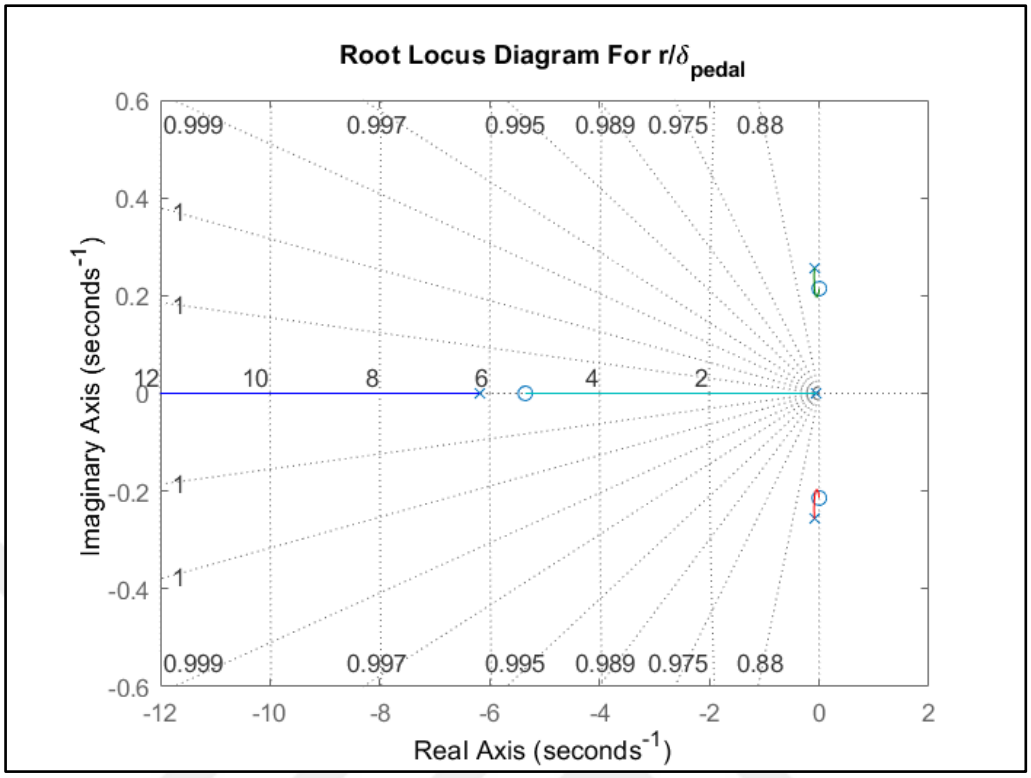


Figure 4.7. Root Locus Diagram for r/δ_{pedal}

According to Figure 4.7, the oscillatory poles are not affected too much from a proportional controller. However, the real pole close to the origin can be moved to the left with this particular type of controller. Considering that the major servo tracking control problem will mainly be solved with the outer loop autopilots, providing certain amount of proportional gain without deteriorating the damping of the oscillatory poles too much is considered as sufficient at this stage. Hence, G_{cr} is determined as follows:

$$G_{cr} = 4.63 \tag{4.9}$$

4.2 Autopilot Design

Given that stability augmentation system design is completed, the outer loop autopilots need to be implemented to the overall system. The list of autopilots is provided below:

- Pitch attitude hold
- Roll attitude hold
- Heading hold
- Altitude hold

To enhance the overshoot and steady state characteristics, the autopilots are implemented as PID controllers. The design of autopilots is accomplished with the help of Simulink's PID Tuner function by taking the robustness and tracking performance into account. Each of the autopilots is illustrated with representative results below.

4.2.1 Pitch Attitude Hold Autopilot

Block diagram for the pitch attitude hold autopilot is given below:

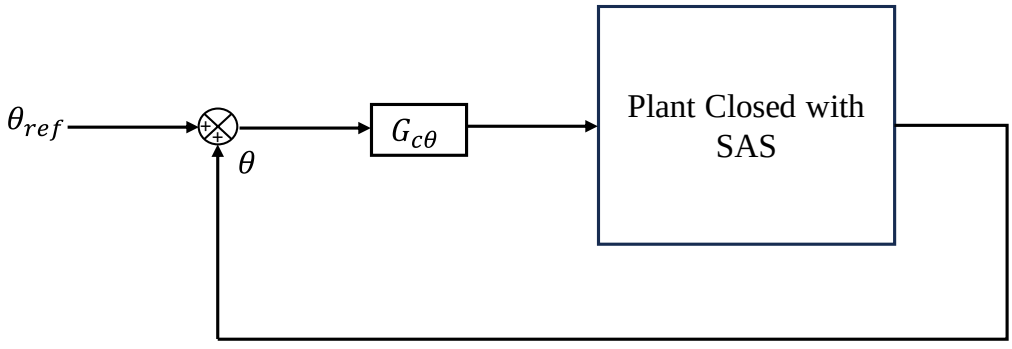


Figure 4.8. Pitch Attitude Hold Autopilot

The pitch attitude hold autopilot is implemented by feeding back the pitch attitude of the helicopter (θ) to the reference pitch attitude command (θ_{ref}) such that the controller $(G_{c\theta})$ output acts through the longitudinal cyclic.

It should be noted that due to the negative sign in the numerator coefficients of the related transfer function from reference command to the pitch attitude, the feedback loop is integrated with positive sign.

Response of the closed loop system to the unit step pitch attitude reference input of 1° is illustrated in the following figure:

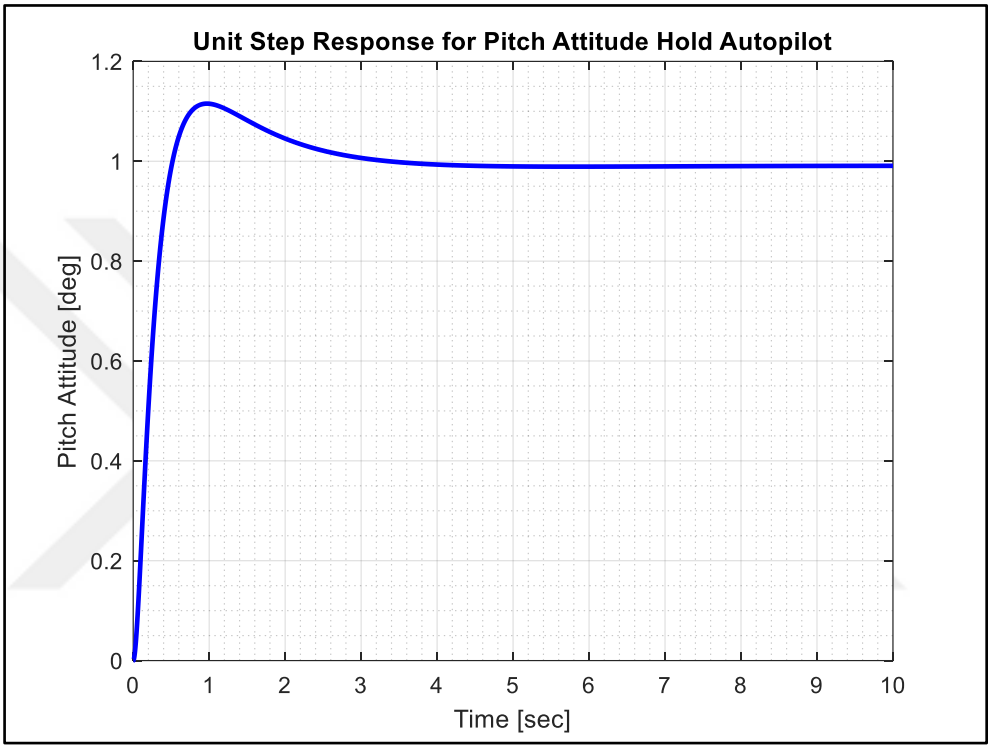


Figure 4.9. Unit Step Response for Pitch Attitude Hold Autopilot

From Figure 4.9, it can be seen that the overshoot in the unit step response does not exceed 20% and the pitch attitude settles down to the final value of 1° in a relatively short amount of time. Also, because of the negative sign in the numerator coefficients of the respective transfer function, negative of the real output is drawn in the figure above.

The gain and phase margins are provided in the Bode plot below to verify the robustness of the closed loop system:

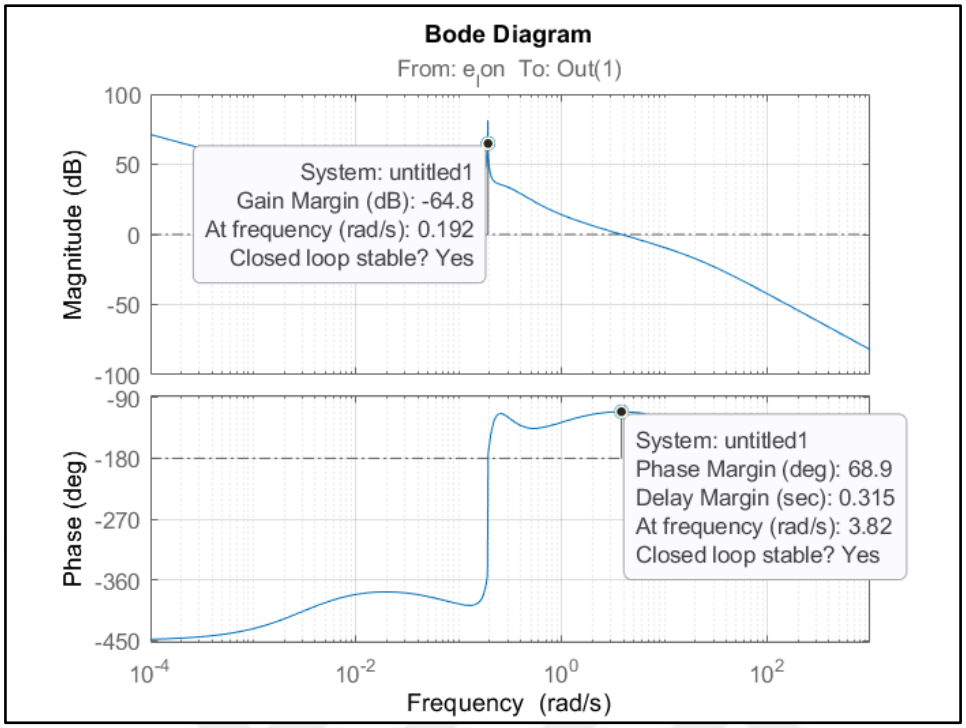


Figure 4.10. Bode Diagram for Pitch Attitude Hold Autopilot

From Figure 4.10, it can be seen that the closed loop system has a minimum gain margin of -64.8 dB, whereas the phase margin is 68.9°. These values indicate that the system is sufficiently robust.

4.2.2 Roll Attitude Hold Autopilot

Block diagram for the roll attitude hold autopilot is given below:

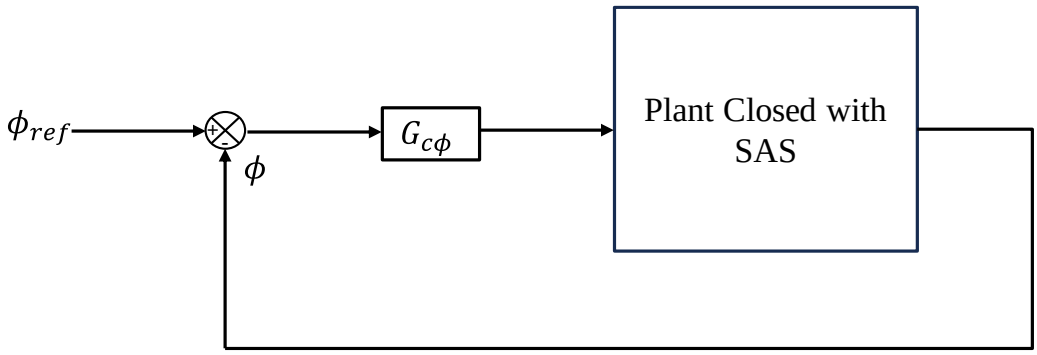


Figure 4.11. Roll Attitude Hold Autopilot

The roll attitude hold autopilot is implemented by feeding back the roll attitude of the helicopter (ϕ) to the reference roll attitude command (ϕ_{ref}) such that the controller $(G_{c\phi})$ output acts through the lateral cyclic.

Response of the closed loop system to the unit step roll attitude reference input of 1° is illustrated in the following figure:

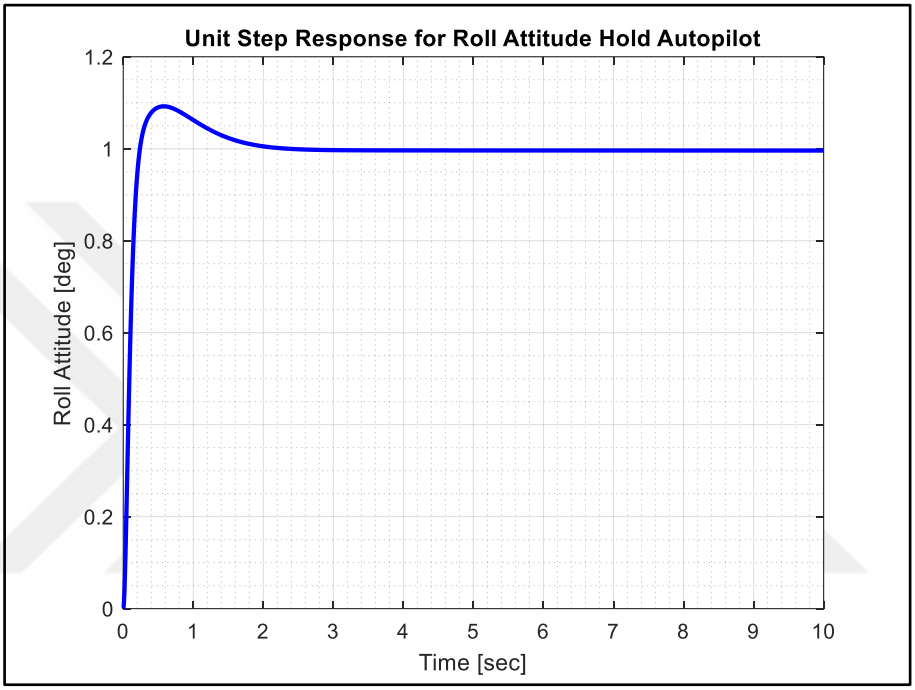


Figure 4.12. Unit Step Response for Roll Attitude Hold Autopilot

From Figure 4.12, it can be seen that the overshoot in the unit step response does not exceed 20% and the roll attitude settles down to the final value of 1° in a relatively short amount of time.

The gain and phase margins are provided in the Bode plot below to verify the robustness of the closed loop system:

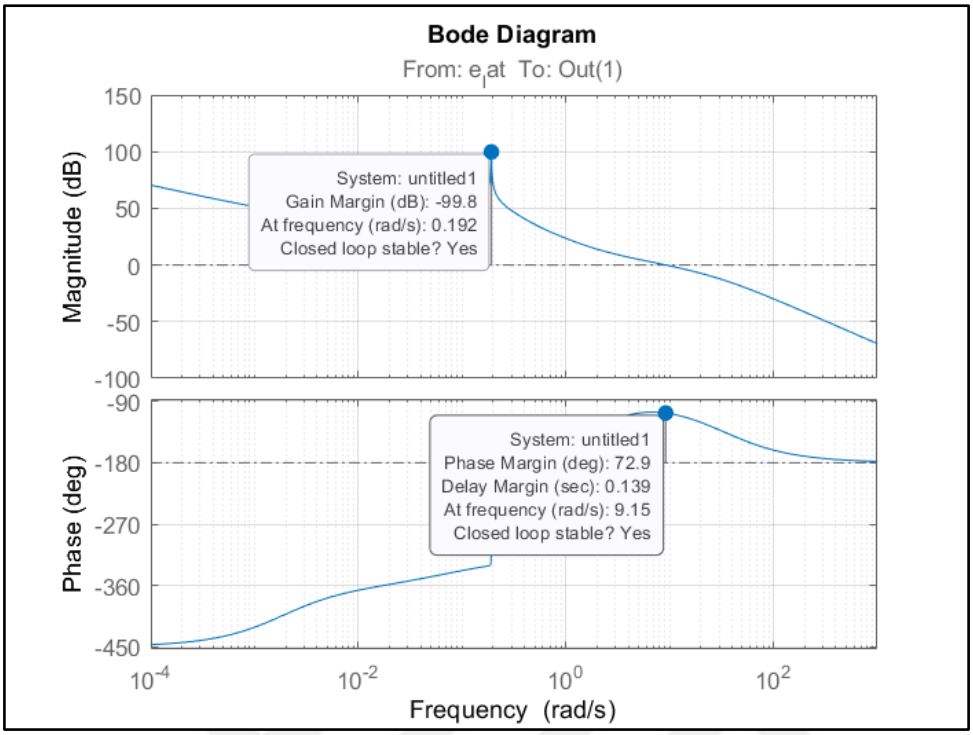


Figure 4.13. Bode Diagram for Roll Attitude Hold Autopilot

From Figure 4.13, it can be seen that the closed loop system has a minimum gain margin of -99.8 dB, whereas the phase margin is 72.9°. These values indicate that the system is sufficiently robust.

4.2.3 Heading Hold Autopilot

Block diagram for the heading hold autopilot is given below:

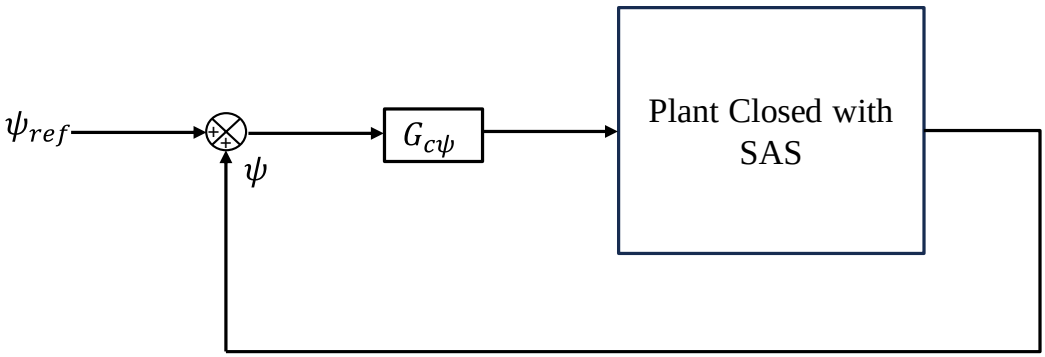


Figure 4.14. Heading Hold Autopilot

The heading hold autopilot is implemented by feeding back the heading attitude (yaw angle) of the helicopter (ψ) to the reference heading attitude command (ψ_{ref}) such that the controller $(G_{c\psi})$ output acts through the pedal. It should be noted that, the heading attitude ψ is omitted from the original 8 longitudinal and lateral states of the helicopter. Hence, to design this particular autopilot it is included as an additional output of the plant.

It should be noted that due to the negative sign in the numerator coefficients of the related transfer function from reference command to the heading attitude, the feedback loop is integrated with positive sign.

Response of the closed loop system to the unit step heading attitude reference input of 1° is illustrated in the following figure:

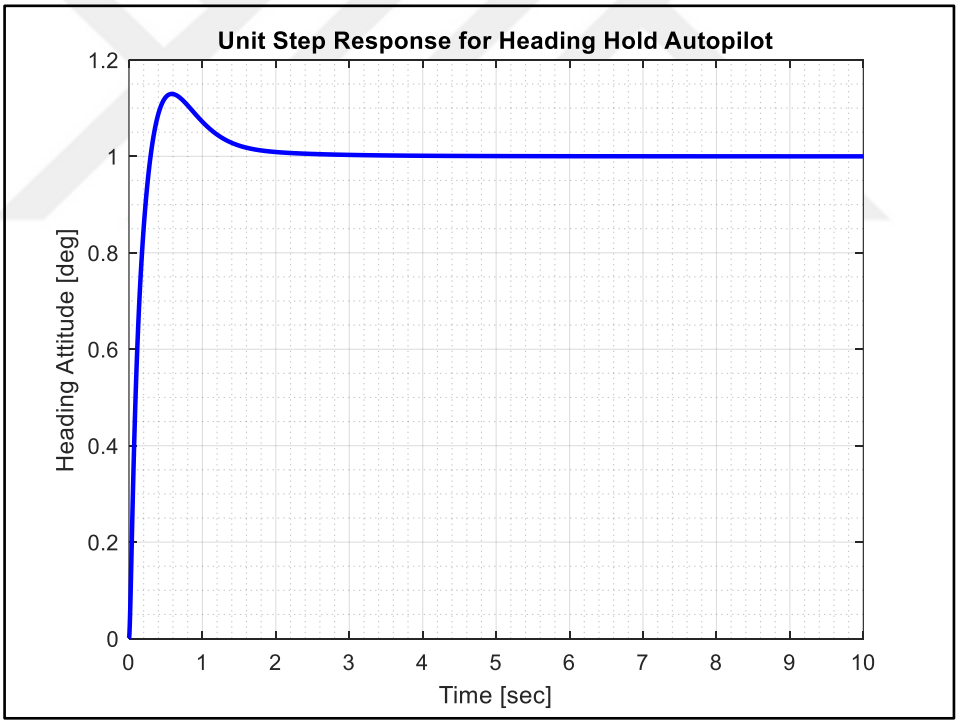


Figure 4.15. Unit Step Response for Heading Hold Autopilot

From Figure 4.15, it can be seen that the overshoot in the unit step response does not exceed 20% and the heading attitude settles down to the final value of 1° in a relatively short amount of time. Also, because of the negative sign in the numerator

coefficients of the respective transfer function, negative of the real output is drawn in the figure above.

The gain and phase margins are provided in the Bode plot below to verify the robustness of the closed loop system:

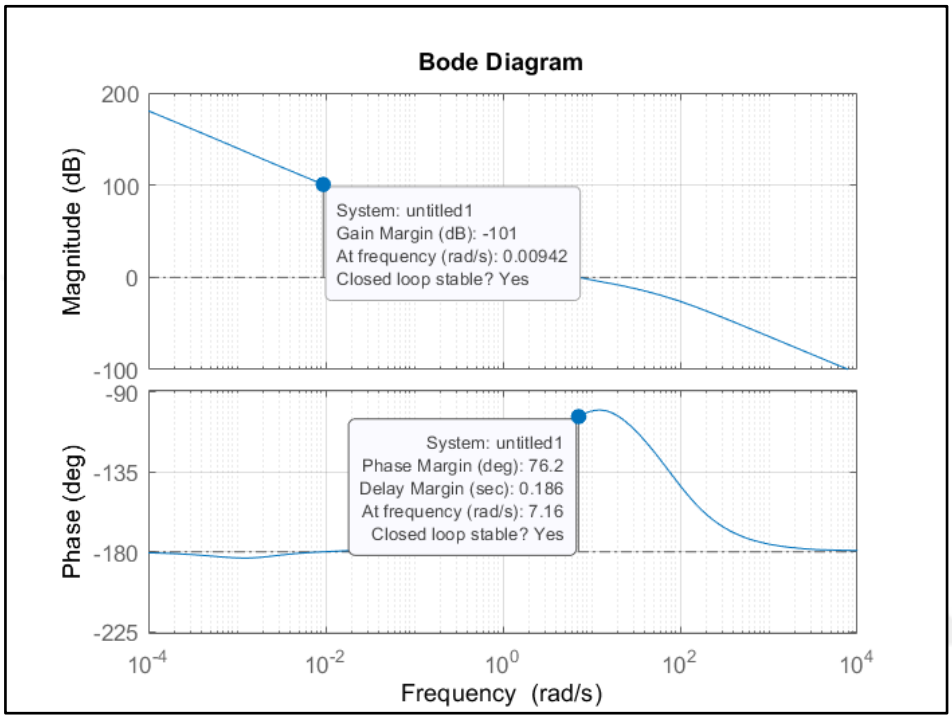


Figure 4.16. Bode Diagram for Heading Hold Autopilot

From Figure 4.16, it can be seen that the closed loop system has a minimum gain margin of -101 dB, whereas the phase margin is 76.2°. These values indicate that the system is sufficiently robust.

4.2.4 Altitude Hold Autopilot

The altitude hold autopilot is implemented by feeding back the inertial altitude of the helicopter (h) to the reference altitude command (h_{ref}) such that the controller (G_{ch}) output acts through the collective input. It should be noted that, the inertial altitude h is omitted from the original 8 longitudinal and lateral states of the

helicopter. Hence, to design this particular autopilot it is included as an additional output of the plant.

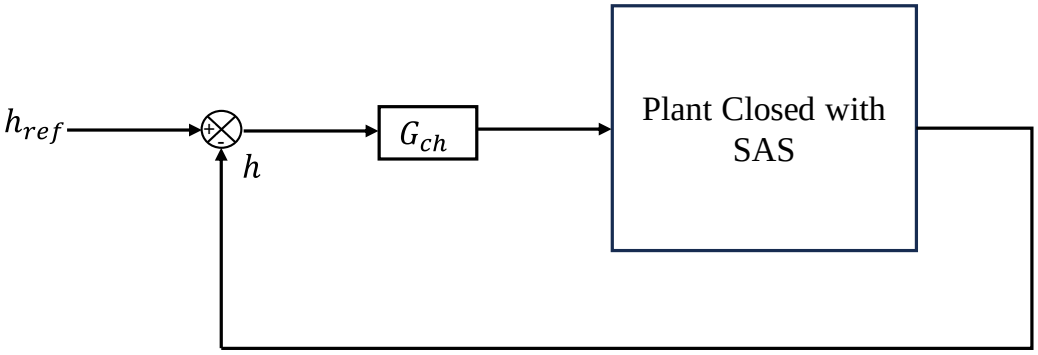


Figure 4.17. Altitude Hold Autopilot

Response of the closed loop system to the step altitude reference input of 1 meter is illustrated in the following figure:

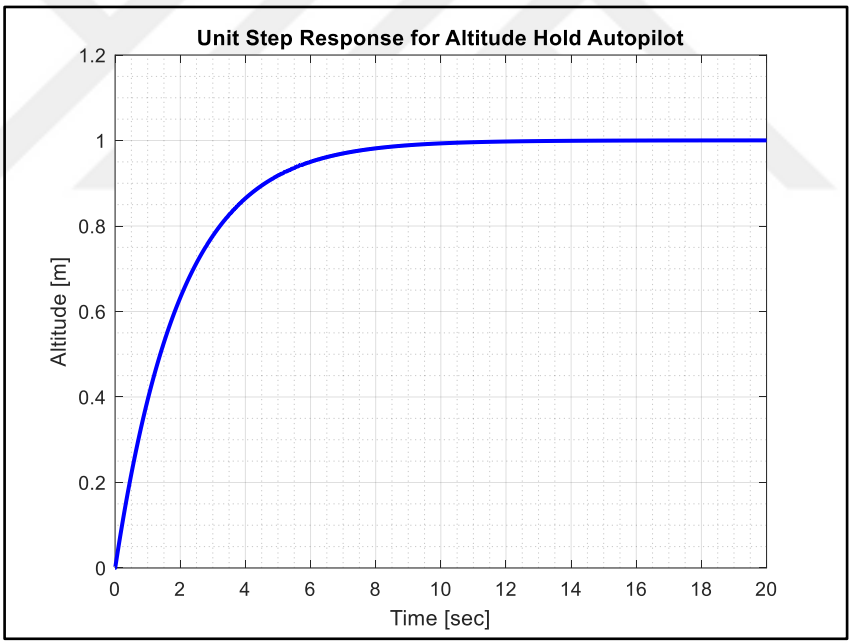


Figure 4.18. Step Response for Altitude Hold Autopilot

From Figure 4.18, it can be noticed, that the altitude hold autopilot designed in such a way that it does not settle to the reference input in an aggressive manner unlike the previously proposed autopilots. This is done purposely and the reason is to prevent occurrence of excessive collective input and climb rate as the altitude hold autopilot

is engaged. This approach regarding the altitude hold autopilot design is based on the reference [26], where it is explicitly stated that altitude hold autopilot should not be activated when there is an excessive amount of deviation from the commanded altitude.

The gain and phase margins are provided in the Bode plot below to verify the robustness of the closed loop system:

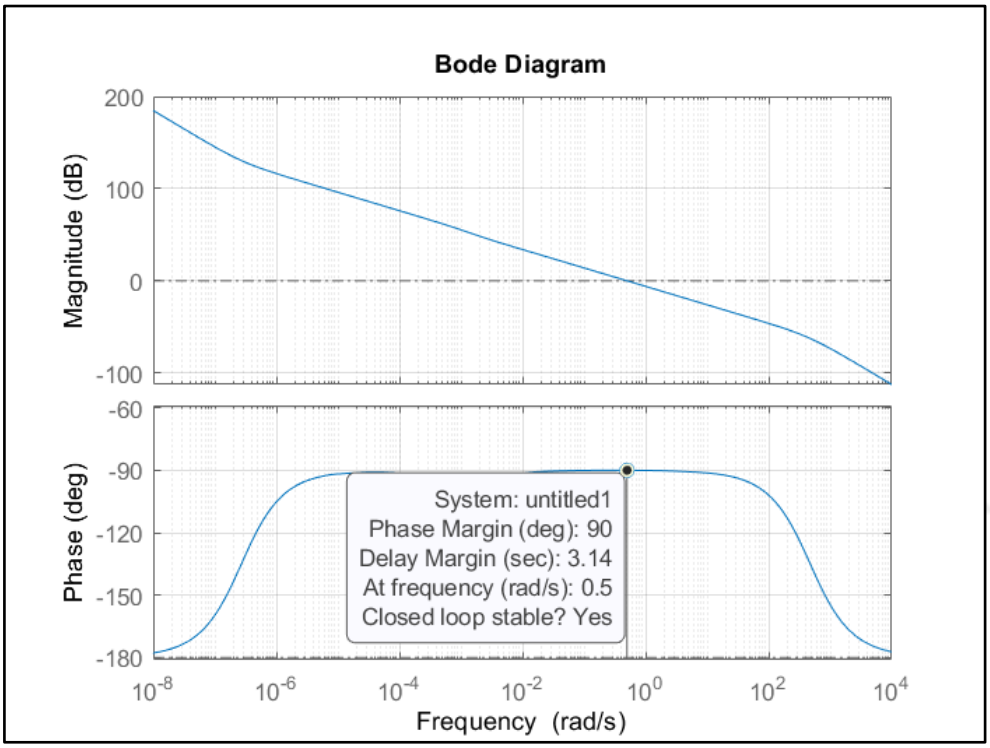


Figure 4.19. Bode Diagram for Altitude Hold Autopilot

From Figure 4.19, it can be seen that the closed loop system has a gain margin of infinity, whereas the phase margin is 90°. These values indicate that the system is sufficiently robust.

The summary of the developed autopilots can be found in the following table with their respective time response characteristics and stability margins:

Table 4.1. List of Autopilots for Hovering Flight Condition

Pitch Attitude Hold Autopilot			
$G_{c\theta} = 7.5 + \frac{2.03}{s} + 6.37\frac{20.82s}{20.82 + s}$			
Overshoot [%]	**Settling Time [sec]**	**Gain Margin [dB]**	**Phase Margin [deg]**
11.5	2.53	-64.8	68.9
Roll Attitude Hold Autopilot			
$G_{c\phi} = 12.34 + \frac{15.58}{s} + 1.73\frac{33.37s}{33.37 + s}$			
Overshoot [%]	**Settling Time [sec]**	**Gain Margin [dB]**	**Phase Margin [deg]**
9.22	1.56	-99.8	72.9
Heading Hold Autopilot			
$G_{c\psi} = 25.39 + \frac{12.92}{s} + 9.83\frac{77.07s}{77.07 + s}$			
Overshoot [%]	**Settling Time [sec]**	**Gain Margin [dB]**	**Phase Margin [deg]**
12.9	1.55	-101	76.2
Altitude Hold Autopilot			
$G_{ch} = 0.184 + \frac{5 \times 10^{-8}}{s} + 0.6\frac{473.82s}{473.82 + s}$			
Overshoot [%]	**Settling Time [sec]**	**Gain Margin [dB]**	**Phase Margin [deg]**
-	7.82	∞	90

For a clear illustration, block diagram of the overall closed loop helicopter model that contains the developed SAS and autopilots is provided in the following figure:

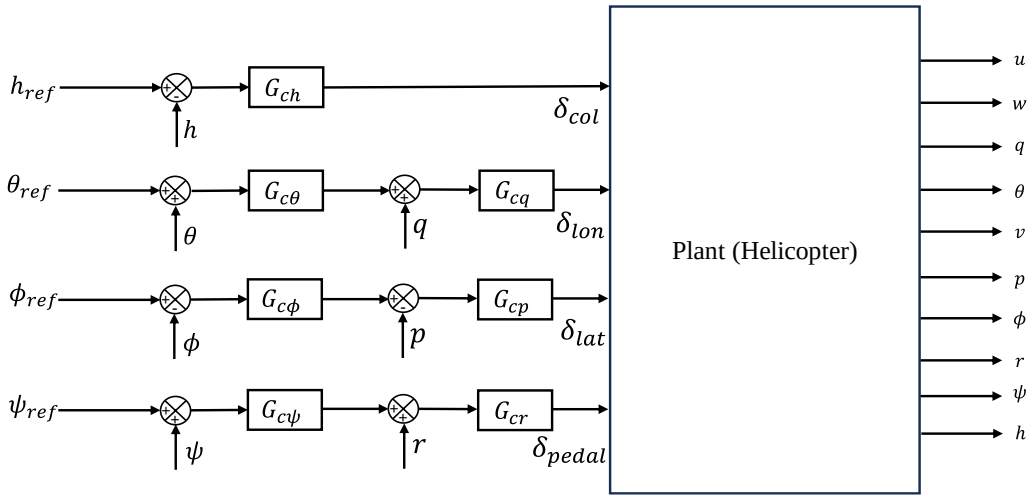


Figure 4.20. Block Diagram of the Closed Loop System

In order to examine the effectiveness of the proposed flight control system, the linear and nonlinear models are simulated with the identical input profiles given below. It should be noted the inputs are applied to the longitudinal and lateral channels by defining reference pitch and roll attitude commands. The reference altitude and heading angle are defined as zero. These particular input profiles represent a realistic maneuver that translates a hovering helicopter to the forward and right. Also, the same profiles will be utilized in the inspection of slung dynamics as well, which will be discussed in detail later on.

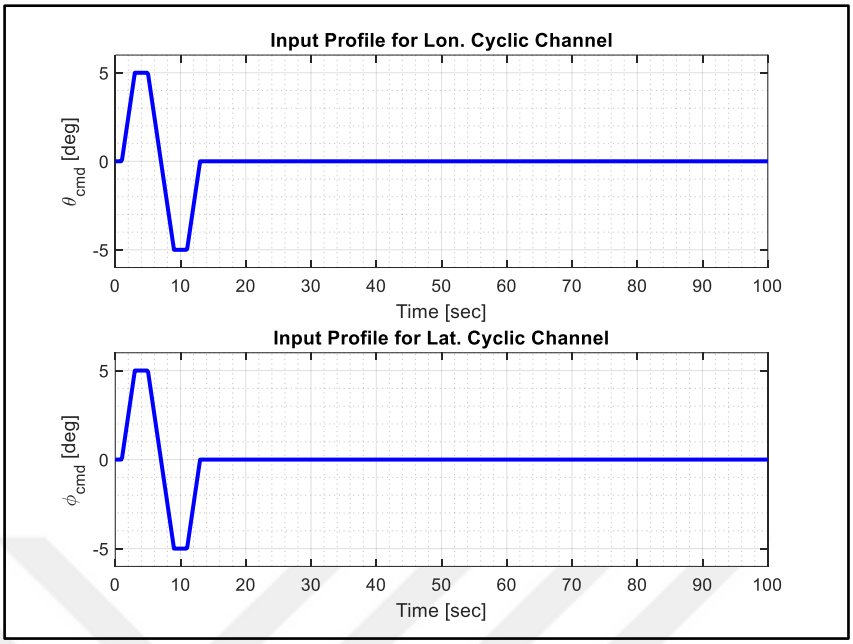


Figure 4.21. Input Profiles for Simulation

The simulation results with linear and nonlinear models are provided in a superimposed manner in the following figure.

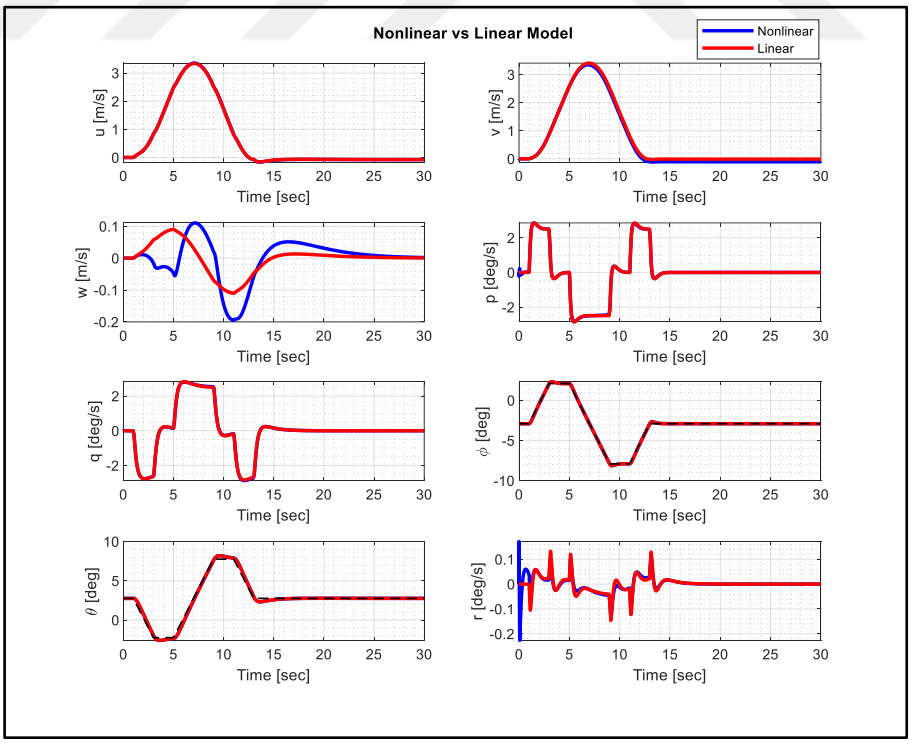


Figure 4.22. Nonlinear and Linear Model Comparison with Engaged Flight Control System

From Figure 4.22, it can be seen that nonlinear and linear models agree quite well as far as all the helicopter states are concerned. In addition, tracking of the reference commands is satisfactory as well, as it can be observed from the black dashed lines that denote the applied pitch and roll attitude commands. As a further inspection of the control effort, the resultant control inputs for the both models are also compared and provided in the following figure:

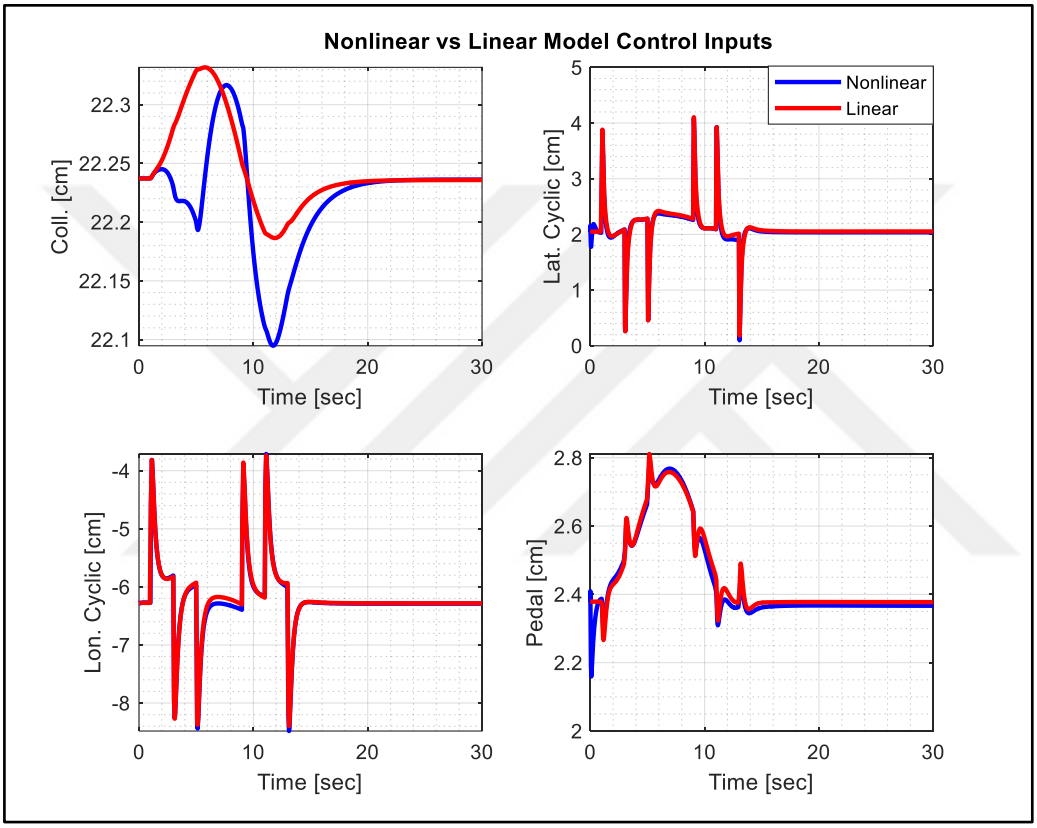


Figure 4.23. Control Effort Comparison for Nonlinear and Linear Models

As it can be seen from Figure 4.23, the control inputs for nonlinear and linear models are also in the close vicinity of each other. Considering the consistency in the helicopter states, this is an expected result.

Comparison between the two models yields that the flight control system developed for the linearized model can be used for the nonlinear model as well.

Given that a stable helicopter system is obtained with autopilots that are capable of performing a variety of tasks, the slung load part of the study will be examined in the following sections.

CHAPTER 5

MATHEMATICAL MODELING OF THE HELICOPTER SLUNG LOAD SYSTEM

5.1 Mathematical Modeling of the Slung Load System

The slung load system is modeled using generic Newton-Euler equations. It should be noted that in the literature there are several acknowledged studies that treat the connection cables as elastic or inelastic. Due to the fact that eigenvalue-based model validation will be performed with a verified model that uses rigid cable approach, the slung load modeling will be accomplished with massless rigid cables. In addition, identification of the pendulum modes, the damping of which are major concern in terms of control, becomes more obvious with rigid cable modeling since the rotation of the slung load about the longitudinal and lateral axes passing through its center of gravity is prevented.

Regarding the mathematical modeling, it should be noted that hovering flight and forward flight with 60 knots of airspeed are examined. The reason is that developed mathematical model could be verified through existing literature studies for these particular flight conditions. In addition, the main rotor downwash effect on the slung load is not taken into account. Even though there are certain studies that involve this concept such as [4], there are acknowledged modeling research done without downwash effect.

It should be noted that the major effect of the downwash on the slung load is present during the hover. However, this effect is noticeable with low load weight and it prevails mainly the lateral pendulum mode by imposing certain amount of additional stabilization and increase in natural frequency as mentioned in [4]. Hence, for this particular study, it is sufficient to perform slung load modeling without main rotor

downwash effect. It is also worth to mention that at 60 knots the main rotor downwash no longer prevails.

One additional remark regarding the slung load modeling is that, due to resulting in a more restrained load yaw motion, 3 cable-configuration is implemented. It should be noted that, 4 cable-configuration can also be used for this purpose. However, as far as the Newton-Euler equations are concerned, the cable forces cannot be solved individually with this approach since number of unknowns exceeds the number of equations as it is mentioned in [7]. Given that inspection of individual cable forces can be necessary for further analyses, 3 cable-configuration is implemented.

The simulation model of the slung load is integrated as a separate block to the already existing helicopter model in MATLAB/Simulink environment. For a clear illustration, the overall block diagram of the compound system is provided below:

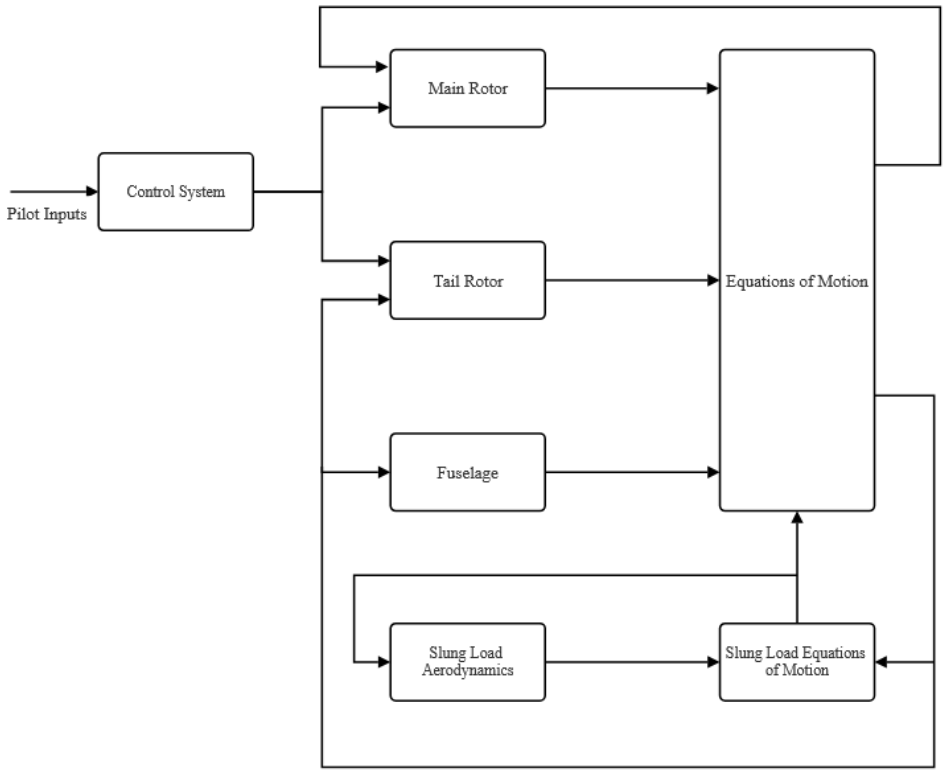


Figure 5.1. Overall Block Diagram for Compound Helicopter-Slung Load System

Schematics of the slung load system from left, rear and top view along with the cable angles and the respective slung load body reference frame are presented below:

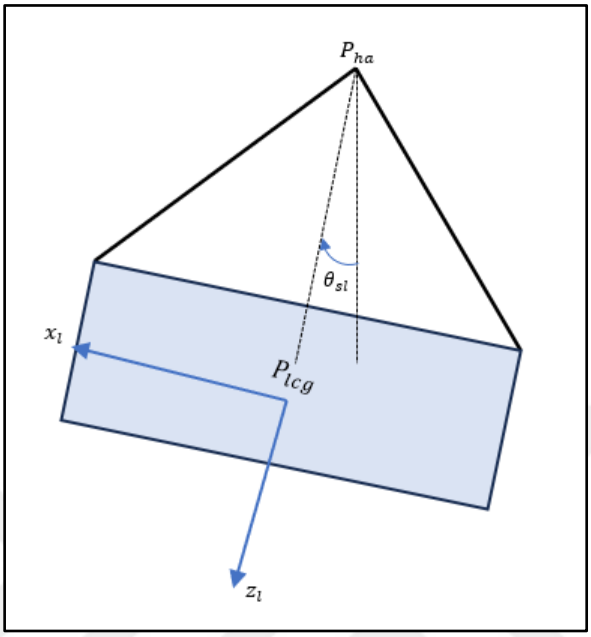


Figure 5.2. Left View of Slung Load System

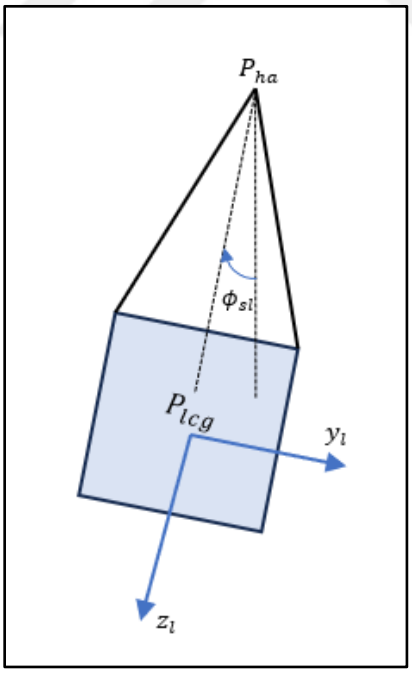


Figure 5.3. Rear View of Slung Load System

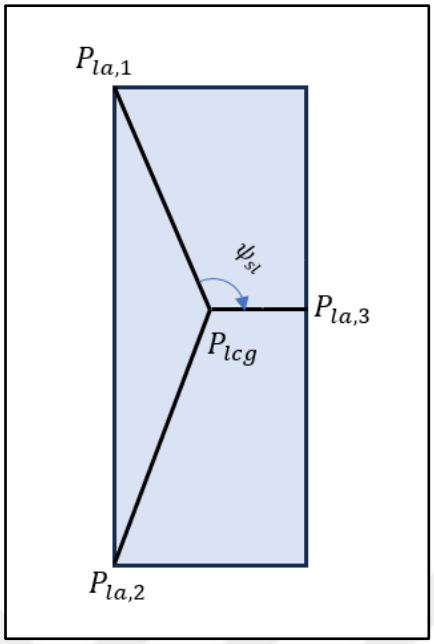


Figure 5.4. Top View of Slung Load System

In Figure 5.2-Figure 5.4, P_{ha} and P_{lcg} denote the helicopter cable attachment point and slung load center of gravity respectively. Whereas, the slug load cable attachment points are represented by $P_{la,1}$, $P_{la,2}$, and $P_{la,3}$.

In the same set of figures, θ_{sl}, ϕ_{sl} and ψ_{sl} designate the slung load cable angles in pitch, roll and yaw axes with respect to inertial frame of reference. In this study, initial frame-based rotation approach is utilized and rotational sequence for writing the equations of motion follows θ_{sl}, ϕ_{sl} and ψ_{sl} respectively.

5.1.1 Derivation of the Governing Equations of Motion

For convenience in writing the equations of motion, P_{ha} will be denoted by c to imply point of confluence, whereas P_{lcg} will be designated by b to represent the body frame of the slung load.

The equations of motion derived below by starting with the following identity:

$$\vec{r}_b^{\,b} = \vec{r}_c^{\,b} + \vec{r}_{cb}^{\,b} \tag{5.1}$$

In Equation (5.1), $\vec{r}_b^b$, $\vec{r}_c^b$ and $\vec{r}_{cb}^b$ denote inertial position vector of the slung load center of gravity, inertial position vector of helicopter confluence point and fixed distance vector between these two respectively in the slung load body frame. This simplified notation is selected based on the study [27], in which 3-DOF modeling of the compound helicopter-slung load system with a single cable is considered by starting from defining the position vector of the slung load center of gravity. In order to illustrate the vectoral quantities defined above clearly, following figure is provided. The related figure also contains the body axis systems of the helicopter and the slung load along with the inertial frame of reference for convenience.

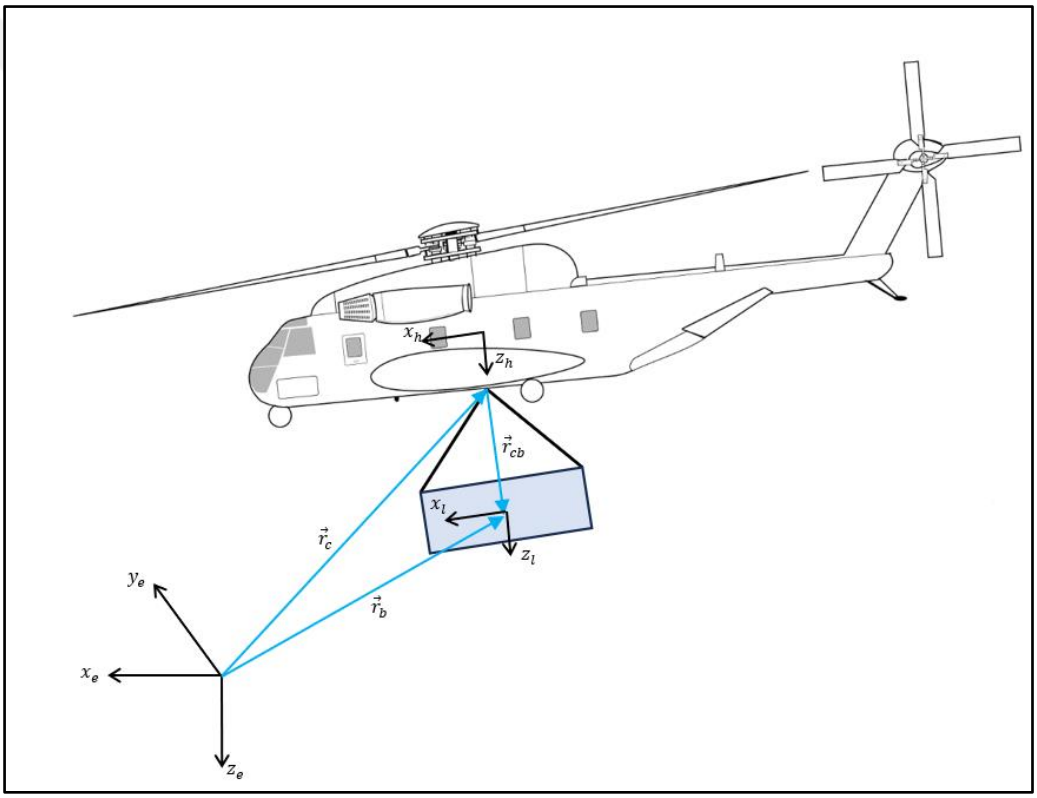


Figure 5.5. Frames of Reference and Kinematic Relations for the Compound Model

Next, this vector summation is differentiated in slung load body frame by using Coriolis Transport Theorem as shown below:

$$\begin{aligned}\vec{v}_b^b = D_i\vec{r}_b^b &= D_b\left(\vec{r}_c^b + \vec{r}_{cb}^b\right) + \omega_b^b \times \left(\vec{r}_c^b + \vec{r}_{cb}^b\right) \\ &= D_b\vec{r}_c^b + D_b\vec{r}_{cb}^b + \omega_b^b \times \vec{r}_c^b + \omega_b^b \times \vec{r}_{cb}^b\end{aligned} \tag{5.2}$$

In Equation (5.2), $D_b\vec{r}_c^b + \omega_b^b \times \vec{r}_c^b = C_{bi}\vec{v}_c^i$, where, C_{bi} is the transformation matrix from inertial frame to the slung load body frame and $\vec{v}_c^i$ is the helicopter confluence point velocity in inertial frame. Also, given that $\vec{r}_{cb}^b$ is a constant vector, $D_b\vec{r}_{cb}^b = 0$.

Similarly, Equation (5.2) is differentiated in slung load body frame using Coriolis Transport Theorem.

$$\begin{aligned}\vec{a}_b^b = D_i\vec{v}_b^b = D_b\big(&D_b\vec{r}_c^b + \omega_b^b \times \vec{r}_c^b + \omega_b^b \times \vec{r}_{cb}^b\big) \\ &+ \vec{\omega}_b^b \times \left(D_b\vec{r}_c^b + \omega_b^b \times \vec{r}_c^b + \omega_b^b \times \vec{r}_{cb}^b\right)\end{aligned} \tag{5.3}$$

Expanding Equation (5.3) and rearranging yields:

$$\begin{aligned}\vec{a}_b^b = D_b^2\vec{r}_c^b + \vec{\alpha}_b^b \times \vec{r}_c^b + \vec{\omega}_b^b \times D_b\vec{r}_c^b + \vec{\alpha}_b^b \times \vec{r}_{cb}^b \\ +\vec{\omega}_b^b \times D_b\vec{r}_c^b + \vec{\omega}_b^b \times \vec{\omega}_b^b \times \vec{r}_c^b + \vec{\omega}_b^b \times \vec{\omega}_b^b \times \vec{r}_{cb}^b\end{aligned} \tag{5.4}$$

Here, $D_b^2\vec{r}_c^b + \vec{\alpha}_b^b \times \vec{r}_c^b + 2\vec{\omega}_b^b \times D_b\vec{r}_c^b + \vec{\omega}_b^b \times \vec{\omega}_b^b \times \vec{r}_c^b = C_{bi}\vec{a}_c^i$, where, $\vec{a}_c^i$ is the helicopter confluence point acceleration in inertial frame. Using this identity, Equation (5.4) can be rearranged as shown below:

$$\begin{aligned}\vec{a}_b^b &= C_{bi}\vec{a}_c^i + \vec{\omega}_b^b \times \vec{\omega}_b^b \times \vec{r}_{cb}^b + \vec{\alpha}_b^b \times \vec{r}_{cb}^b \\ &= C_{bi}\vec{a}_c^i + \vec{\omega}_b^b \times \vec{\omega}_b^b \times \vec{r}_{cb}^b - \vec{r}_{cb}^b \times \vec{\alpha}_b^b\end{aligned} \tag{5.5}$$

Using skew symmetric matrix expressions, Equation (5.5) can be rewritten in matrix form as shown below:

$$a_b^b = C_{bi}a_c^i + \Omega_b\Omega_b r_{cb}^b - R_{cb}^b\alpha_b^b \tag{5.6}$$

Angular acceleration of the slung load which is given by α_b^b in Equation (5.6), should be expressed in slung load body frame. Considering that initial frame-based rotation approach is utilized and rotational sequence for writing the equations of motion follows θ_{sl}, ϕ_{sl}, ψ_{sl} respectively, the transformation matrix from the inertial frame to the slung load body frame can be expressed as follows:

$$C_{bi} = \begin{bmatrix} \cos(\theta_{sl}) & 0 & -\sin(\theta_{sl}) \\ 0 & 1 & 0 \\ \sin(\theta_{sl}) & 0 & \cos(\theta_{sl}) \end{bmatrix} \begin{bmatrix} 1 & 0 & 0 \\ 0 & \cos(\phi_{sl}) & \sin(\phi_{sl}) \\ 0 & -\sin(\phi_{sl}) & \cos(\phi_{sl}) \end{bmatrix} \begin{bmatrix} \cos(\psi_{sl}) & \sin(\psi_{sl}) & 0 \\ -\sin(\psi_{sl}) & \cos(\psi_{sl}) & 0 \\ 0 & 0 & 1 \end{bmatrix} \quad (5.7)$$

Angular velocity of the slung load can be expressed in the inertial frame as follows:

$$\omega_b^i = \begin{bmatrix} \dot{\phi}_{sl} \\ \dot{\theta}_{sl} \\ \dot{\psi}_{sl} \end{bmatrix} \quad (5.8)$$

Then, angular velocity of the slung load in its body frame (ω_b^b) can be written as follows:

$$\omega_b^b = \begin{bmatrix} \omega_{b_x}^b \\ \omega_{b_y}^b \\ \omega_{b_z}^b \end{bmatrix} = C_{bi}\omega_b^i \quad (5.9)$$

Expanded form of (5.9) is given in the following set of equations to represent the angular velocity of the slung load in each body axis:

$$\omega_{b_x}^b = \dot{\phi}_{sl}\begin{pmatrix} \cos(\psi_{sl})\cos(\theta_{sl}) - \\ \sin(\phi_{sl})\sin(\psi_{sl})\sin(\theta_l) \end{pmatrix} + \dot{\theta}_{sl}\begin{pmatrix} \cos(\theta_{sl})\sin(\psi_l) + \\ \cos(\psi_l)\sin(\phi_{sl})\sin(\theta_{sl}) \end{pmatrix} - \dot{\psi}_{sl}\cos(\phi_{sl})\sin(\theta_{sl}) \quad (5.10)$$

$$\omega_{b_y}^b = \dot{\psi}_{sl}\sin(\phi_{sl}) + \dot{\theta}_{sl}\cos(\phi_{sl})\cos(\psi_l) - \dot{\phi}_{sl}\cos(\phi_{sl})\sin(\psi_{sl}) \quad (5.11)$$

$$\omega_{b_z}^b = \dot{\phi}_{sl}\begin{pmatrix} \cos(\psi_{sl})\sin(\theta_{sl}) + \\ \cos(\theta_{sl})\sin(\phi_{sl})\sin(\psi_{sl}) \end{pmatrix} + \dot{\theta}_{sl}\begin{pmatrix} \sin(\psi_{sl})\sin(\theta_{sl}) - \\ \cos(\psi_{sl})\cos(\theta_{sl})\sin(\phi_{sl}) \end{pmatrix} + \dot{\psi}_{sl}\cos(\phi_{sl})\cos(\theta_{sl}) \quad (5.12)$$

The angular acceleration of the slung load can be written in column matrix format by differentiating Equation (5.9) with respect to time:

$$\alpha_b^b = \frac{d\omega_b^b}{dt} = \begin{bmatrix} \alpha_{b_x}^b \\ \alpha_{b_y}^b \\ \alpha_{b_z}^b \end{bmatrix} \quad (5.13)$$

Similar to the angular velocity case, following set of equations are provided to represent the angular acceleration of the slung load in each body axis:

$$
\begin{aligned}
\alpha^b_{b\,x} = {} & \ddot{\phi}\begin{pmatrix}\cos(\psi_{sl})\cos(\theta_{sl}) - \\ \sin(\phi_{sl})\sin(\psi_{sl})\sin(\theta_l)\end{pmatrix} \\
& + \dot{\phi}_{sl}\begin{pmatrix}-\dot{\psi}_{sl}\sin(\psi_{sl})\cos(\theta_{sl}) - \dot{\theta}_{sl}\cos(\psi_{sl})\sin(\theta_{sl}) - \\ \dot{\phi}_{sl}\cos(\phi_{sl})\sin(\psi_{sl})\sin(\theta_{sl}) - \dot{\psi}_{sl}\sin(\phi_{sl})\cos(\psi_{sl})\sin(\theta_{sl}) - \\ \dot{\theta}_{sl}\sin(\phi_{sl})\sin(\psi_{sl})\cos(\theta_{sl})\end{pmatrix} \\
& + \ddot{\theta}_{sl}\begin{pmatrix}\cos(\theta_{sl})\sin(\psi_l) + \\ \cos(\psi_l)\sin(\phi_{sl})\sin(\theta_{sl})\end{pmatrix} \\
& + \dot{\theta}_{sl}\begin{pmatrix}-\dot{\theta}_{sl}\sin(\theta_{sl})\sin(\psi_{sl}) + \dot{\psi}_{sl}\cos(\theta_{sl})\cos(\psi_{sl}) - \\ \dot{\psi}_{sl}\sin(\psi_{sl})\sin(\phi_{sl})\sin(\theta_{sl}) + \dot{\phi}_{sl}\cos(\psi_{sl})\cos(\phi_{sl})\sin(\theta_{sl}) + \\ \dot{\theta}_{sl}\cos(\psi_{sl})\sin(\phi_{sl})\cos(\theta_{sl})\end{pmatrix} \\
& - \ddot{\psi}_{sl}\cos(\phi_{sl})\sin(\theta_{sl}) + \dot{\psi}_{sl}\dot{\phi}_{sl}\sin(\phi_{sl})\sin(\theta_{sl}) - \dot{\psi}_{sl}\dot{\theta}_{sl}\cos(\phi_{sl})\cos(\theta_{sl})
\end{aligned} \tag{5.14}
$$

$$
\begin{aligned}
\alpha^b_{b\,y} = {} & \ddot{\psi}_{sl}\sin(\phi_{sl}) + \dot{\psi}_{sl}\dot{\phi}_{sl}\cos(\phi_{sl}) + \ddot{\theta}_{sl}\cos(\phi_{sl})\cos(\psi_{sl}) - \dot{\theta}_{sl}\dot{\phi}_{sl}\sin(\phi_{sl})\cos(\psi_{sl}) \\
& - \dot{\theta}_{sl}\dot{\psi}_{sl}\cos(\phi_{sl})\sin(\psi_{sl}) - \ddot{\phi}_{sl}\cos(\phi_{sl})\sin(\psi_{sl}) + \dot{\phi}^2_{sl}\sin(\phi_{sl})\sin(\psi_{sl}) \\
& - \dot{\phi}_{sl}\dot{\psi}_{sl}\cos(\phi_{sl})\cos(\psi_{sl})
\end{aligned} \tag{5.15}
$$

$$
\begin{aligned}
\alpha^b_{b\,z} = {} & \ddot{\phi}\begin{pmatrix}\cos(\psi_{sl})\sin(\theta_{sl}) + \\ \cos(\theta_{sl})\sin(\phi_{sl})\sin(\psi_{sl})\end{pmatrix} \\
& + \dot{\phi}_{sl}\begin{pmatrix}-\dot{\psi}_{sl}\sin(\psi_{sl})\sin(\theta_{sl}) + \dot{\theta}_{sl}\cos(\psi_{sl})\cos(\theta_{sl}) - \\ \dot{\theta}_{sl}\sin(\theta_{sl})\sin(\phi_{sl})\sin(\psi_{sl}) + \dot{\phi}_{sl}\cos(\theta_{sl})\cos(\phi_{sl})\sin(\psi_{sl}) + \\ \dot{\psi}_{sl}\cos(\theta_{sl})\sin(\phi_{sl})\cos(\psi_{sl})\end{pmatrix} \\
& + \ddot{\theta}_{sl}\begin{pmatrix}\sin(\psi_{sl})\sin(\theta_{sl}) - \\ \cos(\psi_{sl})\cos(\theta_{sl})\sin(\phi_{sl})\end{pmatrix} \\
& + \dot{\theta}_{sl}\begin{pmatrix}\dot{\psi}_{sl}\cos(\psi_{sl})\sin(\theta_{sl}) + \dot{\theta}_{sl}\sin(\psi_{sl})\cos(\theta_{sl}) + \\ \dot{\psi}_{sl}\sin(\psi_{sl})\cos(\theta_{sl})\sin(\phi_{sl}) + \dot{\theta}_{sl}\cos(\psi_{sl})\sin(\theta_{sl})\sin(\phi_{sl}) - \\ \dot{\phi}_{sl}\cos(\psi_{sl})\cos(\theta_{sl})\cos(\phi_{sl})\end{pmatrix} \\
& + \ddot{\psi}_{sl}\cos(\phi_{sl})\cos(\theta_{sl}) - \dot{\psi}_{sl}\dot{\phi}_{sl}\sin(\phi_{sl})\cos(\theta_{sl}) \\
& - \dot{\psi}_{sl}\dot{\theta}_{sl}\cos(\phi_{sl})\sin(\theta_{sl})
\end{aligned} \tag{5.16}
$$

Now that the necessary quantities are expressed symbolically, Newton-Euler equations can be written as follows:

$$m_b a^b_b = F^b_{aero} + W^b_b + F^b_{cable} \tag{5.17}$$

$$I_b \alpha^b_b + \Omega_b I_b \omega^b_b = M^b_{aero} + r^b_{c1} \times F^b_{c1} + r^b_{c2} \times F^b_{c2} + r^b_{c3} \times F^b_{c3} \tag{5.18}$$

In Equations (5.17) and (5.18), F^b_{aero} and M^b_{aero} denote the aerodynamic force and moment acting on the slung load respectively. Also, W^b_b is the slung load weight expressed in the load frame and F^b_{cable} is the total cable force acting on the slung load and it is the summation of the individual cable forces given in Equation (5.18), i.e., $F^b_{cable} = F^b_{c1} + F^b_{c2} + F^b_{c3}$. As a further remark, each cable force vector can be represented by their magnitude and direction vector, such as: $F^b_{c1} = F_{c1} u^b_{c1}$, where u^b_{c1} is the unit direction vector.

Finally, the direction vector between the cable attachment points and the slung load center of gravity are designated by r_{c1}^{b}, r_{c2}^{b} and r_{c3}^{b} in Equation (5.18).

Regarding the modeling approach presented above, there is a crucial point that needs to be mentioned. Considering that the cables are modeled as massless rigid links, there should be no net force acting on them to prevent infinite acceleration. Moreover, massless cable assumption also yields that there is no moment of inertia associated with cables. Hence, the net moment acting on each cable should be zero as well to prohibit infinite angular acceleration. This discussion implies that the forces acting on each end of the cables should be equal in magnitude and point in opposite directions.

In addition, regardless of how the slung load is oriented in space, resolution of the vector connecting the helicopter attachment point and slung load center of gravity in slung load body frame is constant. The same discussion is valid for the vectors connecting the slung load center of gravity to the cable attachment points on the slung load. This yields that, the cable force vector directions are along the rigid cables and they remain the same in the slung load body frame.

In the light of the discussion above, it can be asserted that Equations (5.17) and (5.18) consists of a total of 6 scalar equations that involve the following 6 unknowns: $\ddot{\phi}_{sl}, \ddot{\theta}_{sl}, \ddot{\psi}_{sl}, F_{c1}, F_{c2}, F_{c3}$, and they yield a solvable set.

Given that the helicopter cable attachment point is involved in slung load equations of motion, the slung load dynamics are integrated to the already existing helicopter mathematical model as a separate subsystem. At each timestep, Equations (5.17) and (5.18) are solved and total of cable forces and resultant moments about the helicopter center of gravity are included in the helicopter equations of motion as well.

In the next section, a discussion on the aerodynamic characteristics of the slung load will be provided.

5.1.2 Slung Load Aerodynamics

It should be noted that even though at 60 knots of airspeed, the slung load aerodynamic characteristics become a concern, in hovering flight the they do not have a significant impact in terms of trimmed parameter values. However, in terms of linearization through the small perturbation theorem and response simulations performed with given input profiles, the aerodynamic characteristics of the slung load should still be considered for a more accurate representation.

Governing equations are taken from the reference [5] for an 8 ft.×8 ft.×20 ft. MILVAN cargo container and they are based on the wind tunnel test data provided in [6]. The resultant aerodynamic forces and moments are provided as inputs to the slung load equations of motion module that represented above in detail. It should be noted that there are various studies that involve more complicated load aerodynamics representation. However, with the formulation given in [5], dynamic characteristics of the slung load are captured fairly well. This will be discussed later on in detail by comparing the linearized model poles with a study that involves similar configuration.

As the initial step in the formulation, the angle of attack and angle of sideslip the slung load is subjected to should be calculated in a similar manner to the fuselage aerodynamics case. The total velocity of the slung load can be represented in its respective body frame by using the dynamics formulation provided in the previous section. Following set of equations represent the calculation of angle of attack, angle of sideslip, dynamic pressure and total airspeed respectively:

$$\alpha_l = \tan^{-1}\left(\frac{w_l}{u_l}\right) \tag{5.19}$$

$$\beta_l = \sin^{-1}\left(\frac{v_l}{V_l}\right) \tag{5.20}$$

$$\bar{q}_l = \frac{1}{2}\rho V_l^2 \tag{5.21}$$

$$V_l = \sqrt{u_l^2 + v_l^2 + w_l^2} \tag{5.22}$$

Upon the calculation of the aforementioned parameters, the cargo container lift, drag and side forces in the wind tunnel axes at the load center of gravity are obtained from the following set of equations in the light of the aerodynamic data provided in [6]:

$$\tilde{L}_l = [6.5 \sin(2\alpha_l) \cos(\beta_l)]\bar{q}_l \tag{5.23}$$

$$\tilde{D}_l = [20.9 - 7.66(1 + \cos(2\alpha_l) \cos(\beta_l))]\bar{q}_l \tag{5.24}$$

$$\tilde{Y} = [-7.9 \sin(2\beta_l) \cos(2\alpha_l)]\bar{q}_l \tag{5.25}$$

The forces given in the equations above, are expressed in the slung load body frame by using the following transformation:

$$\begin{bmatrix} X_l \\ Y_l \\ Z_l \end{bmatrix} = \begin{bmatrix} -\cos(\alpha_l)\cos(\beta_l) & -\cos(\alpha_l)\sin(\beta_l) & \sin(\alpha_l) \\ -\sin(\beta_l) & \cos(\beta_l) & 0 \\ -\sin(\alpha_l)\cos(\beta_l) & -\sin(\alpha_l)\sin(\beta_l) & -\cos(\alpha_l) \end{bmatrix} \begin{bmatrix} \tilde{D}_l \\ \tilde{Y}_l \\ \tilde{L}_l \end{bmatrix} \tag{5.26}$$

In the formulation represented in [5], it is stated that the static pitching and rolling aerodynamic moments of the load are small compared to those induced by the motion resulting from the presence of attachment cable. Hence, only the static yawing moment is used in equations of motion and it is given by the following formula according to [6]:

$$N_{s,l} = [-7.73 \sin(2\beta_l) + 4.47 \sin(4\beta_l) \, |\cos(\alpha_l)|]\bar{q} \tag{5.27}$$

The aerodynamic moments due to rolling, pitching and yawing angular velocities are assumed to be proportional to the product of airspeed and angular velocities as it can be seen from the following set of equations:

$$L_{d,l} = -89 V_l p_l \tag{5.28}$$

$$M_{d,l} = -89 V_l q_l \tag{5.29}$$

$$N_{d,l} = -89 V_l r_l \tag{5.30}$$

Hence, the total slung load aerodynamic moments can be expressed as follows:

$$L_l = L_{d,l} \tag{5.31}$$

$$M_l = M_{d,l} \tag{5.32}$$

$$N_l = N_{d,l} + N_{s,l} \tag{5.33}$$

Given that a complete model for the slung load is obtained, trim and linearization procedure for the compound system consisting of helicopter and slung load will be discussed in the following sections.

5.2 Trim Algorithm for the Compound Helicopter and Slung Load System

Trim algorithm for the compound system is similar to the that of helicopter by itself, which was explained in the second chapter of this study. That is, a suitable cost function is determined and MATLAB's "fmincon" function is utilized for minimization through the simulation-based optimization. The cost function for the compound system includes the linear and angular accelerations of the helicopter and the slung load in their body frames as shown below:

$$\begin{aligned} J = {} & \dot{u}^2 + \dot{v}^2 + \dot{w}^2 + \dot{p}^2 + \dot{q}^2 + \dot{r}^2 + \\ & \dot{u}_{sl}{}^2 + \dot{v}_{sl}{}^2 + \dot{w}_{sl}{}^2 + \dot{p}_{sl}{}^2 + \dot{q}_{sl}{}^2 + \dot{r}_{sl}{}^2 \end{aligned} \tag{5.34}$$

In Equation (5.34), the last 6 terms represent the linear and angular accelerations of the slung load which were determined based on the governing equations of motion explained in the previous section and given by Equations (5.6) and (5.13).

5.3 Linearization of the Compound Helicopter and Slung Load System

As in the case of trim algorithm, the linearization procedure is similar to that of helicopter by itself. That is, the small perturbation approach with central differencing is implemented by including the slung load states. The state vector of the overall system is provided below:

$$x^T = [u \quad w \quad q \quad \theta \quad v \quad p \quad \phi \quad r \quad \phi_{sl} \quad \dot{\phi}_{sl} \quad \theta_{sl} \quad \dot{\theta}_{sl} \quad \psi_{sl} \quad \dot{\psi}_{sl}] \tag{5.35}$$

To obtain the state space representation for the compound system, each state and control input is perturbed from both the positive and negative directions and state matrix A and control input matrix B are determined with central differencing, which is identical to the methodology described for the helicopter by itself.

5.4 Validation of the Mathematical Model

Validation of the developed compound mathematical model consisting of the helicopter and slung load is performed by using the linearized model. The reason is that there is no suitable time history regarding the slung load states in the literature neither as test data nor as the output of a verified mathematical model.

Hence, the eigenvalues of the A matrix in the state space representation of the compound model are examined to investigate the dynamic modes and results are compared to a study with verified mathematical model given in [8]. The study upon which the comparison is made is the same one given in the helicopter linearization section and it includes the linearized compound helicopter-slung load model besides the helicopter by itself. Following set of figures illustrate pole locations in hovering flight. The related dynamic modes, which were identified based on the eigenvectors of the A matrix, are also included in the figure just below.

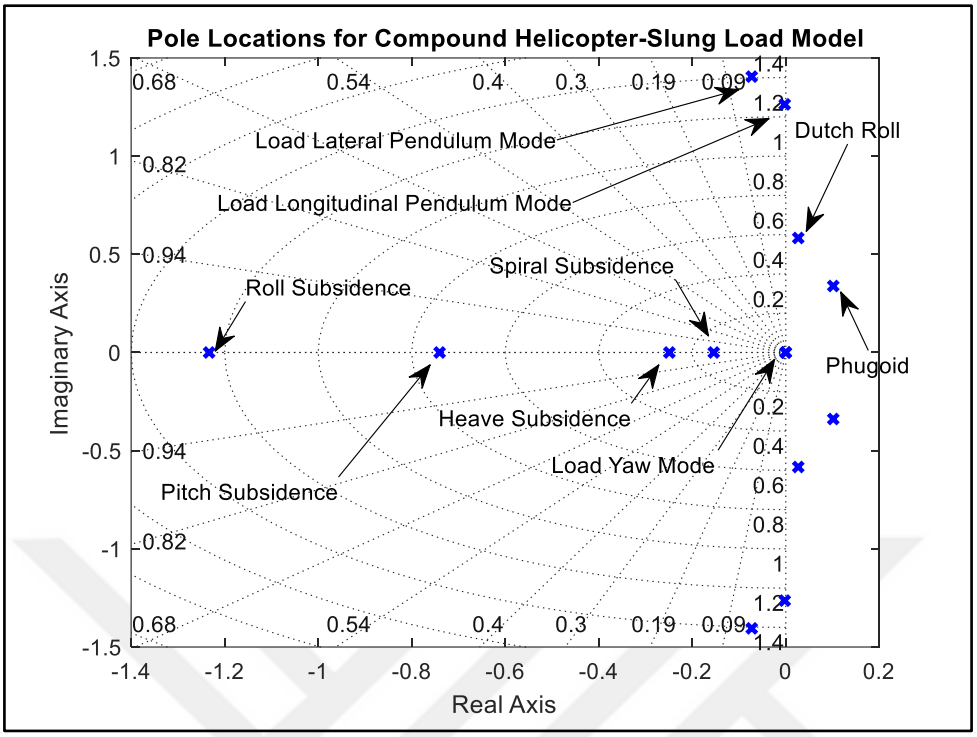


Figure 5.6. Pole Locations for the Compound Helicopter-Slung Load Model in Hovering Flight

From Figure 5.6, it can be seen that, there are six additional poles related to the slung load, which is the expected outcome. Also, it can be noticed that even though there are certain amount of alteration in the helicopter modes, these are not excessive. The same figure clearly shows that the yaw mode of the slung load is at the vicinity of the origin and it consists of two real poles that are almost coincident with each other. More importantly, the longitudinal and lateral pendulum modes of the slung load are also evident. These pendulum modes are crucial and they lead to sustained oscillations in the absence of a slung load controller and they will be tried to dampen out as it will be shown in the slung load control section.

In order to provide a clear comparison, the dynamic modes of the linearized system are given below in a superimposed manner with the results of the aforementioned study that can be found in the literature.

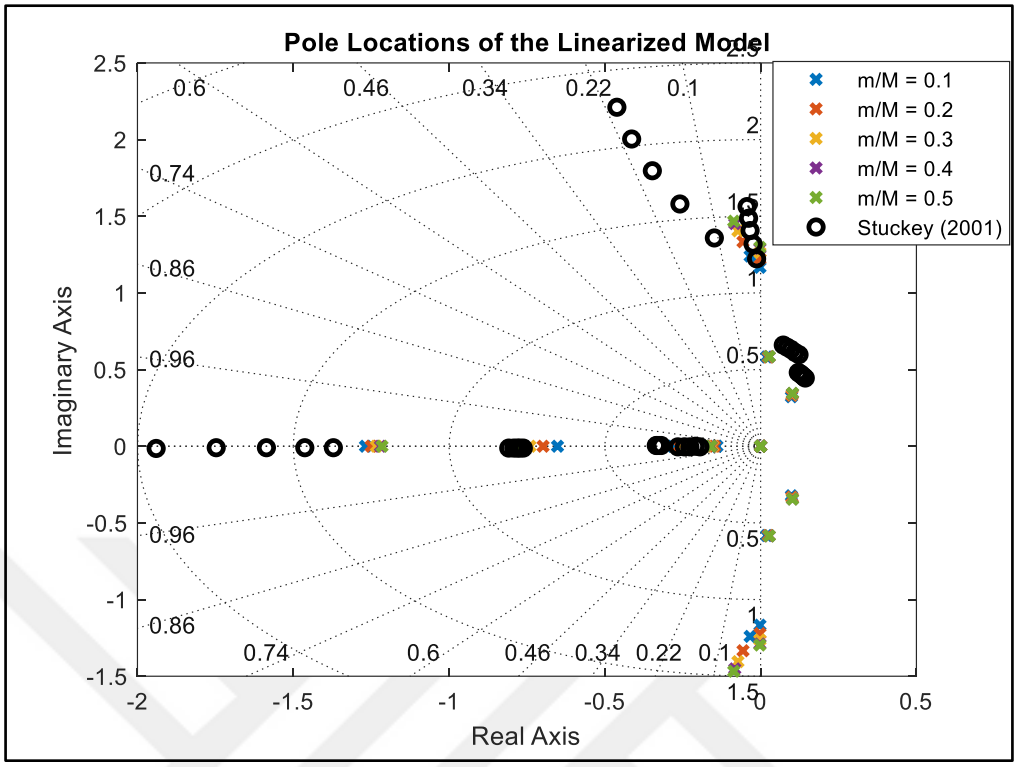


Figure 5.7. Pole Locations for the Compound Helicopter-Slung Load Model in Hovering Flight (Comparison with Literature)

In Figure 5.7, the poles are plotted with respect to varying slung load to helicopter mass ratio, which is ranging from 0.1 to 0.5. It should also be noted that the yaw mode of the slung load is not included in the reference study.

From the same figure, it can also be seen that the overall pole locations are consistent with the literature. That is, with the integration of the slung load system, additional pendulum modes are introduced on top of the existing helicopter modes. The locations of the poles related to the phugoid, Dutch roll, heave subsidence and pitch subsidence modes are close to the reference study. Moreover, variation of the location of these poles with increasing load mass can be evaluated as insignificant as in the case of reference study. The same figure also shows that the location of the longitudinal load pendulum modes and variation of these modes with increasing load mass are consistent with the study given in literature.

On the other hand, the discrepancies observed between the two studies can be explained as follows. Firstly, the change of roll subsidence mode location with increasing load mass is more significant in the reference study. Considering that this mode is placed on the far left-half plane, it is quite stable and the dynamics related to it die out very quickly. Hence, it does not play a significant role in the overall system dynamics.

The discrepancy in the lateral load pendulum mode can also be noticed. The difference increases remarkably with increasing load mass. It should be noted that, even though the overall configuration of the reference study is similar to the one used in this study, there are certain differences. That is, the helicopter mass and center of gravity are not exactly the same, which results is certain deviation between the load masses as well. In addition, it is highly possible that there is a difference in terms of the slung load attachment point location on the helicopter.

However, even if these discrepancies are taken into account, it can be asserted that the overall dynamic behavior of the compound helicopter-slung load models can be evaluated as consistent. That is, the same helicopter modes exist and variation of this modes have the same trend with increasing load mass. Also, two additional pendulum modes are introduced with implementation of the slung load for both models. Finally, the trend shown by pendulum modes with increasing load mass is consistent between the two models.

In order to identify the dynamics of the compound system, one additional case study is performed. In order to observe the variation of the pendulum modes with increasing cable length, the simulations are performed in the hovering flight condition with the distance between helicopter attachment point and load center of gravity ranging from 25 ft to 65 ft in the increments of 10 ft. Resultant pole locations are illustrated in the following figure:

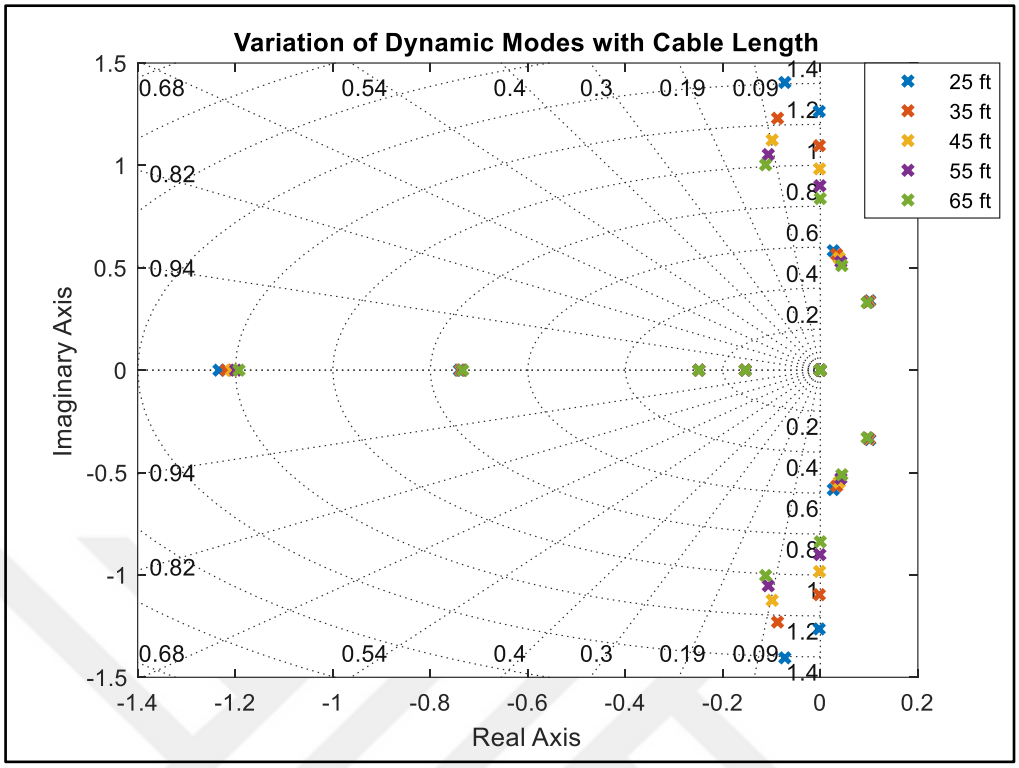


Figure 5.8. Variation of System Poles with Increasing Cable Length

From Figure 5.8, it can be seen that even though there are no remarkable difference in the helicopter modes with increasing cable length, there are noticeable variations in the both longitudinal and lateral pendulum modes. That is, as the cable length increases the natural frequency of the pendulum modes decreases whereas there is an increase in the damping ratio, which is an expected outcome.

Given that a mathematical model with sufficient accuracy is obtained according to the discussion provided above, the control schemes for the slung load system shall be discussed in the next section.

It should also be noted that the discussion on the mathematical model verification provided above includes the hovering flight. The poles of the linearized model for forward flight with 60 knots of airspeed will be discussed after elaborating on the control strategies for the slung load system. That is, the optimal control algorithm will be proposed based on hovering flight condition but its application on forward

flight with 60 knots of airspeed will separately be shown once the discussion on the hovering flight case is completed.

CHAPTER 6

CONTROL OF THE HELICOPTER SLUNG LOAD SYSTEM

Under the scope of the slung load system control, four separate control schemes will be proposed, namely:

- Input Shaping
- Delayed Cable Angle Feedback
- Cable Angle Rate Feedback
- Model Predictive Control

It should be pointed out that the slung load control schemes will be implemented with existing helicopter controllers that were explained in Sections 4.1 and 4.2. Before going into details of the slung load controllers, the current state of the compound helicopter-slung load configuration should be examined in the presence of only the helicopter flight control system. As it is mentioned at the end of the previous section, all the discussions regarding the slung load control will be provided particularly for hovering flight. The forward flight case will be elaborated on separately at the end once the optimal control scheme is selected.

6.1 Helicopter-Slung Load Dynamics Inspection with the Existing Helicopter Controllers

Previously proposed helicopter stability augmentation systems and autopilots are wrapped around the plant consisting of the helicopter and slung load. Then, the dynamic characteristics of the slung load are investigated by simulating the closed loop system. Block diagram for the compound configuration is provided below:

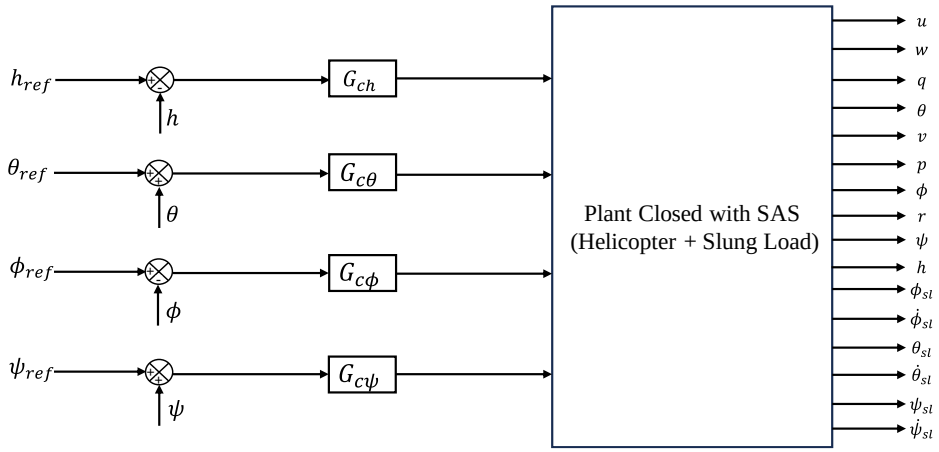


Figure 6.1. Block Diagram for the Closed Loop System with Helicopter and Slung Load

Simulation with the closed loop system is performed by giving inputs to the longitudinal and lateral cyclic to excite the longitudinal and lateral pendulum modes of the slung load respectively. It should be noted that even though certain amount of coupling exists such that longitudinal cyclic input excites the lateral pendulum mode and vice versa, the main contribution to the pendulum modes comes from the respective on axis input channels.

The inputs consist of ramp profiles and they are given as the reference pitch and roll attitudes. The overall profiles provided to each input channel are illustrated in the figure below:

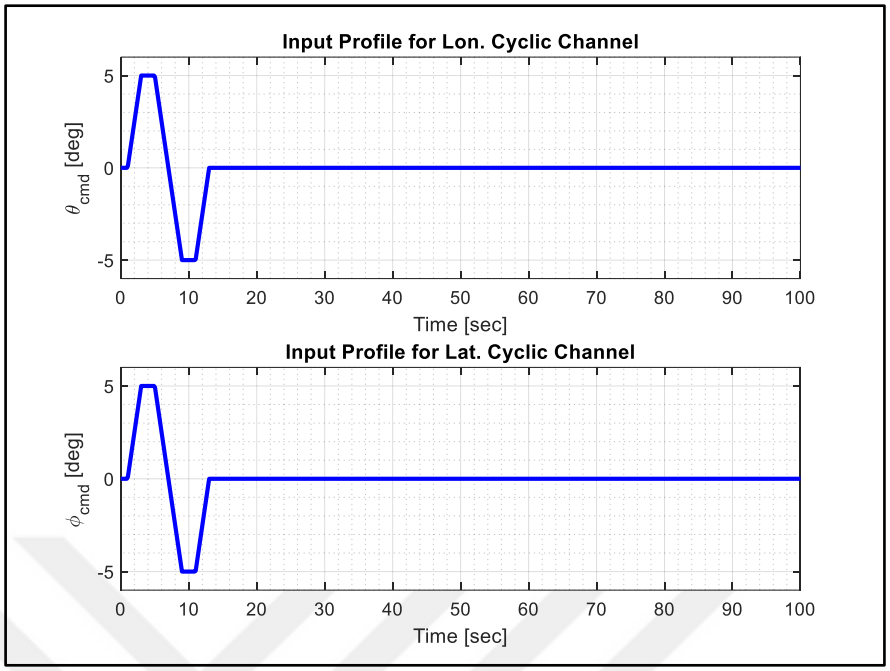


Figure 6.2. Input Profiles for Simulation

Resultant slung load cable angles are illustrated below:

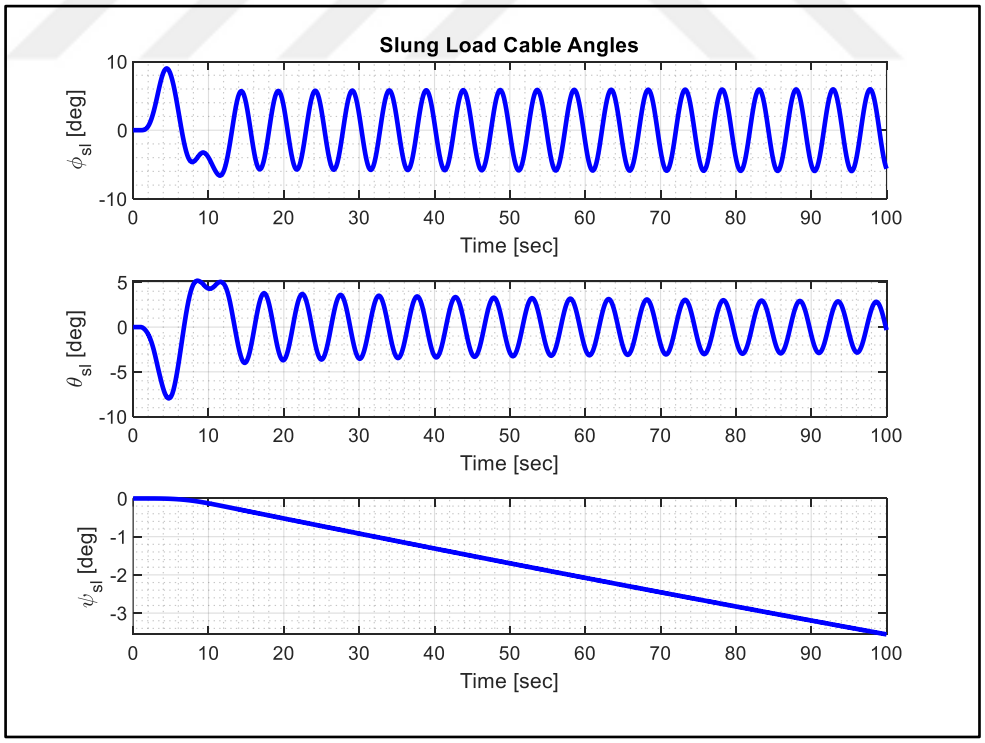


Figure 6.3. Slung Load Cable Angles

From Figure 6.3 it can be seen that there is sustained oscillation in the lateral cable angle ϕ_{sl} and lightly damped oscillatory behavior in θ_{sl}. In addition, the yaw angle of the slung load ψ_{sl} shows a slightly divergent response. Given that this particular angle reaches to the vicinity of –3° in a large simulation time of 100 seconds, the divergence is not a major concern.

To observe the effect of the presence of the slung load on helicopter, resultant helicopter states from the same simulation are also investigated and they are shown in the following figure:

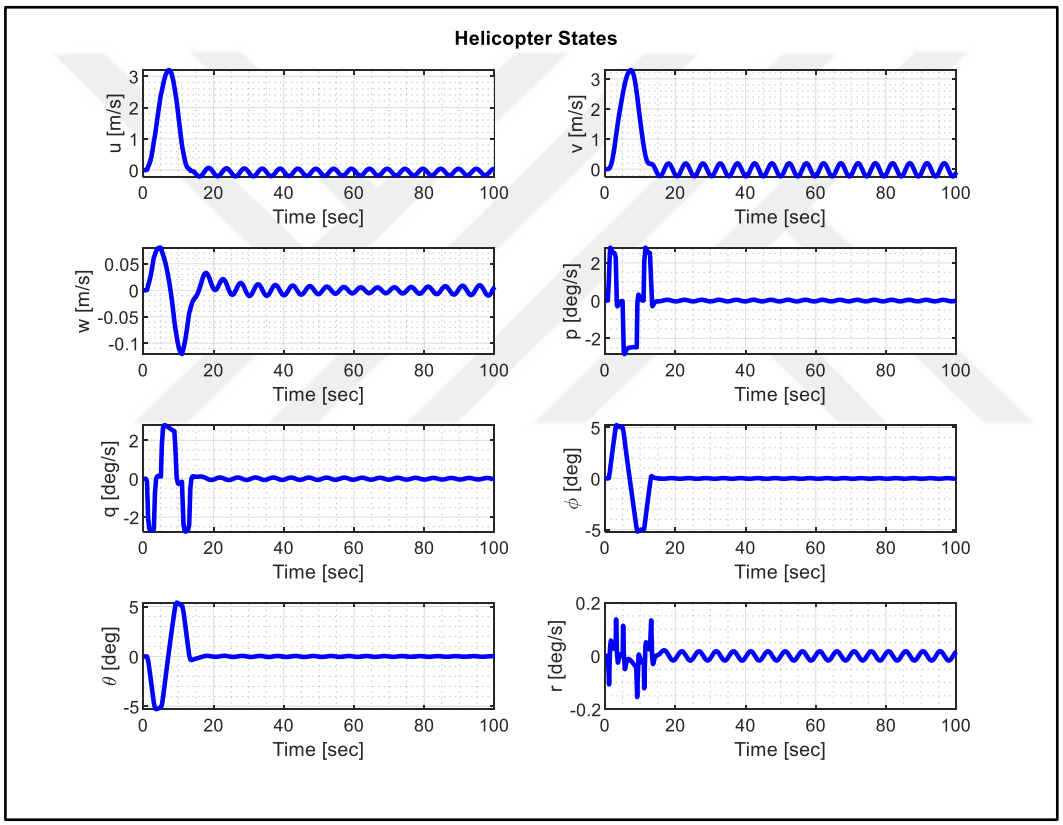


Figure 6.4. Helicopter States

From Figure 6.4, it can be seen that helicopter states show oscillatory behavior as well. Considering that helicopter and the slung load are coupled through the cable forces, this is an expected outcome. In the upcoming sections, aforementioned slung load control strategies will be discussed.

6.2 Slung Load Control with Input Shaping

Before going into the details of implementing the concept of input shaping to the slung load control, some theoretical background will be provided in the next section for convenience.

6.2.1 Theoretical Background for Input Shaping

Input shaping is a reference command prefiltering method utilized for removing unwanted residual oscillations so that precise position control is acquired. This particular method is utilized in a variety of applications including spacecrafts, robots, cranes and even chemical processes. A comprehensive and easy to follow resource regarding the input shaping theory can be found in reference [28]. The notation and governing equations presented below are taken from this reference as well.

The concept of input shaping can be detailed as follows. It is known that a system can represent oscillatory behavior when it is subjected to an impulse input. However, if a second impulse is applied to the same system, the oscillations induced by the first one can be canceled out. The concept is illustrated in the following figure:

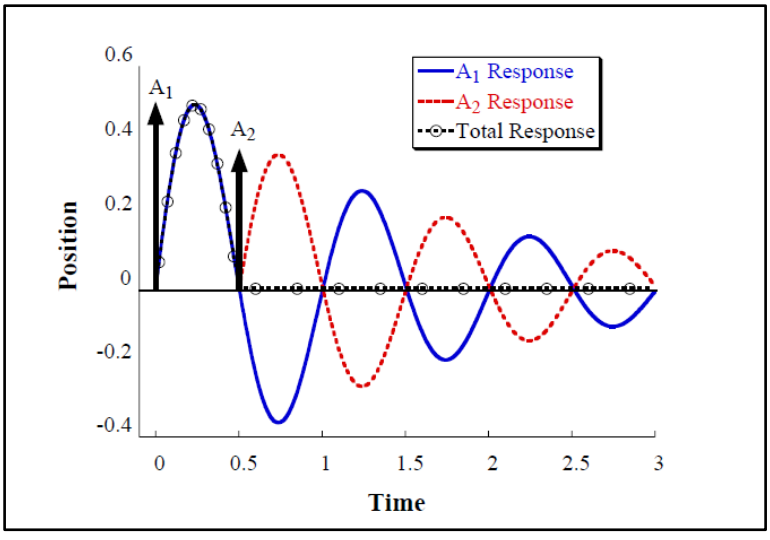


Figure 6.5. Concept of Input Shaping [28]

It should be noted that amplitudes and time locations of the two-impulse command sequence shown in Figure 6.5 can be derived in a relatively simple manner. If the systems natural frequency ω_n and damping ratio ζ are estimated reasonably, then the residual oscillations that results from the sequence of impulses can be described by the following equation:

$$V(\omega_n, \zeta) = e^{-\zeta \omega_n t_n} \sqrt{C(\omega_n, \zeta)^2 + S(\omega_n, \zeta)^2} \tag{6.1}$$

Where,

$$C(\omega_n, \zeta) = \sum_{i=1}^{n} A_i e^{\zeta \omega_n t_i} \cos(\omega_d t_i) \tag{6.2}$$

$$S(\omega_n, \zeta) = \sum_{i=1}^{n} A_i e^{\zeta \omega_n t_i} \sin(\omega_d t_i) \tag{6.3}$$

In Equations (6.2) and (6.3), A_i and t_i represent the amplitudes and time locations of the impulses, n is the number of impulses in the impulse sequence, whereas $\omega_d = \omega_n \sqrt{1 - \zeta^2}$ is the damped natural frequency of the system of concern.

The impulse amplitudes and time locations that would lead to zero residual oscillation can be determined by setting (6.1) to zero. However, there are certain additional constraints that need to be imposed on the impulses such that convergence to zero-valued or infinitely-valued impulses is prevented. To avoid the trivial solution of all zero-valued impulses and obtain a normalized result, it is required that the impulse amplitudes sum to one:

$$\sum A_i = 1 \tag{6.4}$$

It should be noted that Equation (6.4) can be satisfied with very large positive and negative impulse amplitudes. Hence, the impulses amplitudes are restricted to be positive for a bounded solution.

$$A_i > 0, i = 1,2, \dots, n \tag{6.5}$$

For a two-impulse sequence, the problem has four unknowns, namely the two impulse amplitudes (A_1, A_2) and the two impulse time locations (t_1, t_2). Without loss of generality, time location of the first impulse can be set to zero, i.e. $t_1 = 0$. In order for Equation (6.1) to equal zero, the expressions in Equation (6.2) and (6.3) must be set to zero. Hence, following conditions must be satisfied:

$$A_1 + A_2 e^{\zeta \omega_n t_2} \cos(\omega_d t_2) = 0 \tag{6.6}$$

$$A_2 e^{\zeta \omega_n t_2} \sin(\omega_d t_2) = 0 \tag{6.7}$$

Equation (6.7) can be solved nontrivially with the sine term equals zero. This occurs when the following holds:

$$\omega_d t_2 = n\pi \rightarrow t_2 = \frac{n\pi}{\omega_d} = \frac{nT_d}{2} \; n = 1,2, \ldots \tag{6.8}$$

In Equation (6.8), T_d stands for the damped period of vibration. From the same equation, it can be interpreted that there is an infinite number of possible values for the location of the second impulse. In order eliminate the residual vibrations in the shortest amount of time, t_2 is chosen as the lowest allowable value:

$$t_2 = \frac{T_d}{2} \tag{6.9}$$

For this particular two impulse case, the constraint given by Equation (6.4) reduces to the following expression:

$$A_1 + A_2 = 1 \tag{6.10}$$

Using the expression for the damped natural frequency given by $\omega_d = \omega_n \sqrt{1 - \zeta^2}$, and substituting Equations (6.9) and (6.10) into Equation (6.6), following identity is obtained:

$$A_1 - (1 - A_1) e^{\frac{\zeta \pi}{\sqrt{1-\zeta^2}}} = 0 \tag{6.11}$$

Rearranging and solving Equation (6.11) yields the following:

$$A_1 = \frac{e^{\frac{\zeta\pi}{\sqrt{1-\zeta^2}}}}{1 + e^{\frac{\zeta\pi}{\sqrt{1-\zeta^2}}}} \tag{6.12}$$

Defining $K = e^{\frac{\zeta\pi}{\sqrt{1-\zeta^2}}}$, the resultant two impulse sequence named as Zero Vibration input shaping can be summarized as follows:

$$A_1 = \frac{1}{1+K} \quad t_1 = 0 \tag{6.13}$$

$$A_2 = \frac{K}{1+K} \quad t_2 = 0.5T_d = \frac{\pi}{\omega_n\sqrt{1-\zeta^2}} \tag{6.14}$$

It should be noted that real systems are not operated with impulse inputs in general, so properties of the impulse sequence given by Equations (6.13) and (6.14) needs to be converted to usable commands. This is performed by convolving the impulse sequence with any desired command signal. The convolution product is then used as command to the system. The command generation process is illustrated in the following figure for a particular pulse input profile:

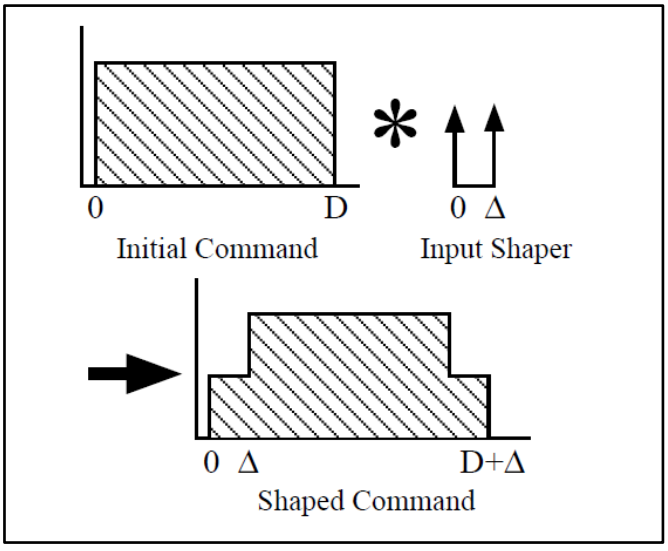


Figure 6.6. Process of Input Shaping [28]

It should be pointed out that robustness is a major concern for input shaping process. That is, the determined amplitudes and time locations of the impulses depend on the

system parameters ω_n and ζ and if errors are present in these values, then residual vibration will not be eliminated perfectly upon the application of the respective impulse sequence. Following figure illustrates the effect of modeling errors on the capability of vibration cancelling:

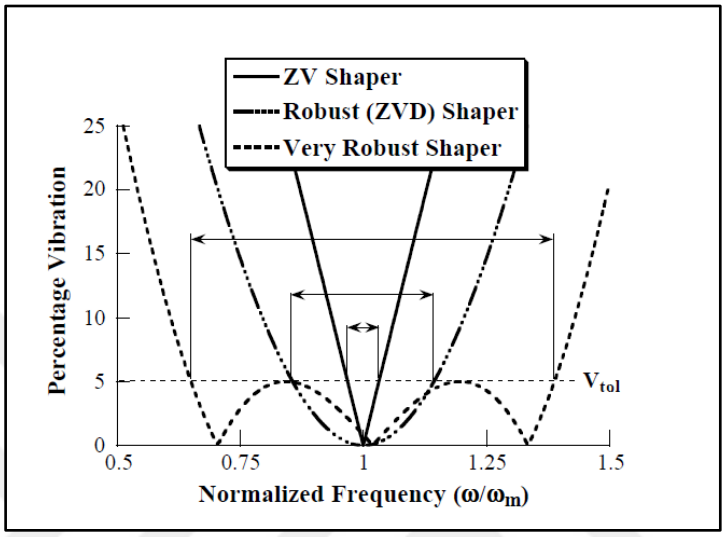


Figure 6.7. Sensitivity Curves for Input Shaping Process [28]

From Figure 6.7 it can be seen that as the predicted natural frequency deviates from the actual frequency, the percent residual vibration increases more rapidly for less robust input shapers. In fact, the zero vibration (ZV) input shaper is the one most susceptible to the parameter error.

In order to enhance the robustness of the input shaper, additional constraints must be defined according to [28]. One such constraint is to set the derivative of the identity given in Equation (6.1) that represents the residual vibration amplitude with respect to natural frequency and damping ratio to zero:

$$\frac{d}{d\omega_n}V(\omega_n,\zeta)=0 \tag{6.15}$$

$$\frac{d}{d\zeta}V(\omega_n,\zeta)=0 \tag{6.16}$$

Once these additional constraints are satisfied with $V=0$, the result is a Zero Vibration and Derivative (ZVD) input shaper. The derivation of the impulse

magnitudes and times is similar to that of the ZV shaper and it leads to three impulse sequence. The related equations are provided below:

$$A_1 = \frac{1}{1+2K+K^2} \quad t_1 = 0 \tag{6.17}$$

$$A_2 = \frac{2K}{1+2K+K^2} \quad t_2 = \frac{\pi}{\omega_n\sqrt{1-\zeta^2}} \tag{6.18}$$

$$A_3 = \frac{K^2}{1+2K+K^2}\ [54.1] \quad t_3 = \frac{2\pi}{\omega_n\sqrt{1-\zeta^2}}\ [54.2] \tag{6.19}$$

Where, $K = e^{\frac{\zeta\pi}{\sqrt{1-\zeta^2}}}$, as in the previous ZV case.

Returning to Figure 6.7, the comparison between the ZV and ZVD curves shows that ZVD shaper is significantly more robust with 5% deviation in natural frequency. It should be noted that, it is possible to increase the robustness of the input shaper even further by designing specified intensity shapers [28]. However, the enhancement in the robustness comes with a price. That is, as the shaper becomes more robust, the time delay imposed on the actuation lasts longer. This concept is illustrated in the following figure:

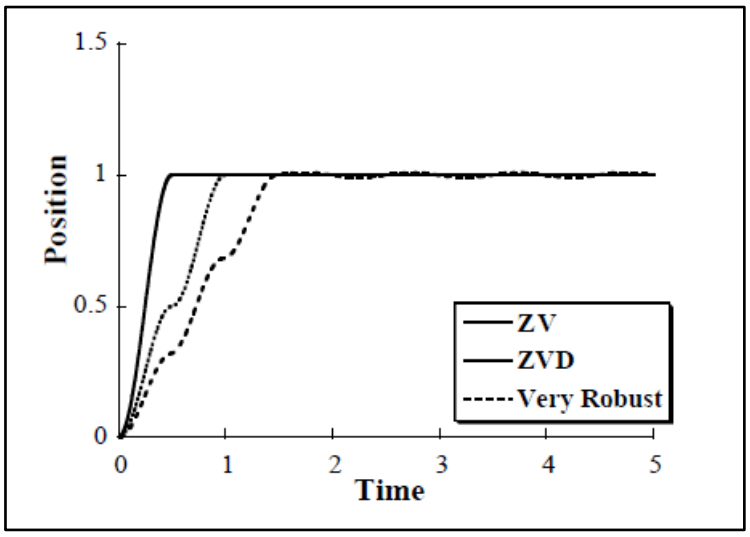


Figure 6.8. Response Characteristics Comparison for Different Input Shapers [28]

As it can be seen from Figure 6.8, enhanced robustness indeed yields slower response characteristics. Considering the balance between the robustness and actuation time delay, ZVD input shaper is utilized in the slung load control as it will be discussed in the next section.

6.2.2 Application of Input Shaping to Slung Load Control

In order to apply input shaping to the slung load case, the natural frequency and damping ratio of the undesirable oscillations should be determined. In addition, the input shaping is applied to the longitudinal cyclic based on the characteristics of the longitudinal load pendulum mode and application of the input shaping on the lateral cyclic is based on the lateral load pendulum mode characteristics. The reason is that the cross coupling between the cyclic inputs and pendulum modes is small as mentioned previously.

To determine the related natural frequency and damping ratio for the pendulum modes, two separate approaches that yield quite similar results will be illustrated. Firstly, related parameters of concern will be obtained from the pole locations on the complex plane corresponding to the pendulum modes. Then, for a further verification of the calculated natural frequency and damping ratio, logarithmic decrement method will be utilized based on the time histories of the slung load cable angles.

6.2.2.1 Calculation of the Natural Frequencies and Damping Ratios Based on the Pole Locations on the Complex Plane

In order to calculate the related natural frequencies and damping ratios, the oscillatory poles corresponding to the longitudinal and lateral pendulum modes should be identified in the complex plane. This can be accomplished by obtaining the state matrix of the overall closed loop system given in Figure 6.1 and examining its eigenvalues. The related state matrix can easily be obtained by using MATLAB's 'connect' function. Following figure illustrates the locations of the closed loop

system poles. Considering that the oscillatory poles of concern should be near the imaginary axis, the figure is zoomed in to the close vicinity of the imaginary axis for a clear demonstration.

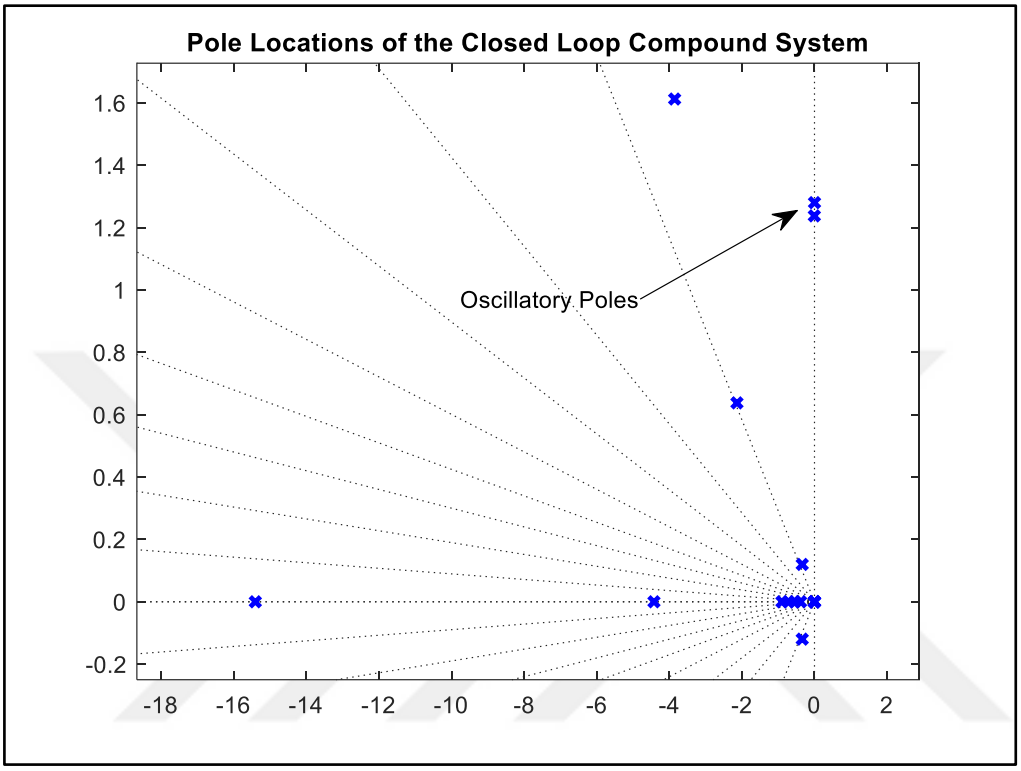


Figure 6.9. Closed Loop Poles of the Compound System without Slung Load Controller (Close View)

From Figure 6.9, it can be seen that there are indeed two complex pole pair in the very close vicinity of the imaginary axis corresponding to the longitudinal and lateral pendulum motion of the slung load. Investigation on the eigenvectors corresponding to these particular poles shows that the major contributors to oscillatory poles are the longitudinal and lateral cable angle rates, i.e., $\dot{\theta}_{sl}$ and $\dot{\phi}_{sl}$. Following table summarizes these poles numerically and identifies which complex pair corresponds to oscillation in each axis:

Table 6.1. Oscillatory Slung Load Poles

Poles	
Long. Oscillatory Slung Load Motion	Lat. Oscillatory Slung Load Motion
-0.0043 ± 1.2376i	0.0006 ± 1.2800i

Given that the oscillatory pole locations are known, the natural frequencies and damping ratios can be computed for each mode by solving the following set of equations:

$$\text{Real(pole)} = \omega_n \zeta \tag{6.20}$$

$$\text{Imag(pole)} = \omega_n \sqrt{1-\zeta^2} \tag{6.21}$$

The resultant natural frequencies and damping ratios of the longitudinal and lateral pendulum modes are summarized in the following table:

Table 6.2. Natural Frequency and Damping Ratio of the Slung Load Pendulum Modes

	Long. Cable Angle (θ_{sl})	Lat. Cable Angle (ϕ_{sl})
ω_n [rad/sec]	1.2376	1.2800
ζ	0.0035	-4.87×10^{-4}

6.2.2.2 Calculation of the Natural Frequencies and Damping Ratios Based on Logarithmic Decrement Method

In the previous section, the natural frequency and damping ratio of the related slung load pendulum modes have been determined based on pole locations on the complex plane. In this section, the same set of parameters are calculated with logarithmic decrement method based on the time histories of the cable angles for further verification. In addition, this approach could be beneficial to obtain the natural frequency and damping ratio from real-life test data. To illustrate the concept of logarithmic decrement method, the successive peak values and peak occurrence instants of oscillatory load motions are provided in the following figure:

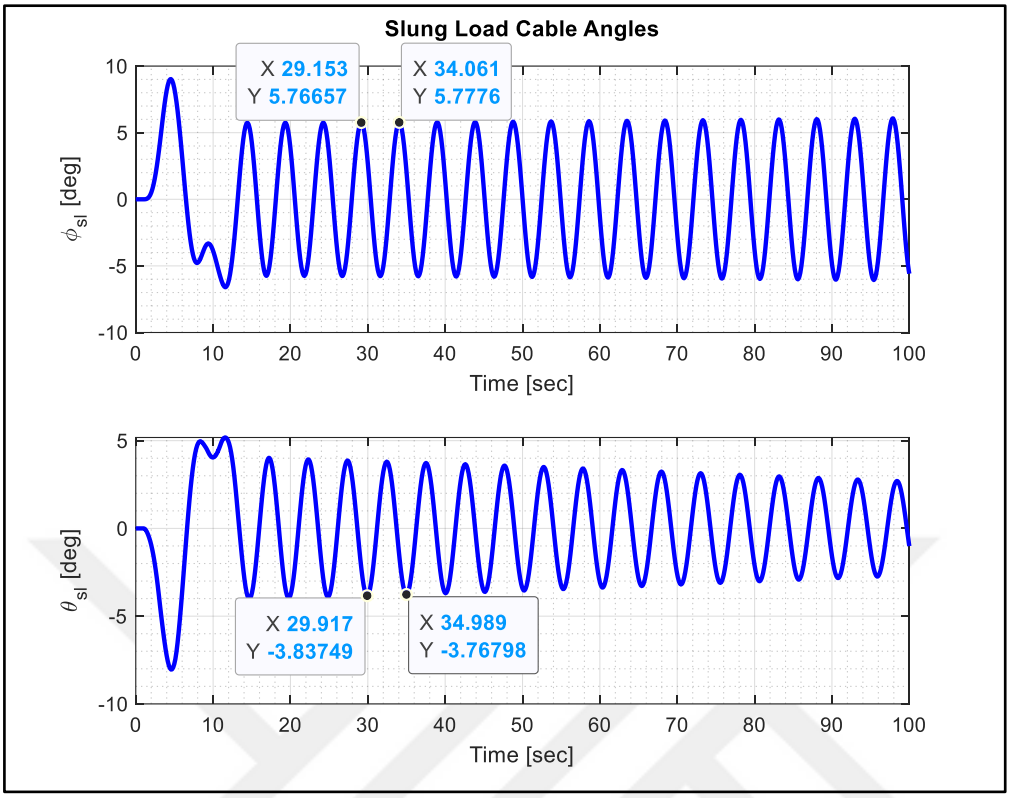


Figure 6.10. Time History of Longitudinal and Lateral Slung Load Cable Angles

The logarithmic decrement is defined as the natural log of the ratio of the amplitudes of any two successive peaks [29]:

$$\delta = \frac{1}{n}\ln\left(\frac{y_{os}(t)}{y_{os}(t+nt)}\right) \tag{6.22}$$

Where, y_{os} is the overshoot in the slung load cable angle of concern at time t and $y_{os}(t+nt)$ is the overshoot of the peak n periods away, which in this case is $n = 1$ according to Figure 6.10. The damping ratio can then be found from the logarithmic decrement by using the following formula:

$$\zeta = \frac{\delta}{\sqrt{4\pi^2 + \delta^2}} \tag{6.23}$$

It should be noted that once the damping ratio is determined, the natural frequency ω_n can be calculated from the damped natural frequency. The damped natural frequency ω_d on the other hand, can be determined from the duration between the

successive peaks in the related time history plot. Following set of equations summarize this concept:

$$\omega_d = \frac{2\pi}{T_d} \tag{6.24}$$

$$\omega_n = \frac{\omega_d}{\sqrt{1-\zeta^2}} \tag{6.25}$$

The natural frequency and damping ratio parameters calculated by using Equations (6.22)-(6.25) are given in the following table:

Table 6.3. Natural Frequency and Damping Ratio Parameters Calculated by Logarithmic Decrement Method

	Long. Cable Angle (θ_{sl})	Lat. Cable Angle (ϕ_{sl})
ω_n [rad/sec]	1.2388	1.2802
ζ	0.0021	-3.04×10^{-4}

The comparison of the Table 6.2 and Table 6.3 shows that calculation of the natural frequency and damping ratio based on pole locations and logarithmic decrement method yields quite similar results, which is the expected outcome. In the next section, the related ZVD input shaper parameters will be calculated by taking the results given in Table 6.2 into account. The reason is that the pole locations provide the exact natural frequency and damping ratio values as far as the linear model is concerned. However, input shapers designed with the parameters calculated by logarithmic decrement method also give satisfactory results.

6.2.2.3 Design of the Input Shapers for Oscillatory Slung Load Motion

Upon the calculation of the related natural frequency and damping ratio, the ZVD input shaping filters can be designed by using the set of equations given in Equations (6.17)-(6.19). The impulse amplitudes and instances of the input shapers for the longitudinal and lateral motion of the slung load are provided in the table below:

Table 6.4. Impulse Amplitudes and Instances for ZVD Input Shapers

	Long. Cable Angle (θ_{sl})	Lat. Cable Angle (ϕ_{sl})
A_1	0.2528	0.2496
A_2	0.5000	0.5000
t_2 [sec]	2.5385	2.4543
A_3	0.2473	0.2504
t_3 [sec]	5.0770	4.9086

For a clear illustration of the ZVD input shaping filters, following schematic is provided:

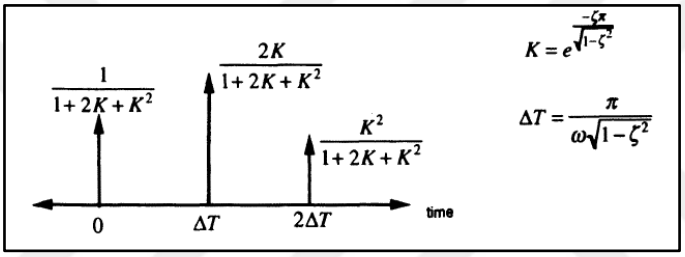


Figure 6.11. ZVD Input Shaping Filter [30]

Block diagram of the overall system with input shaping filters integrated after the reference commands is illustrated in the following figure:

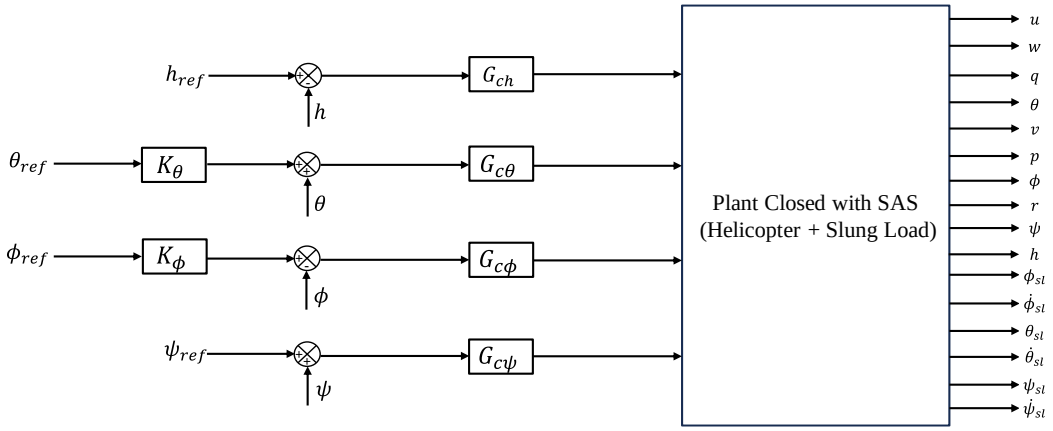


Figure 6.12. Block Diagram for the Closed Loop System with Input Shaping Filters

The same simulation discussed in Section 5.1 is run with the derived input shapers. Following figure illustrates the modified commands in the longitudinal and lateral cyclic channels:

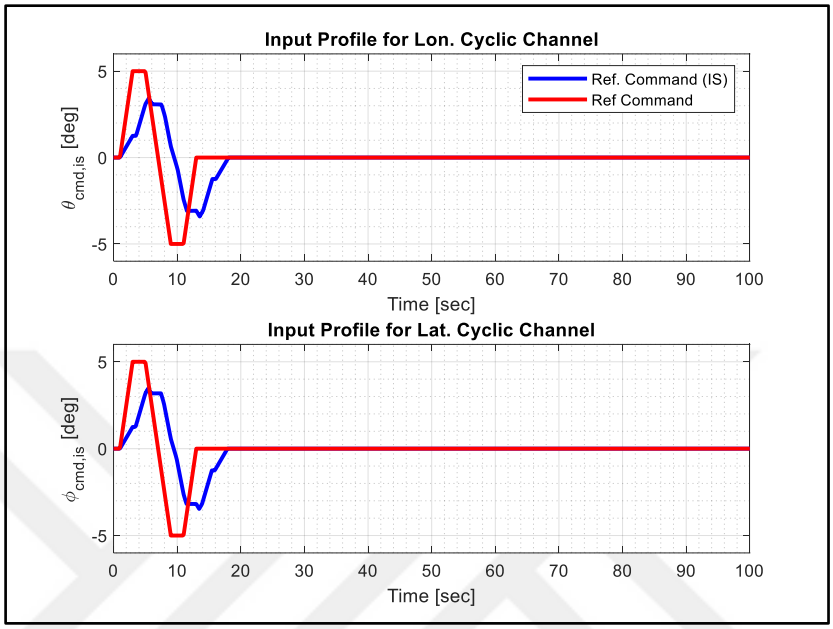


Figure 6.13. Input Shaped Reference Commands

Resultant slung load cable angles are provided in the following figure:

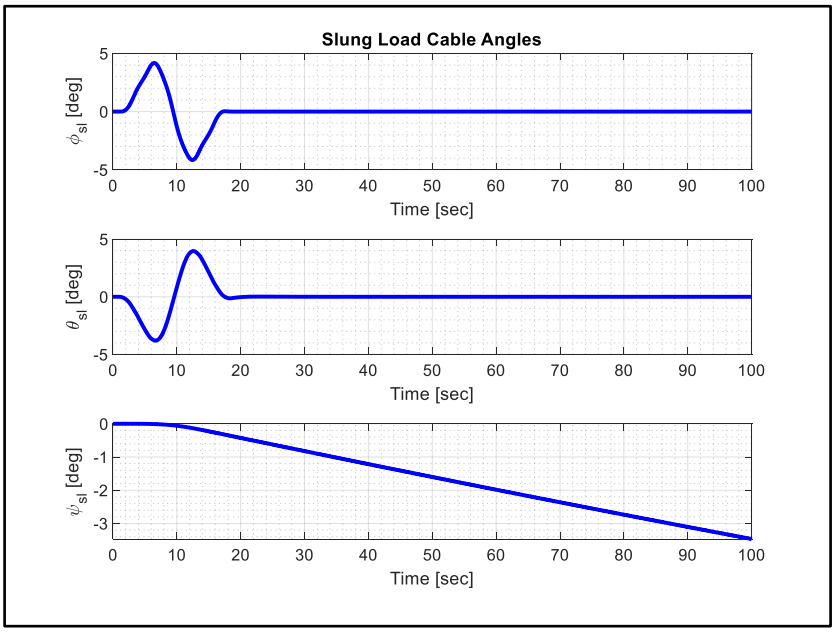


Figure 6.14. Slung Load Cable Angles with ZVD Input Shaped Reference Commands

From Figure 6.14, it can be seen that with the input shaped reference commands, oscillations in the longitudinal and lateral slung load cable angles are damped out very quickly without excessive overshoot. As expected, there is no remarkable change in the yaw angle of the load compared to the previous simulation results with the original reference commands.

Also, from Figure 6.13 it is evident that the input shaping induced noticeable time delay on the reference command, which also meets the expectations.

To investigate the effect of the input shaping, the resultant helicopter states with modified reference commands are provided as well in the following figure:

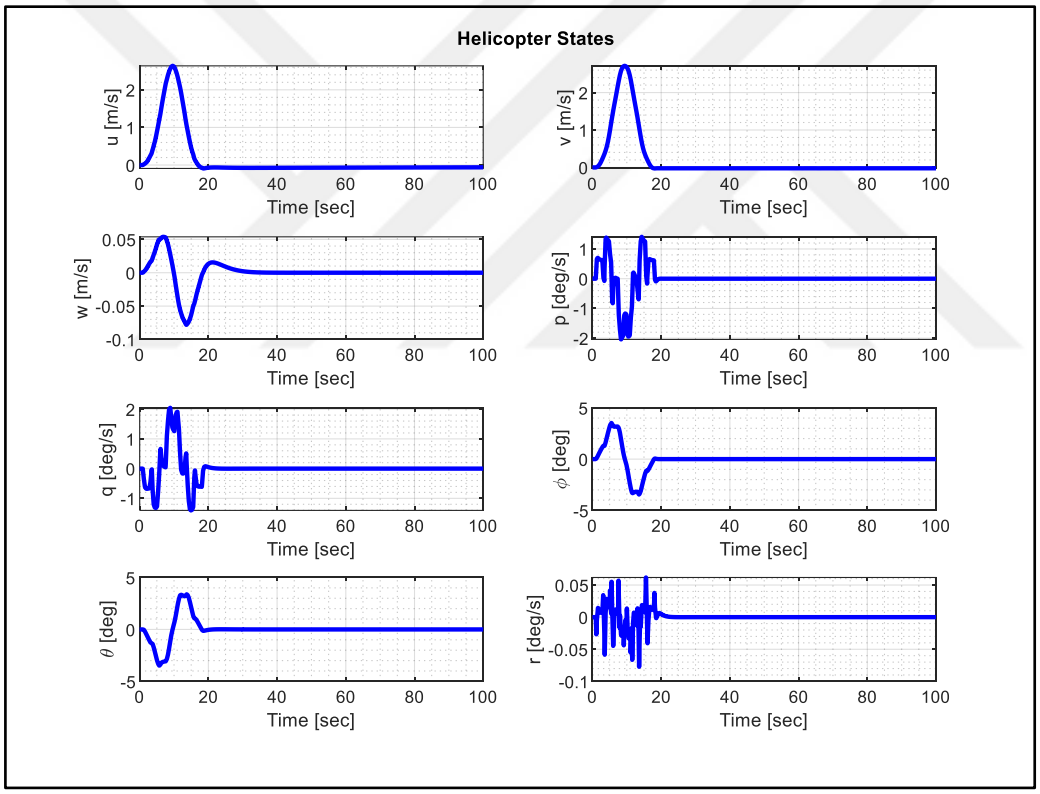


Figure 6.15. Helicopter States with ZVD Input Shaped Reference Commands

From Figure 6.15, it can be seen that the sustained oscillations observed in the helicopter states have also been removed due to implementation of the input shaping. This is an expected outcome considering that the oscillatory behavior observed in the states was a result of the strong coupling between the helicopter and slung load

induced by the forces and moments transferred through the cables. In other words, given that the load oscillations are suppressed, there are no oscillatory cable forces and moments acting on the helicopter.

To observe the enhanced robustness of ZVD input shaper a comparison is performed with ZV input shaper. As discussed above, ZV input shaper is a two-impulse sequence filter and derived impulse amplitudes and instances are provided in the table below for the longitudinal and lateral motion of the slung load.

Table 6.5. Impulse Amplitudes and Instances for ZV Input Shapers

	Long. Cable Angle (θ_{sl})	Lat. Cable Angle (ϕ_{sl})
A_1	0.5029	0.4996
A_2	0.4971	0.5004
t_2 [sec]	2.4176	2.3374

Following figure illustrates the modified commands in the longitudinal and lateral cyclic channels:

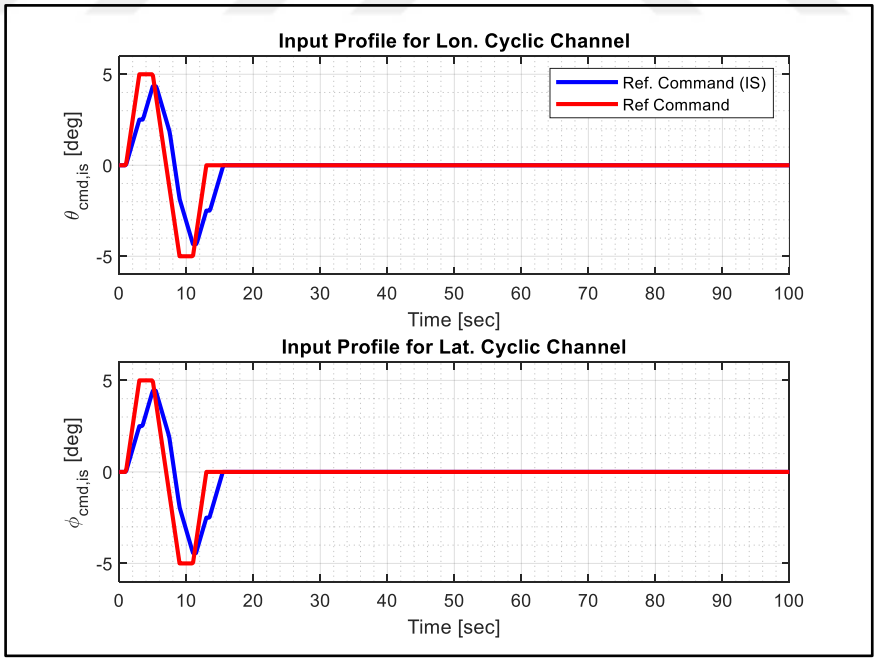


Figure 6.16. ZV Input Shaped Reference Commands

Resultant slung load cable angles with shaped reference commands are illustrated in the following figure:

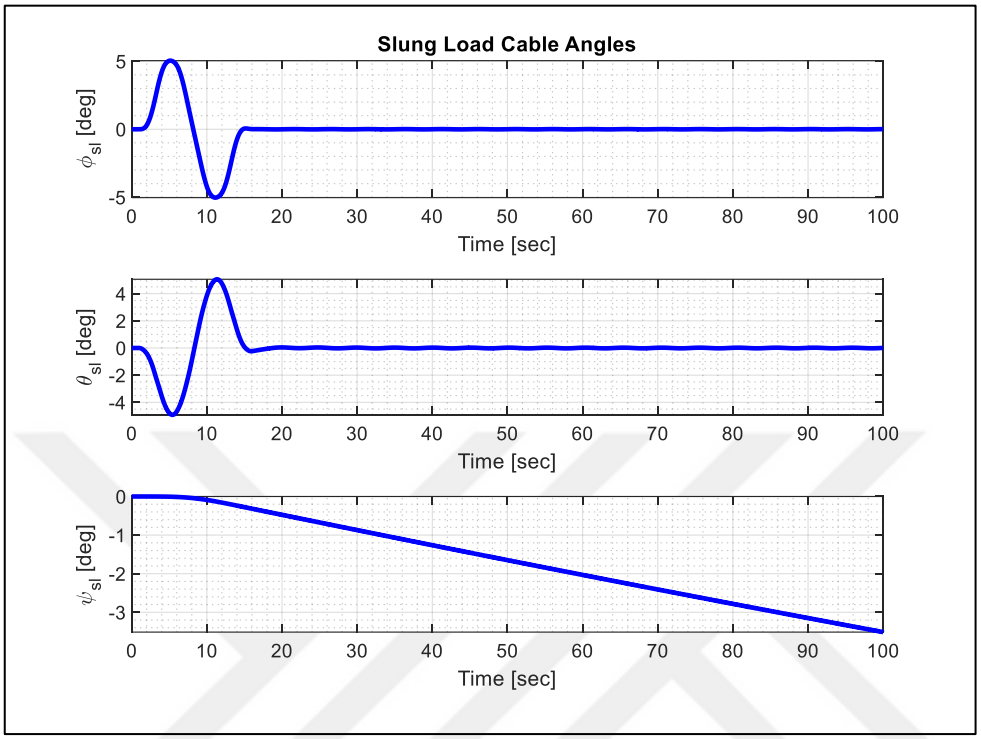


Figure 6.17. Slung Load Cable Angles with ZV Input Shaped Reference Commands

From Figure 6.17, it can be seen that even though there is almost unrecognizable sustained oscillation in the longitudinal and lateral cable angles, the remainder of the response characteristics are quite similar to the ZVD input shaper case given in Figure 6.14. That is, the oscillations are damped out quite quickly with this particular shaper as well. However, as it can easily be noticed, the maximum amplitude of the longitudinal and lateral load cable angles are greater than ZVD case due to the fact that amplitude of the reference command is greater for ZV input shaper.

Previous discussion shows that both the ZV and ZVD input shapers provide quite satisfactory results in the case of perfect natural frequency ω_n estimation. For a clear robustness comparison, the impulse amplitudes and instances for both shapers will be determined with erroneous natural frequency greater than the original one by 5%. The procedure is identical to the one given above and for convenience detailed derivation of the related parameters will not be provided.

The resultant cable angles for both ZV and ZVD cases are provided in a superimposed manner in the following figure.

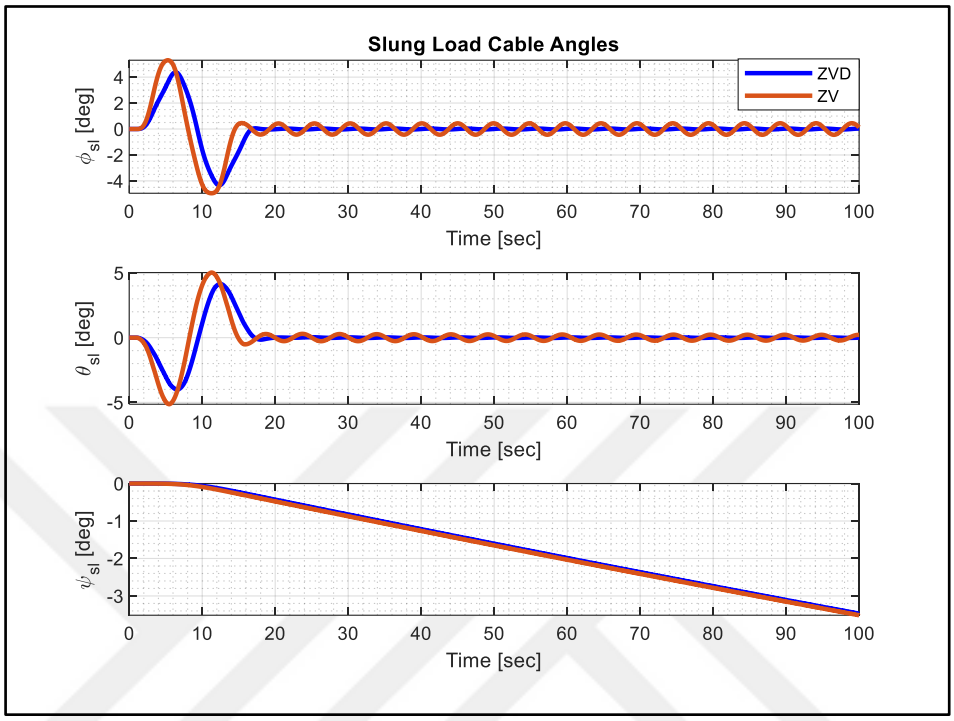


Figure 6.18. ZV vs ZVD Input Shaper Response Comparison

From Figure 6.18, it can clearly be seen that amplitude of the sustained oscillations in both the longitudinal and lateral load cable angles increases remarkably with 5% deviation from the originally estimated natural frequency in the case of ZV shaper, whereas ZVD shaper still performs quite satisfactorily without yielding any noticeable sustained oscillation.

This additional case study emphasizes that ZV shapers are quite susceptible to modeling errors and choosing ZVD for damping out undesirable sustained oscillations in helicopter slung load applications is a more appropriate choice.

6.3 Slung Load Control with Delayed Cable Angle Feedback

The motivation behind the delayed feedback control is that by using intentionally delayed feedback, it is possible to damp out vibrations in an oscillatory system.

This particular controller consists of a proportional gain and certain amount of time delay on the related feedback parameter. The concept is implemented by feeding back the output of the of delayed feedback controller to the reference command as an additional displacement.

In the slung load case, two separate controllers are used for the longitudinal and lateral channels respectively. The input of the controller in the longitudinal channel is longitudinal slung load cable angle θ_{sl} and its output is added to the reference helicopter pitch angle (θ) command. Whereas, lateral slung load cable angle ϕ_{sl} is the input of the lateral delayed feedback controller and output of this controller is added to the reference helicopter roll angle (ϕ) command.

Block diagram of the overall system with delayed feedback controllers is illustrated in the following figure:

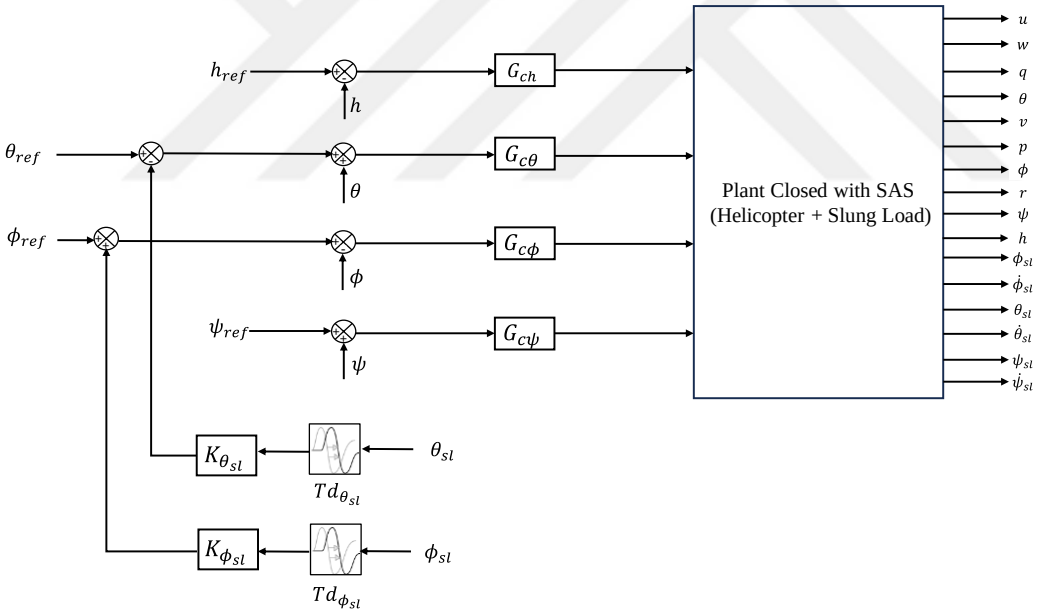


Figure 6.19. Block Diagram of the Closed Loop System with Delayed Feedback Controllers

To determine the related gain and time delay parameters in the controllers, simulation-based optimization based on Particle Swarm Optimization is utilized. In the developed algorithm, settling time of the oscillatory longitudinal and lateral slung load cable angles are tried to be minimized. A similar study that involves

combination of helicopter LQR controller and delayed feedback controllers optimized with Particle Swarm Optimization can be found in [15].

Before going into the further details of the application on the slung load, some theoretical background will be provided regarding the Particle Swarm Optimization in the next section.

6.3.1 Particle Swarm Optimization Algorithm

In particle swarm optimization method, individuals called as particles are evolved by cooperation and competition among themselves through generations. Each particle can be interpreted as a column vector in N-dimensional space and represents a potential solution to the problem of interest. In this case N is 4 (a gain and time delay for each controller in the longitudinal and lateral axes) and the particles constitute a possible set of optimal controller gain and time delay. The governing equations of this particular approach are provided below [31]:

$$v_i(k+1) = wv_i(k) + c_1 rand(\,)\big(p_i(k) - x_i(k)\big) + c_2 rand(\,)\big(g(k) - x_i(k)\big) \tag{6.26}$$

$$x_i(k+1) = x_i(k) + v_i(k+1) \tag{6.27}$$

Now, a brief discussion on each term in the equation set above will be provided hereafter. Firstly, k in both Equation (6.26) and (6.27) denotes the iteration number. Whereas, x_i and v_i designate the position and velocity of the i^{th} particle respectively. Next, p_i represents the personal best position of each particle as far as the minimization of the cost function is concerned. Finally, g is the global best, that is the optimal solution among the all particles of interest.

According to the PSO algorithm, certain amount of randomness needs to be introduced in the formulation of velocity, which is designated by $rand(\,)$ in the second and third terms on the right-hand side of Equation (6.26). Another important point to note is that c_1 and c_2 are predefined constants according to PSO, both of

which are equal to 2. The last but not least, w is the damping added to the inertia term given by the first quantity in the right-hand side of Equation (6.26).

In the next section, the application of PSO on the slung load control will be discussed.

6.3.2 Application of Particle Swarm Optimization on Slung Load Control

To perform PSO for the optimization of the slung load controller parameters, a suitable cost function needs to be determined. Given that major concern of the slung load control is to eliminate sustained oscillations present in the both longitudinal and lateral axes, using settling time of the cable angles as the cost function to be minimized seems a quite reasonable approach.

Previous discussion on the uncontrolled slung load motion has shown that the sustained oscillations in both the longitudinal and lateral cable angles occur around zero. Hence, the settling time is determined such that both angles remain in between $\pm 0.05°$ beyond this particular time. Considering this, the cost function to be minimized can be written as follows:

$$J = t_{s,\theta_{sl}}^2 + t_{s,\phi_{sl}}^2 \tag{6.28}$$

Using the aforementioned PSO algorithm, several simulations are run with 100 particles and 100 iterations and satisfactory damping in both axes are obtained. The resultant optimal gain and time delay values in both axes are provided in the following set of equations:

$$K_{\theta_{sl}} = 0.6619 \tag{6.29}$$

$$T_{d,\theta_{sl}} = 0.8391 \tag{6.30}$$

$$K_{\phi_{sl}} = 0.5547 \tag{6.31}$$

$$T_{d,\phi_{sl}} = 0.9431 \tag{6.32}$$

Following figure illustrates the simulation results obtained with the optimal controller parameters given in equations (6.29)-(6.32).

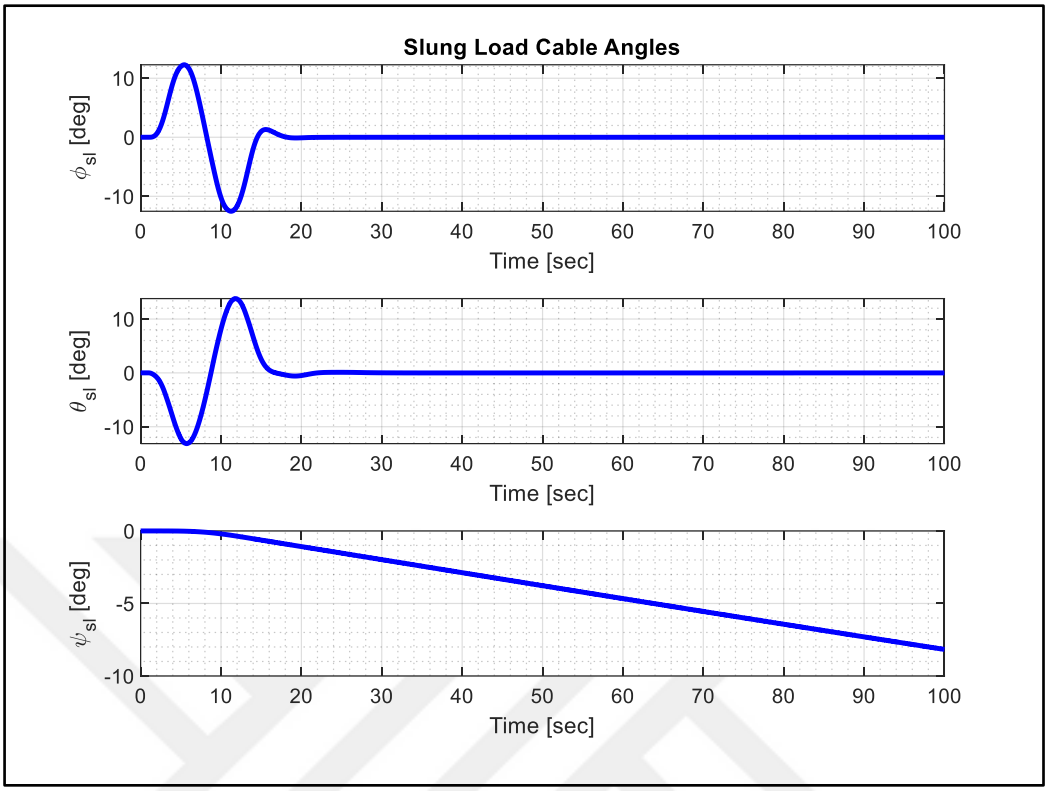


Figure 6.20. Slung Load Cable Angles with Delayed Cable Angle Feedback

Figure 6.20 shows that oscillations in the longitudinal and lateral cable angles damp out very quickly with delayed cable angle feedback. However, the overshoot in these angles are considerably large compared to the input shaping case. Also, the deviation in the load yaw angle is rather large as well.

It should be noted that, certain amount of improvement can be obtained in the overshoot characteristics by including the maximum cable angle in both axes in the cost function. But this will lead to larger settling times and deterioration in the oscillation damping.

All in all, delayed cable angle feedback results in quite efficient damping of the longitudinal and lateral cable angles. Nevertheless, the maximum angle amplitudes are rather large compared to the those obtained in the input shaping case.

To inspect the effect of delayed feedback control on the overall helicopter behavior, following figure consisting of the helicopter states is provided:

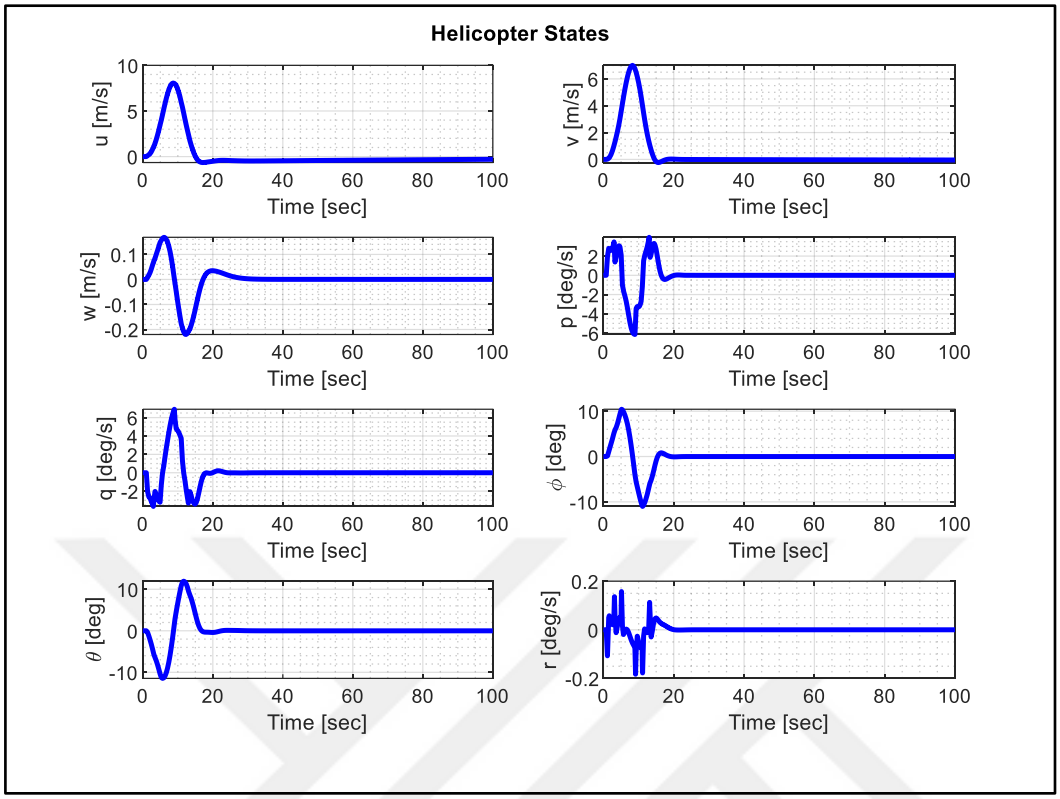


Figure 6.21. Helicopter States with Delayed Cable Angle Feedback

From Figure 6.21, it can be seen that due to the effective removing of the slung load oscillations, the oscillatory behavior in the helicopter states are damped out as well. This is an expected outcome as in the input shaping case. That is, since there are no oscillatory forces and moments acting on the helicopter transferred by the slung load cables, the helicopter states also become oscillation-free as a direct result of delayed cable angle feedback.

In the next section, slung load control with cable angle rate feedback approach will be discussed:

6.4 Slung Load Control with Cable Angle Rate Feedback

The cable angle rate feedback controllers examined in this section are designed based on the pole locations of the system of interest. That is, for some systems, it is possible that certain poles can be positioned at the close vicinity of the imaginary axis, which

leads to oscillatory behavior with very light damping. The cable angle rate feedback controllers are designed such that these poles are dragged further into the left-half of the complex plane to enhance the damping characteristics.

As it is discussed in detail in Section 6.2.2.1, system poles corresponding to the slung load pendulum motion indeed shows such characteristics. That is, the related dynamic modes possess oscillatory behavior with almost no damping at all. For convenience, the poles of concern are provided here as well in the following table:

Table 6.6 Oscillatory Slung Load Poles

Poles	
Long. Oscillatory Slung Load Motion	Lat. Oscillatory Slung Load Motion
-0.0043 ± 1.2376i	0.0006 ± 1.2800i

The cable angle rate feedback controllers that enhance the damping characteristics of these highly oscillatory poles are integrated to the existing helicopter AFCS by wrapping feedback controllers to the longitudinal and lateral cyclic from the longitudinal and lateral cable angle rates. In other words, slung load controller outputs are added to the SAS outputs before entering the input channels of the helicopter. Another important point regarding these particular type of controllers is that they can be designed with both cable angle and cable angle rate feedback [13]. In fact, there are certain studies in the literature that involves both of these quantities [12]. Even though it is possible to obtain promising results with all of these approaches, using the cable angle rate feedback leads to better load oscillation damping as it is stated in [12]. The investigation on the difference between cable and cable angle rate feedback under the scope of this study has also shown that cable angle rate feedback indeed results in faster oscillation damping characteristics. Hence, from this point on, cable angle rate feedback controllers will be discussed.

Block diagram of the closed loop system containing the cable angle rate feedback controllers is illustrated in the following figure:

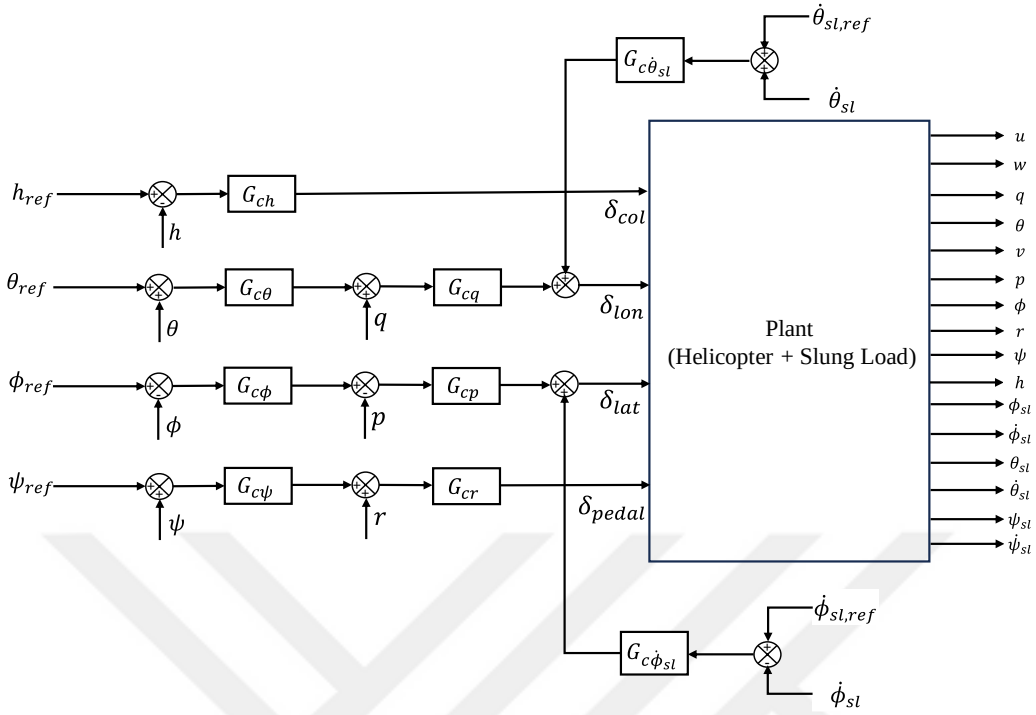


Figure 6.22. Closed Loop Compound System with Cable Angle Rate Feedback

From Figure 6.22, it can be seen that it is possible to set an arbitrary reference cable angle rate in both axes. However, to damp out the oscillations in the slung load cable angles effectively, these reference angle rates are defined as zero.

It should be noted that the overall compound system with AFCS consists of a total of 25 states and it is quite complex. Hence, it would be quite cumbersome to obtain controllers with well-known compensator design methodologies. Hence, in this study, MATLAB's "sisotool" function is utilized. That is, firstly the single input-single output transfer functions from the reference cable angle rates to the respective cable angle rates are determined. Then, using these SISO transfer functions, the cable angle rate feedback controllers are designed based on the root locations of the closed loop system.

Before discussing the design procedure in detail, it should be pointed out that the closed loop system will appear as unstable due to the slung load yaw mode poles regardless of how left the oscillatory poles are drawn with cable angle rate feedback controllers. However, as discussed previously, the unstable load yaw mode poles are

in the very close vicinity of the origin and they do not lead to any noticeable divergence of the overall system or deviation from the reference inputs. The time history plots of the simulations that have been shown so far agrees with discussion.

Another important point that needs to be mentioned is that due to the complexity of the overall system, the necessary transfer functions for cable angle rate feedback controller design are obtained by using the "connect" function of MATLAB. Utilization of this particular function is quite intuitive. That is, all one needs to do is to write out the equations that govern the inputs and outputs of the dynamic subsystems of concern.

Given that the design procedure is identical in both axes, the methodology discussed so far will be illustrated specifically for longitudinal cable angle rate $(\dot{\theta}_{sl,i})$. However, the overall results that involve both of these cable angle rate feedback controllers will be elaborated on to evaluate the controller adequacy.

Following figure illustrates the root locus diagram of the transfer function from the reference longitudinal cable angle rate to the longitudinal cable angle rate output of the overall system:

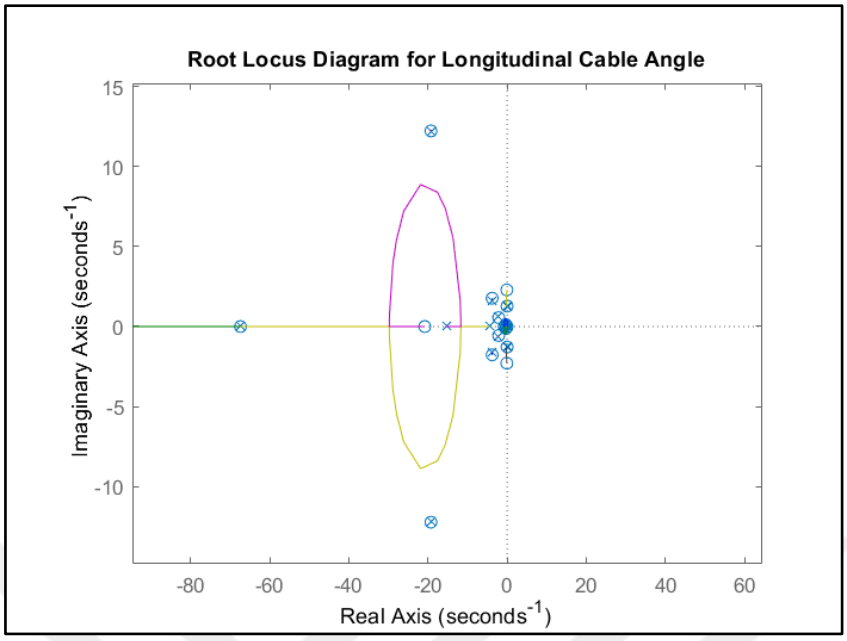


Figure 6.23. Root Locus Diagram for Longitudinal Cable Angle

Given that major concern at this point is to inspect the poles and zeros at the close vicinity of the imaginary axis, following figure that illustrates the closed-up view of Figure 6.23 is provided:

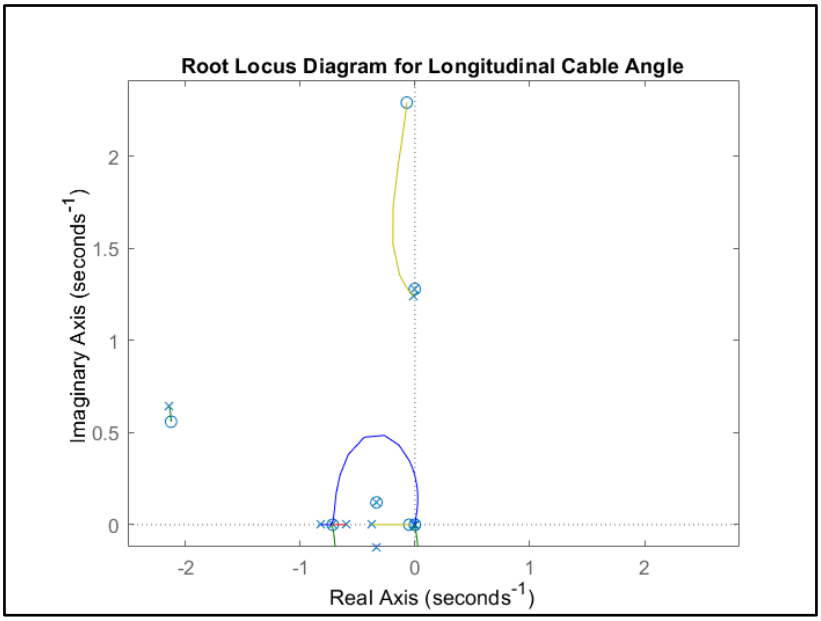


Figure 6.24. Root Locus Diagram for Longitudinal Cable Angle (Closed-Up View)

From Figure 6.24, it can be seen that the complex pole belonging to the longitudinal pendulum mode moves towards a complex zero located very close to the imaginary axis. There is also another complex pole in the close vicinity of the imaginary axis as well, which denotes the lateral pendulum motion and it is dealt with lateral cable angle rate feedback controller.

This figure clearly shows that it is not possible to obtain desirable pole location for the longitudinal pendulum motion of the load with only proportional controller. Hence, to drag this particular pole further to the left, a suitable cable angle rate feedback controller, i.e., a second order dynamic compensator, is implemented. To reshape the root locus accordingly, the zero locations of the controller are determined as follows by using the "sisotool" function of MATLAB.

$$z_{1,2} = -1.5606 \pm 1.5481i \tag{6.33}$$

It should be noted that with the implementation of this complex zero pair, the locus emerging from the pole corresponding to the longitudinal load motion moves further to the left with increasing gain.

The accompanying poles of the cable angle rate feedback controller are placed by paying attention to properness of the related transfer function and keeping the order of the overall dynamic system the same. Also, it is tried to prevent remarkable change in the overall root locus diagram. Following double pole location is assigned as suitable:

$$p_{1,2} = -9.3 \tag{6.34}$$

Finally, gain of the cable angle rate feedback controller is also determined based on the intention of dragging the complex pole of concern further to the left half plane:

$$K = 1238 \tag{6.35}$$

Hence, the cable angle rate feedback controller for the longitudinal slung load motion becomes the following:

$$G_{c,\dot{\theta}_{sl,i}} = \frac{1238s^2 + 3864s + 5982}{s^2 + 18.6s + 86.49} \tag{6.36}$$

To investigate the effect of the cable angle rate feedback controller on the longitudinal slung load dynamics, pole locations of the closed loop SISO system from the reference cable angle rate input to the longitudinal cable angle rate is provided in the following figure:

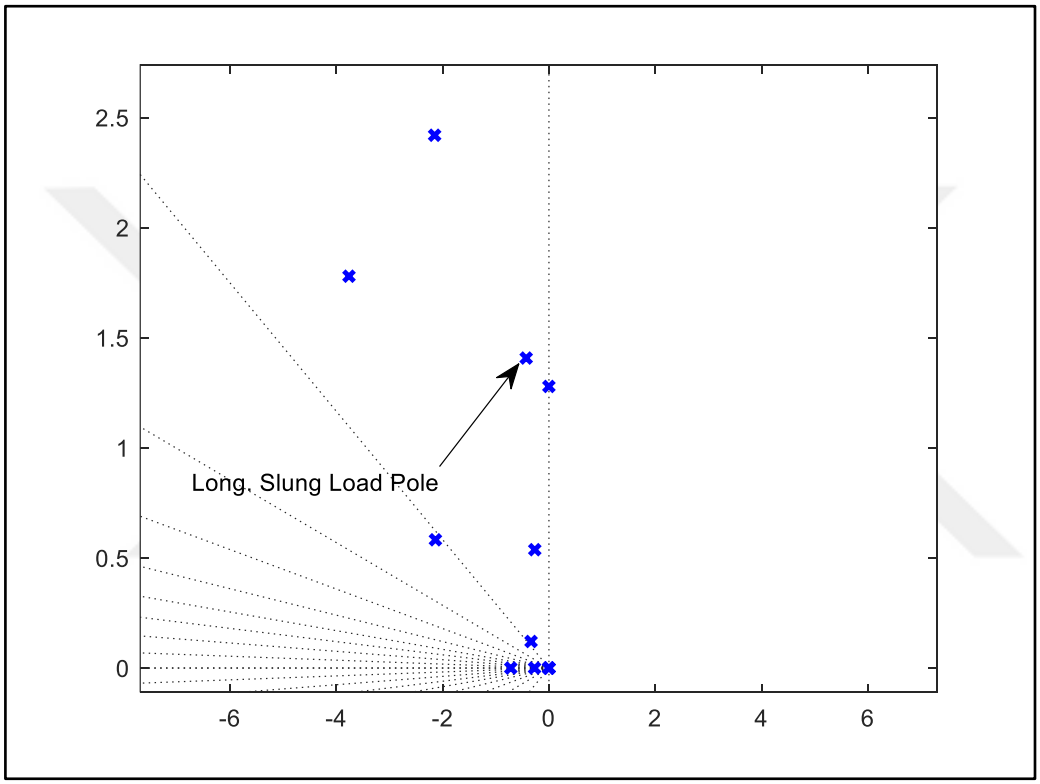


Figure 6.25. Closed Loop System Poles with Cable Angle Rate Feedback Controller

In Figure 6.25, the closed-up view is provided to easily distinguish the related slung load poles. The same figure shows that the longitudinal pole indeed moves to the further left half plane with the implementation of the cable angle rate feedback controller. In fact, the change in this particular mode can be quantified by the following identity:

$$s_{\theta_{sl}} = -0.0043 \pm 1.2376\text{i} \rightarrow -0.42766 \pm 1.4077\text{i} \tag{6.37}$$

From Equation (6.37), it can be seen that the real part of the complex pole pair changes by almost two orders of magnitude. This implies that the cable angle rate feedback controller introduces significant amount of damping compared to the uncontrolled slung load case.

It should be noted that the pole in the close vicinity of the imaginary axis comes from the lateral load motion and it will be taken care of with the cable angle rate feedback controller designed for the lateral axis.

Given that satisfactory damping characteristics for the longitudinal load motion is obtained with the cable angle rate feedback controller, similar approach is applied on the lateral cable angle rate and following compensator is obtained:

$$G_{c,\dot{\phi}_{sl,i}} = \frac{202.7s^2 + 756.5s + 2137}{s^2 + 2.349s + 1.379} \tag{6.38}$$

Next, effect of the cable angle rate feedback controllers on the dynamic characteristics of the compound system will be examined by performing the simulation with the same longitudinal and lateral input profiles discussed so far. Following figure illustrates the resultant time history of the slung load cable angles:

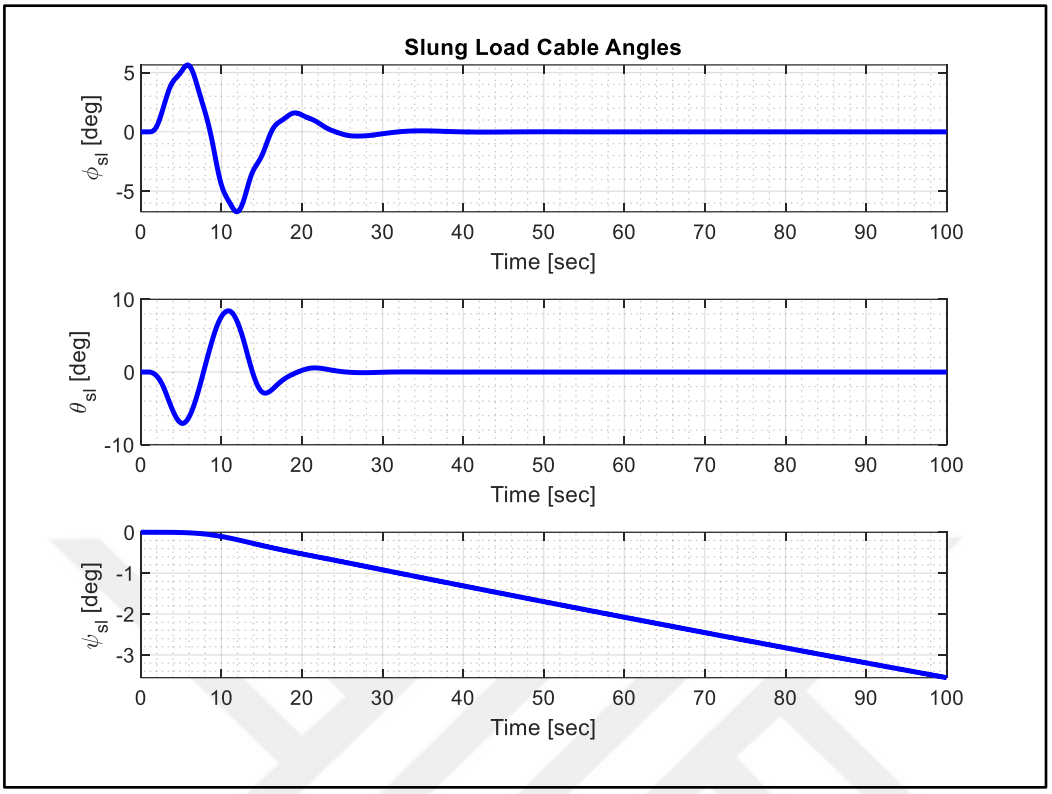


Figure 6.26. Slung Load Cable Angles with Cable Angle Rate Feedback Controllers

From Figure 6.26, it can be seen that the cable angle rate feedback controllers effectively damps out the sustained oscillations in the longitudinal and lateral slung load cable angles. Given that no control is imposed on the slung load yaw angle, it shows similar characteristics as in the previous discussions. As mentioned previously, overall deflection in the load yaw axis is not significant considering that it only deviates about 3° within a large time interval of 100 seconds.

As in the case of previously discussed controllers, effect of cable angle rate feedback controller implementation on the helicopter is examined. Following figure illustrates the time history of the helicopter states:

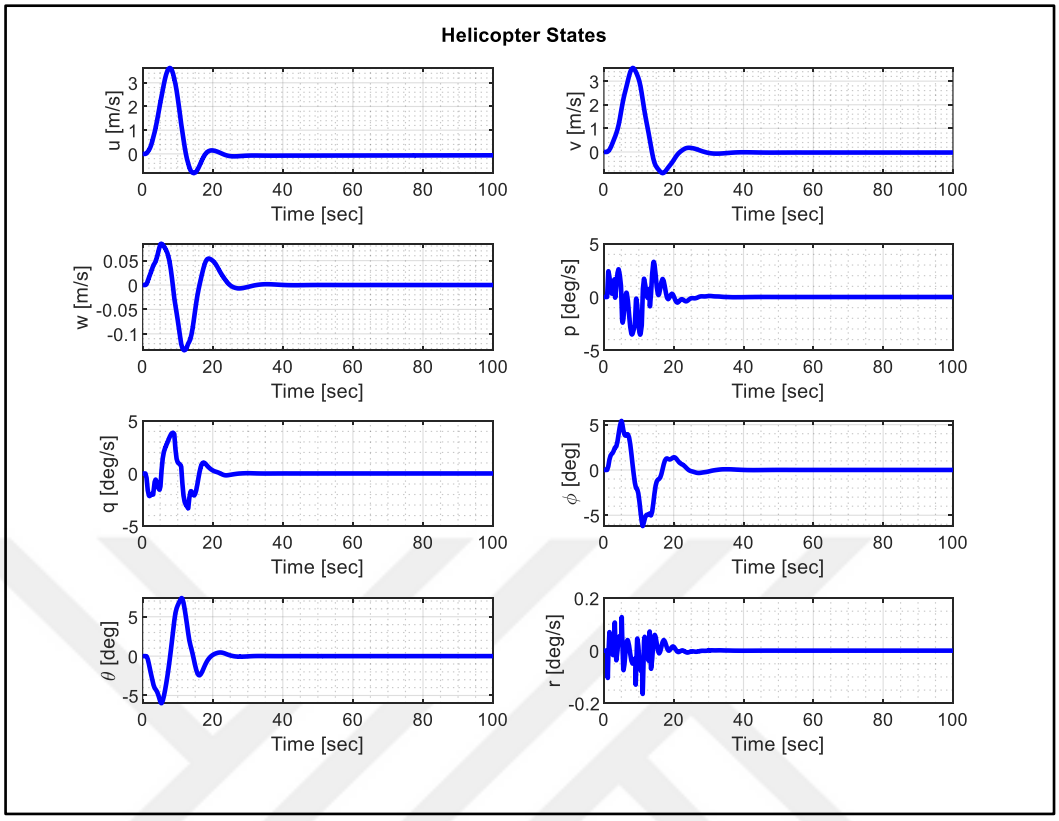


Figure 6.27. Helicopter States with Cable Angle Rate Feedback Controllers

From Figure 6.27, it can be seen that the sustained oscillations on the helicopter states have also been removed due to absence of oscillatory forces and moments acting through slung load cables as in the cases of input shaping and delayed cable angle feedback.

The same figure also shows that there is a remarkable deviation from the commanded reference pitch and roll attitudes. This is an expected result, considering that the cable angle rate feedback controllers are placed just before the plant inputs and they directly affect the performance of the helicopter flight control system consisting of previously discussed stability augmentation systems and autopilots.

This discussion shows that, a trade-off should be performed between the desired amount of oscillation damping of the slung load and helicopter reference command tracking performance. That is, if one sets the helicopter reference tracking ability as the main priority, then certain amount of load damping introduced by the cable angle

rate feedback controllers should be sacrificed. However, a more detailed design procedure can be performed by taking both of these aspects into account. In other words, cable angle rate feedback controllers that induces load damping without deteriorating the tracking performance significantly can be designed. In fact, there are certain studies in the literature that discuss this issue [12].

Given that three separate effective strategies regarding the slung load control are introduced, a performance comparison among them shall be provided. However, before going into the details of this comparison a discussion on the Kalman Filter design will be provided regarding the acquisition of the slung load cable angles and angular rates.

6.5 Kalman Filter Design for Slung Load System State Estimation

In most simple terms, the Kalman Filter is an algorithm that estimates the state of a system from the measured data in an optimal manner [32]. The reason why the Kalman Filter is included in this study is that, depending on the helicopter configuration, measuring slung load states (angles and rates) to be used in the control algorithm can be difficult to accomplish. Even though there are various studies that utilizes measured slung load states in control applications, it may be beneficial to design a Kalman Filter that performs sufficient estimation of the respective load states to eliminate the need of implementing complicated data acquisition hardware to the compound system consisting of helicopter and slung load.

Before going into the details, it should be noted that all the states of the helicopter can be measured by appropriate integration of the related sensors, which is the common practice in aviation industry. Hence, the concern of this section will be estimation of the slung load cable angles and angular rates based on the measured helicopter states.

The Kalman Filters can be designed for both continuous and discrete time systems. As far as this study is concerned, both of these approaches are tested and they yielded

satisfactory results. For the remainder of this section discrete Kalman Filter will be formulized and detailed. Also, the simulation results that will be provided will be based on discrete Kalman Filter.

It should be noted that in order to design a Kalman Filter, the dynamic system of concern should be observable. Hence, firstly the continuous state space model will be discretized and observability of the discretized model will be checked.

Even though there are several viable options that can be utilized to derive the related discrete model by hand, MATLAB's "c2d" function performs adequately well to serve this purpose. Majority of the discretization methods available in the literature can be entered as an option to this particular function. Default option is zero order hold method. Discrete model obtained with this method and a suitable time step sufficiently captures the continuous system dynamics and it will be used in this study as well. Once the discretized state space model is obtained, it can be written in the following format:

$$x_{k+1} = Ax_k + Bu_k \tag{6.39}$$

$$y_k = Cx_k \tag{6.40}$$

In Equations (6.39) and (6.40), k denotes the current time step. It should be noted that C matrix designates the measured states and in this particular case it is of size 8×14 and arranged in such a way that only the entries that correspond to helicopter states are equal to one and remaining entries are zero. In addition, it is worth to mention that the time step selected for the discretization procedure is 0.001 seconds, which is sufficient to capture the continuous system dynamics.

To verify the observability of the dynamic system, it is sufficient to illustrate that the observability matrix is of full rank. That is, in order for system to be fully observable, the rank of the observability matrix must be equal to the number of states, for this particular case it should be 14.

The observability matrix can be calculated by the following equation [33]:

$$O = \begin{bmatrix} C \\ CA \\ \vdots \\ CA^{n-1} \end{bmatrix} \tag{6.41}$$

In Equation (6.41), n stands for the number of states in the dynamic system. The observability matrix for the discretized state space model of compound helicopter-slung load system is indeed rank of 14, which indicates that the system is fully observable and the slung load states can be estimated from the measured helicopter states.

Without any rigorous derivation, the well-known Kalman Filter equations for discrete time systems can be written as follows [32]:

$$\hat{x}_k^- = A\hat{x}_{k-1} + Bu_k \tag{6.42}$$

$$P_k^- = AP_{k-1}A^T + Q \tag{6.43}$$

$$K_k = P_k^- C^T (CP_k^- C^T + R)^{-1} \tag{6.44}$$

$$\hat{x}_k = \hat{x}_k^- + K_k(y_k - C\hat{x}_k^-) \tag{6.45}$$

$$P_k = (I - K_k C)P_k^- \tag{6.46}$$

It should be noted that Equations (6.42) and (6.43) are the prediction equations, whereas Equations (6.44)-(6.46) represent the update equations. The Kalman Filter calculations are performed in MATLAB-Simulink environment. The filter is implemented as a separate function block as shown in the following figure:

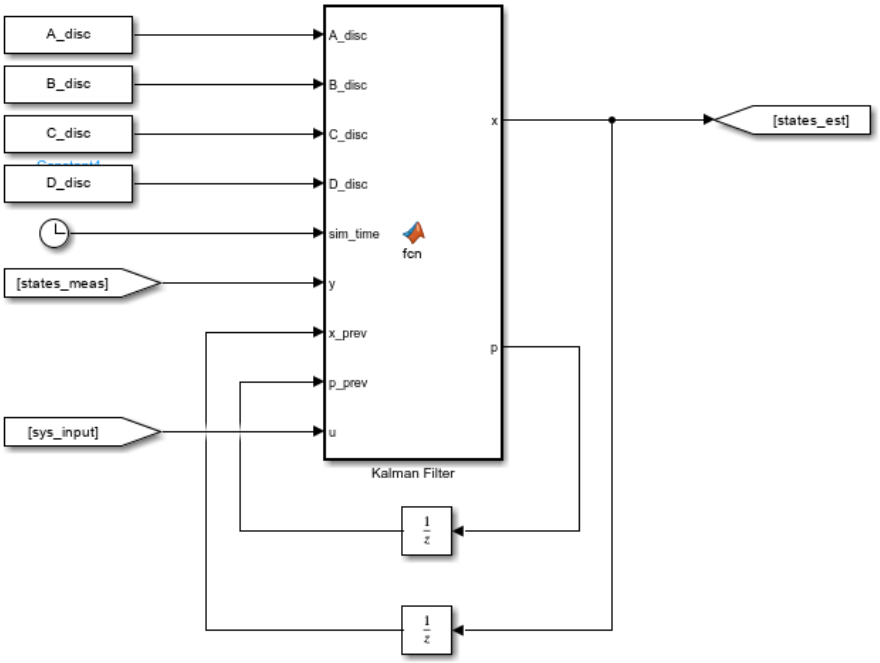


Figure 6.28. Kalman Filter for Estimation of Slung Load States

At this point, before going into the details of the simulation results with Kalman Filter, some discussion regarding the selection of Q and R matrices in the governing Kalman Filter equations (Equations (6.43)-(6.44)) will be provided in conjunction with the possible sensor noise and plant disturbance the system may be subjected to.

The Q and R matrices are the covariance matrices and they are determined based on the power spectral density of the plant disturbance and measurement noise respectively. In this study, these are injected to the system by utilizing 'band limited white noise' block of the Simulink. According to the related reference page of the block [34], user enters a noise power that represents the height of the power spectral density of the disturbance and the sample time utilized in the model simulation. The relation between the entered noise power and covariance can be approximated by the following identity:

$$Power = \sigma t_s \tag{6.47}$$

In Equation (6.47), σ represents the related covariance, whereas t_s is the sample time. Several simulations with the system of interest has shown that, slung load state estimation can be performed effectively for a measurement noise power of $10^{-6}\pi/180$ for the angular states of the helicopter. To be consistent among the units, 1 deg/s is assumed to be in the vicinity of 1 m/s and the measurement noise is determined as 10^{-6} for the linear velocity states of the helicopter. This yields that the corresponding elements of the diagonal covariance matrix R shall be obtained by using the simple identity given in Equation (6.47) with the utilized sample time of 1 millisecond as shown below:

$$R = \begin{bmatrix} 10^{-3} & 0 & 0 & 0 & 0 & 0 & 0 & 0 \\ 0 & 10^{-3} & 0 & 0 & 0 & 0 & 0 & 0 \\ 0 & 0 & 10^{-3}\frac{\pi}{180} & 0 & 0 & 0 & 0 & 0 \\ 0 & 0 & 0 & 10^{-3} & 0 & 0 & 0 & 0 \\ 0 & 0 & 0 & 0 & 10^{-3}\frac{\pi}{180} & 0 & 0 & 0 \\ 0 & 0 & 0 & 0 & 0 & 10^{-3}\frac{\pi}{180} & 0 & 0 \\ 0 & 0 & 0 & 0 & 0 & 0 & 10^{-3}\frac{\pi}{180} & 0 \\ 0 & 0 & 0 & 0 & 0 & 0 & 0 & 10^{-3}\frac{\pi}{180} \end{bmatrix} \quad (6.48)$$

The covariance matrix Q on the other hand is a diagonal matrix of size 14×14 with entries determined based on relation among the system states in the presence of plant disturbance. For accurate slung load state estimation, the related covariance is selected upon performing several simulations by taking the consistency between the units into account. In the finalized form, the diagonal elements corresponding to the helicopter linear velocities are chosen as 10^{-11}, whereas all the remaining elements are assigned as $10^{-11}\pi/180$.

This selection of matrices shows that the Kalman Filter should strongly depend on the process governed by the model instead of measurements for accurate state estimation.

Next, in order to evaluate the adequacy of the Kalman Filter, the simulations performed with delayed feedback control and cable angle rate feedback control are repeated and results are compared to the system with full state output.

6.5.1 Simulation Results with Kalman Filter and Delayed Feedback Control

Simulation results with the Kalman filter and the delayed feedback controllers designed in Section 6.3 are provided in the following figure. In the same figure, the slung load states obtained with full-state output are provided as well in order to evaluate the adequacy of the Kalman Filter. It should be noted that no measurement noise or plant disturbance is injected to the system at this stage. Kalman Filter's capability of slung load state estimation in the presence of noise and disturbance will be discussed under a separate section in 6.5.3.

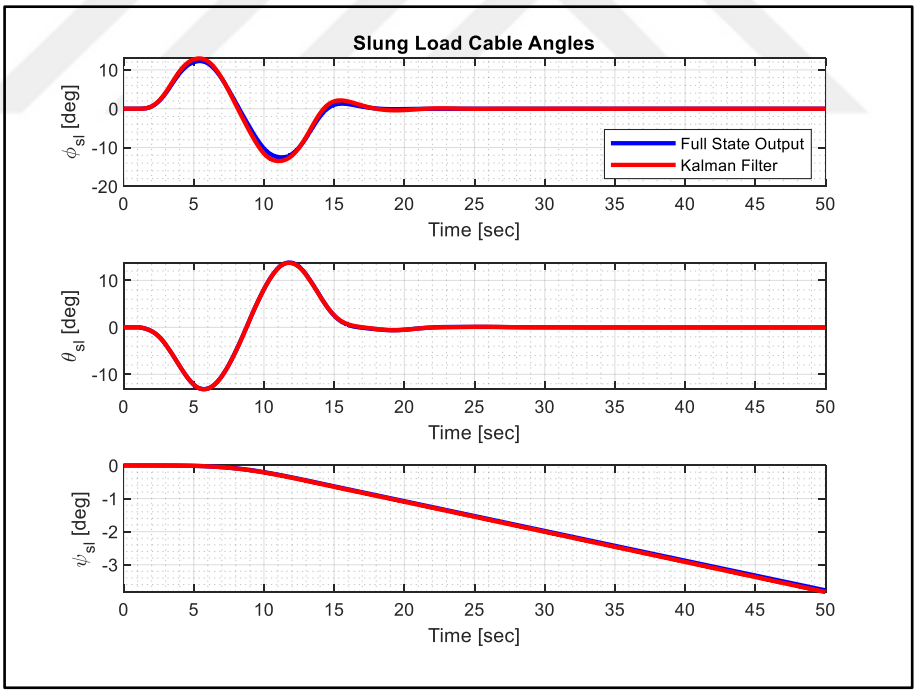


Figure 6.29. Simulation Results with Delayed Feedback Controllers and Kalman Filter

From Figure 6.29, it can be seen that cable angles obtained by feeding back the estimated states show very close trend to the full state output case, which indicates the Kalman Filter is capable of performing accurate estimation. Hence, the estimated states can indeed be utilized for feedback applications so that sustained slung load oscillations are damped out.

6.5.2 Simulation Results with Kalman Filter and Cable Angle Rate Feedback controllers

Similar to the previous case discussed just above, the simulation results with the Kalman Filter and the cable angle rate feedback controllers discussed in section 6.4 are provided in the following figure in a superimposed manner with full-state output case in the absence of measurement noise and plant disturbance:

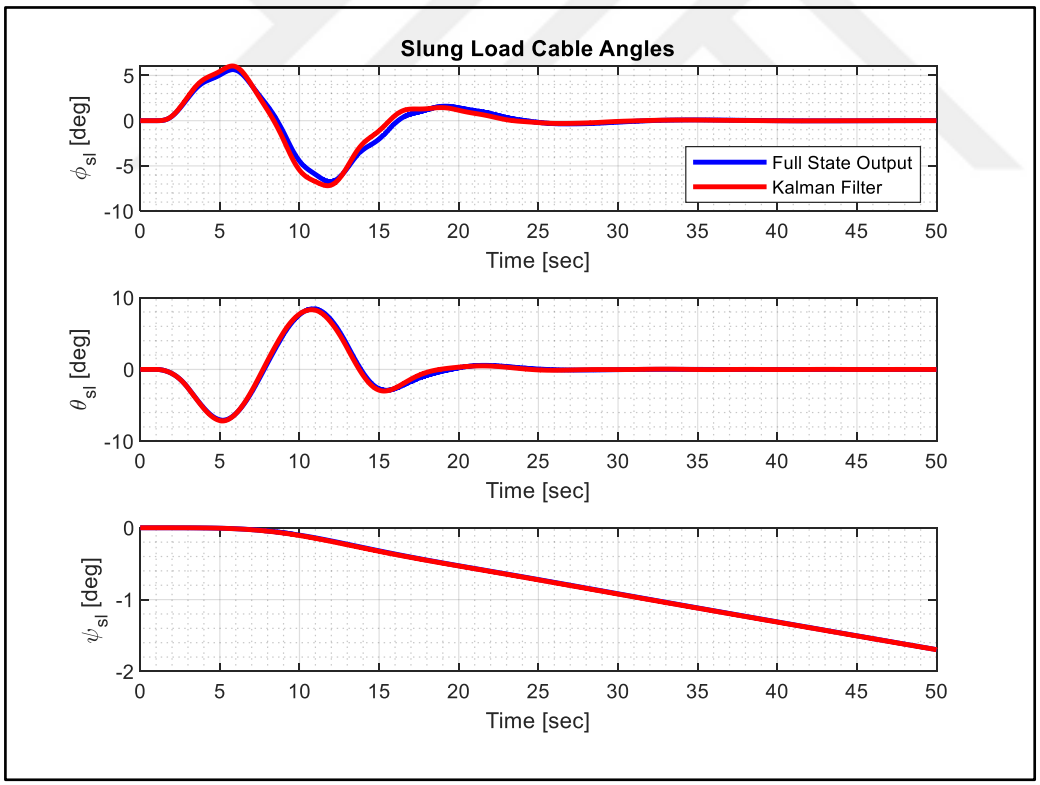


Figure 6.30. Simulation Results with Cable Angle Rate Feedback Controllers and Kalman Filter

From Figure 6.29, it can be seen that cable angles obtained by feeding back the estimated states show very close trend to the full state output case, which indicates that the adequacy of the Kalman in terms of estimating the overall slung load dynamics is satisfactory as in the case of delayed feedback controller. Hence, the estimated states can indeed be used for feedback applications to eliminate sustained slung load oscillations.

6.5.3 Kalman Filter Performance Evaluation

In Sections 6.5.1 and 6.5.2, it was discussed that the proposed Kalman Filter is capable of estimating the load states satisfactorily. However, in real life applications, sensor noises and system disturbances are likely to exist. In addition, there may be deviations between the real-life plant and the one used for Kalman Filter design. Hence, in order to investigate the performance characteristics of the proposed Kalman Filter an additional case study is performed. The noise is injected to the measured helicopter states through the Simulink's band limited white noise block as it is discussed in section 6.5 by taking the units of the states into account. The peak value of the applied noise to the linear velocity states is around 1 m/s. The same noise applied to the angular states by scaling it down with $\pi/180$ considering their units are radians and radians per second. Following figure illustrates the injected measurement noise to the linear velocities:

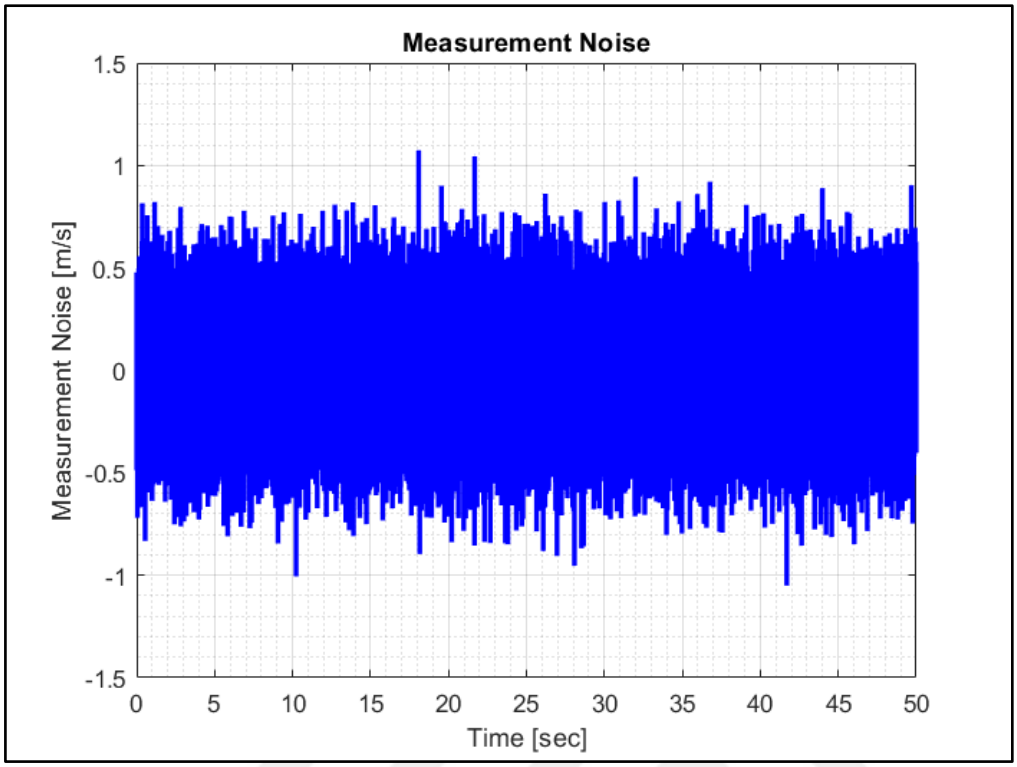


Figure 6.31. Measurement Noise Injected to Linear Velocity States

For the plant disturbance on the other hand, a plant model different from the one used in the Kalman Filter design is utilized in the simulation. In order to prevent excessive deviation from the model used in Kalman Filter design, the following discrepancies are evaluated as reasonable:

- The plant is linearized with helicopter mass and inertia values increased by 5%
- The plant is linearized with the slung load mass is 1000 kg greater than the original case.
- The plant is linearized by taking the distance between the helicopter attachment point and slung load center of gravity as 8.62 meters instead of 7.62 meters (25 ft.).

In order to illustrate the degree of inconsistency between the linearized models, following pole locations map is provided:

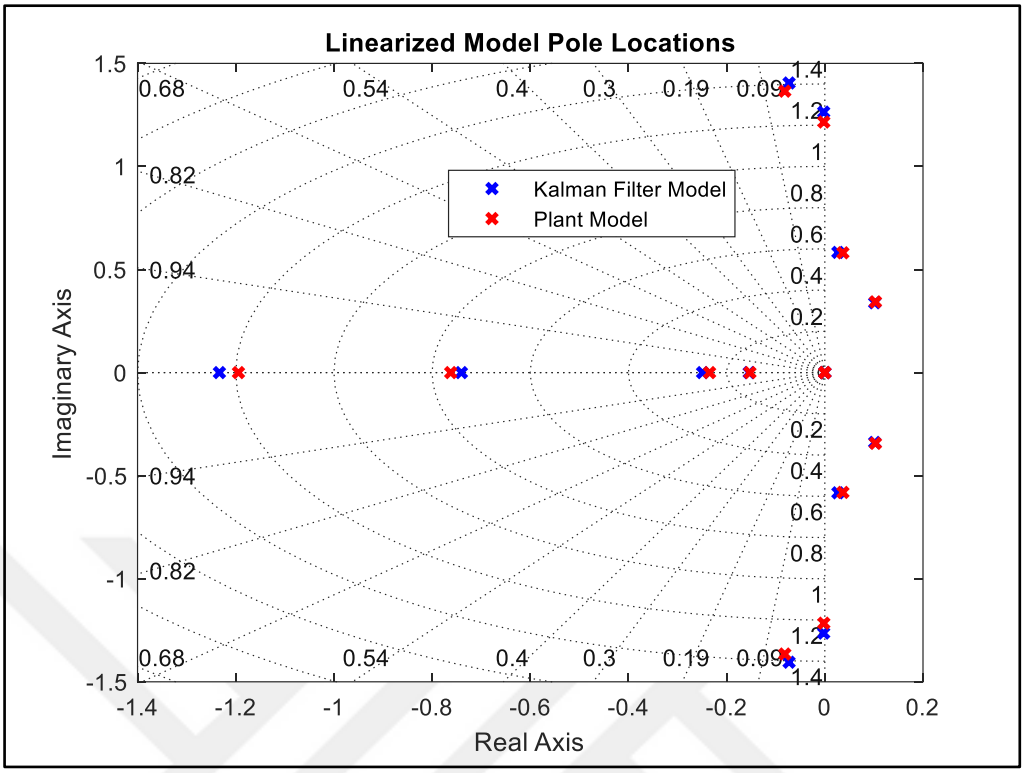


Figure 6.32. Pole Locations of the Linearized Models

From Figure 6.32, it can be seen that even though it is not remarkable, there is certain amount of difference among the pole locations of the linear models of concern, resulting from the aforementioned discrepancies.

Simulation results with the measurement noise and linear model inconsistency described above are illustrated in the following figure for the cable angle rate feedback controller case discussed in section 6.5.2 but it should be noted that similar outcomes are obtained for the delayed feedback controller case as well.

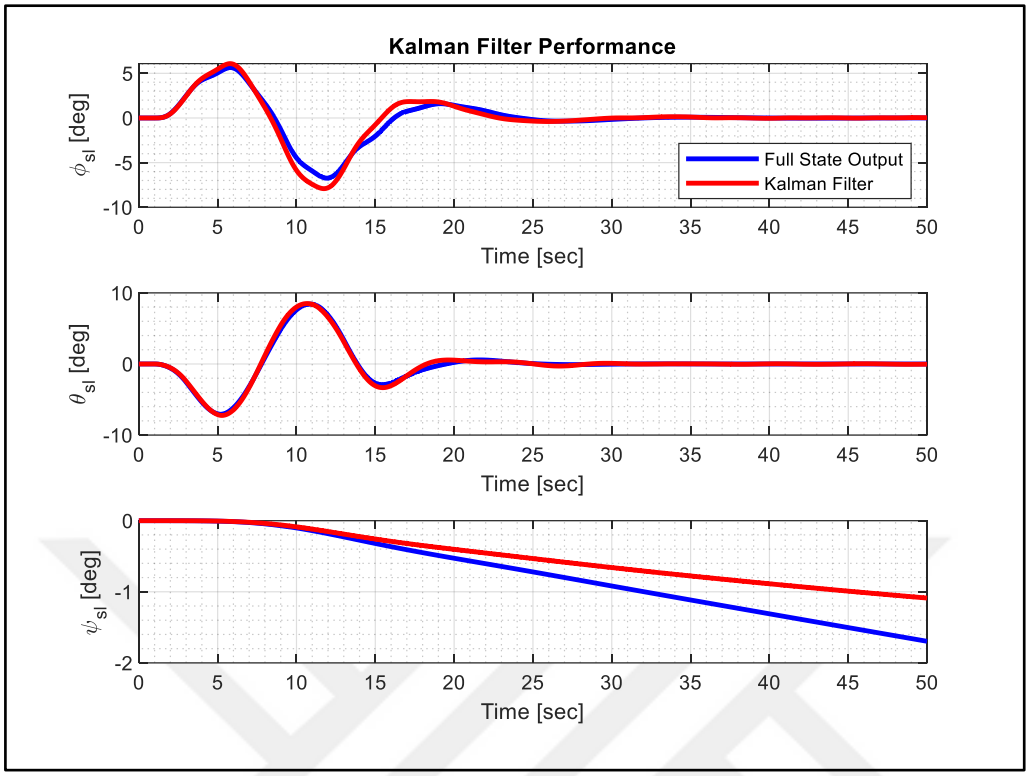


Figure 6.33. Kalman Filter Performance in the Presence of Noise and Disturbance

From Figure 6.33, it can be seen that the performance of the Kalman Filter is slightly degraded compared to the previous cases, which did not include measurement noise and model discrepancy. That is, longitudinal and lateral cable angles obtained in the presence of Kalman Filter deviates visibly from the full state output case. Also, there is certain amount of discrepancy in the slung load yaw angle as well. However, considering that magnitudes of these inconsistencies are obviously small and overall trend in all the states are captured accurately, it can be asserted that the Kalman Filter functions properly in terms of state estimation.

This particular case study shows that the proposed Kalman Filter is able to provide reliable state estimation in the presence of measurement noise and model discrepancy. These estimated states can be utilized for the feedback control applications to damp out undesirable oscillatory load motion discussed so far.

6.6 Slung Load Control Strategy Comparison

In this section, a comparison regarding the previously proposed slung load control strategies will be provided based on the slung load oscillation damping performance. To do so, the same compound mathematical model consisting of the helicopter and slung load are simulated with three separate controllers and the results are provided in a superimposed manner. The input profiles for the simulations are identical to those given in Figure 6.2. Following figure illustrates the comparative results with the controllers discussed in the previous sections:

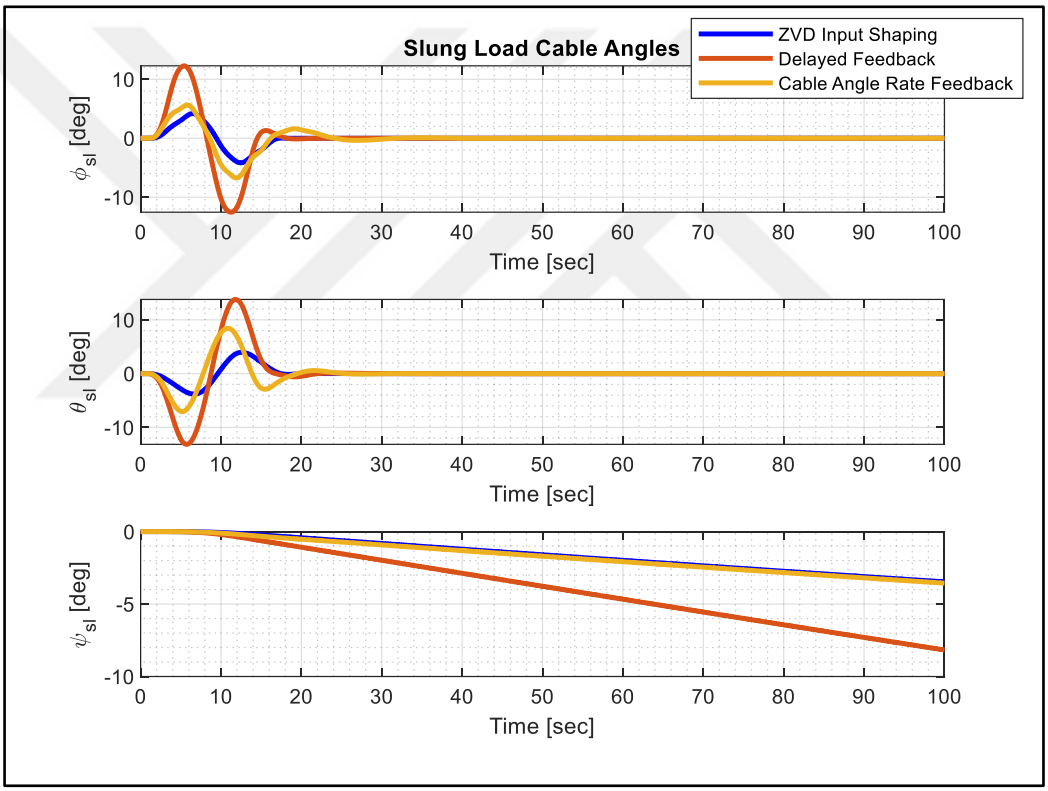


Figure 6.34 Comparison of Slung Load Control Strategies

From Figure 6.34, it can be seen that input shaping and delayed feedback yields faster damping compared to the cable angle rate feedback controller. However, it can also be observed that the peak amplitudes of the oscillations in the longitudinal and lateral axes are remarkably greater in the case of delayed feedback controller. The amplitude of the deviation in the yaw angle is greater for this particular controller as

well. Considering that it results in a very fast sustained oscillation damping without inducing excessive peak amplitudes, ZVD input shaping is regarded as the most viable option.

It should be noted that, even though input shaping provides very promising results regarding the load oscillation damping, it is susceptible to outside effects. That is, the command filter coefficients and time delays are determined purely based on the natural frequency and damping ratio of the respective poles of the system. If the oscillations characteristics are altered in the presence of an arbitrary disturbance, then the input shaping method can become ineffective in obtaining an oscillation-free response. To remedy this problem, the input shaping will be combined with model predictive control as it will be discussed in the next section.

6.7 Model Predictive Control of Slung Load System

Before going into the further details of implementation of model predictive control on slung load control, some theoretical background on this particular subject will be provided in the following section.

6.7.1 Theoretical Background for Model Predictive Control

Model predictive control is an optimal control technique in which the calculated control actions minimize a cost function for a constrained or unconstrained system over a finite, receding horizon [35].

In model predictive control, at each sampling instant, the current input-output measurements and states of the plant along with the model of the plant are utilized to compute a future control sequence that optimizes a predetermined performance index over a finite horizon. The optimization process can be constrained or unconstrained depending on the application of concern.

It should be noted that according to this particular control algorithm, only the first computed control action is applied to the plant and rest are disregarded. At the following time steps the same procedure is repeated [36].

It is worth to mention that MPC algorithm can be applied to both the continuous and discrete time systems [36]. However, given that it yields an easier and less complicated implementation, discrete time MPC algorithm will be utilized in this study. That is, the necessary control action at each simulation time step will be calculated and fed to the system. As it will be discussed later on, MPC will be integrated to the already existing flight control system as the outermost control loop.

A general schematic regarding the MPC strategy is provided in the following figure:

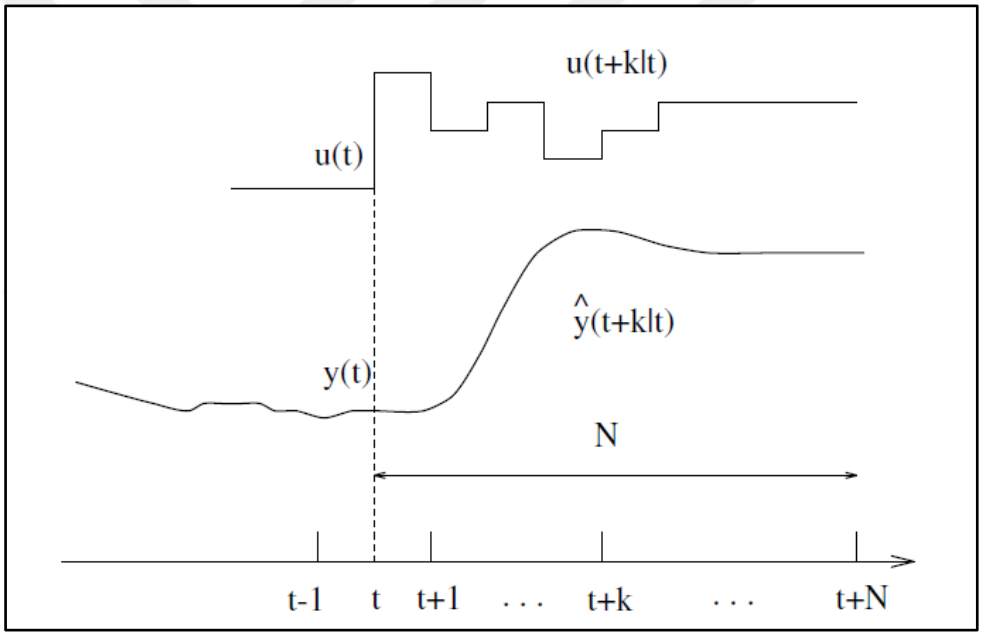


Figure 6.35. MPC Strategy [37]

Figure 6.35 needs some further elaboration regarding the related parameters of MPC. The future outputs for a determined horizon N, which is called as the prediction horizon, are predicted at each instant t using the plant model. These predicted outputs $y(t+k|t)$ for $k = 1 \ldots N$ depend on the known values up to instant t (past inputs and outputs) and on the future control signals $u(t+k|t), k = 0 \ldots N-1$, which are to be computed based on optimization. It should be noted that $(t+k|t)$ denotes the

value of the related parameter at the instant $t + k$ calculated at instant t. At this point it should be addressed that there is another MPC parameter called control horizon which is denoted by V and it is the horizon over which the control inputs are allowed to change. Even though in Figure 6.35, this parameter is not explicitly shown, V is generally less than N, although it can be equal to N as well. The developed MPC algorithm takes both of these options into account.

The set of future control signals is calculated by optimizing a predetermined cost function to keep the process as close as possible to the reference trajectory. This criterion usually takes the form of a quadratic function of the errors between the predicted output signal and the reference trajectory. In most cases, the control effort is also included in the related cost function to prevent occurrence of excessive and unrealistic input values.

The control signal $u(t|t)$ is sent to the process whilst rest of the calculated control signals are disregarded as mentioned previously. After applying $u(t|t)$ as the input to the plant, the computation procedure is repeated to determine $u(t + 1|t + 1)$.

Overall block diagram of the MPC algorithm is illustrated in the following figure:

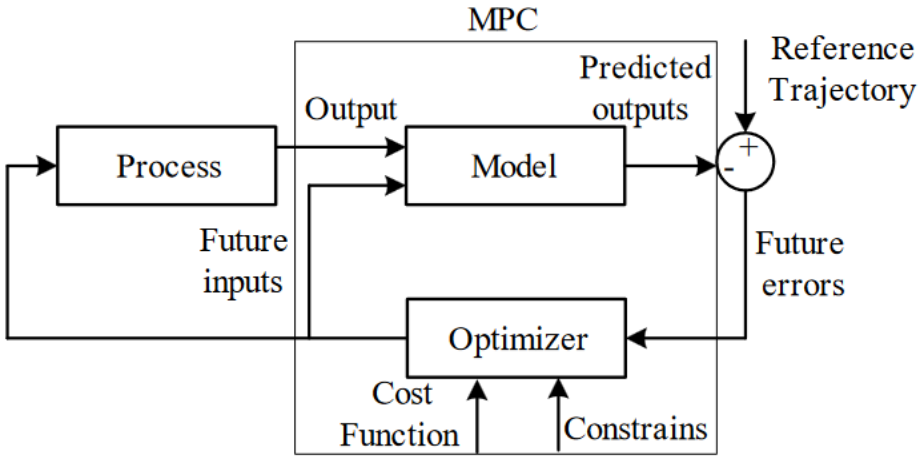


Figure 6.36. Block Diagram for MPC Algorithm [38]

In the remainder of this section, derivation of the MPC algorithm will be provided. Given that discrete time MPC algorithm will be implemented, the first thing that one

needs to obtain is the discrete time state space model of the plant to be controlled. The required model can be calculated by discretization of the already available continuous time state space model. Necessary discretization procedure is identical to the one given in the Kalman Filter design in Section 6.4. That is, by using zero order hold method and MATLAB's "c2d" function the discretized state space model can be written as follows:

$$x_{t+1} = Ax_t + Bu_t \tag{6.49}$$

$$y_t = Cx_t \tag{6.50}$$

Equations (6.49) and (6.50) can be used to predict the outputs at the successive time instances up to $t + N$. To start with, at time instant t, following identities can be written to determine the predicted outputs at time instant $t + 1$:

$$x_{t+1|t} = Ax_t + Bu_{t|t} \tag{6.51}$$

$$y_{t+1|t} = Cx_{t+1|t} = CAx_t + CBu_{t|t} \tag{6.52}$$

Then, equations (6.51) and (6.52) can be used to write the state and output equations at time instant $t + 2$ as shown below:

$$x_{t+2|t} = Ax_{t+1|t} + Bu_{t+1|t} = A^2x_t + ABu_{t|t} + Bu_{t+1|t} \tag{6.53}$$

$$y_{t+2|t} = Cx_{t+2|t} = CA^2x_t + CABu_{t|t} + CBu_{t+1|t} \tag{6.54}$$

Upon continuation on this procedure, one can obtain the following identity for the predicted output at time instant $t + N$ calculated at time instant t:

$$y_{t+N|t} = CA^N x_t + \begin{bmatrix} CA^{N-1}B & CA^{N-2}B & CA^{N-3}B & \cdots & CA^{N-V}B \end{bmatrix} \begin{bmatrix} u_{t|t} \\ u_{t+1|t} \\ u_{t+2|t} \\ \vdots \\ u_{t+V-1|t} \end{bmatrix} \tag{6.55}$$

All the prediction equations can be combined into a single one within a matrix format as shown below:

$$\begin{bmatrix} y_{t+1|t} \\ y_{t+2|t} \\ y_{t+3|t} \\ \vdots \\ y_{t+N|t} \end{bmatrix} = \begin{bmatrix} CA \\ CA^2 \\ CA^3 \\ \vdots \\ CA^N \end{bmatrix} x_t + \begin{bmatrix} CB & 0 & 0 & \dots & \dots \\ CAB & CB & 0 & \dots & \dots \\ CA^2B & CAB & CB & \dots & \dots \\ \vdots & \vdots & \vdots & \dots & \dots \\ CA^{N-1}B & CA^{N-2}B & CA^{N-3}B & \dots & CA^{N-V}B \end{bmatrix} \begin{bmatrix} u_{t|t} \\ u_{t+1|t} \\ u_{t+2|t} \\ \vdots \\ u_{t+V-1|t} \end{bmatrix} \tag{6.56}$$

Equation (6.56) can be rewritten in a more compact form as shown below:

$$\underline{y} = Fx_t + \Phi \underline{u} \tag{6.57}$$

The quantities in Equation (6.57) are summarized in the following set of equations:

$$\underline{y} = \begin{bmatrix} y_{t+1|t} \\ y_{t+2|t} \\ y_{t+3|t} \\ \vdots \\ y_{t+N|t} \end{bmatrix} \tag{6.58}$$

$$F = \begin{bmatrix} CA \\ CA^2 \\ CA^3 \\ \vdots \\ CA^N \end{bmatrix} \tag{6.59}$$

$$\Phi = \begin{bmatrix} CB & 0 & 0 & \dots & \dots \\ CAB & CB & 0 & \dots & \dots \\ CA^2B & CAB & CB & \dots & \dots \\ \vdots & \vdots & \vdots & \dots & \dots \\ CA^{N-1}B & CA^{N-2}B & CA^{N-3}B & \dots & CA^{N-V}B \end{bmatrix} \tag{6.60}$$

$$\underline{u} = \begin{bmatrix} u_{t|t} \\ u_{t+1|t} \\ u_{t+2|t} \\ \vdots \\ u_{t+V-1|t} \end{bmatrix} \tag{6.61}$$

In order to formulate the model predictive control algorithm, a reference trajectory should be defined as shown in the following equation:

$$\bar{y}^d = \begin{bmatrix} y_{t+1}^d \\ y_{t+1}^d \\ \vdots \\ y_{t+N}^d \end{bmatrix} \tag{6.62}$$

Then, to formulate the optimization problem, a quadratic cost function can be defined by taking the difference between the reference trajectory and predicted outputs as well as the control effort into account:

$$J = \left(\underline{y}^d - \underline{y}\right)^T Q\left(\underline{y}^d - \underline{y}\right) + \underline{u}^T R\underline{u} \tag{6.63}$$

In Equation (6.63), Q is a real, symmetric and positive semi-definite weighting matrix consisting of symmetric submatrices $(Q_k, k = 1,2 \dots N)$ that penalize the deviation from the desired trajectory at the successive time instances. Hence, Q matrix can be written as shown in the following identity:

$$Q = \begin{bmatrix} Q_1 & 0 & 0 & \dots & 0 \\ 0 & Q_2 & 0 & \dots & 0 \\ \dots & \dots & \ddots & \dots & \dots \\ 0 & 0 & 0 & \dots & Q_N \end{bmatrix} \tag{6.64}$$

Similarly, R in Equation (6.63) is a real, symmetric and positive definite matrix containing symmetric submatrices $(R_k, k = 0,1,2, \dots, V-1)$ that penalizes the control effort. This yields that R can be written in the following format:

$$R = \begin{bmatrix} R_0 & 0 & 0 & \dots & 0 \\ 0 & R_1 & 0 & \dots & 0 \\ \dots & \dots & \ddots & \dots & \dots \\ 0 & 0 & 0 & \dots & R_{V-1} \end{bmatrix} \tag{6.65}$$

Therefore, the cost function given in (6.63), can be written in the expanded form as shown below:

$$\begin{aligned} J = {} & \left(y^d_{t+1|t} - y_{t+1|t}\right)^T Q_1 \left(y^d_{t+1|t} - y_{t+1|t}\right) \\ & + \left(y^d_{t+2|t} - y_{t+2|t}\right)^T Q_2 \left(y^d_{t+2|t} - y_{t+2|t}\right) + \cdots \\ & + \left(y^d_{t+N|t} - y_{t+N|t}\right)^T Q_N \left(y^d_{t+N|t} - y_{t+N|t}\right) + u^T_{t|t} R_0 u_{t|t} \\ & + u^T_{t+1|t} R_1 u_{t+1|t} + u^T_{t+2|t} R_2 u_{t+2|t} + \cdots \\ & + u^T_{t+V-1|t} R_{V-1} u_{t+V-1|t} \end{aligned} \tag{6.66}$$

To formulate the MPC algorithm further, expression for the desired trajectory given in Equation (6.57), should be substituted into (6.63):

$$J = \left(\underline{y}^d - Fx_t - \Phi\underline{u}\right)^T Q\left(\underline{y}^d - Fx_t - \Phi\underline{u}\right) + \underline{u}^T R\underline{u} \tag{6.67}$$

For convenience, following substitution can be made in Equation (6.67):

$$\underline{z} = \underline{y}^d - Fx_t \tag{6.68}$$

Then, Equation (6.67) can be rewritten as follows:

$$J = (\underline{z} - \Phi\underline{u})^T Q(\underline{z} - \Phi\underline{u}) + \underline{u}^T Ru \tag{6.69}$$

The MPC algorithm can be formulated as finding the optimal control input that minimizes the cost function given in Equation (6.69):

$$\underline{u}^{opt} = \min_{\underline{u}}[(\underline{z} - \Phi\underline{u})^T Q(\underline{z} - \Phi\underline{u}) + \underline{u}^T Ru] \tag{6.70}$$

To perform the optimization procedure, Equation (6.70) is expanded as shown below:

$$J = z^T Qz - \underline{z}^T Q\Phi\underline{u} - \underline{u}^T\Phi^T Q\underline{z} + \underline{u}^T\Phi^T Q\Phi\underline{u} + \underline{u}^T R\underline{u} \tag{6.71}$$

In order to find the control input that minimizes the cost function given in Equation (6.71), one needs to take the first derivative of the scalar expression in (6.71) with respect to the control input vector $\underline{u}$ and then equate it to zero [36]:

$$\frac{\partial J}{\partial \underline{u}} = \frac{\partial(\underline{z}^T Qz)}{\partial \underline{u}} - \frac{\partial(\underline{z}^T Q\Phi\underline{u})}{\partial \underline{u}} - \frac{\partial(\underline{u}^T\Phi^T Qz)}{\partial \underline{u}} + \frac{\partial(\underline{u}^T\Phi^T Q\Phi\underline{u})}{\partial \underline{u}} + \frac{\partial(\underline{u}^T R\underline{u})}{\partial \underline{u}} \tag{6.72}$$

Calculating the derivative of each individual term on the right-hand side of equation leads to the following:

$$\frac{\partial J}{\partial \underline{u}} = -\Phi^T Q\underline{z} - \Phi^T Q\underline{z} + 2\Phi^T Q\Phi\underline{u} + 2R\underline{u} \tag{6.73}$$

Setting Equation (6.73) to zero leads to the following:

$$-2\Phi^T Q\underline{z} + 2\Phi^T Q\Phi\underline{u} + 2R\underline{u} = 0 \rightarrow (\Phi^T Q\Phi + R)u = \Phi^T Qz \tag{6.74}$$

Finally, the optimal solution for the model predictive control scheme becomes the following:

$$\underline{u}^{opt} = (\Phi^T Q \Phi + R)^{-1} \Phi^T Q \underline{z} = (\Phi^T Q \Phi + R)^{-1} \Phi^T Q \left(\underline{y}^d - F x_t\right) \qquad (6.75)$$

It is worthwhile to note that, only the first entry of the optimal control $\underline{u}_{opt}$ is applied to the system at the instant t, that is $\underline{u}_{t|t}^{opt}$. Then at the next time instant, $t+1$, the optimization procedure will be carried out again to determine $\underline{u}_{t+1|t+1}^{opt}$.

It should be noted that the MPC algorithm described above is for unconstrained problems. As mentioned previously, it is possible to optimize the related cost function of concern to find the optimal input while satisfying certain constraints imposed by the requirements of the application, such as control input limitations.

As far as the slung load application of MPC is concerned, the applicable constraints are the control margins of the helicopter inputs, namely the collective, longitudinal and lateral cyclic and pedal. However, applying unconstrained MPC has shown that there is no violation regarding these limits with a proper choice of reference trajectory. In addition, the resultant optimal control inputs cause no excessive helicopter attitude that may result in uncomfortable flight characteristics for the pilots. Hence, the algorithm described above is evaluated as adequate for the control of the slung load system.

6.7.2 Application of Model Predictive Control on Slung Load System

In this section, application of the model predictive control on the slung load system will be discussed.

Model predictive control algorithm is implemented as the outermost control loop to the existing closed loop plant consisting of helicopter, slung load and flight control system. The block diagram of the proposed system is provided in the following figure:

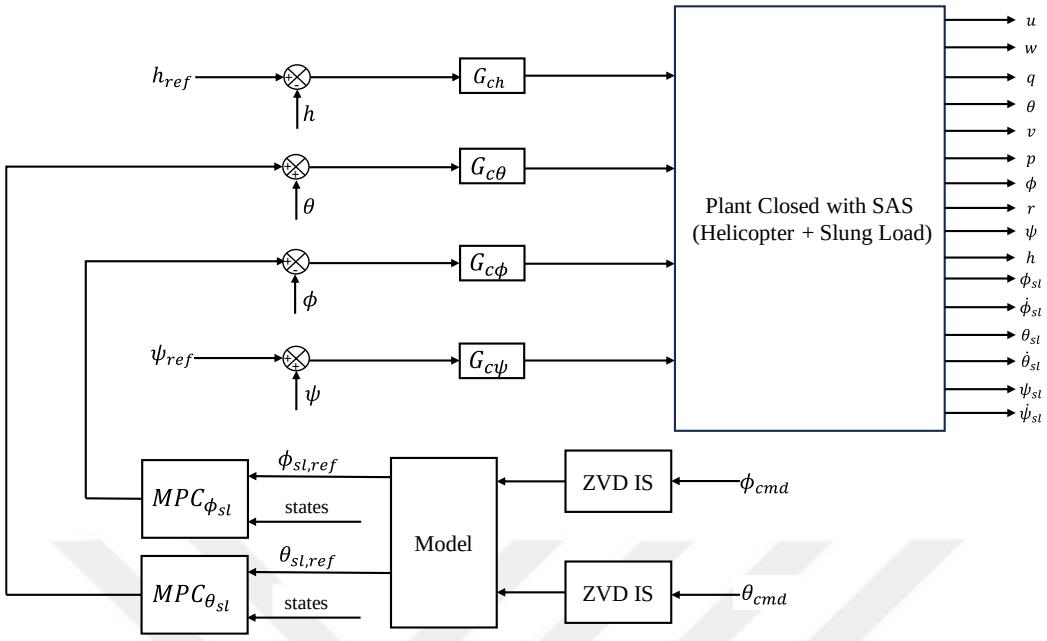


Figure 6.37. Block Diagram of the Closed Loop System with MPC

In Figure 6.37, $MPC_{\theta_{sl}}$ and $MPC_{\phi_{sl}}$ denote the model predictive controllers in the longitudinal and lateral channels respectively.

In order to design model predictive controllers, suitable reference trajectories that yield oscillation free motion for the slung load should be determined and integrated to the respective MPC algorithm.

According to the previous discussion given in Section 6.2.2, reference commands that were modified with ZVD input shaping yielded slung load trajectories without sustained oscillations. Hence, in this section, previously obtained longitudinal and lateral slung load cable angles with ZVD input shaping are chosen as the reference trajectories. In real-life applications, these trajectories can be obtained as the response of the closed loop model with ZVD input shapers illustrated in Figure 6.12, which is the process described in Figure 6.37.

In the overall system there will be two separate SISO model predictive controllers. One will be using the longitudinal slung load cable angle as the reference trajectory and the calculated optimal input will be the new reference pitch attitude command. Similarly, for the second controller lateral slung load cable angle will be the

reference trajectory and the computed optimal input profile will be the reference roll attitude command. The reason behind this is that, the closed loop system is quite complicated considering the augmented states of the previously discussed PID controllers. Hence, simplifying the overall system for model predictive controllers will ease the computational burden. These additional controllers will be integrated as separate function blocks to the original closed loop Simulink model.

Then, for MPC algorithm the first practice will be to obtain the state space representation of the SISO systems from the reference pitch angle to the longitudinal slung load cable angle and reference roll angle to the lateral slung load cable angle respectively. This can be accomplished by keeping the full state matrix of the closed loop system containing the flight control system and truncating the irrelevant columns of the input matrix. The output matrix will be the single row matrix that include the related state of concern and finally the feedthrough matrix will be zero as in the case of original system. Once the continuous state space representations of the respective SISO systems are obtained, they are discretized to be used in the MPC algorithm as it was discussed in detail in the previous section. As before, discretization is performed by using MATLAB's "c2d" function with zero order hold approach. The discrete state space representations of the SISO systems of concern can be summarized as shown below:

$$x_{t+1} = Ax_t + B_{\theta_{sl}} u_t \tag{6.76}$$

$$y_{\theta_{sl}}{}_t = C_{\theta_{sl}} x_t \tag{6.77}$$

$$x_{t+1} = Ax_t + B_{\phi_{sl}} u_t \tag{6.78}$$

$$y_{\phi_{sl}}{}_t = C_{\phi_{sl}} x_t \tag{6.79}$$

As it is apparent from the convention used, Equations (6.76) and (6.77) represent the SISO longitudinal slung load cable angle dynamics whereas Equations (6.78) and (6.79) are for the SISO lateral slung load cable angle dynamics. The required time step for discretization is selected as 0.001 seconds as in the case of Kalman Filter

design for estimation of the slung load states. Overall continuous system dynamics can be effectively captured with this particular value.

In order to implement MPC as the outermost control loop, the states of the closed loop system with already existing flight control system should be obtained. It should be noted that states of the helicopter and the dynamic controllers represented in Section 4 can be measured as a common practice and states of the slung load can be effectively estimated as it is discussed in detail in Section 6.5.

Once the states of the system of concern are completely obtained, the MPC algorithm described in the previous section can be implemented. As it was stated previously, the necessary reference trajectories are selected as the longitudinal and lateral slung load cable angle time histories obtained from the simulation with ZVD input shaper discussed in section 6.2.2. For convenience, these trajectories are re-illustrated in the following figure:

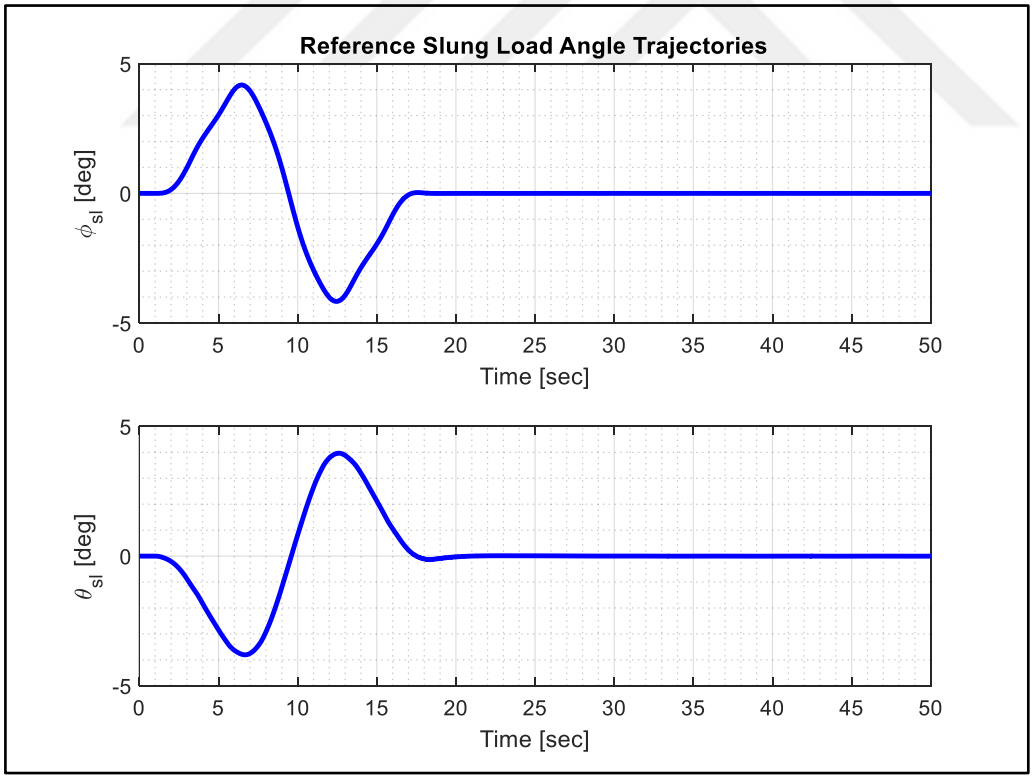


Figure 6.38. Reference Slung Load Trajectories

It should be noted that the original duration was 100 seconds. However, given that the oscillations die out very efficiently in a short period of time, 50 seconds of simulation time assigned as adequate regarding the MPC implementation.

As it was discussed in the previous section, there are certain additional parameters required for the MPC algorithm. These are the prediction and control horizons and weighting matrices of the cost function to be minimized. These values are determined based on an educational guess at the initial phase and several performed simulations later on. Following are the finalized values and as it will be shown they yield satisfactory results.

$$N = 25 \tag{6.80}$$

$$V = 20 \tag{6.81}$$

$$Q = \begin{bmatrix} 1000 & 0 & 0 & \dots & 0 \\ 0 & 1000 & 0 & \dots & 0 \\ \dots & \dots & \ddots & \dots & \dots \\ 0 & 0 & 0 & \dots & 1000 \end{bmatrix} \tag{6.82}$$

$$R = \begin{bmatrix} 10^{-5} & 0 & 0 & \dots & 0 \\ 0 & 10^{-6} & 0 & \dots & 0 \\ \dots & \dots & \ddots & \dots & \dots \\ 0 & 0 & 0 & \dots & 10^{-6} \end{bmatrix} \tag{6.83}$$

It should be noted that, as it can be seen from Equations (6.82) and (6.83), the penalization on the input vector is significantly small compared to that on the discrepancy between the slung load cable angles and reference trajectories. The reason is that, according to the various simulation results, small penalization on the input vector does not lead to excessive input values and giving more importance to the reference trajectory tracking is appropriate as far as the slung load control is concerned.

Given that all the necessary quantities regarding the MPC algorithm are obtained, the system can be simulated. In the first simulation to be represented, the Kalman Filter that estimates the slung load states is removed from the system and it is assumed that all the states are available to evaluate the sufficiency of the proposed

model predictive controllers with an ideal case. The related results are provided in the following figure:

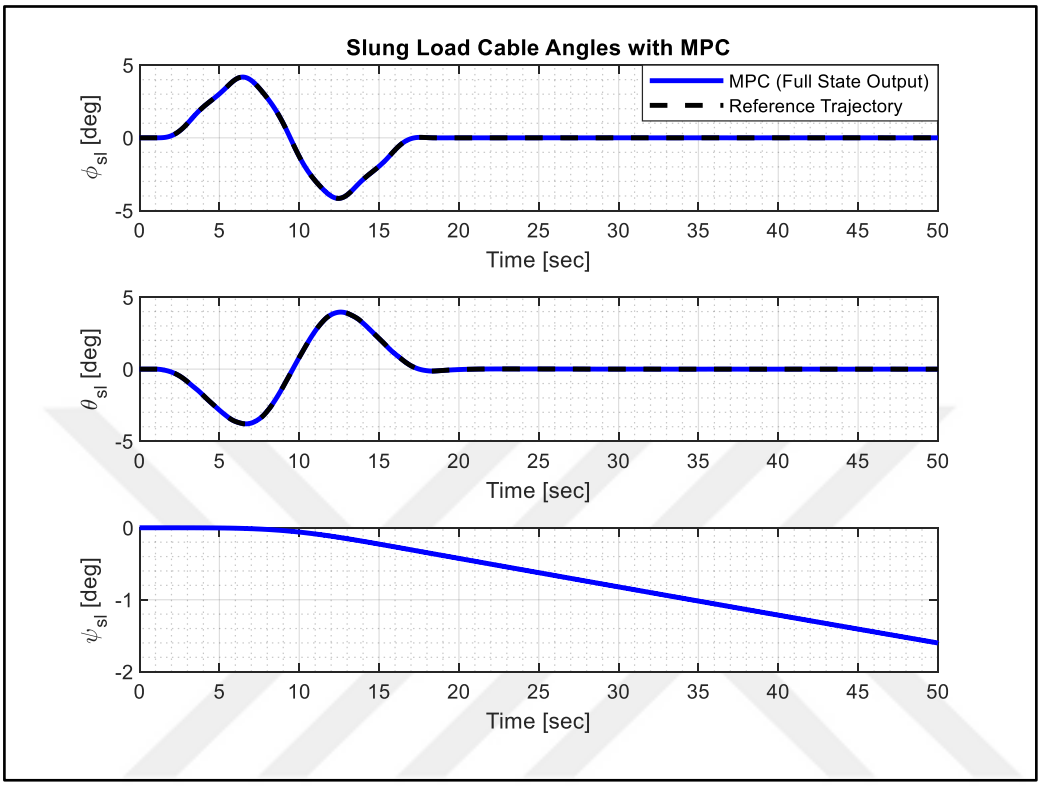


Figure 6.39. Slung Load Cable Angles with MPC and Full-State Output

From Figure 6.39, it can be seen that the slung load cable angles obtained from the simulation with the proposed model predictive control algorithm agrees perfectly well with the given reference trajectories. In fact, there is almost no noticeable difference. In addition, the slung load yaw angle shows a slightly divergent behavior, which is reasonable and consistent with the discussions provided under the previously mentioned control strategies.

Considering that the desired slung load trajectories are obtained through the modified reference pitch and roll attitudes and the reference trajectories determined based on ZVD input shaping, it is expected that the reference helicopter pitch and roll attitudes of the system with MPC should be close to the input shaped reference commands

given in Figure 6.13. The comparison between the two can be seen in the following figure:

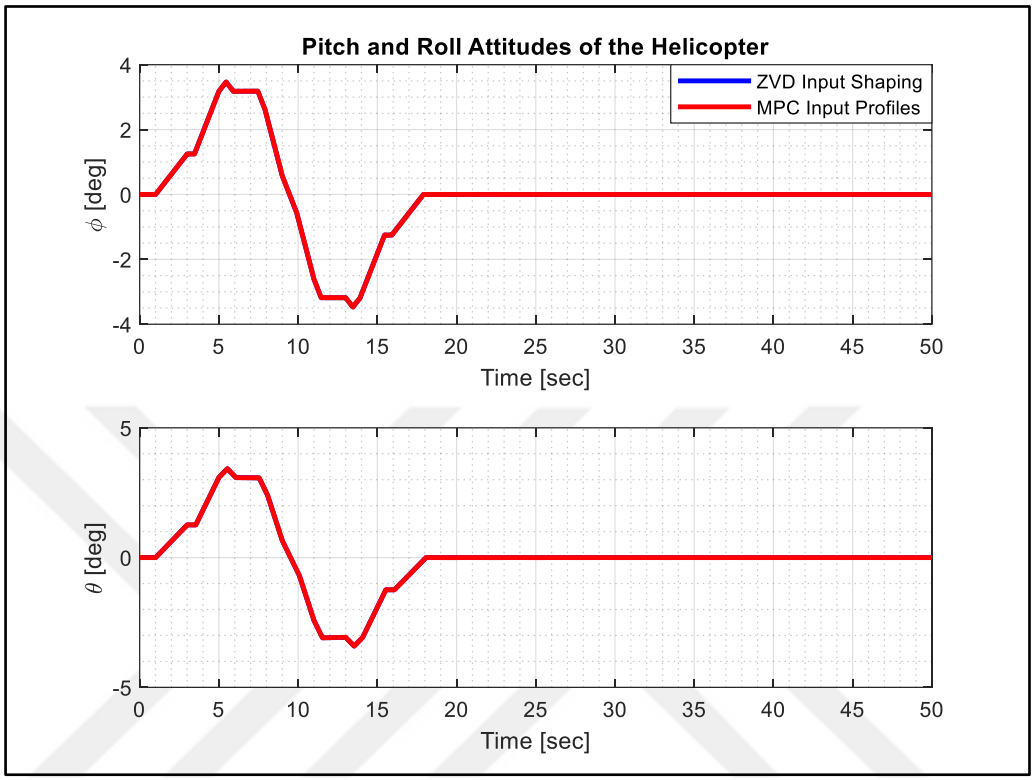


Figure 6.40. Helicopter Reference Roll and Pitch Attitudes with MPC

From Figure 6.40, it can be seen that there is no noticeable difference between the input shaped commands and the reference commands obtained through model predictive control algorithm, which is the expected outcome.

Next, the Kalman Filter is integrated to the overall system to observe whether the proposed model predictive control algorithm is capable of functioning properly with estimated slung load states. It should be noted that no disturbance or measurement noise is introduced at this stage. Following figure illustrates the simulation results in a superimposed manner with those obtained from full state output case discussed just above.

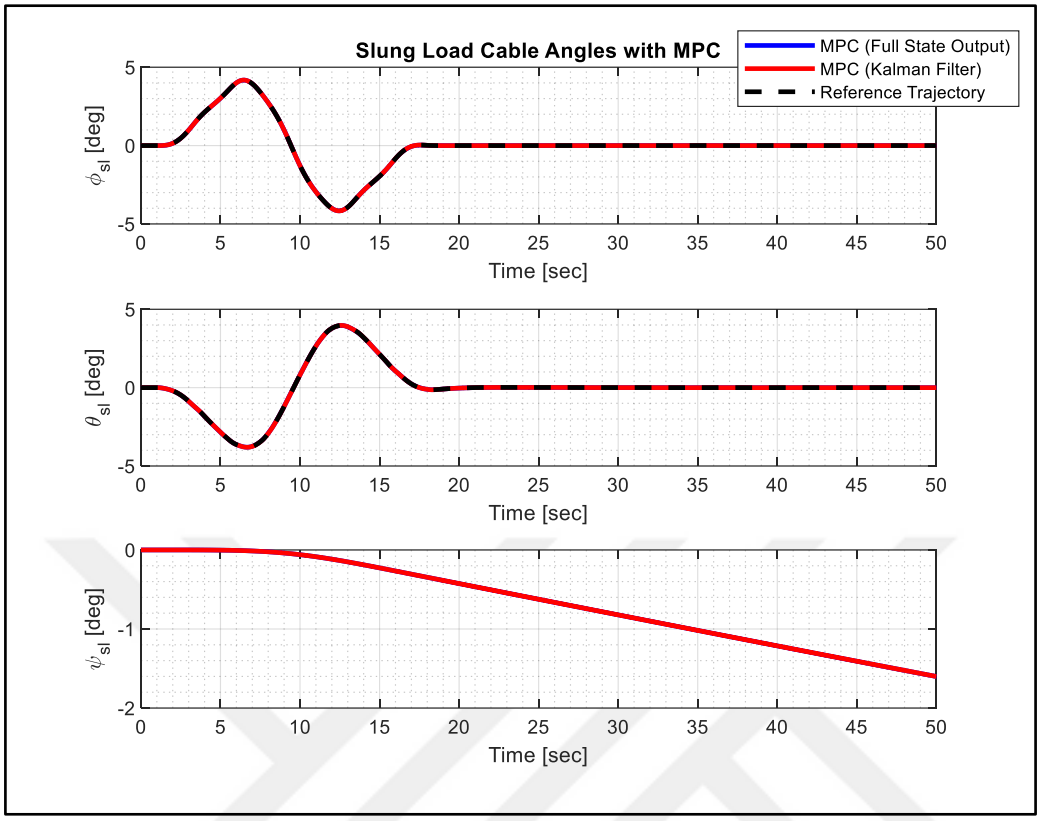


Figure 6.41. Slung Load Cable Angles with MPC and Kalman Filter

From Figure 6.41, it can be seen that the simulation results obtained with integration of the Kalman Filter to the system agrees perfectly well with those of the full state output case. This indicates that the Kalman Filter is capable of estimating the slung load dynamics accurately and estimated slung load states can indeed be utilized in the proposed model predictive control algorithm to eliminate sustained oscillations

Simulation results with MPC have shown that, with a suitable choice of reference trajectories, perfect tracking of the slung load cable angles is possible. As a direct result of the implementation of this approach, the oscillation free slung load motion becomes possible in the presence of outside disturbances, which is obviously not the case with only input shaping of the reference commands. In fact, to evaluate the robustness and performance characteristics of the proposed model predictive controllers, additional case studies are performed, which will be elaborated on in detail in the next section.

6.7.2.1 Model Predictive Control Performance Evaluation

To make an assessment of the performance characteristics of MPC in the presence of plant disturbance, aforementioned simulations with input shaping and model predictive control are repeated by injecting disturbance through the longitudinal and lateral cyclic input channels. It should also be noted that the model predictive control is considered with full state output. In other words, the simulation is carried out in the absence of the Kalman Filter. The performance of the model predictive control combined with the Kalman Filter will be discussed later on as a separate case study.

Similar to the discussion provided in the Kalman Filter section in 6.5.3, the disturbance is given by utilizing Simulink's 'band limited white noise' block and the power quantity is specified as 0.001 with sample time of 1 millisecond. As a reminder, the specified power represents the height of the power spectral density of the noise signal of concern.

Simulation results are provided in a superimposed manner in the following figure:

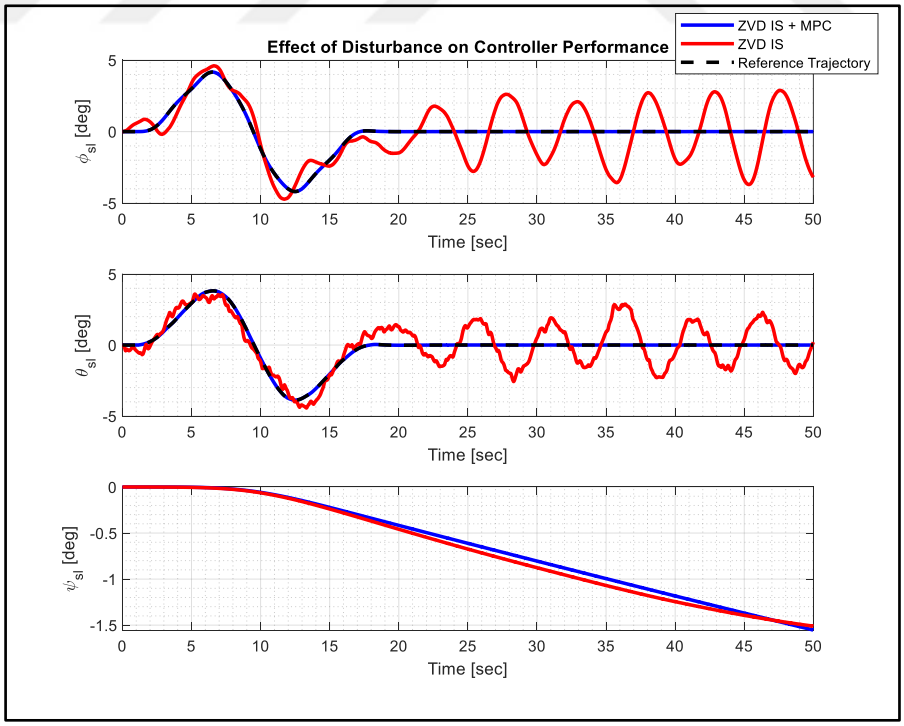


Figure 6.42. Effect of Disturbance on Controller Performance

From Figure 6.42, it can clearly be seen that ZVD input shaper by itself is highly susceptible to disturbances and its effective oscillation damping characteristics discussed so far are completely deteriorated. On the other hand, when ZVD input shaping is combined with model predictive control, the system is able to track the reference trajectories quite well in the presence of disturbances.

To pursue the performance investigation of the model predictive controller, an additional case study with the Kalman Filter is conducted. That is, the measurement noise discussed in 6.5.3 is injected to the helicopter states and plant model different from the one used in Kalman Filter and model predictive control algorithm design is used to represent the plant disturbance. For convenience, the deviations in the plant model are explained provided here as well:

- Helicopter mass and inertia values are increased by 5%
- Slung load mass is defined as 1000 kg greater than the original case
- The distance the helicopter attachment point and slung load center of gravity is defined as 8.62 meters instead of 7.62 meters (25 ft.).

Results of the simulation are provided in the following figure in a superimposed manner with the ideal full state output case discussed above:

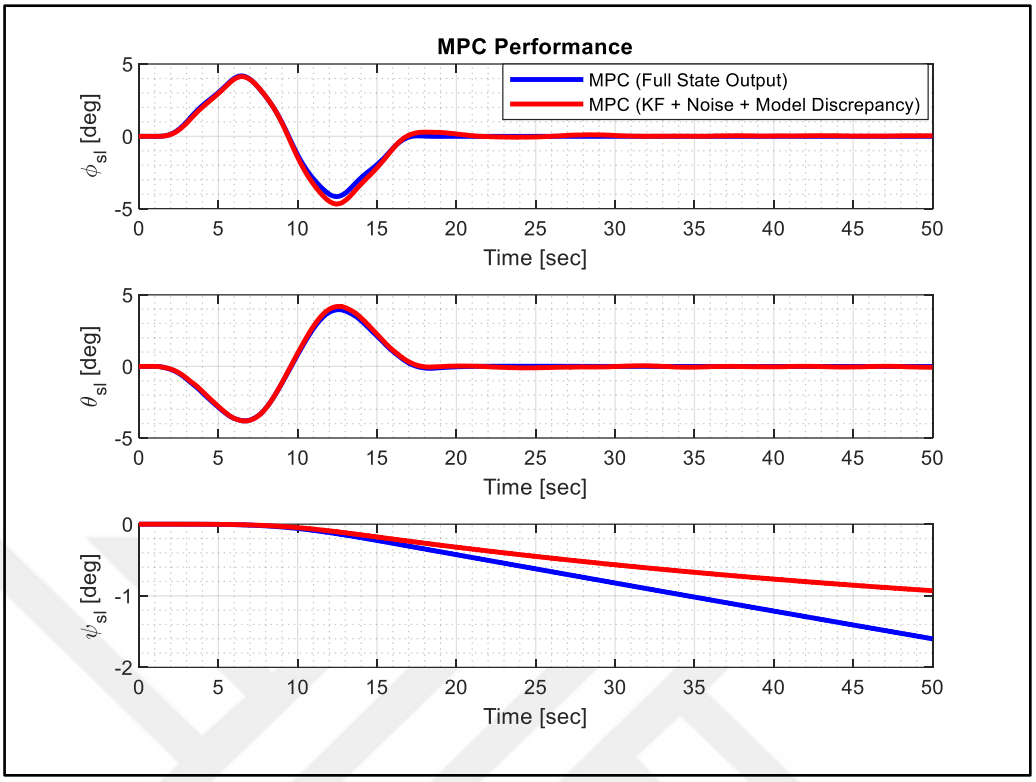


Figure 6.43. Effect of Measurement Noise and Plant Model Discrepancy on Model Predictive Controller Performance

From Figure 6.43, it can be seen that, there are certain amount of difference in all the slung load cable angles. That is, the oscillations observed in the longitudinal and lateral angles last longer compared to the ideal full-state output case. Also, there is a slight deviation from the yaw angle obtained from the full-state output case. However, it is also evident that neither of these differences are excessive and sustained oscillations of concern are eventually damped out.

This implies that the MPC algorithm can perform effectively in the presence of measurement noise with a plant model deviated from the one used for Kalman Filter and model predictive controller design.

6.7.3 Application of Model Predictive Control to Full-Nonlinear Model

As the final part of the application of the model predictive control on the slung load system in hovering flight condition, proposed controller is implemented to the full-nonlinear model. It is assumed that all related states of the compound system are available since the previously designed Kalman Filter is obtained for the linearized system and integrating the feedback controllers based on the estimated states could lead to erroneous results. Therefore, it would be a better choice to design unscented or extended Kalman Filters for the nonlinear system. However, evaluating the performance of the proposed model predictive controller with the full-nonlinear system is still valuable in terms of assigning its adequacy in a more realistic case. The simulation is also performed in the absence of process and measurement noise.

The initial simulations have shown that the system did not function properly with the previously chosen MPC algorithm parameters given in Equations (6.80)-(6.83). This problem is solved by modifying the cost function. That is, the penalization on the tracking error is increased at each progressing time step to obtain better consistency with the reference trajectory. The prediction and control horizons are also changed. Following set of equations illustrate finalized version of the MPC algorithm parameters.

$$N = 50 \tag{6.84}$$

$$V = 10 \tag{6.85}$$

$$Q = \begin{bmatrix} 100e^{0.1\times1} & 0 & 0 & \dots & 0 \\ 0 & 100e^{0.1\times2} & 0 & \dots & 0 \\ \dots & \dots & \ddots & \dots & \dots \\ 0 & 0 & 0 & \dots & 100e^{0.1\times50} \end{bmatrix} \tag{6.86}$$

$$R = \begin{bmatrix} 10^{-5} & 0 & 0 & \dots & 0 \\ 0 & 10^{-6} & 0 & \dots & 0 \\ \dots & \dots & \ddots & \dots & \dots \\ 0 & 0 & 0 & \dots & 10^{-6} \end{bmatrix} \tag{6.87}$$

The simulation results with the MPC parameters given above are illustrated in the following figure in a superimposed manner with those of the full state output case discussed in section 6.7.2.

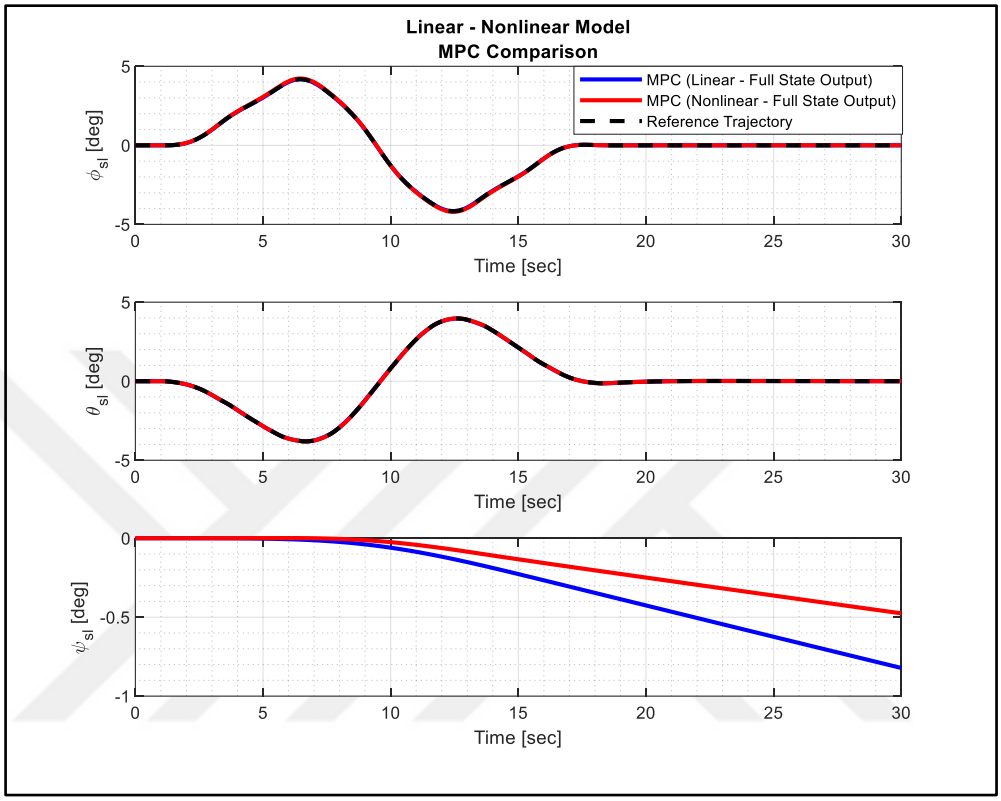


Figure 6.44. Linear-Nonlinear Model MPC Comparison

From Figure 6.44, it can be seen that model predictive controller designed for the linear model performs satisfactorily well with the full-nonlinear model in terms of tracking of the reference trajectories and damping of the undesirable slung load oscillations. The same figure shows that the slung yaw angle of the nonlinear model deviate slightly from that of the linearized model. However, considering that the discrepancy is small and the yaw motion of the slung load is not a major concern, this does not constitute a problem.

6.7.4 Application of Input Shaping and Model Predictive Control for Forward Flight

It was previously mentioned that all the control methodologies have been discussed so far are based on the hovering flight condition. In this section, proposed control scheme that consists of input shaping and model predictive control will be applied to the forward flight case with airspeed of 60 knots (30.87 m/s). However, before going into the details, design of the helicopter flight control system for forward flight with 60 knots of airspeed as well as the validity of the mathematical model at 60 knots of airspeed should be discussed.

6.7.4.1 Helicopter Flight Control System Design for 60 Knots Forward Flight

In this section, the helicopter flight control system designed for hovering flight condition is inspected to observe whether it is able to function properly in the case of 60 knots forward flight as well instead of designing a separate flight control system for 60 knots from scratch for convenience. The same evaluation criteria used in hovering flight is applied here as well. That is, the unit step input response characteristics and robustness of the closed loop system are taken into account.

The simulation results have shown that stability augmentation systems of concern are adequate to enhance the stability characteristics of the open loop system at a certain degree. Regarding the autopilots, it can be asserted that except for a necessity of slight modification on altitude hold autopilot, the remainder of them perform satisfactorily for 60 knots forward flight case as well. The unit step response characteristics and minimum gain and phase margins for each channel of concern are summarized in the following table:

Table 6.7. Proposed Autopilots for 60 Knots Forward Flight

Pitch Attitude Hold Autopilot			
$G_{c\theta} = 7.5 + \frac{2.03}{s} + 6.37\frac{20.82s}{20.82 + s}$			
Overshoot [%]	**Settling Time [sec]**	**Gain Margin [dB]**	**Phase Margin [deg]**
9.92	3.22	∞	70.7
Roll Attitude Hold Autopilot			
$G_{c\phi} = 12.34 + \frac{15.58}{s} + 1.73\frac{33.37s}{33.37 + s}$			
Overshoot [%]	**Settling Time [sec]**	**Gain Margin [dB]**	**Phase Margin [deg]**
9.31	1.60	∞	73.2
Heading Hold Autopilot			
$G_{c\psi} = 25.39 + \frac{12.92}{s} + 9.83\frac{77.07s}{77.07 + s}$			
Overshoot [%]	**Settling Time [sec]**	**Gain Margin [dB]**	**Phase Margin [deg]**
7.71	1.1	∞	79.8
Altitude Hold Autopilot			
$G_{ch} = 0.391 + \frac{6 \times 10^{-8}}{s} + 0.587\frac{1574.91s}{1574.91 + s}$			
Overshoot [%]	**Settling Time [sec]**	**Gain Margin [dB]**	**Phase Margin [deg]**
-	8.4	∞	90.1

From table given above, it can be seen that all of the autopilots are closed-loop stable and they possess sufficient gain and phase margins as well as satisfactory settling time and overshoot characteristics. In the next section, validation of compound system consisting of helicopter and slung load at 60 knots of airspeed will be discussed.

6.7.4.2 Validation of the Mathematical Model at 60 Knots Forward Flight

Validation of the developed compound mathematical model at 60 knots forward flight is performed by using the linearized model as in the case of hovering flight. That is, pole locations of the linear model in the complex plane are examined and compared to those of a verified study that can be found in reference [4]. This

particular reference study also utilizes CH-53 helicopter model and overall configuration is similar to the model used in this study. As a reminder, the study upon which the comparison is to be made constitutes a base for the previously examined study [8] with which the validation of the model in hovering flight is performed.

Firstly, pole locations of the open loop plant model are provided in the following figure and corresponding dynamic modes are identified based on the eigenvectors of the state matrix in the state space representation.

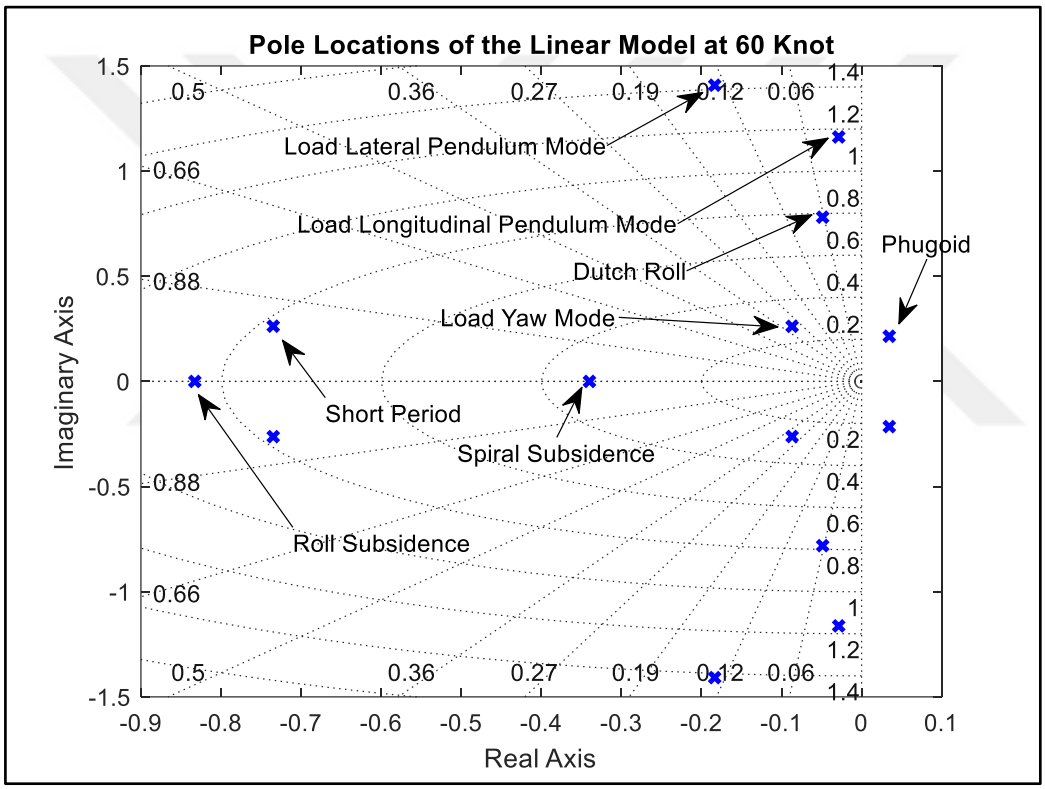


Figure 6.45. Pole Locations of the Linearized Model at 60 Knots Forward Flight

From Figure 6.45, it can be seen that, there are six additional poles related to the slung load. As in the case of hovering flight, two pairs of these additional poles correspond to the longitudinal and lateral pendulum modes. The same figure also shows that characteristics of the load yaw mode are altered compared to the hovering flight. That is, in forward flight with 60 knots of airspeed, the yaw mode moves

further into the left half plane and it shows certain amount of oscillatory behavior due to imaginary part of the corresponding poles. Now that the identification of the related dynamic modes is completed, the results are compared to the those of the reference study in [4], as shown in the following figure.

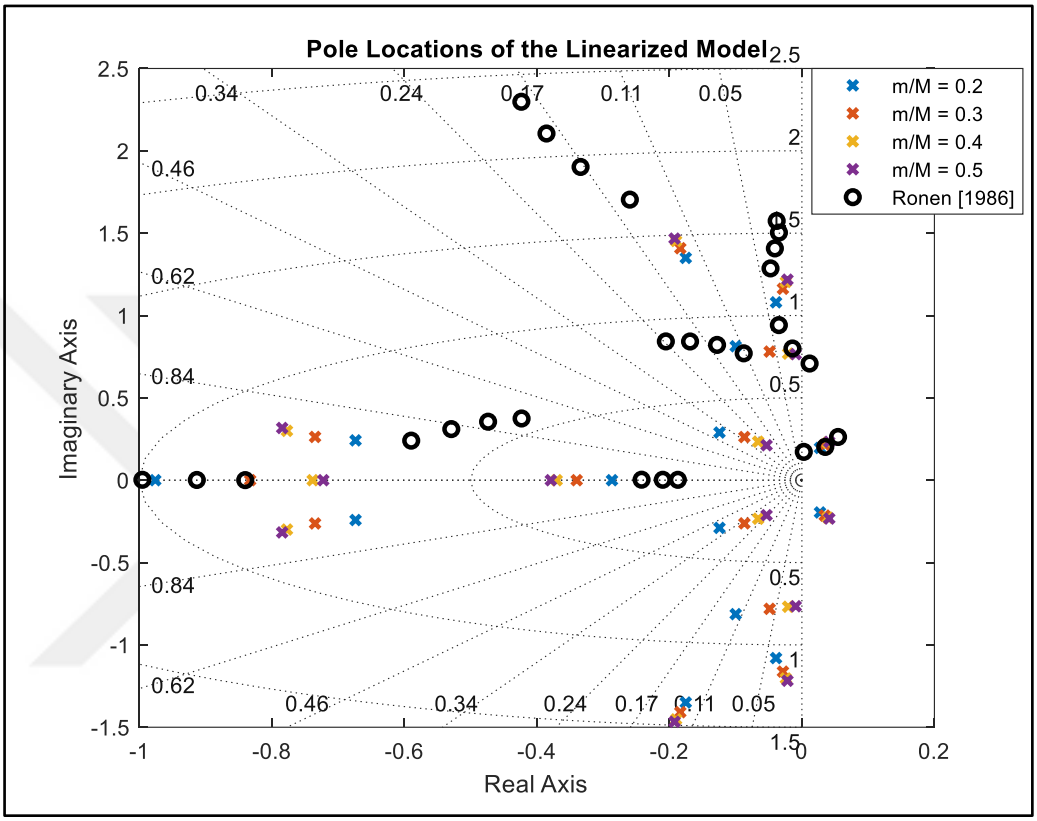


Figure 6.46. Comparison of the Pole Locations of the Compound Helicopter-Slung Load Model with the Reference in [4]

In Figure 6.46, the poles are plotted with respect to varying slung load to helicopter mass ratio, which is ranging from 0.2 to 0.5. From the same figure, it can be seen that consistency between the overall pole locations can be assigned as adequate. That is, there are two pairs of poles corresponding to the longitudinal and lateral pendulum modes. In addition, the existence of the complex pole pair belonging to the load yaw mode can also be observed. Regarding the helicopter modes, it can be asserted that both models have similar locations on the complex plane. Moreover, the trend observed in all these poles with increasing load mass in consistent among the models.

It should also be pointed out that even though the overall consistency between the models can be evaluated as sufficient, some elaboration regarding the discrepancies shall be provided as well for completeness. From Figure 6.46, it can be observed that the most significant deviation is in the lateral slung load pendulum mode and it becomes more evident with increasing load mass, which was also the case in hovering flight condition as discussed previously in Section 5.4. In forward flight, this trend can also be explained by noting that the configurations utilized in the models are not identical. That is, the helicopter mass and center of gravity are not exactly the same, which results is certain discrepancy between the load masses as well. In addition, it is likely that there is a difference in terms of slung load attachment point location on the helicopter. Also, with increasing airspeed, accuracy of modeling of the slung load aerodynamics becomes more important. The reference study utilizes a more detailed approach regarding this aspect, which may also affect the consistency between the models.

Another noticeable discrepancy can be seen in the slung load yaw mode. Even though the damping ratio of the corresponding mode is similar among the models, the one used in the reference study has greater damped natural frequency as far as this particular mode is concerned.

The final major inconsistency is in the short period mode. From Figure 6.46, it can be seen that damping ratio of this mode is similar among the models. However, its damped natural frequency is noticeably smaller in the reference study.

However, even if these discrepancies are taken into account, it can be asserted that the developed mathematical model in this study captures the overall dynamic behavior of the compound helicopter-slung load system accurately. That is, the same helicopter modes with the reference study exist and variation of this modes have the same trend with increasing load mass. Moreover, introduction of longitudinal and lateral load pendulum modes along with the complex yaw mode agrees with the reference study. Finally, as mentioned above, the trend shown by pendulum modes with increasing load mass is consistent between the two models. Considering that a

mathematical model with capability of capturing overall helicopter and slung load dynamics accurately at a sufficient extent is obtained, application of the control law consisting of input shaping and model predictive control will be discussed in the next section.

6.7.4.3 Input Shaper Design for 60 Knots Forward Flight

In this section, ZVD input shaper design for the linearized model in 60 knots forward flight condition will be discussed. Firstly, state of the compound system in the presence of only the helicopter flight control system proposed in Section 6.7.4.1 will be examined. The system is simulated with the input profiles given in Figure 6.2 and resultant slung load cable angles are provided below:

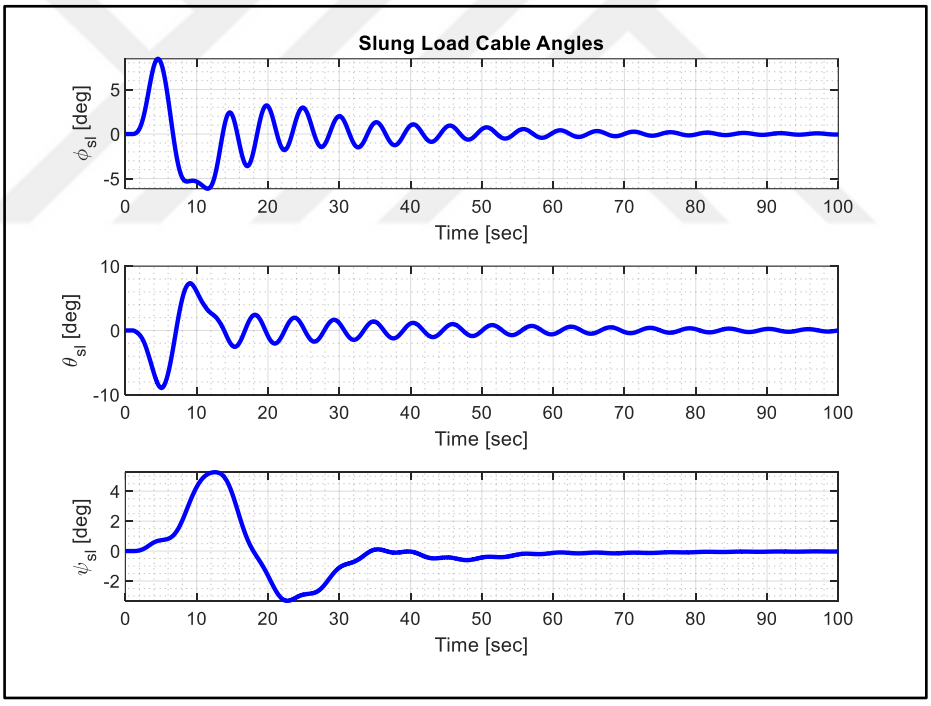


Figure 6.47. Slung Load Cable Angles at 60 Knots Forward Flight

From Figure 6.47, the oscillatory behavior of the longitudinal and lateral slung load cable angles can clearly be seen. Also, the yaw angle has a slightly oscillatory response characteristics as well. However, unlike the hovering flight case, these

oscillations are eventually suppressed, which indicates that the damping characteristics have improved with increasing airspeed. Nevertheless, it can be asserted that oscillations sustain for a considerable amount of time. To remedy this problem, input shaping is applied through the longitudinal and lateral cyclic channels. The necessary impulse amplitudes and instances are determined based on the closed loop poles corresponding to the longitudinal and lateral pendulum modes. The locations of closed loop system poles are provided in the following figure. As in the hovering flight case, the poles near the imaginary axis are of concern and the given figure is zoomed in to this particular area.

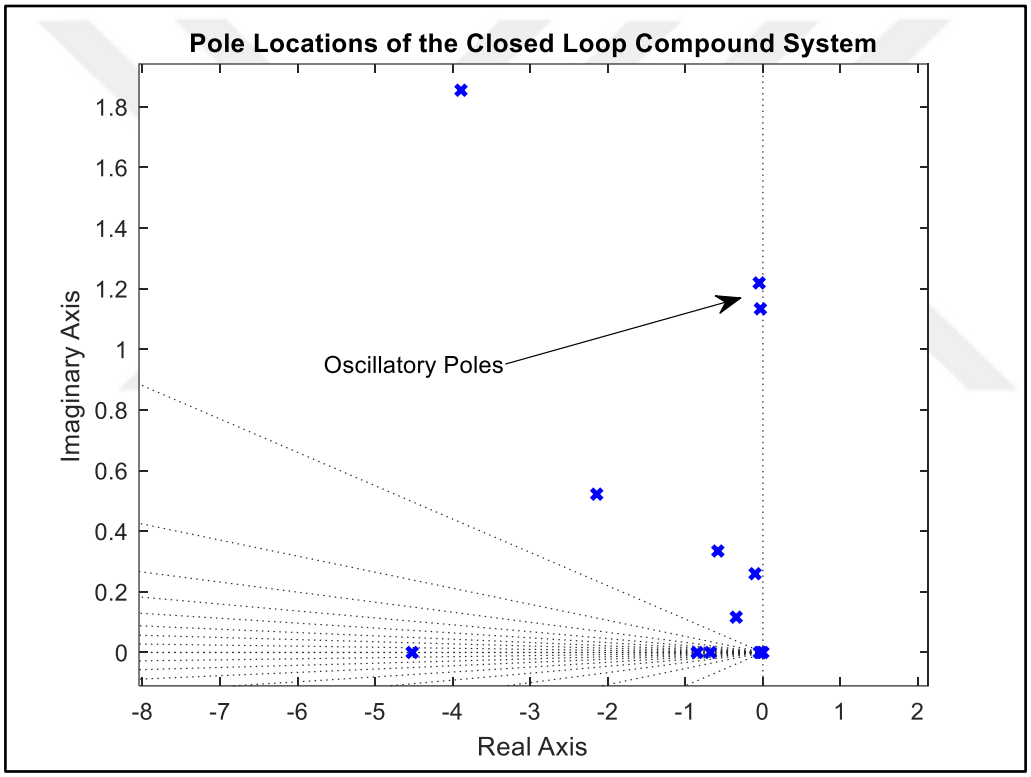


Figure 6.48. Pole Locations of the Closed Loop Compound System at 60 Knots

From Figure 6.48, it can be seen that there are indeed two complex pole pair in the very close vicinity of the imaginary axis that stands for the longitudinal and lateral pendulum motion of the slung load. Inspection of the eigenvectors corresponding to these particular poles shows that the major contributors are the longitudinal and lateral cable angle rates, i.e., $\dot{\theta}_{sl}$ and $\dot{\phi}_{sl}$. Following table summarizes these poles

numerically and identifies which complex pair corresponds to oscillation in each axis:

Table 6.8. Oscillatory Slung Load Poles at 60 Knots Forward Flight

Poles	
Long. Oscillatory Slung Load Motion	Lat. Oscillatory Slung Load Motion
-0.032 ± 1.134i	-0.048 ± 1.219i

Given that pole locations of the related pendulum modes are identified, corresponding natural frequencies and damping ratios can be calculated by the following set of equations as in the case of hovering flight.

$$\text{Real(pole)} = \omega_n \zeta \tag{6.88}$$

$$\text{Imag(pole)} = \omega_n \sqrt{1-\zeta^2} \tag{6.89}$$

Resultant natural frequencies and damping ratios of the longitudinal and lateral pendulum modes are summarized in the following table:

Table 6.9. Natural Frequency and Damping Ratio of the Slung Load Pendulum Modes at 60 Knots Forward Flight

	Long. Cable Angle (θ_{sl})	Lat. Cable Angle (ϕ_{sl})
ω_n [rad/sec]	1.1341	1.2200
ζ	0.0282	0.0392

The detailed formulation of the impulse amplitudes and instances of ZVD input shapers were previously provided in Section 6.2.1. Hence, these parameters corresponding to the pole locations in Table 6.8 are provided below without rigorous derivation:

Table 6.10. Impulse Amplitudes and Instances for ZVD Input Shapers at 60 Knots

	Long. Cable Angle (θ_{sl})	Lat. Cable Angle (ϕ_{sl})
A_1	0.2726	0.2817
A_2	0.4990	0.4981
t_2 [sec]	2.7712	2.5771
A_3	0.2284	0.2202
t_3 [sec]	5.5423	5.1541

Following figure illustrates the modified commands with input shapers along with the original ones.

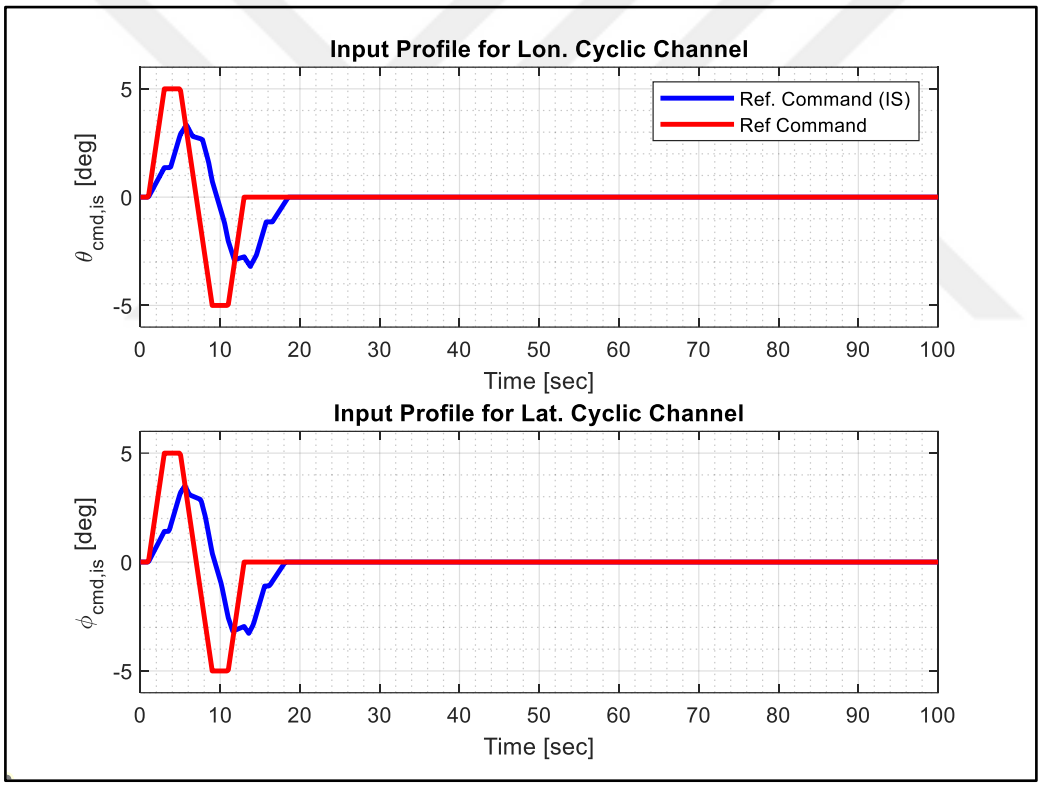


Figure 6.49. Input Shaped Reference Commands

Simulation results obtained with the modified reference commands through the input shapers are provided in the following figure.

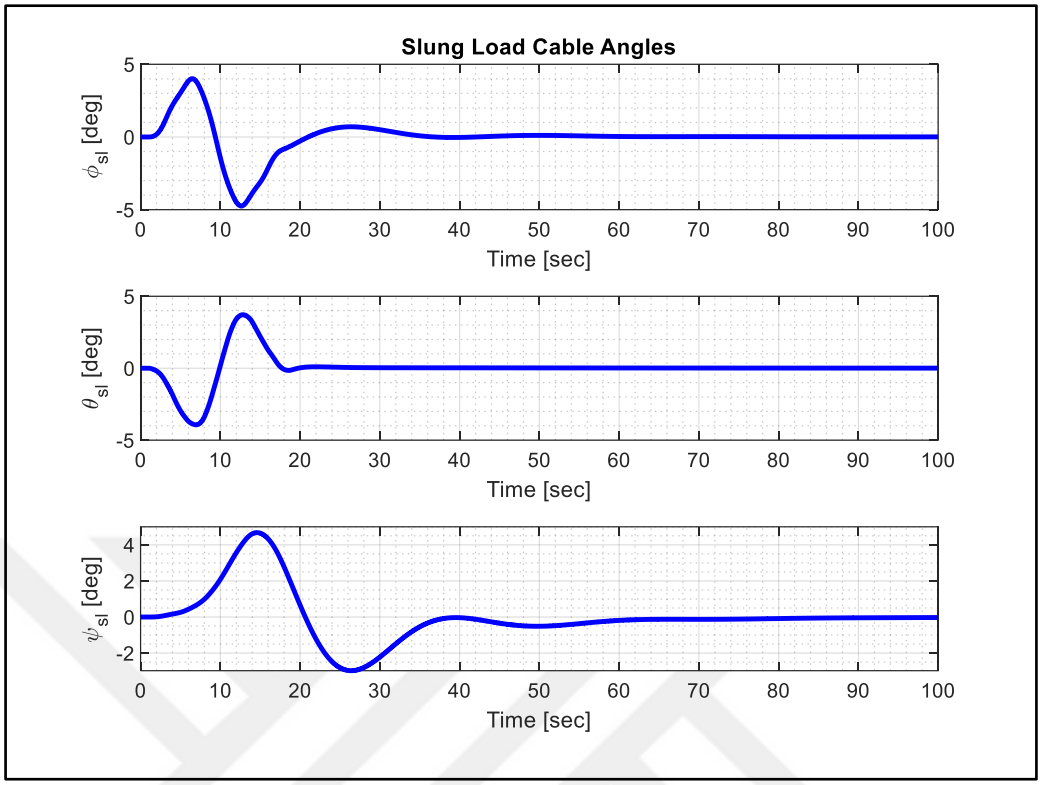


Figure 6.50. Slung Load Cable Angles with ZVD Input Shaped Reference Commands

From Figure 6.50, it can be seen that the sustained oscillations in the longitudinal and lateral slung load angles are effectively damped out with modified reference commands. The same figure also shows that the slightly oscillatory characteristic of the slung load yaw angle are improved as well.

Given that oscillation free motion of the slung load with ZVD input shapers is obtained, resultant longitudinal and lateral cable angles will be utilized as reference trajectories in the model predictive control algorithm that will be discussed in the next section.

6.7.4.4 Application of Model Predictive Control on Slung Load System at 60 Knots Forward Flight

In this section, application of the model predictive control on the slung load system at 60 knots forward flight case will be examined. As a starting point, the same algorithm discussed in hovering flight case is proposed. That is, the longitudinal and lateral slung load cable angle trajectories obtained with ZVD input shapers given in Figure 6.50 are supplied as the reference trajectories and the simulations are performed with the model predictive control scheme described in Section 6.7.1.

At this point, it is crucial to note that this approach does not yield satisfactory results unlike the hovering flight. That is, even though the proposed MPC algorithm was able to track the reference slung load trajectories at the initial phase of the simulation, the system started to deviate after a certain amount of time. The tuning performed on the MPC parameters including the prediction horizon and control horizon or the cost function weights did not resolve this problem either.

Hence, for the forward flight case a slightly modified algorithm is put forward. That is, the helicopter pitch and roll attitudes resulting from ZVD input shaping are provided as reference trajectories along with the slung load trajectories discussed above. That is, for the longitudinal cyclic channel, the pitch attitude of the helicopter and the longitudinal slung load cable angle are determined as the reference trajectories. Whereas, the helicopter roll attitude and lateral slung load cable angle are fed as the reference trajectories for the lateral cyclic channel. This yields that there are two single output and two input model predictive controllers in the overall closed loop system. The related block diagram is provided below for a clear illustration of the proposed control scheme:

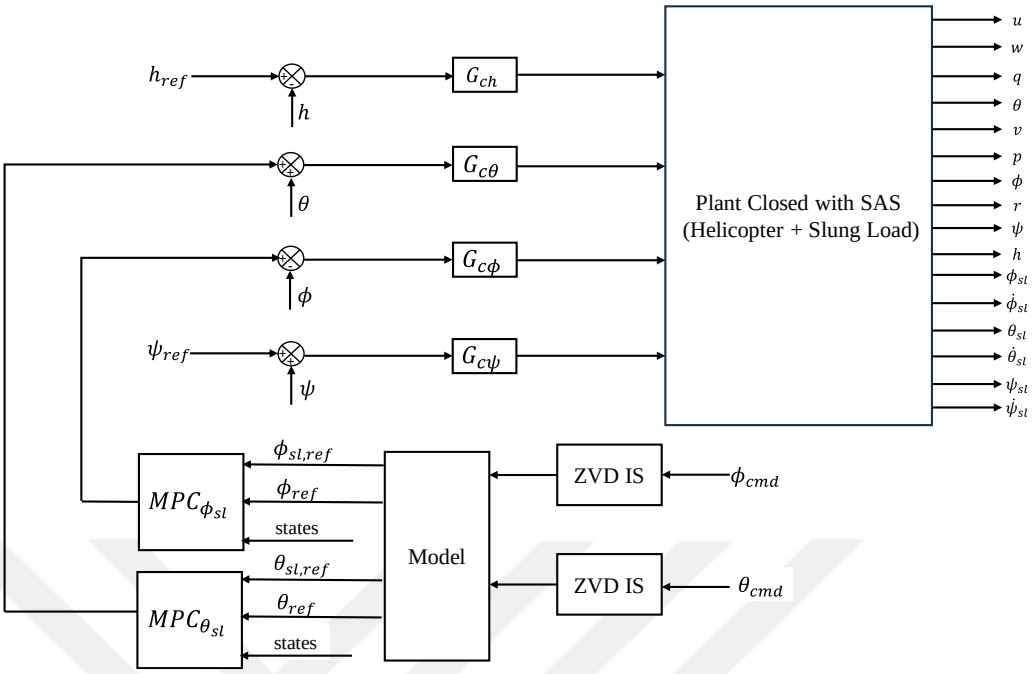


Figure 6.51. Model Predictive Controller Structure for 60 Knots Forward Flight

Figure 6.51 can interpreted as follows. The pitch and roll attitude commands first pass through the input shapers. The modified commands are then applied to the mathematical model consisting of the compound helicopter-slung load system and helicopter controllers. Finally, the helicopter pitch and roll attitudes as well as the oscillation free slung load trajectories constitutes the reference trajectories for the model predictive controllers in the longitudinal and lateral channels. The reference trajectories for each channel are illustrated separately in the following set of figures for completeness.

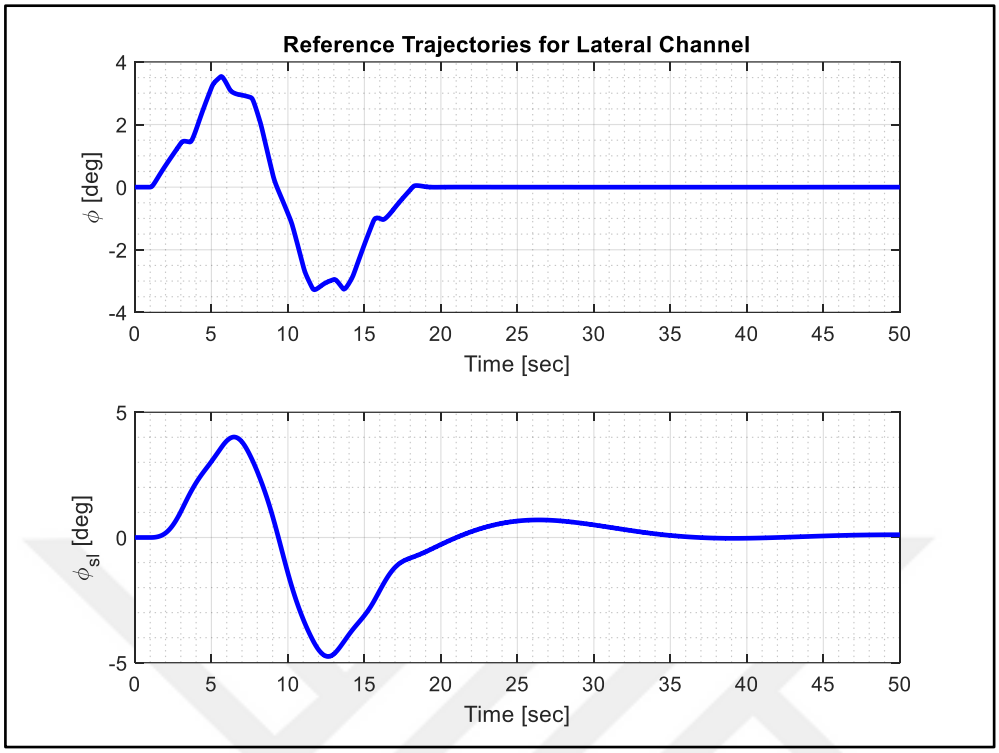


Figure 6.52. Reference Trajectories for Lateral Channel

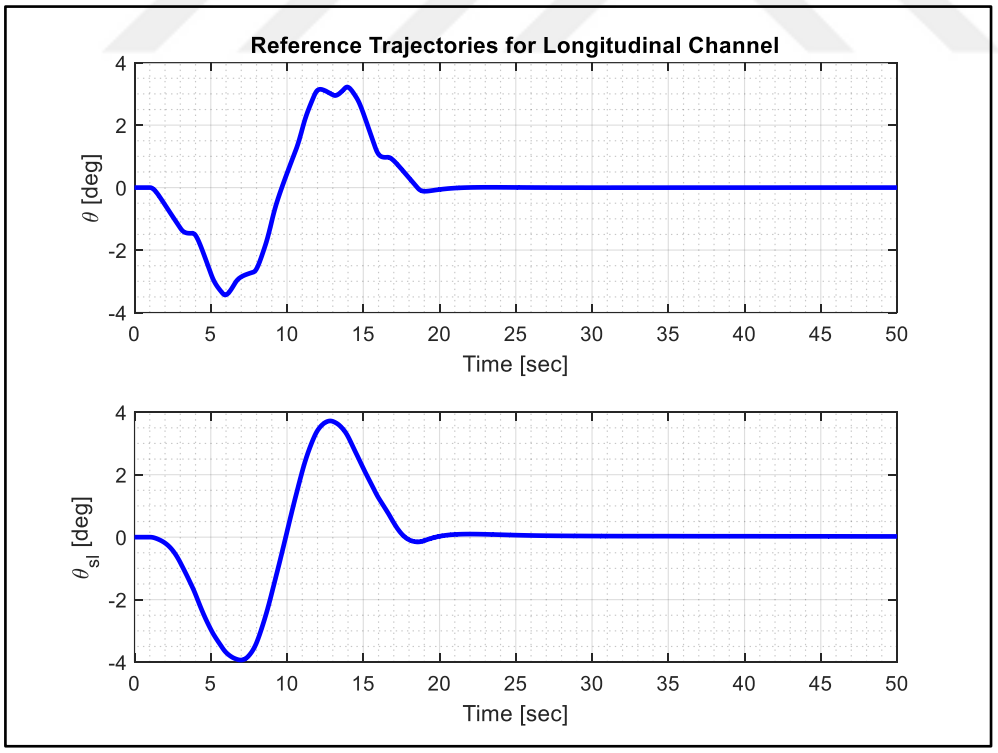


Figure 6.53. Reference Trajectories for Longitudinal Channel

With the aforementioned modification on the model predictive control algorithm, the closed loop system functions properly in terms obtaining slung load motion without sustained oscillatory behavior. In the proposed MPC formulation, the same prediction and control horizons in the hovering flight are utilized. The cost function is only altered to take the additional reference trajectories for helicopter attitudes into account. As in the hovering flight case as long as reasonable parameters are selected, the overall system operates in the desired manner. In the following set of figures, the simulation results in the absence of Kalman Filter are illustrated to show the effectiveness of the proposed control scheme in an ideal case.

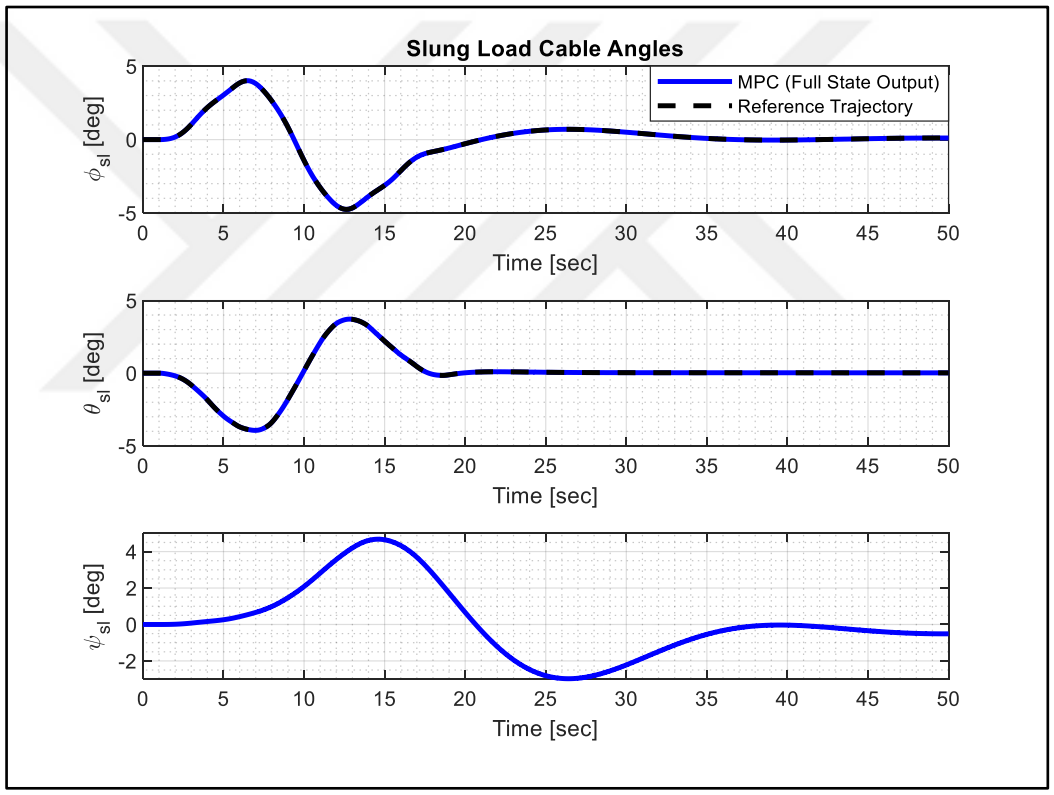


Figure 6.54. Slung Load Cable Angles with MPC and Full-State Output

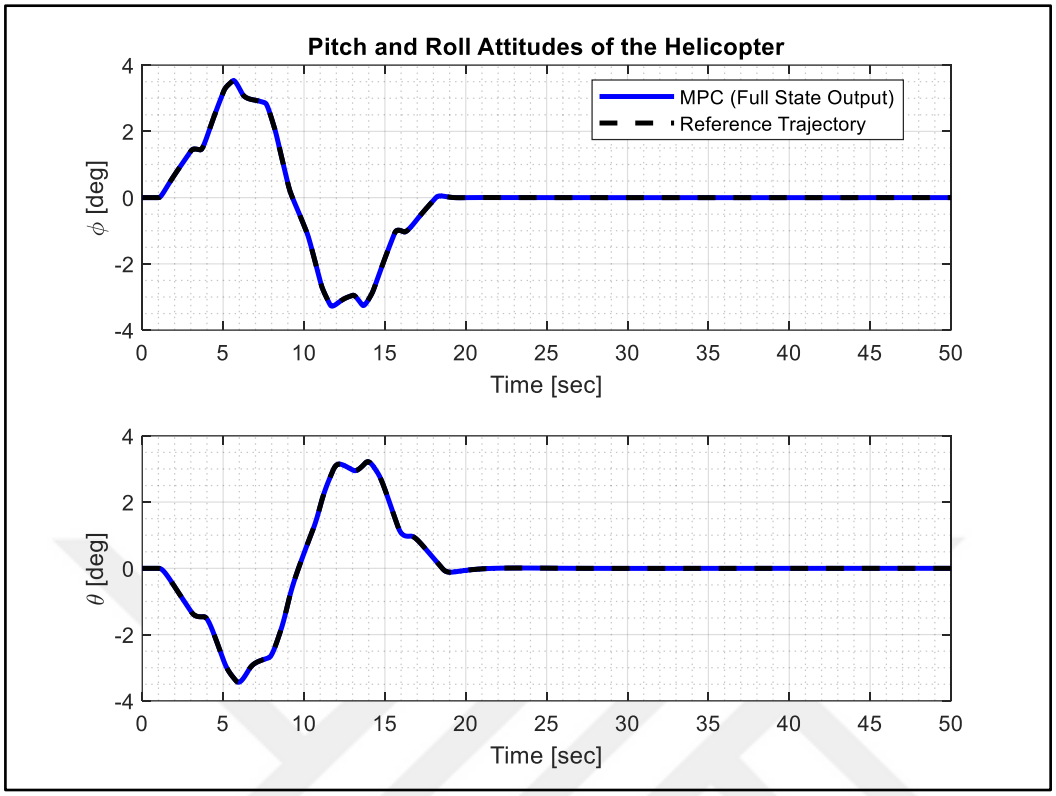


Figure 6.55. Helicopter Pitch and Roll Attitudes with MPC and Full-State Output

From Figure 6.54 and Figure 6.55, it can be seen that with the proposed model predictive controllers, the system is capable of tracking the reference trajectories of concern perfectly. Next, the performance of the system in the presence of Kalman Filter will be investigated. That is, instead of using full state feedback, the simulation will be conducted with Kalman Filter that estimates the slung load states. The related results are provided in the following set of figures in a superimposed manner with those obtained from the full state output case discussed above. It should also be noted the same Kalman Filter proposed in the hovering flight condition is integrated to the system and the measurement noises and plant disturbances are not taken into account in the simulation.

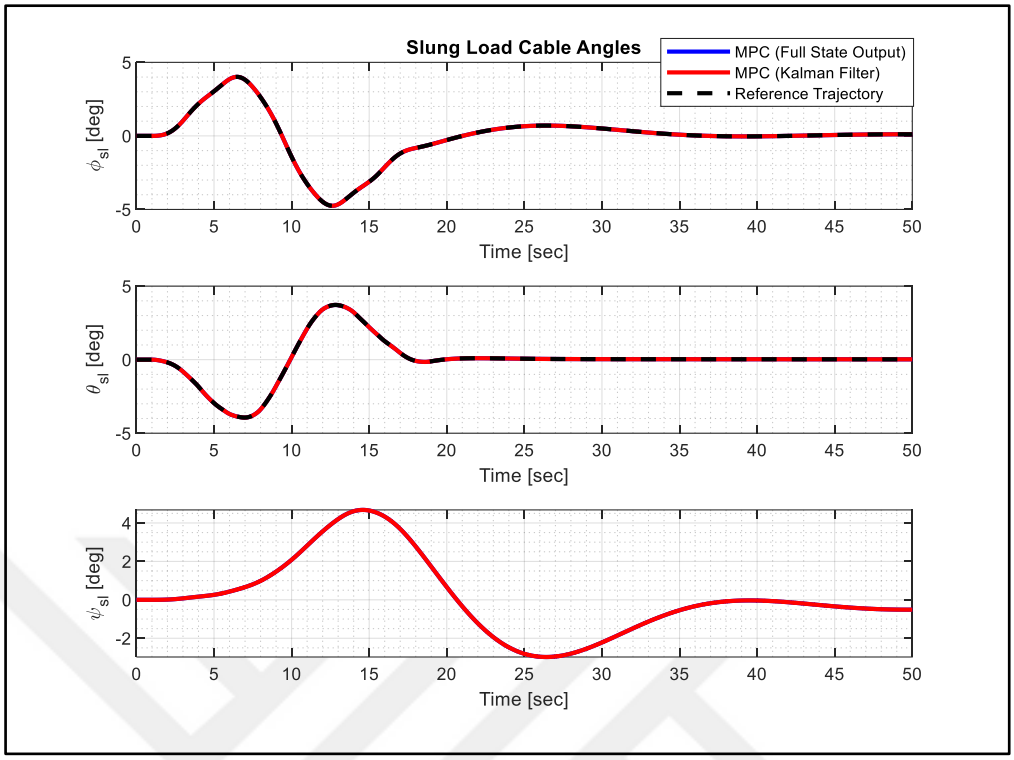


Figure 6.56. Slung Load Cable Angles with MPC and Kalman Filter

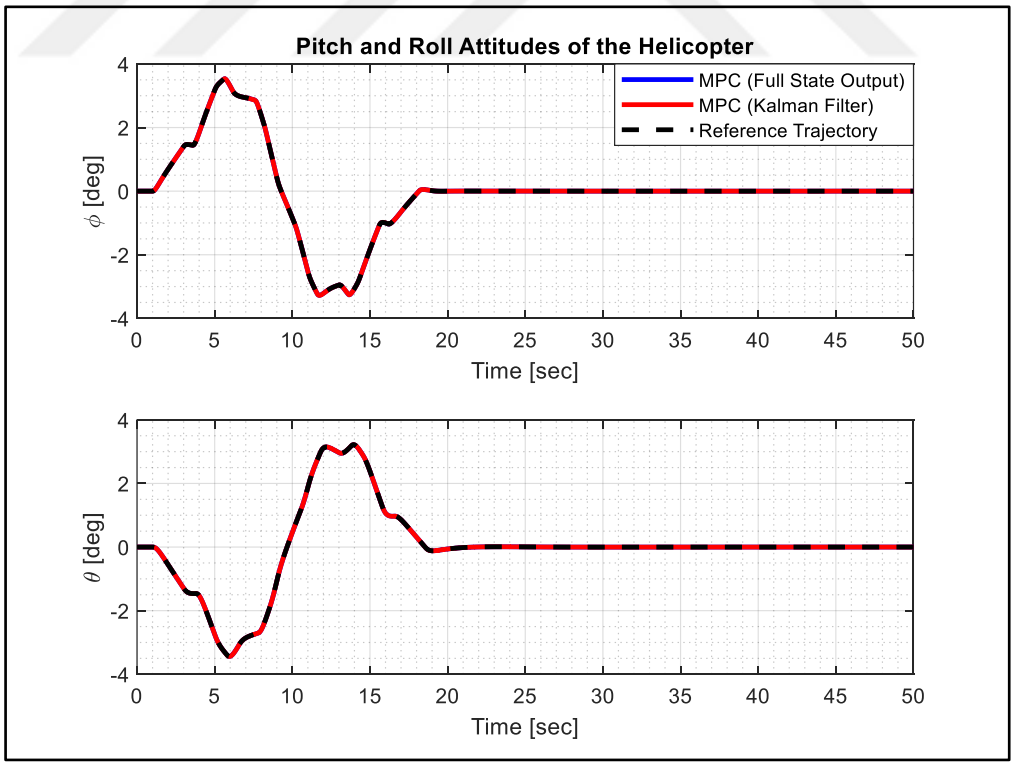


Figure 6.57. Helicopter Pitch and Roll Attitudes with MPC and Kalman Filter

Figure 6.56 and Figure 6.57 show that that the simulation results obtained with integration of the Kalman Filter to the system agrees perfectly well with those of the full state output case. This indicates that the Kalman Filter is capable of capturing the slung load dynamics accurately and estimated slung load states can indeed be utilized in the proposed model predictive control algorithm to eliminate sustained oscillations.

It should be noted that, the simulation results discussed so far for the forward flight case are evaluated as sufficient to illustrate the capability of the proposed model predictive control algorithm. Hence, unlike the hovering flight, effect of the measurement noises and plant disturbances will not be considered.

As the final step of the inspection of model predictive control algorithm in forward flight condition, the proposed model predictive control algorithm is applied to the full-nonlinear model for completeness. Regarding this particular simulation, all the states including those of the slung load are assumed to be available and the Kalman Filter is not integrated to the system. As it discussed in the hovering flight case, designed Kalman Filter is obtained for the linearized system and integrating the feedback controllers based on the estimated states could lead to erroneous results. Regarding the nonlinear model simulation, the MPC parameters are selected in a similar manner to those given in hovering flight case through Equations (6.84)-(6.87).

$$N = 50 \tag{6.90}$$

$$V = 10 \tag{6.91}$$

$$Q = \begin{bmatrix} 100e^{0.1\times1}I_{2\times2} & 0 & 0 & \dots & 0 \\ 0 & 100e^{0.1\times2}I_{2\times2} & 0 & \dots & 0 \\ \dots & \dots & \ddots & \dots & \dots \\ 0 & 0 & 0 & \dots & 100e^{0.1\times50}I_{2\times2} \end{bmatrix} \tag{6.92}$$

$$R = \begin{bmatrix} 10^{-5} & 0 & 0 & \dots & 0 \\ 0 & 10^{-6} & 0 & \dots & 0 \\ \dots & \dots & \ddots & \dots & \dots \\ 0 & 0 & 0 & \dots & 10^{-6} \end{bmatrix} \tag{6.93}$$

Simulation results obtained with the full-nonlinear model are provided in the figure below in a superimposed manner with those obtained from the full state output case given in Figure 6.54 and Figure 6.55.

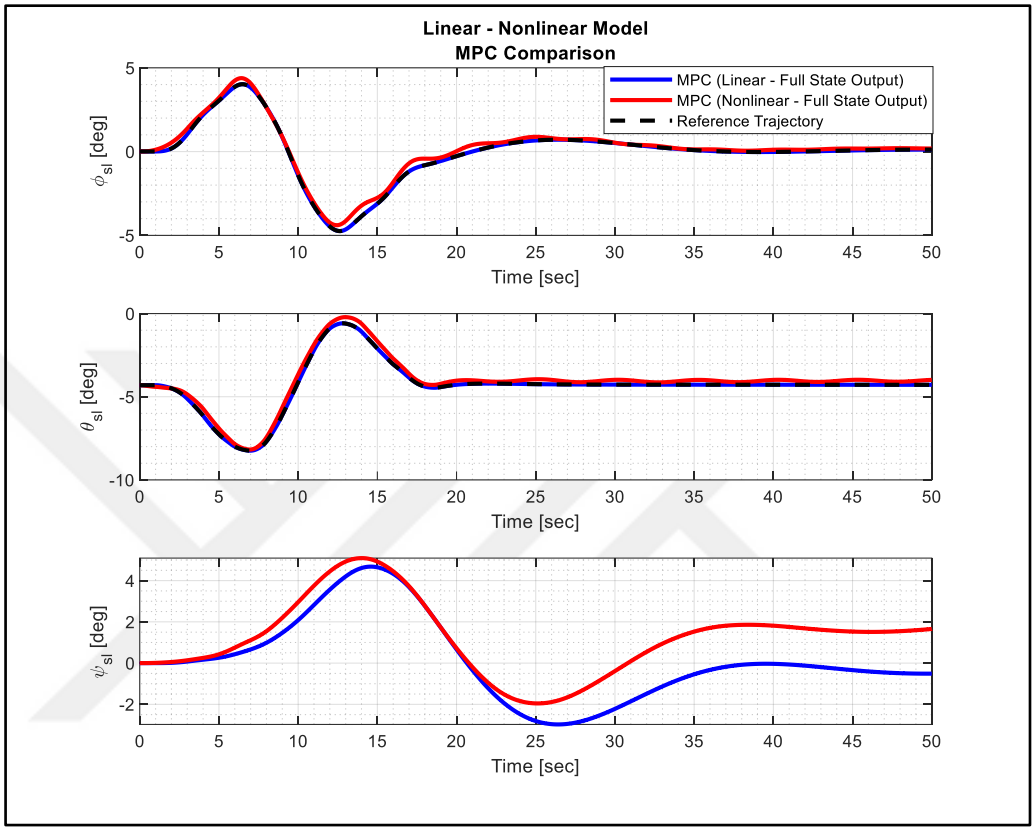


Figure 6.58. Linear-Nonlinear Model MPC Comparison of Slung Load Cable Angles

Before elaborating on the results given in Figure 6.58, it should be noted that the longitudinal cable angle starts from the vicinity of -4°. This particular angle is the trimmed value at 60 knots of forward flight condition and it is used as the initial condition in the nonlinear model. Hence, the same angle is also added to the reference trajectory and linear model output to make a valid comparison with the nonlinear model. The trimmed values of the remaining cable angles are still close to the zero and there is no noticeable offset unlike the longitudinal cable angle.

From Figure 6.58, it can clearly be seen that the nonlinear model agrees with the full state output linear model and the reference trajectories in trend. On the other hand,

the same figure shows that, there are also some visible discrepancies. That is, both the longitudinal and lateral slung load cable angles possess oscillatory characteristics that lasts for a noticeable amount of time. Moreover, there is certain amount of inconsistency in the yaw angle as well. At this point, it is reminded that overall agreement of the nonlinear and linear models in terms of slung load cable angles was much better in the case of hovering flight. This can be explained by the modification on the model predictive control algorithm. That is, unlike the hovering flight case, the helicopter pitch and roll attitudes are provided as reference trajectories as well. Given that the proposed algorithm tries to keep these additional quantities close to the reference trajectories and the linear model does not capture the nonlinear model dynamics exactly, certain amount of deviation from the ideal case is inevitable.

However, it can be asserted that neither of these discrepancies are excessive and the amplitudes of the residual oscillations in the longitudinal and lateral cable angles are quite low, which indicates that the proposed model predictive controller performs satisfactorily with the nonlinear model at forward flight with 60 knots of airspeed.

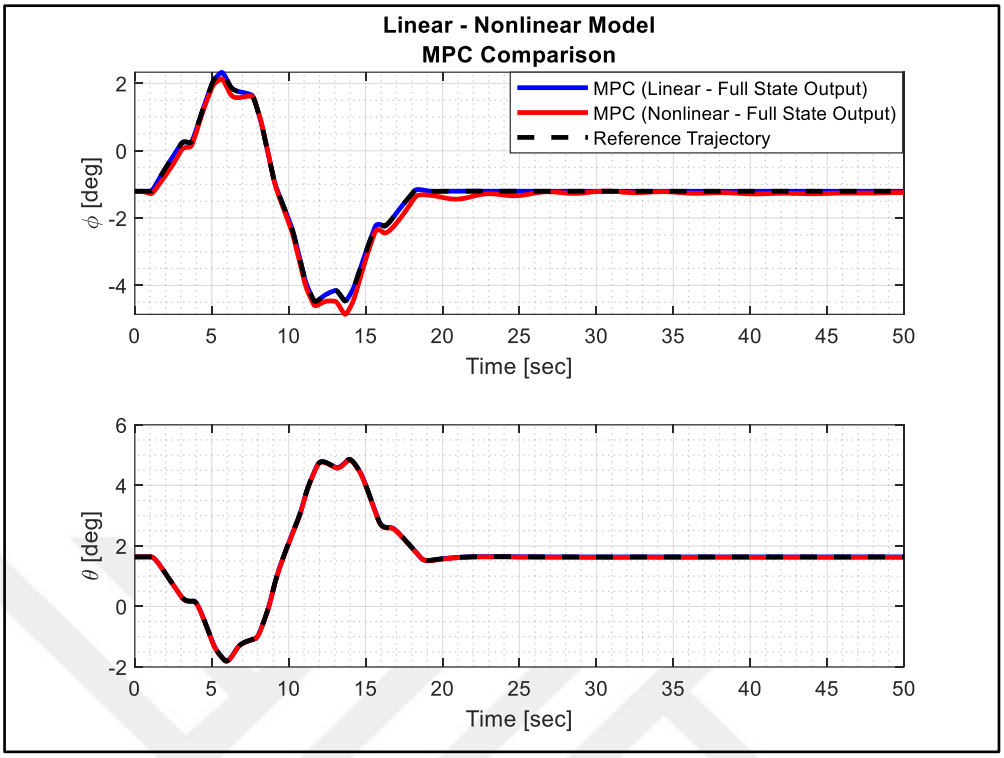


Figure 6.59. Linear-Nonlinear Model MPC Comparison of Helicopter Pitch and Roll Attitudes

In Figure 6.59, the offsets in the roll and pitch attitudes at the initial time step can be explained in the same manner with the longitudinal slung load cable angle in Figure 6.58. That is, these particular angles are the trimmed values and they are provided as the initial condition for the nonlinear model. Hence, to make a valid comparison among the linear and nonlinear models, these are added to the linear model outputs and reference trajectories.

From the same figure, it can be seen that overall agreement of the helicopter pitch angle with the linear model and reference trajectory is quite satisfactory. Whereas, there is a certain amount of deviation in the roll angle. This phenomenon can be explained in a similar manner to the slung load cable angle discrepancies. That is, the proposed model predictive control algorithm requires both the helicopter attitudes and slung load cable angles as reference trajectories. Given that linear and nonlinear models does not have identical characteristics, certain amount of deviation is likely to occur. However, it should also be noted that this inconsistency of concern

is not excessive and it can be asserted that the roll angle also follows a trend similar to the linear model and reference trajectory.

The discussion on the results given in Figure 6.58 and Figure 6.59 shows that the proposed model predictive control algorithm performs sufficiently well with the full-nonlinear model at forward flight condition with 60 knots of airspeed.

CHAPTER 7

CONCLUSION

7.1 Conclusion

In this study, a full-scale nonlinear helicopter mathematical model is developed and the resultant model is verified at a certain extent with literature and flight tests. In addition, an inner loop-outer loop flight control system architecture with preferable performance and robustness characteristics is proposed.

As the core part of the study, a mathematical model for a slung load system is derived based on generic Newton-Euler equations. The model is constructed with massless rigid cables. The model is verified with studies in the literature that involve a similar configurations. The slung load model is integrated to the already existing helicopter model as a separate module.

After obtaining the compound helicopter-slung load configuration, different control strategies are proposed and discussed. The methodologies involve input shaping, delayed feedback control and cable angle rate feedback control. It is determined that input shaping provides the most satisfactory outcome in terms of slung load oscillation damping performance. Moreover, regarding the feedback control applications, a Kalman Filter capable of estimating the slung load states based on the measured helicopter states is designed with satisfactory performance characteristics. Robustness of the Kalman Filter is verified with case studies that involve measurement noise and plant model discrepancies.

At the final stage of the study, susceptibility of input shaping to outside disturbances due to its open-loop architecture is discussed. To remedy this problem, an alternative method that combines input shaping with model predictive control is proposed.

Regarding the model predictive control, the necessary reference trajectories for oscillation free slung load motion are determined to be the slung load trajectories obtained by input shaping. Implementation of the MPC algorithm has shown that even in the presence of measurement noise and plant model discrepancy, the closed loop system is capable of tracking the given reference trajectories satisfactorily. The proposed model predictive control algorithm is also utilized in the full-nonlinear model. The simulation results have shown that the control methodology of concern functions properly with the nonlinear model and removes the sustained oscillatory behavior of the slung load system.

After verifying effectiveness of the model predictive control algorithm in hovering flight condition, it is examined for the forward flight case. The airspeed is chosen as 60 knots due to the fact that the mathematical model could be verified with literature at this particular speed. Regarding the forward flight case, firstly the flight control system proposed for the hovering flight case is examined to observe whether it is necessary to design a control system from scratch. The simulation results have shown that except for a necessity of slight modification on the altitude hold autopilot, remainder of the control system function satisfactorily for forward flight with 60 knots of airspeed as well. Then, validation of the compound helicopter-slung load system is discussed. As in the hovering flight case, the verification is performed by comparing the pole locations of linearized system in complex plane to those of the reference study in the literature. Once it is determined that the accuracy of the mathematical model is sufficient, application of the input shaping and model predictive control algorithm is discussed. Like the hovering flight, firstly input shaping is applied based on the closed loop system pole locations. Then the resultant slung load trajectories are provided as reference to the model predictive control algorithm. Considering that this approach results in a divergent behavior after a certain point, the MPC algorithm is modified by adding the helicopter pitch and roll attitudes resulting from input shaping to their respective input channels as well. The simulation results with both full state output and Kalman Filter cases have shown that, the proposed algorithm is capable of tracking the relevant reference trajectories

perfectly. As the last step, the MPC algorithm is implemented to the full-nonlinear model as in the hovering flight case. Through the simulation results, it is observed that even though there is certain amount of inconsistency with the linearized model, the proposed control algorithm functions satisfactorily with the full-nonlinear model as well.

7.2 Future Work

There are certain aspects that can be improved regarding this particular study. As mentioned previously, the consistency of the developed mathematical model with verified models and flight test data can further be enhanced. To do so, a detailed aerodynamic database that involves separate coefficient tables for fuselage, horizontal tail and vertical tail can be generated based on a wide range of angle of attack and angle of sideslip values. In addition, main rotor interference on the aerodynamic surfaces can also be modeled more effectively to capture the dynamics more accurately. Fidelity of the rotor models can also be improved by using more complicated modeling approaches such as blade element method.

The slung load model presented in this study can also be improved. That is, even though the dynamic characteristics of the slung are obtained properly, there are certain additional points that can be taken into account for further enhancement. Regarding the hovering and low speed flight regime, a model for main rotor downwash can be integrated. Moreover, as in the case of the helicopter by itself, aerodynamic properties of the slung load can be implemented in a more detailed manner, which gains importance with increasing airspeed. As a final remark regarding the mathematical modeling aspect, generated compound helicopter-slung load model can be validated and examined for highspeed flight regime.

The last but not least, the proposed MPC algorithm can be examined for a variety of airspeeds with improved mathematical model such that gain scheduling can be performed to cover a wide operational envelope. In addition, unscented or extended

Kalman Filters can be designed for efficient slung load state estimation from the nonlinear model.

REFERENCES

[1] Sturgeon, W. R., and Phillips, J. D., "A Mathematical Model of the CH-53 Helicopter," 1980.

[2] Cliff, E. M., and Bailey, D. B., "Dynamic Stability of a Translating Vehicle with a Simple Sling Load," *Journal of Aircraft*, Vol. 12, No. 10, 1975, pp. 773–777. https://doi.org/10.2514/3.44492

[3] Prabhakar, A., "Stability of a Helicopter Carrying an Underslung Load," 1977.

[4] Ronen, T., Bryson, Jr., A., and Hindson, W., "Dynamics of a Helicopter with a Sling Load," presented at the 13th Atmospheric Flight Mechanics Conference, Williamsburg,VA,U.S.A., 1986. https://doi.org/10.2514/6.1986-2288

[5] Shaughnessy, J. D., Deaux, T. N., and Yenni, K. R., "Development and Validation of a Piloted Simulation of a Helicopter and External Sling Load," 1979.

[6] Laub, G. H., and Kodani, H. M., "Wind Tunnel Investigation of Aerodynamic Characteristics of Scale Models of Three Rectangular Shaped Cargo Containers," 1972.

[7] Cicolani, L. S., "Equations of Motion of Slung-Load Systems, Including Multilift Systems," NASA, 1992.

[8] Stuckey, R. A., "Mathematical Modelling of Helicopter Slung-Load Systems," 2001.

[9] Bisgaard, M., Bendtsen, J. D., and La Cour-Harbo, A., "Modeling of Generic Slung Load System," *Journal of Guidance, Control, and Dynamics*, Vol. 32, No. 2, 2009, pp. 573–585. https://doi.org/10.2514/1.36539

[10] Cao, Y., Nie, W., Wang, Z., and Wan, S., "Dynamic Modeling of Helicopter-Slung Load System under the Flexible Sling Hypothesis," *Aerospace Science and Technology*, Vol. 99, 2020, p. 105770.

[11] Gupta, N. K., and Bryson, A. E., "Near-Hover Control of a Helicopter with a Hanging Load," *Journal of Aircraft*, Vol. 13, No. 3, 1976, pp. 217–222. https://doi.org/10.2514/3.44521

[12] Ivler, C., Tischler, M., and Powell, J. D., "Cable Angle Feedback Control Systems to Improve Handling Qualities for Helicopters with Slung Loads," presented at the AIAA Guidance, Navigation, and Control Conference, Portland, Oregon, 2011. https://doi.org/10.2514/6.2011-6686

[13] Brenner, H., "Helicopter Sling Load Pendulum Damping," 2009.

[14] Bisgaard, M., La Cour-Harbo, A., and Bendtsen, J., "Swing Damping for Helicopter Slung Load Systems Using Delayed Feedback," presented at the AIAA Guidance, Navigation, and Control Conference, Chicago, Illinois, 2009. https://doi.org/10.2514/6.2009-5795

[15] Omar, H. M., "Anti-Swing Controller Based on Time-Delayed Feedback for Helicopter Slung Load System near Hover," *Journal of Aerospace Technology and Management*, Vol. 4, 2012, pp. 297–305.

[16] Adams, C., Potter, J., and Singhose, W., "Input-Shaping and Model-Following Control of a Helicopter Carrying a Suspended Load," *Journal of Guidance, Control, and Dynamics*, Vol. 38, No. 1, 2015, pp. 94–105. https://doi.org/10.2514/1.G000326
[17] Ren, Y., Li, K., and Ye, H., "Modeling and Anti-Swing Control for a Helicopter Slung-Load System," *Applied Mathematics and Computation*, Vol. 372, 2020, p. 124990.
[18] Bailey, F. J., "A Simplified Theoretical Method of Determining the Characteristics of a Lifting Rotor in Forward Flight," US Government Printing Office Washington, DC, USA, 1941.
[19] Seckel, E., and Curtiss, H. C., "Aerodynamic Characteristics of Helicopter Rotors," Princeton University. Department of Aerospace and Mechanical Sciences, 1963.
[20] Amer, K. B., and Gustafson, F. B., "Charts for Estimation of Longitudinal-Stability Derivatives for a Helicopter Rotor in Forward Flight," 1951.
[21] Heffley, R. K., Jewell, W. F., Lehman, J. M., and Vanwinkle, R. A., "A Compilation and Analysis of Helicopter Handling Qualities Data. Volume 1: Data Compilation," 1979.
[22] Barbini, W. J., Balfe, P. J., Lovrien Jr, C. E., and CA, A. F. F. T. C. E. A., "Category II Performance and Flying Qualities Tests of the HH-53C Helicopter. Supplement. Evaluation of the HH-53C Single-Engine Height-Velocity Characteristics," 1970.
[23] Padfield, G. D., "Helicopter Flight Dynamics: The Theory and Application of Flying Qualities and Simulation Modelling," John Wiley & Sons, 2008.
[24] Yechout, T. R., "Introduction to Aircraft Flight Mechanics," Aiaa, 2003.
[25] Talbot, P. D., Tinling, B. E., Decker, W. A., and Chen, R. T., "A Mathematical Model of a Single Main Rotor Helicopter for Piloted Simulation," 1982.
[26] Stevens, B. L., Lewis, F. L., and Johnson, E. N., "Aircraft Control and Simulation: Dynamics, Controls Design, and Autonomous Systems," John Wiley & Sons, 2015.
[27] Gursoy, G., Tarimci, O., and Yavrucuk, I., "Helicopter Slung Load Simulations Using Heli-Dyn+," presented at the AIAA Modeling and Simulation Technologies Conference, Minneapolis, Minnesota, 2012. https://doi.org/10.2514/6.2012-4851
[28] Singh, T., and Singhose, W., "Input Shaping/Time Delay Control of Maneuvering Flexible Structures," Vol. 3, 2002, pp. 1717–1731.
[29] Magalas, L. B., and Malinowski, T., "Measurement Techniques of the Logarithmic Decrement," *Solid State Phenomena*, Vol. 89, 2003, pp. 247–260.
[30] Robinett III, R. D., Feddema, J., Eisler, G. R., Dohrmann, C., Parker, G. G., Wilson, D. G., and Stokes, D., "Flexible Robot Dynamics and Controls," Springer Science & Business Media, 2012.
[31] Parsopoulos, K. E., and Vrahatis, M. N., "Particle Swarm Optimization Method in Multiobjective Problems," presented at the SAC02: 2002 ACM

Symposium on Applied Computing, Madrid Spain, 2002. https://doi.org/10.1145/508791.508907
[32] Welch, G., and Bishop, G., “An Introduction to the Kalman Filter,” 1995.
[33] Ogata, K., and Yang, Y., “Modern Control Engineering,” Prentice hall India, 2002.
[34] “Introduce White Noise into Continuous System - Simulink.” https://www.mathworks.com/help/simulink/slref/bandlimitedwhitenoise.html
[35] “What Is Model Predictive Control? - MATLAB & Simulink.”
[36] “Model Predictive Control System Design and Implementation Using MATLAB®,” Springer London, London, 2009. https://doi.org/10.1007/978-1-84882-331-0
[37] Camacho, E. F., and Bordons, C., “Constrained Model Predictive Control,” *Model Predictive control*, Springer London, London, 2007, pp. 177–216. https://doi.org/10.1007/978-0-85729-398-5_7
[38] Sarbanzadeh, M., Hosseinzadeh, M. A., Sarebanzadeh, E., and Rivera, M., “Trends and Challenges of Predictive Control in Power Electronics,” 2018.

APPENDICES

A. Helicopter Mathematical Model Parameters

Required parameters for helicopter mathematical model development are provided here. In the following set of tables, the subscript m stands for the main rotor whereas the parameters related to the tail rotor are denoted by subscript t.

Table A.1. Values of Parameters for CH-53 Helicopter

a_m, [1/rad]	5.73	i_{t0}, [deg]	3
a_t, [1/rad]	5.73	K_f, [m]	0.099
B_m	0.97	K_1, [rad]	0.0436
B_t	0.97	K_2, [rad/cm]	0.00989
b_m	6	K_3, [rad]	0.0524
b_t	4	K_4, [rad/cm]	0.0146
c_m, [m]	0.66	K_5, [rad]	-0.0175
c_t, [m]	0.391	K_6, [rad/cm]	0.00930
e_{kf}	0.5	K_7, [rad/cm]	-0.000989
e_{kt}	1.8	K_8, [rad]	0.0262
e_m, [m]	0.610	K_9, [rad/cm]	0.0364
e_t, [m]	0.122	K_{10}, [rad/cm]	0.00989
I_{bm}, [kg×m^2]	5489	M_{wm}, [kg×m]	819
I_{bt}, [kg×m^2]	22.72	M_{wt}, [kg×m]	18.76
I_{mr}, [kg×m^2]	40478	m_h, [kg]	15227
$I_{xx,h}$, [kg×m^2]	48891	R_m, [m]	11.01
$I_{yy,h}$, [kg×m^2]	239491	R_t, [m]	2.44
$I_{zz,h}$, [kg×m^2]	223361	δ_{3m}, [rad]	0
$I_{xz,h}$, [kg×m^2]	22518	δ_{3t}, [rad]	0.78

Table A.2. Values of Parameters for CH-53 Helicopter (Continued)

$x_{r_{m,h}}$, [m]	-0.112	θ_{sm}, [deg]	-5
$y_{r_{m,h}}$, [m]	0	θ_{st}, [deg]	0
$z_{r_{m,h}}$, [m]	-2.438	θ_{1m}, [rad]	-0.105
$x_{r_{t,h}}$, [m]	-13.68	θ_{1t}, [rad]	-0.140
$y_{r_{t,h}}$, [m]	-0.853	σ_m	0.1145
$z_{r_{t,h}}$, [m]	-2.819	σ_t	0.2042
$x_{wt,h}$, [m]	-0.102	τ_{vm}, [sec]	0.20
$y_{wt,h}$, [m]	0	τ_{vt}, [sec]	0.20
$z_{wt,h}$, [m]	0.0584	ϕ_{sm}, [deg]	0
Ω_m, [rad/sec]	19.3	ϕ_{st}, [deg]	90
Ω_t, [rad/sec]	82.9		

B. Aerodynamic Coefficient Tables for Fuselage

Aerodynamic coefficient tables utilized in the fuselage module of the helicopter mathematical model are provided here.

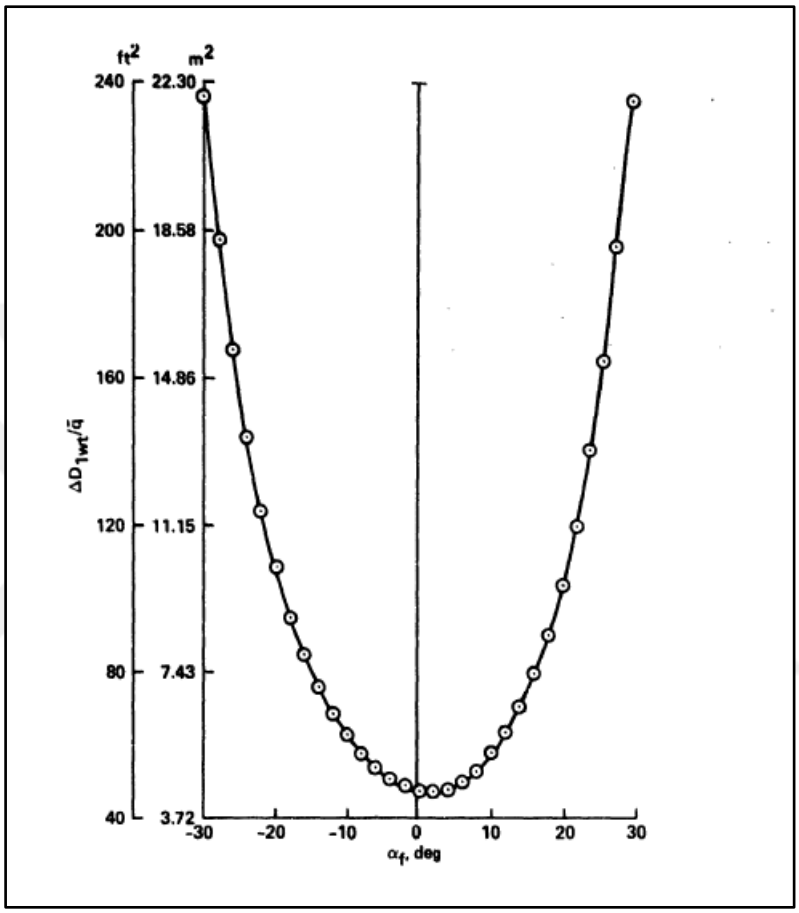


Figure B.1. Fuselage Incremental Drag as a Function of Angle of Attack [1]

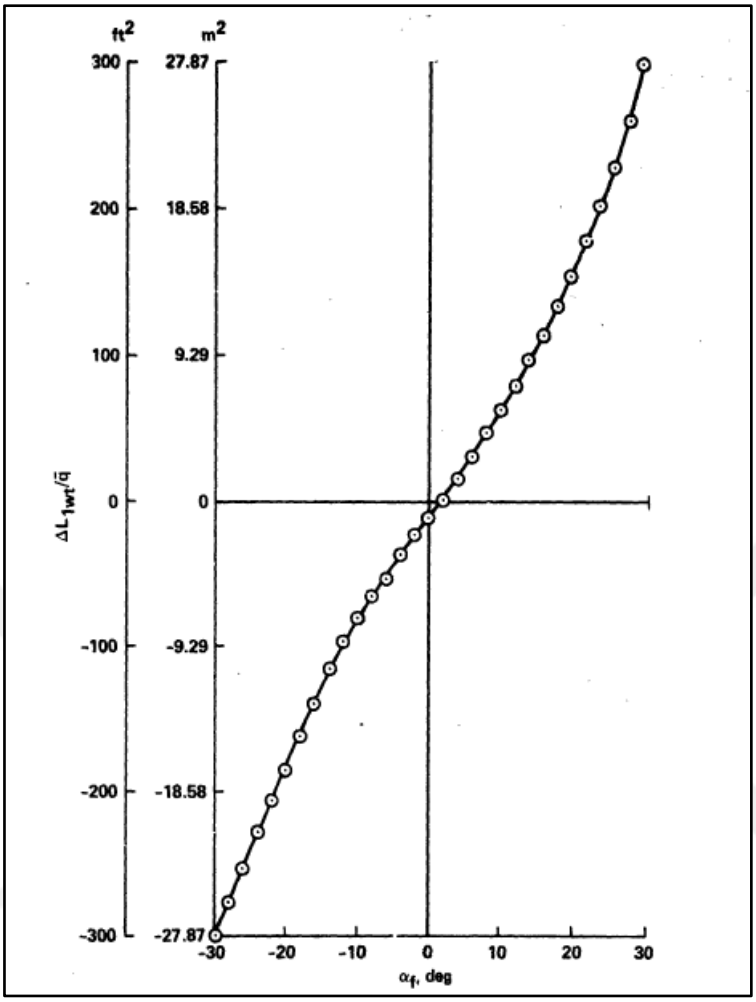


Figure B.2. Fuselage Incremental Lift as a Function of Angle of Attack [1]

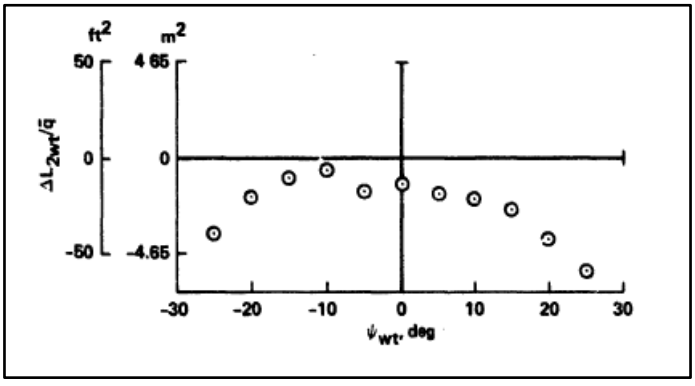


Figure B.3. Fuselage Incremental Lift as a Function of Sideslip [1]

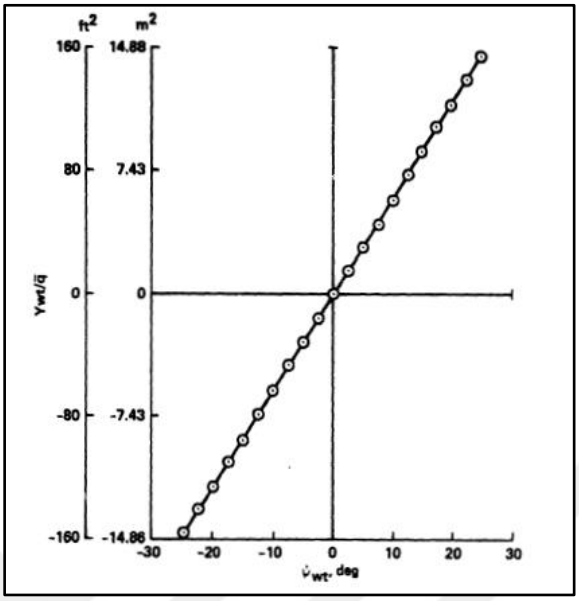


Figure B.4. Fuselage Side Force as a Function of Sideslip [1]

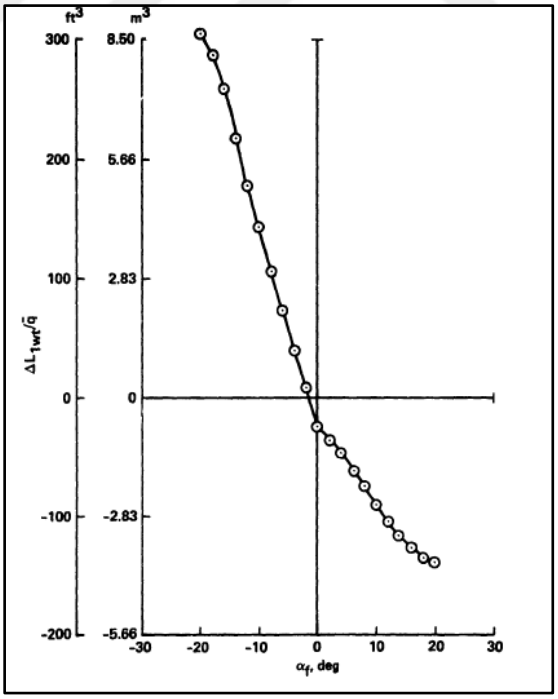


Figure B.5. Fuselage Incremental Rolling Moment as a Function of Angle of Attack [1]

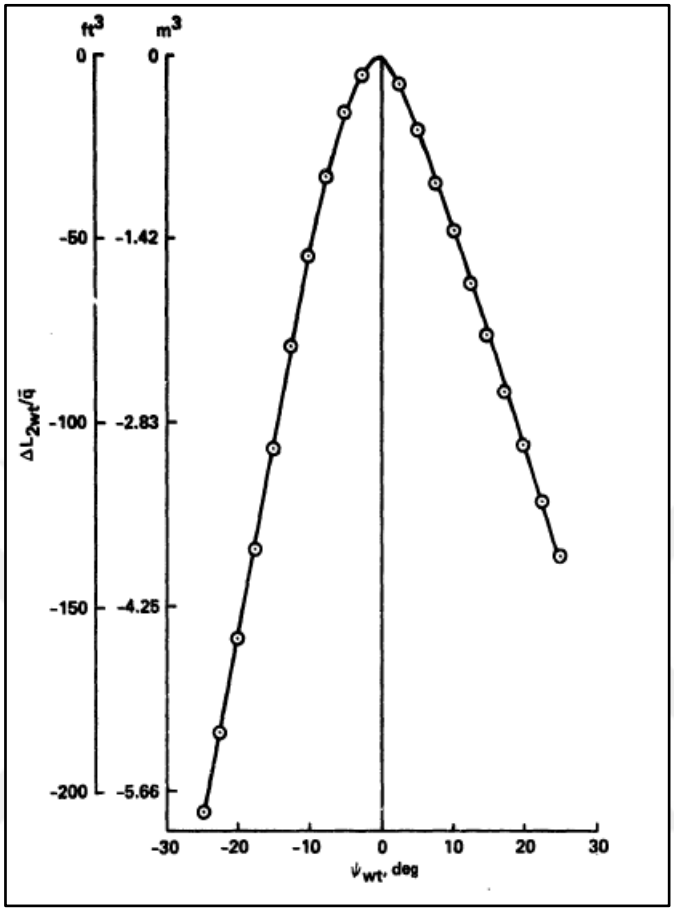


Figure B.6. Fuselage Incremental Rolling Moment as a Function of Sideslip [1]

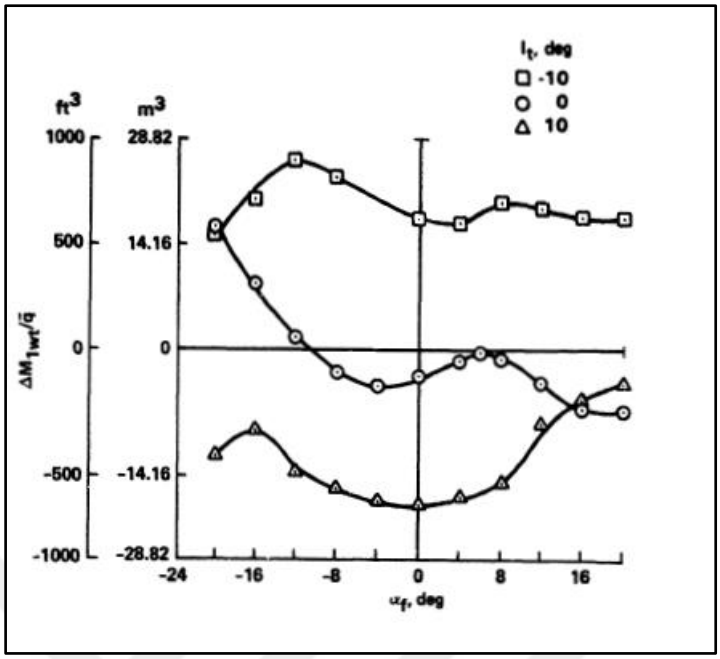


Figure B.7. Fuselage Incremental Pitching Moment as a Function of Angle of Attack and Incidence at the Tail [1]

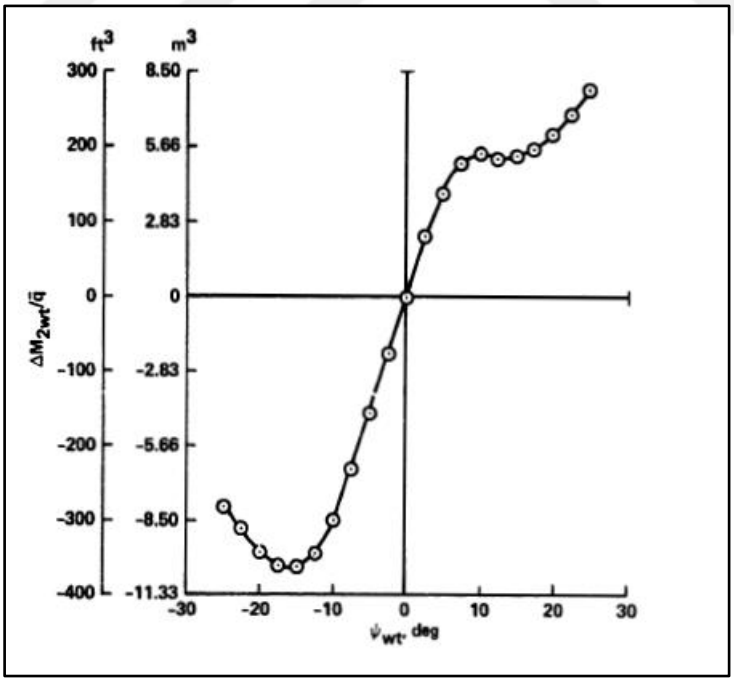


Figure B.8. Fuselage Incremental Pitching Moment as a Function of Sideslip [1]

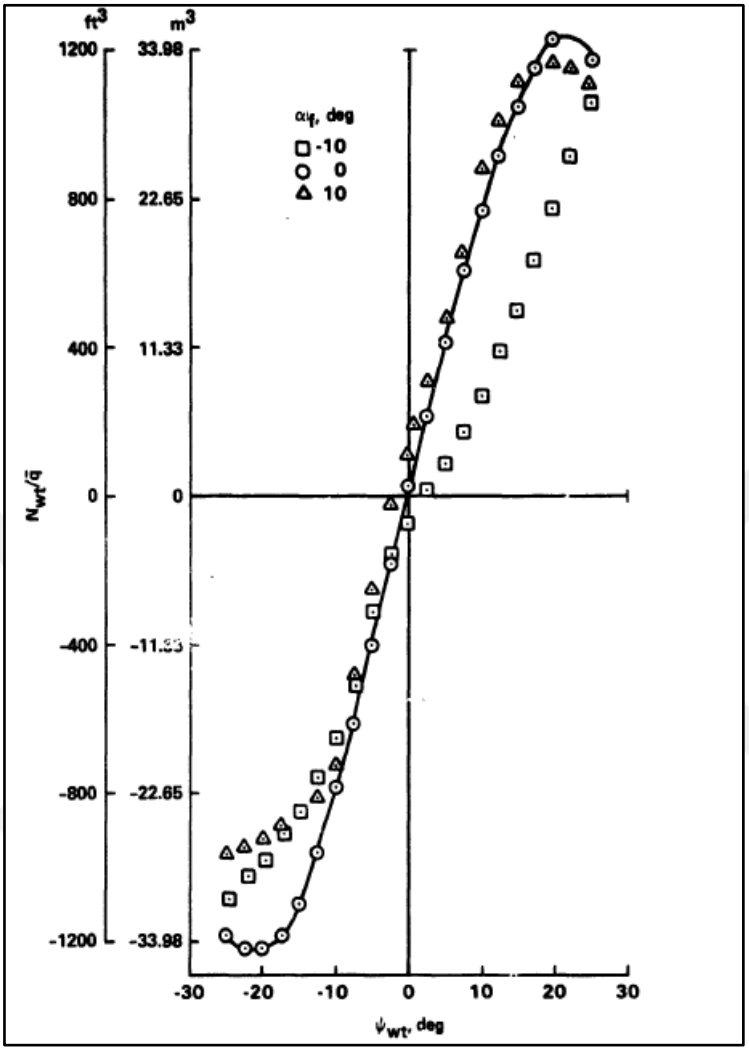


Figure B.9. Fuselage Yawing Moment as a Function of Sideslip and Angle of Attack [1]

C. Slung Load Mass and Inertia Values

Mass and inertia values of the slung load required for the mathematical model development are provided in the table below.

Table C.1. Values of Parameters for Slung Load

m_l, [kg]	4536
$I_{xx,l}$, [kg×m^2]	1124
$I_{yy,l}$, [kg×m^2]	14610
$I_{zz,l}$, [kg×m^2]	14610
$I_{xz,l}$, [kg×m^2]	0